Author:
Matos Silva Junior, Agesinaldo

Title:
A modelling approach to design of ultrasonic tweezers devices

A modelling approach to design of ultrasonic tweezers devices

By

AGESINALDO MATOS SILVA JUNIOR

Department of Mechanical Engineering
UNIVERSITY OF BRISTOL

A dissertation submitted to the University of Bristol in accordance with the requirements of the degree of DOCTOR OF PHILOSOPHY in the Faculty of Engineering.

JANUARY 2020

WORD COUNT : 48013

Abstract

Acoustic manipulators are devices designed to generate ultrasonic waves that alter the dynamics of small-scale objects which are applied to a wide range of applications. Acoustic tweezers are focused wave fields which enable high-contrast trapping forces and enhanced manipulation dexterity. In-plane closed devices manipulate particles in a contained two-dimensional acoustic chamber but may produce high-fidelity traps only in a narrow area. Devices built with complex manufacturing processes may render simplified models to predict accurately experimental results. Parts assembly may limit devices' performance whose simplified assumptions fails to predict. This work implements a modelling approach combining physics-based models to investigate system-wide responses applied to high-fidelity reproduction of acoustic traps in a new array transducer. Monolithic Ultrasonic Tweezers Device is proposed as a multi-electrode transducer with mechanically coupled elements for ultrasonic tweezing. An acoustic chamber surrounded by a backed monolithic piezoceramic is modelled by a unique interface which separates the internal acoustic from the external piezoelectric fields. This thesis presents numerical simulations of pressure fields and performances for various shapes, sizes and material properties. Three physics-based models investigate the system's response in alternative approximation levels. The Equivalent Source and the Finite Element methods solve for fluid and piezoelectric external domains, respectively. Two protocols are investigated based on the position of sources relative to the interface. Internal sources define internal wave incidence and reflection in the analysis protocol whereas external sources define wave scattering and internal transmission in the synthesis protocol. A simplified model associates analysis with synthesis performances. The inverse filtering technique is employed to pressure field synthesis. Mathematical models relate boundary data across protocols and correlate generating with solution waves in a performance-based parameter study. Mapping analysis performance between models is achieved by tuning electromechanical coefficients. A new wave superposition technique is employed to the reproduction of wide-area high-fidelity acoustic traps in a large-scale realistic model.

Author's Declaration

I declare that the work in this dissertation was carried out in accordance with the requirements of the University's Regulations and Code of Practice for Research Degree Programmes and that it has not been submitted for any other academic award. Except where indicated by specific reference in the text, the work is the candidate's own work. Work done in collaboration with, or with the assistance of, others, is indicated as such. Any views expressed in the dissertation are those of the author.

SIGNED: ..... DATE: .....

Dedication and Acknowledgements

I am profoundly grateful to my supervisors, Professor Bruce Drinkwater and Professor Paul Wilcox, for their persistent encouragement and guidance throughout the duration of this project. It was their experience and inspiration that kept the research going.

My research would have been impossible without the aid and support of Dr Mihai Caleap who shared his insight into many related fields of interest and Dr Alexander Velichko who incented me to widen my research by making hard questions.

My sincere thanks to past and present colleagues in the UNDT group who never hesitated to give a helping hand.

Heartfelt thanks go to my parents Agesinaldo and Laura , who gave me all the opportunities one can wish for and to my brother Yuri, who helped me keep my feet on the ground when things were a bit off.

Finally, a special dedication goes to Fernanda De Santi for supporting me spiritually during the challenges of Ph.D. life.

This study was financed in part by the Coordenação de Aperfeiçoamento de Pessoal de Nível Superior - Brasil (CAPES) - Finance Code 001.

TABLE OF CONTENTS

LIST OF TABLES

TABLE **Page**

List of Figures

Figure **Page**

ABBREVIATIONS

AL Absorption Layer. 69, 71, 73, 99

ALID Absorption Layer with Increasing Damping. 69, 71, 73, 77, 80, 81, 92, 96, 99, 105, 134, 136

ARP Acoustic Radiation Potential. 10, 123, 135, 137

BEM Boundary Element Method. 15–17

BIE Boundary Integral Equation. 15

BVP Boundary Value Problem. 35

DPSM Distributed Point Source Method. 16

ES Equivalent Source. 7, 10, 43, 47, 118, 131

ESM Equivalent Source Method. 23, 24, 35–37, 39, 59, 77, 134

ESWS Equivalent Source Wave Scattering. 10, 19, 20, 27, 34–36, 39, 41, 44–48, 50, 51, 53–58, 61–63, 68, 70, 74, 76, 77, 82–95, 104, 112, 117–120, 135, 136, 138

FBB Fractional Bessel Beam. 127

FE Finite Element. 5, 64–66, 68, 70, 72, 75, 77, 87, 96, 99, 100, 103, 105, 110, 112, 115, 118, 130, 131, 134

FEM Finite Element Method. 10, 12, 16, 23, 27, 29, 30, 61–64, 68, 69, 71, 74, 76, 77, 97, 100, 110, 113, 114, 136–138

IAP Intermediate Analysis Performance. 93–96, 137

KHI Kirchhoff-Helmholtz Integral. 10, 12, 22, 23, 25, 34, 70, 75, 76

MoM Method of Moments. 16

MUTD Monolithic Ultrasonic Tweezer Devices. 6, 10, 18, 34, 61, 62, 68, 72, 77, 97, 99–102, 105, 107, 111, 118, 120, 121, 123, 124, 129, 130, 134, 135, 137, 138

PML Perfectly Matched Layers. 69, 73, 77–80, 92, 96, 136

PSP Potential Sculpting Performance. 128, 129, 131

PZT Lead Zirconate Titanate. 116

RAP Realistic Analysis Performance. 118, 121

RMS Root Mean Squared. 53, 79, 80, 83, 91, 115, 136

RPP Realistic Potential Sculpting Performance. 129, 131, 137

RSP Realistic Synthesis Performance. 120, 121, 123, 124, 129, 131, 137

SAP Simplified Analysis Performance. 55, 56, 94, 95, 116–118, 121, 136, 137

SARP Standard Acoustic Radiation Potential. 127–129

SAW Surface Acoustic Wave. 5

SSP Simplified Synthesis Performance. 57, 136

SVD Singular Value Decomposition. 43, 112, 131, 137

TPFE Transducer Parameter Finite Element. 10, 27, 34, 61, 97–107, 110–115, 118–123, 129, 130, 135, 137

UARP User-defined Acoustic Radiation Potential. 123–125, 127–130

VS Virtual Source. 7, 10, 23, 61, 96

VSFE Virtual Source Finite Element. 10, 20, 34, 61–63, 65, 68–70, 72, 74–96, 101–107, 118, 119, 135–138

CHAPTER 1

INTRODUCTION

This thesis presents a comprehensive modelling framework of a monolithic design concept for two-dimensional, in-plane, closed acoustic manipulators by investigating physics-based models using a modular approach which addresses design problems due to acoustic chamber response. This is achieved by building numerical models focused on designing monolithic ultrasonic array transducers applied to micro particles manipulation. The main objectives of this research are to review practical devices and existing models, validate and optimize a more realistic model to evaluate optimal devices. A combination of wavefield modelling and robust design method is applied to search for disruptive interface response in particular manipulation devices. The optimal design sought is characterized by having the least sensitive performance loss due to material properties perturbation.

Designing the propagation of acoustic pressure field has been a traditional practice by which a sound experience is imposed on a designated public in a particular space. In open spaces sound field can be exemplified by a speaker in an amphitheatre delivering their speech whereas in closed spaces a contemporary cinema theatre reproducing a complex soundtrack. Acoustic manipulators are devices designed to alter the dynamics of micrometre scale objects by illuminating them with ultrasonic waves providing opportunities for application in the biosciences and material science. Significant forces on micro-scale particles in inviscid fluid are expected when applying acoustical waves at ultrasonic frequencies. Applications of these forces include cell sorting [Coakley et al., 2000; Johnson and Feke, 1995], filtering [Coakley, 1997; Nilsson et al., 2004], bio-engineering [Marx, 2015; Saito et al., 1998], and composites assembly [Llewellyn-Jones et al., 2016; Scholz et al., 2014]. Designing dynamic-fields for micro-scale ultrasonic manipulators has been extensively reviewed by Drinkwater [2016]. The author draws attention to the difficulty in fabricating and electronically controlling devices based on multi-element arrays. In another

review, Andrade et al. [2018] pointed out a plethora of functionalities acoustic levitation can be used for by manipulating milli-scale objects in mid-air. Such air based levitation devices commonly require less complex manufacturing processes. Designing reconfigurable devices, as opposed to application specific functionality, and miniaturizing broad manipulation capability devices are the challenges research on acoustic manipulators faces recently. The solution for widespread use of such devices calls for an urgent robust design approach with minimum complexity level [Drinkwater, 2016]. This thesis presents a robust modelling approach to the design of a micro-scale acoustic manipulator for high-fidelity and reconfigurable field focused on simplifying both model and manufacturing process.

Understanding the acoustic forces impinging on target particles plays an important role in the development of ultrasonic manipulators. Lord Rayleigh initiated early studies on radiation pressure due to a propagating acoustic wave [Rayleigh, 1902]. The basis of knowledge for acoustic manipulation lays emphasis on the forces acting on small particles as the scattering phenomenon is simplified to simple source contributions and gives analytical expressions for the resulting force. Analytical expressions were derived for the effects of the acoustic radiation force on incompressible [King, 1934] and compressible [Yosioka and Kawasima, 1955] spheres in an inviscid fluid. Gor'Kov, L P extended this theory and derived an elegant expression for the potential of acoustic forces as a gradient field produced by an arbitrarily shaped wave field on compressible sphere, such as a biological cell. Furthermore, the radiation force applied to trapping sufficiently small spheres in the Rayleigh regime ($a \leqslant 0.15\lambda$) is largely due to the gradient component of pressure field [Baresch et al., 2013].

Ultrasonic particle manipulation has historically been investigated by several acoustic mechanism and two distinct approaches are singled out: standing and progressive waves. Although standing waves have been extensively applied due to their simple and established theory, much of the recent theoretical development of acoustical radiation forces has been drawn to progressive waves approach such as the single beam acoustical tweezers surveyed by Thomas et al. [2017]. To enhance particle manipulation in acoustic tweezers, further formulation of radiation force was provided by using zero-order Bessel standing acoustic waves [Mitri, 2008]. Either mechanism has also been collectively and theoretically studied by means of dynamics of concentration fields that weakly perturb the fluid density and speed of sound [Karlsen and Bruus, 2017].

Counter-propagating waves have been shown promising manipulation mechanism as they allow the generation of a stable standing wave by superposing two independent and oppositely travelling waves [Kozuka et al., 1998], as shown in Figure 1.1. By extending this principle, multi-sided ultrasonic devices have recently been developed to perform manipulation in two-dimensions, by exploiting counter-propagating waves. Early studies investigated devices generating controllable counter-propagating waves based on one pair and two or four pairs of opposing transducers allowing manipulation in one [Courtney et al., 2010; Greenhall et al., 2013] and two [Courtney et al., 2011] dimensions respectively. Bernassau and Cumming [2011] demonstrated experi-

mentally manipulation to various particle patterning in a two-dimensional heptagon-shaped device by relying on non-parallel multiple reflections to minimize the chamber resonance, as shown in Figure 1.1. A simplified octagonal-shaped device was developed to investigate more complex shapes by combining different pairs of transducers and by delaying the phase of the transducer parameters [Bernassau et al., 2013]. Later development studied non-linear acoustics both experimentally and numerically to mitigate limitations on manipulation area due to acoustic streaming [Bernassau et al., 2014].

On the other hand, acoustical tweezers, analogous to optical tweezers [Ashkin et al., 1986; Neuman and Block, 2004], have been used to trap particles in a potential well by using opposing focused [Wu, 1991] and single-focused [Kang and Yeh, 2010] ultrasonic beam. Furthermore, a circular ultrasonic array designed to generate or reproduce acoustic vortices has also been investigated in order to improve particle manipulation dexterity [Grinenko et al., 2012]. The authors demonstrated both analytically and numerically an array principle based on shifting the center of Bessel functions that focused trapping forces have enhanced dexterity to manipulate particles over a region of interest. The authors suggested further FE analysis is required to provide practical solutions for problems of unknown boundary conditions. Courtney et al. [2013] concluded by investigating a fabricated vortex beam device that increasing the number of elements and adding acoustic matching and damping layers would improve its performance by broadening the spatial range of manipulation. Their circular piezoelectric array concept has proven the capabilities of acoustical tweezers for in-plane, closed devices and has yet to see a design iteration.

The monolithic array construction, or *kerfless* configuration where *kerf* means a slice through

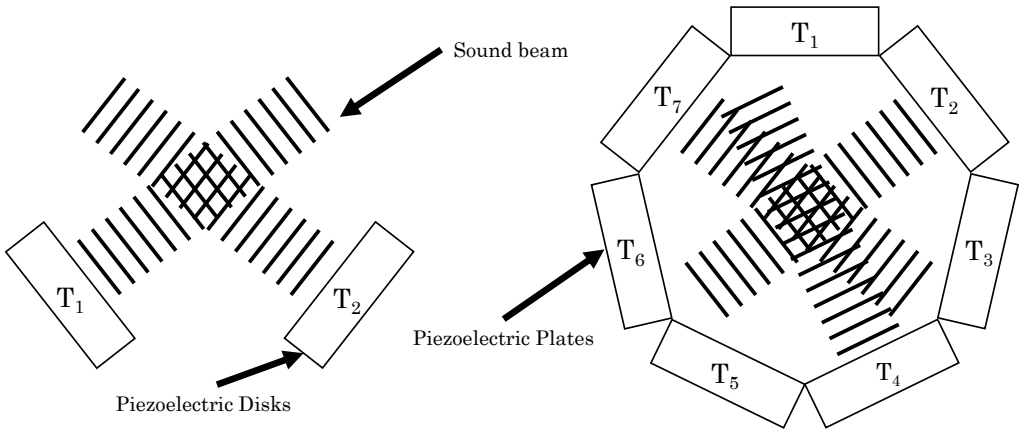

Figure 1.1: Schematic representation of non-resonant counter-propagating waves as a particle manipulation mechanism. Configuration on the left shows two transducers aligned to oblique angles which avoids parallel reflection [Kozuka et al., 1998]. The device on the right is assembled with seven transducers transmitting crossed sound beams allowing multiple pressure field configuration [Bernassau and Cumming, 2011].

the material, was originally conceived for energy trapping in multiple electrode filter crystals [Shockley et al., 1963]. This concept was employed to high spatial resolution acoustic imaging [Auld et al., 1974]. Later saw prospective applications in acoustic manipulation devices [Kozuka et al., 1996]. More recently, particle manipulation along a microfluidic channel was achieved in a planar acoustic resonator by sequentially switching between active electrodes of a *kerfless* array [Glynne-Jones et al., 2012b], as shown in Figure 1.2. Ultrasonic trapping in three-dimensions has been achieved with a two-element monolithic transducer attached to an acoustic Fresnel lens [Franklin et al., 2017], also shown in Figure 1.2. This kerfless design is a relevant option for the proposed ultrasonic tweezer since it has been experimentally employed for acoustic manipulation and greatly simplifies the manufacturing process of the array transducers.

Physical boundaries in otherwise free space medium, or discrete material, cause waves to be affected in certain patterns depending on their nature. Boundary behaviour refers to the collective effects caused by the interface response to waves. Works on in-plane closed ultrasonic manipulators have been reported not modelling such boundary behaviour and the existence of unwanted resonant modes within the chamber may limit the device manipulation capabilities. This suggests the ability to effectively reproduce a desired pressure field inside closed devices regardless of the input method depends on the practical representation of the boundary conditions. Towards solving this issue, a direct method for solving the inverse ultrasound wave field simulation have been derived for a 3D acoustic manipulation device with arbitrary simple geometry and transducer arrangement [Prisbrey et al., 2017]. The authors suggested the patterns of assembled particles using this technique is limited by the reservoir boundaries if operated at its resonant frequency.

A variety of ultrasonic models have been developed to better understand the physical design of ultrasonic manipulation devices. Hill [2003] derived an analytical method which predicts the force profile in layered resonators using a one-dimensional combined acoustic and electro-acoustic model. Moreover, Andrade and Pérez [2011] investigated a single axis acoustic levitator and

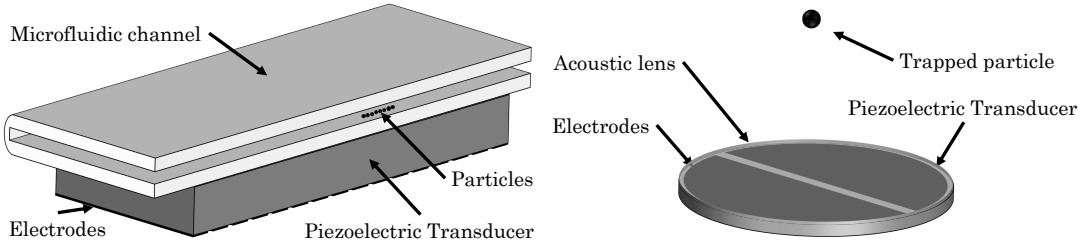

FIGURE 1.2. Schematic representation of two different designs of kerfless transducer for ultrasonic tweezers manipulation. The device on the left shows the microfluidic channel directly attached to a monolithic array transducer allowing locally activation of acoustic resonator [Glynne-Jones et al., 2012b]. On the right, an acoustic lens is attached to a two-element piezoelectric disk to create a three-dimensional trap [Franklin et al., 2017].

developed a matrix method based on the monochromatic transfer matrix [Ibáñez et al., 2010] to determine the acoustic radiation potential between transducer and reflector surface. The authors then applied this method to model a one-dimensional manipulation system consisting of two independent phase controllable resonators for acoustic levitation. According to Courtney et al. [2011], particles can be trapped and manipulated in grid-like shapes within enclosed device by using two pairs of acoustically matched transducer. In this work, analytical results were obtained using one-dimension electro-acoustic model and a Finite Element (FE) model predicted the pressure field and applied force numerically. Riaud et al. [2015] theoretically predicted the behaviour of anisotropic Bessel beams on a Surface Acoustic Wave (SAW) device based on the refraction field to a homogeneous fluid domain. In general, simplified models are key to understand overall the physical phenomenon whereas realistic models are developed to confirm effective characteristics of experiments.

Optimization techniques have been extensively developed to systematise the generation of optimised designs for piezoelectric actuators [Silva, 2003]. A well established research topic is concerned about optimal synthesis methods of microelectromechanical systems. Earlier modelling-based optimization research on array design have preceded works on layered resonators for ultrasonic particle manipulation. In this sense, Abrar and Cochran [2007] utilized simulated annealing similarly applied to array design to investigate optimal multilayer piezoelectric devices. Hill et al. [2008] took a step into optimal ultrasonic manipulators by discussing the influence of specific parameters, such as layer dimensions and material properties, on the robust design of 1-D acoustic resonators. The maximum energetic performance on resonant devices was searched exhaustively in the parameters space [Glynne-Jones et al., 2012a]. The design of a 3-D microfluidic device has been investigated by using evolutionary algorithm optimization and associating design parameters directly with acoustophoretic performance [Hahn et al., 2014]. Additionally, alternative mathematical techniques have been used to maximize the spring constant of acoustic levitation [Andrade et al., 2010] where the optimal solution was found by using optimization methods.

On the other hand, optimization has also been employed to find the transducer operating parameters in a closed in-plane ultrasonic manipulator that minimizes indirectly the error between the system response and some required boundary pressure [Grinenko et al., 2012] or directly the average value of an acoustic radiation potential Greenhall et al. [2016]. Single-beam acoustic levitation has also been investigated by optimization methods in designing optimal traps with different array geometries [Marzo et al., 2015]. Nonetheless, no optimization problem has been formulated to minimise the contribution of the boundary behaviour, i.e. interface response to the acoustic field within ultrasonic manipulation devices. Therefore, there is a need to develop a modelling approach to robust design to provide the background for an optimal design of ultrasonic transducer array for particle manipulation devices.

A further design inspiration comes from the design of optical resonators [Nöckel and Stone,

1997]. The interaction between time-harmonic fields and bodies embedded in different media shares similarities in both acoustic (Helmholtz equation) and electromagnetic (Maxwell equations) waves, as it has been pointed out elsewhere [Bowman et al., 1987; Doicu et al., 2000]. In electromagnetics, a dielectric cavity is a system that is equivalent to the acoustic fluid bodies in a fluid host which is the simplest wave phenomenon discussed in this thesis. On this subject, resonances within optical microcavities have drawn some attention in photonics as the search for long-lived resonant modes with high quality factor for light source arrays offers a wide range of possible applications, such as quantum dots for light displays and photonic interconnects between integrated circuits [Yamamoto and Slusher, 1993]. One of these resonances corresponds to rays internally confined to the cavity travelling around the perimeter undergoing reflections at the interface. These are also referred to as whispering gallery modes, by Lord Rayleigh, who explained that acoustic modes cause the efficient propagation of sound along the walls of St. Paul's Cathedral [Rayleigh, 1910]. Moreover, there are various types of microcavities which are activated by myriad of resonant modes [Cao and Wiersig, 2015]. The surface shape and material of these resonators can be engineered to change their spectra and optical band [Matsko and Ilchenko, 2006]. Wiersig [2003a] published a study that showed resonances on hexagonally shaped dielectric microcavities are sensitive to rounding of the corners. Also, Lebental et al. [2007]

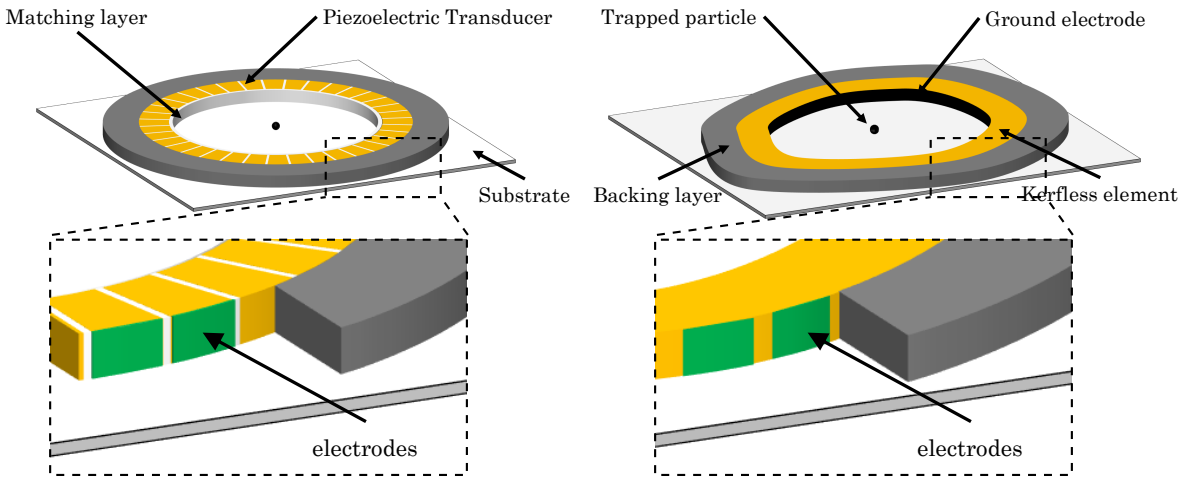

FIGURE 1.3. Physical representation of the design concept for MUTD. Device on the left is a practical circular array implementation [Grinenko et al., 2012] with backing layer (grey), matching layer (white), piezoelectric transducer (orange) and electrodes (green) are fitted on both inner and outer edges of each element of the piezoelectric transducer, shown in inset. Device on the right is the arbitrary shaped kerfless array design concept with backing layer (grey), kerfless element (orange), common ground (black) and multi-electrodes (green) are fitted in between layers, shown in inset. Trapped particle and substrate are shown as common application set up.

studied the formation of long-lived states in polygonal cavities is related to strong diffraction on the corners and concluded that varying the shape of the boundary would lead to a systematic investigation of spectral properties. Although these works are not directly related to acoustic chambers, their insights are well suited to encourage a design study on resonant modes and performance of in-plane acoustic manipulators.

This thesis presents a modelling framework for designing Monolithic Ultrasonic Tweezer Devices (MUTD) inspired by Kozuka et al. [1996], who first introduced a simple ultrasonic manipulator concept based on the radiation of sound from a single crystal with mechanically decoupled elements. This concept works by switching in a controlled manner between activated electrical ports of a multi-electrode transducer and dynamically changing the radiated sound field. Similar approaches can also be found in a 2-D screen-printed array transducer for microparticle manipulation by printing each element separately [Qiu et al., 2015]. However, an in-plane, closed, monolithic transducer array for particle manipulation has yet to be investigated. The device concept proposed in this work is depicted in Figure 1.3 where the individually addressable electrodes arranged over active layer is described. This concept not only allows minimize the complexity level in manufacturing process compared to previous version [Grinenko et al., 2012] but also greatly facilitates the investigation between simplified and realistic models. The developed models are predicted on arbitrary interface shapes, such as the one shown in Figure 1.3, but is always applied to regular, convex, polygonal boundaries with rounded corners. While these polygons simplifies the physical problem geometry hence the device design, they potentially leaves some relevant features of non-regular shapes such as the elimination of symmetries and resonances.

Boundary behaviour in closed devices for acoustic manipulation affects the wave phenomenon and ultimately its performance. Model-based design tools may capitalize on performance measures to provide supporting frameworks for exploring the parameter space of devices at a high abstraction level. Analysing an acoustic manipulator response has proven an effective method to study the performance of single-input devices, such as acoustic resonators. Conversely, the synthesis of specialized acoustic field using multiple-input manipulators, such as ultrasonic tweezers, has capitalized on optimization methods which solves for the applied set of inputs given a transducer configuration. Moreover, modelling approaches to design of multiple-input acoustic manipulators have been applied to limited boundary shapes and acoustic impedance conditions. The investigation of boundary properties of cavities has supported the design of closed acoustic and dielectric devices. An approach to design of ultrasonic tweezers whereby the response analysis and field synthesis are defined under the same modelling framework would be beneficial to investigate the overall performance of these device.

The developed modelling framework shown in Figure 1.4 is therefore proposed to address the issue of modelling as a design technique for ultrasonic tweezer devices. The schematic of the modelling approaches adopted throughout the thesis highlights consecutive models with

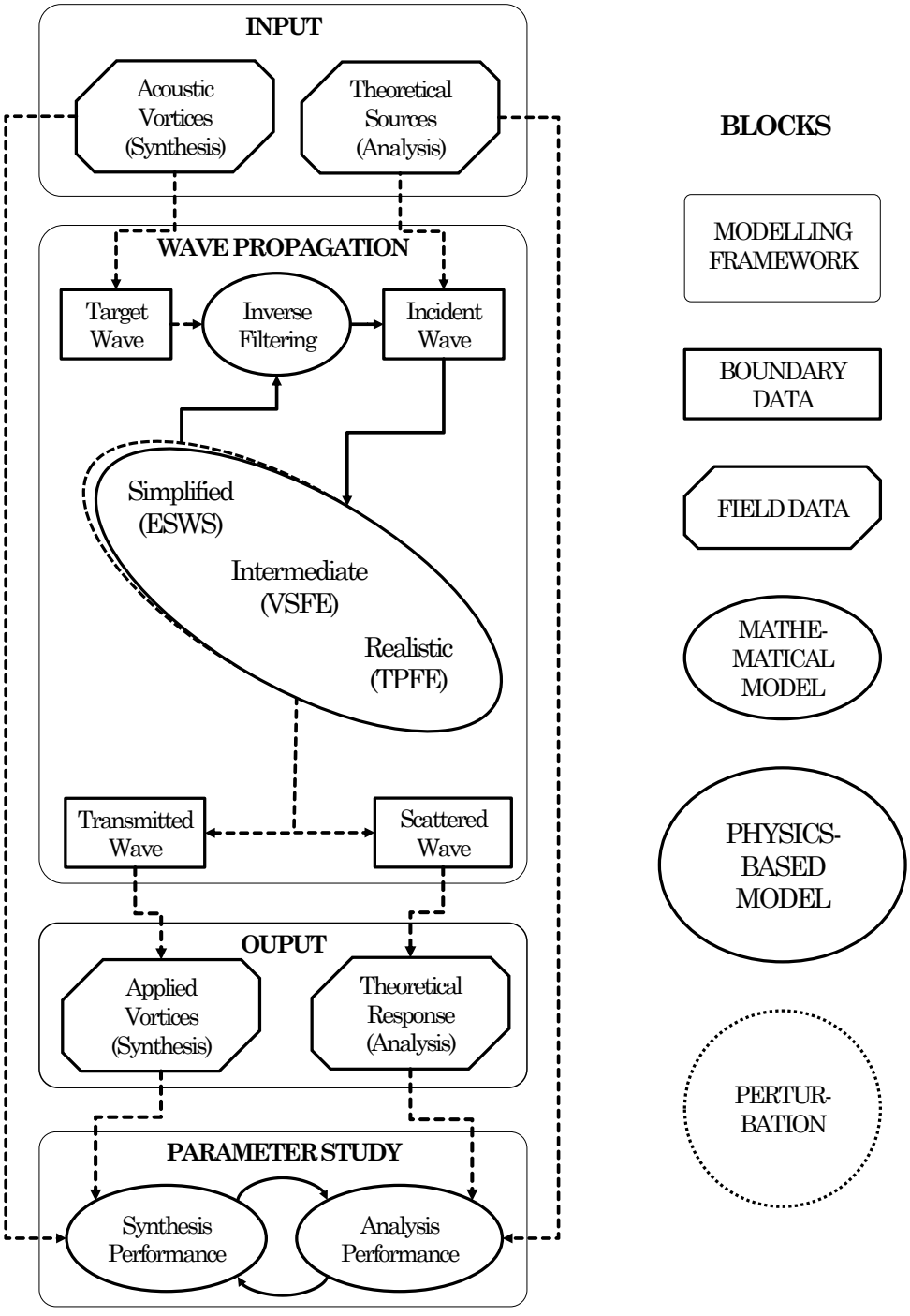

FIGURE 1.4. Diagram for developed modelling framework combining physics-based, mathematical and data modelling.

increasing level of complexity each of which addressing approximations to the solution sought. In this diagram, modelling blocks broadly represent inputs, outputs, wave propagators and parameters study which define and relate its components interchangeably. Two distinct modelling protocols are proposed to study the design of ultrasonic tweezers devices, namely analysis and synthesis protocols. Each protocol follows a modelling sequence starting from a standardized input to determine a performance number based on a parameter study. The analysis protocol is described as a modelling sequence to study the theoretical response of a given closed device based on the radiation of internal, single-input source field and investigate the ability of wave incidence to withstand internally scattered waves. Synthesis protocol is defined as an alternative modelling sequence to study the reproduction of specialized wave fields on a given closed device based on the application of external, multiple-input source field and investigate its ability to withstand perturbations on the transducer characteristics. This framework establishes a relationship between analysis and synthesis performance which allows a strategy to avoid low performance designs to be proposed.

Both the input and output blocks define a data set distinguished by acoustic vortices defined for field reproduction and theoretical field defined for chamber response. The wave propagation is the main modelling block which connects input to outputs by solving a wave propagation problem always via a physics-based model. The parameter study block entails both synthesis and analysis performance obtained by comparing input with output field data. Mathematical model blocks are restricted to either inverse filtering technique which transforms desired data to incident data or performance study which analyses pressure field within the acoustic chamber by implementing a statistical association parameter. Boundary data blocks are contained within the wave propagation block representing theoretical waves defined on the physical boundary which interfaces acoustic chamber and transducers. Boundary data can be either target, transmitted, scattered or incident wave defined on the inside for analysis or applied wave on the outside for synthesis.

Lastly, the physics-based model blocks are represented by simplified, intermediate and realistic models. The simplified model is implemented by a wave scattering model using a Equivalent Source (ES) method being computationally cheap to obtain the solution. The intermediate model is implemented by a finite element model using a Virtual Source (VS) method being a transitioning model to study the boundary behaviour on piezoelectric devices. The realistic model is implemented by a Transducer Parameter FE model being employed for practical electrical sources and user-defined acoustic field reproduction. Perturbation is applied to a physics-based model by varying the material properties and computing the transfer function needed for implementing the inverse filter technique.

The progression established on each model stage supports the study of the synthesis protocol on real physical systems. The physics-based models are developed to progressively predict the complex behaviour of practical manipulation devices. The fist stage is a low physics complexity,

low spatial refinement level model of a system defined by theoretical boundaries and analytical sources for providing basic knowledge of the performances parameters. The second stage is a low to high physics complexity, high spatial refinement level model of a system defined by realistic boundaries and theoretical sources for providing basic knowledge of the performances parameters. The last stage stated as the realistic model is developed to best represent experimental results and suggested as potential for validation. All stages uses non-physical inputs in the analysis protocol to study the boundary behaviour as a passive device for system identification purposes. Numerical results presented throughout studies the solution for the pressure field inside the acoustic chamber. The validation against acoustic manipulation experiments is commonly addressed using Schlieren techniques [G.S. Settles, 2001] in combination with particle manipulation observations [Bernassau et al., 2011; Courtney et al., 2010, 2013; Kozuka et al., 1996]. Moreover, an alternative validation technique may be applied to the realistic model by comparing the electrical impedance of the transducer terminals obtained using FEM [Lerch, 1990] applied to acoustic manipulation devices [Andrade et al., 2010; Benes et al., 2001; Dual and Möller, 2012; Hill M. andShen et al., 2002; Qiu et al., 2015].

1.1 Objectives

This thesis is based on a modelling study of piezo-electric, two-dimensional, in-plane, closed and regular polygon shaped devices which generates static vortex beams in inviscid fluid for acoustic trapping capabilities. The objectives are summarized below:

- Review practical devices and existing models for in-plane ultrasonic particle manipulators then propose a novel multi-electrode, backed array transducer through the use of a physics-based modelling framework methodology to tackle design problems of chamber resonance.
- Build physics-based models for analysis and synthesis of acoustic field inside penetrable chambers; including a simplified model for cheap assessment of fluid-fluid interface, a intermediate model for studying additional piezoelectric wave phenomena and an realistic model for high-fidelity transducer simulation.
- Develop a performance modelling approach to study the reproduction of pressure field as proof-of-concept for robust design of kerfless ultrasonic tweezer devices.

1.2 Thesis outline

Chapter 2 reviews the mathematical background adopted for developing the modelling framework presented for designing ultrasonic dynamic-field devices for particle manipulation. The review provides a discussion of alternative numerical methods for solving the acoustic transmission problem. Then presents a classical solution to this problem using cylindrical wave functions.

The ES and the VS methods based on the Kirchhoff-Helmholtz Integral (KHI) are briefly described. The pressure field reproduction is treated using an inverse filtering technique, and its implementation is discussed. Background on Finite Element Method (FEM) for electroelastic wave propagation in piezoelectric materials is presented based on the variation principle. An introduction to acoustic radiation forces and acoustical vortices is given.

Chapter 3 then goes on to formulate the Equivalent Source Wave Scattering (ESWS) model described as the simplified model based on the transmission problem of an arbitrary shaped fluid bodies in a fluid host. A numerical method is developed for solving the interface response to internal and external sources. The pressure field and performance results are investigated for various boundary shapes and material properties. An inferred performance parameter for perturbed systems is investigated.

In Chapter 4, the proposed Virtual Source Finite Element (VSFE) model is described as the tuning model and implemented in order to solve the scattering problem using the virtual source method in combination with the FEM. This transitioning model allows the investigation of the boundary behaviour from fluid to piezoelectric crystal by tuning the electromechanical coefficient of the material model. This investigation provides a means to gradually compare interface responses using simplified media with ones using realistic media.

In Chapter 5 the Transducer Parameter Finite Element (TPFE) proposed as a realistic model is described extending the VSFE by including practical sources and solves the field reproduction problem by using an inverse filtering formulation based on a prescribed electrical potential of a multi-electrode transducer. A robust approach to MUTD design based on the TPFE is then applied as an optimization tool for a study of device performance. The study of realistic synthesis performance relates to the robustness of transducers with respect to perturbation of the material properties. This model allows the application of acoustic traps reproduction in practical devices and a performance investigation using a novel pressure field landscaping technique based on sculpting Acoustic Radiation Potential (ARP).

Finally, Chapter 6 concludes the thesis and gives an outlook on possible future work.

CHAPTER 2

THEORETICAL BACKGROUND

This chapter reviews the mathematical background for developing numerical models applied to design ultrasonic dynamic-fields devices for particle manipulation. The modelling framework presented solves practical problems related to computing the radiation of acoustic field and radiation potential inside in-plane ultrasonic manipulators. All implemented models solve for a simplified plane strain acoustic problem in a transversal plane section of these devices as many authors have reported good agreement with experiments whilst exploiting bulk waves generation as particle manipulation mechanism [Bernassau et al., 2013; Courtney et al., 2011; Greenhall et al., 2016; Oberti et al., 2007].

To design acoustic field within a closed ultrasonic tweezers device for a given geometrical

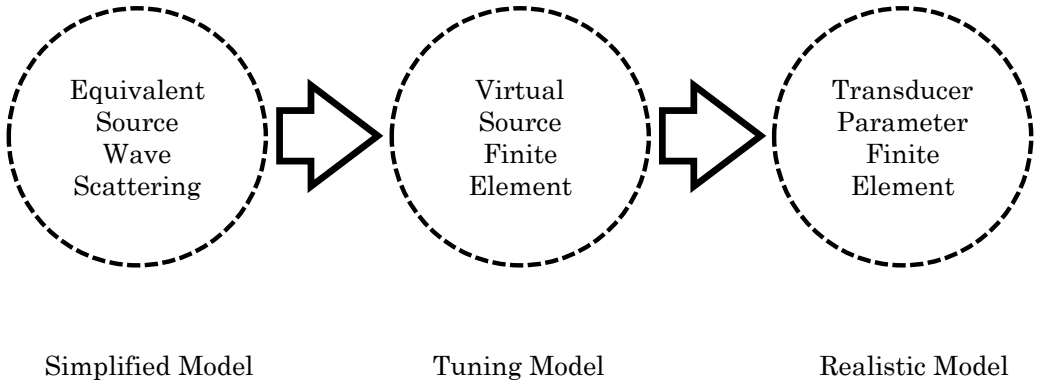

FIGURE 2.1. Schematic diagram for the physics-based modelling methodology with an increasing level of complexity identifying each of the developed models.

configuration of the system boundaries, and a specified configuration of piezo-electric excitation is a complex task. To achieve this a collection of transmission, reproduction and generation of acoustic waves is described and modelled using a common modelling framework such that incident wave is defined in a general form either by theoretical acoustic sources or piezo-electric excitation. Furthermore, two distinct modelling protocols are hypothesized the analysis is designed to understand the boundary response of closed devices to a set of theoretical internal sources and the synthesis is for studying the effects of disturbed properties on the system boundaries on the performance at designing acoustic fields. A common reference solution for the scattered pressure field inside the acoustic chamber for all physics-based models is developed. Figure 2.1 summarizes the developed physics-based models adopted as a proof-of-concept for the proposed device discussed in Chapter 1 and shown in Figure 1.3. The increasing complexity level in these models is intended to investigate various effects physical properties characterization and the definition of boundary conditions have on the boundary behaviour and hence device performance.

Background on each main subject of this chapter is presented separately in the following sections. The first section describes the acoustic wave modelling in the frequency domain for an enclosed space and states the respective Helmholtz problem by presenting the equations solved for and discussing alternative numerical methods for solving these equations. The second section describes the solution for the wave equation given the problem of a point source with transmission conditions on a circular boundary. This is achieved by presenting the analytical solution using cylindrical wave functions for the case of external sources and discussing the implications of the problem for internal sources. The third section states both the equivalent and virtual source method based on the KHI and explains how it is used to support the development of the modelling framework throughout the thesis. In the fourth section, a general inverse filter formulation is described and the application in synthesizing pressure wave fields based on the KHI is discussed. The fifth section introduces the electroelasticity as a mathematical tool for solving the equation of motion in piezoelectric media using the variational principle for the FEM. In this section alternative input methods are discussed by distinguishing between the effects of applying acoustic sources on theoretical boundaries and prescribing electrical potential on transducer electrodes. The last section gives a brief introduction on acoustic radiation force and the application of acoustic vortices as an ultrasonic trapping and manipulation mechanism.

2.1 Acoustic wave modelling

An initial study on relevant modelling approaches to solve acoustic wave propagation in a bounded domain is carried out in this section. The acoustic transmission is described in the frequency domain and the time-harmonic wave equation is stated so to make no distinction between the propagation problem in either an interior or exterior case. As shown in the schematics in Figure 2.2, the the acoustic wave in a two-dimensional domain is represented by scalar potentials

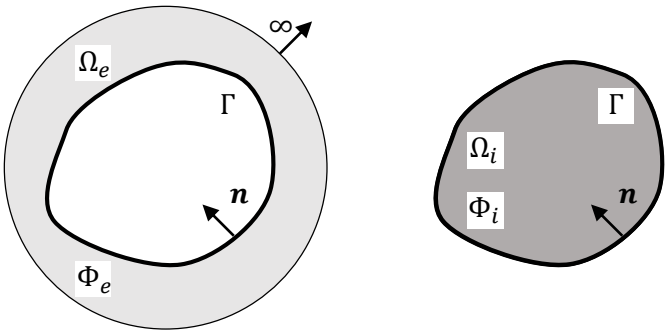

(a) (b)

FIGURE 2.2. Representation of the acoustic transmission problem using equivalent interior and exterior formulations. (a) The exterior problem solves for an external wave field Φ_e defined in an unbounded domain Ω_e and (b) the interior problem solves for an internal wave field Φ_i defined in a bounded domain Ω_i.

Φ for both external and internal cases. Wave propagation in the presence of an obstacle different wave number, otherwise known as scattering by a penetrable inclusion, is shown in Figure 2.2 (a). Wave propagation in a closed chamber surrounded a bounding wall with different wave number otherwise defined as a room acoustics problem as shown in Figure 2.2 (b). This is treated by presenting the associated partial differential equations and boundary continuity conditions for this problem and then discussing alternative numerical methods for solving the resulting system of equations. It is worth noting there are different methods found elsewhere [Domínguez et al., 2006], that provide alternative solutions for this class of problem, hence this discussion is not exhaustive.

Most models of acoustic tweezers use Huygen's model, neglecting reflections, claiming a good approximation for the computed total pressure field. It is clear that more accurate results can be found by considering the reflections inside practical devices and that acoustic manipulation may be prevented as discussed elsewhere [Bernassau et al., 2014; Courtney et al., 2013, 2014] due to additional wave propagation. Moreover, one main goal is to build physics-based models for analysis and synthesis of acoustic field inside penetrable chambers hence the solid theoretical background on these methods presented herein.

In linear acoustics, an ideal fluid can be approximated by an isotropic homogeneous medium whereby only longitudinal waves are allowed [Kinsler, 1982]. Hence the propagation of pressure waves in a homogeneous medium is the starting point of this study on acoustic wave modelling and proceeds by first defining the linear wave equation

$$\nabla^2\Phi - \frac{1}{c^2}\frac{\partial^2\Phi}{\partial t^2} = 0, \quad \text{in } \Omega, \tag{2.1}$$

where c is the wave speed, Φ is velocity potential defined in domain Ω and t is time. By ∇^2 we denote the Laplace operator, which for a two-dimensional space $\mathbb{R}^2$ in Cartesian coordinates is

defined as

$$\nabla^2 \equiv \frac{\partial^2}{\partial x_1^2} + \frac{\partial^2}{\partial x_2^2}, \tag{2.2}$$

where (x_1, x_2) represents the spatial coordinates in the space $\mathbb{R}^2$. The time-harmonic particle velocity field $\boldsymbol{v}(\mathbf{r})e^{-i\omega t}$ for a position $\mathbf{r}$ and time t can be obtained from the gradient of the velocity potential

$$\boldsymbol{v} = \nabla\Phi. \tag{2.3}$$

where a factor of $e^{-i\omega t}$ is assumed and suppressed hereafter. Considering pressure wave field p in terms of velocity potential Φ, the time-harmonic solution without attenuation is given by

$$p = i\rho c k \Phi, \tag{2.4}$$

where ρ is the fluid density, $k = \omega/c$ the wave number and $i = \sqrt{-1}$. Applying the Fourier transformation [Williams, 1999] to the Equation 2.1 and the wave in terms of the velocity potential Φ given by

$$\nabla^2 p + k^2 p = 0, \quad \text{on } \Omega, \tag{2.5}$$

which is known as the free-space Helmholtz equation without attenuation. For an acoustic problem which considers sound transmission through a bounded obstacle (see Figure 2.2) a local complex resistance parameter is defined. In a bounded space, or chamber, the excess of pressure on the boundary is related to the normal component of the particle velocity $v = \boldsymbol{v} \cdot \mathbf{n}$ by a proportional coefficient which corresponds to the homogeneous impedance boundary condition

$$-p + Zv = 0, \tag{2.6}$$

where $\mathbf{n}$ is normal direction to the boundary and $Z = \rho c$ is the characteristic specific acoustic impedance. Consider an internal domain Ω_i surrounded by the external unbounded domain Ω_e having a boundary $\Gamma = \partial\Omega_i = \partial\Omega_e$. Here the domain exterior to the acoustic cavity is also governed by a Helmholtz problem, characterized by a wavenumber k_e, and this coupled problem is known as exterior impedance Helmholtz problem. A common fluid-fluid interface domain in 2D space has been chosen with $\mathbf{n}$ unit normal vector outwardly oriented of the external domain Ω_e, as depicted in Figure 2.2 (a).

The aforementioned exterior Helmholtz impedance boundary value problem formulation is stated such that a total pressure field p, decomposed as $p = p_e + p^o$ by the external and incident field, satisfies a homogeneous impedance boundary condition. In this case, the p_e defines the scattered pressure field governed by the Helmholtz equation and an outgoing Sommerfeld radiation condition, which eliminates the non-physical solutions by specifying a decaying behaviour

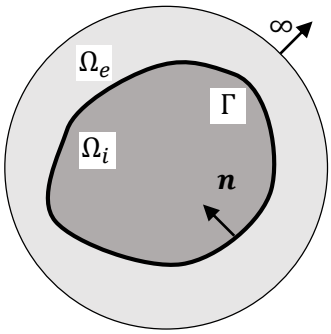

FIGURE 2.3. Representation of the extended interior to exterior formulations of the acoustic transmission problem.

at infinity. The scattered field also needs to satisfy a non-homogeneous impedance boundary condition as

$$\begin{cases} \nabla^2 p_e + k_e^2 p_e &= 0, \quad \text{in } \Omega_e \\ -p_e + Z v_e &= f_z, \quad \text{on } \Gamma \end{cases} \tag{2.7}$$

where p_e is the exterior pressure field, Z is the acoustic impedance on the boundary and f_z due to linearity is the impedance boundary data given by

$$f_z = p^o - Z v^o, \quad \text{on } \Gamma \tag{2.8}$$

where the subscript o refers to the incident field. This system can be extended by considering an equivalent interior problem, as shown in Figure 2.2 (b).

$$\begin{cases} \nabla^2 p_i + k_i^2 p_i &= 0, \quad \text{in } \Omega_i \\ -p_i + Z v_i &= f_z, \quad \text{on } \Gamma \end{cases} \tag{2.9}$$

where the subscript i denotes the interior field. In this case, the total pressure field p is decomposed as $p = p_i + p^o$ and the impedance boundary data is as in Equation 2.8. It is noteworthy, the acoustic impedance Z defined on the boundary Γ characterizes the acoustic media in the alternate domain where pressure field is not defined.

A more general approach to solve either the exterior or the interior problem is by stating a combined problem defined on the entire domain $\Omega = \Omega_e \cup \Omega_i$ by extending the exterior problem and establishing a corresponding interior problem [Hoernig, 2010], shown in Figure 2.3 and given by

$$\begin{cases} \nabla^2 p + k^2 p &= 0, \quad \text{in } \Omega \\ p_e - p_i &= p^o, \quad \text{on } \Gamma \\ v_e - v_i &= v^o, \quad \text{on } \Gamma \end{cases} \tag{2.10}$$

which are described by the pressure continuity and the velocity continuity where the homogeneous equation is stated for both internal and external domain separately with its respective wave number. These problems formulated above appear in relevant engineering applications such as the direct scattering of acoustic waves in homogeneous media for defect characterization [Colton and Kress, 2013]. It is worth noting the system of equation 2.10 solves the fully coupled transmission problem and should give an exact solution for any given parameter range. As the fully coupled approach analyses the behaviour of acoustic cavities capitalises on the solution for both internal and external field. The impedance boundary conditions given by the system of equations 2.7 and 2.9 solve for these problems without explicitly computing the transmitted pressure field. A mathematical viewpoint of a generalized impedance boundary condition is not presented in this thesis and can be found elsewhere [Antoine and Barucq, 2005].

Furthermore, an integral representation of the transmission problem can be developed over the boundary Γ as a Boundary Integral Equation (BIE) which reduces the problem from a two-dimensional infinite to a one-dimensional finite domain. The integral representation makes use of the Green's function, which represents the response of an unperturbed system to a point source. In order to solve this integral equation, it can be converted to its variational or weak formulation by approximating the boundary by a curve composed of rectilinear segments defining a discretized boundary, shown in Figure 2.4(a), and then applying a Galerkin scheme. This describes a method called the Boundary Element Method (BEM) that has been used to find a good approximation for the Green's function in various acoustic scattering problems [Mallardo and Aliabadi, 1998], room acoustics [Seybert et al., 1990] and in electromagnetic resonances in

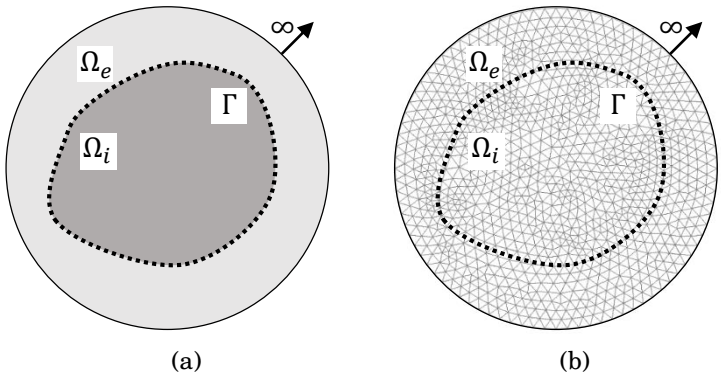

FIGURE 2.4. Representation of modelling approaches used to solve the acoustic transmission problem.(a) The discrete surface boundary and (b) the volumetric domain approaches.

dielectric microcavities [Wiersig, 2003b]. A similar analysis for this equivalent formulation has been studied by using the Method of Moments (MoM) [Raju et al., 1991], a precursor of BEM.

A similar numerical scheme can be employed over the full domain and then solving the problem using FEM, shown in Figure 2.4(b). The FEM consists in dividing the domain of the problem into several sub-domains with relatively simple geometries called finite elements. Each of these elements connects with other elements through some points called nodes. After subdividing the domain into several elements and applying appropriate boundary conditions the physical parameters at each of these nodes an approximation to the solution for the field in the domain is obtained by solving a globally assembled system of equations.

Lastly, a Distributed Point Source Method (DPSM) has been investigated to solve scattering problems originally developed for solving problems of radiation from a transducer [Placko and Kundu, 2007]. A modelling comparison [Kundu and Placko, 2010] concluded that the most efficient technique for solving general two-dimensional acoustic radiation problems with or without the presence scatterer was the using semi-analytical approach over analytical and the FEM. However, the authors stated that investigating the effect of the transducer boundary conditions on the generated ultrasonic field was not the objective of their work.

All the above-mentioned methods, namely BEM, MoM, DPSM, FEM have already been applied to solve a wide range of Helmholtz problems for a number of practical applications. However, it may be difficult to provide a practical insight into modelling particle manipulation devices if the application of these methods lacks the definition of a general incident wave. For this reason, a simplified model is developed in Chapter 3 in order to better approximate the solution compared with the Huygen's principle based on free space Green's function and yet provide a reasonable understanding of the transmission phenomena over the interface. This simplified model considers a general incident wave as an input and configures the first step in the proposed modelling methodology. The results and further discussion on such model should provide solid background and better understanding of the performances of in-plane, closed particle manipulation devices.

Before reviewing the methods employed for developing the models shown in Figure 2.1, an exact solution is presented for the problem shown in Figure 2.4. This solution is solved by using a cylindrical harmonics expansion method and used as a benchmark for a simple circular case for comparison with the other developed models. A similar comparison approach has been used by Hsiao and Xu [2011] to develop a BEM-based solution for a two-dimensional transmission problem in acoustic scattering. Nevertheless, a classical cylindrical wave expansion method for solving the problem for a circular shape is discussed in the following section. The derivation of the analytical solution for the wave field resolved into a series of waves repeatedly reflected within a cylinder has been investigated in both electromagnetics [Gérard et al., 1999] and acoustics [Brill and Überall, 1970].

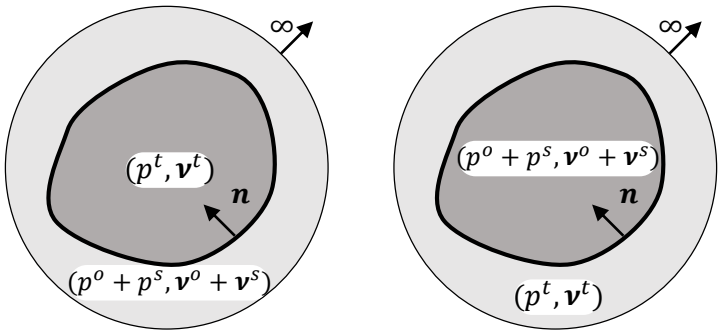

FIGURE 2.5. Schematic of a general solution for the acoustic wave transmission phenomena through a bounded space in a otherwise infinite space. Transmitted wave (v^t, p^t) can be due to either (a) external or (b) internal incident wave (v^o, p^o) generating a scattered wave (v^s, p^s).

2.2 General solution for the wave transmission

The acoustic wave transmission phenomena is discussed to develop the physics-based modelling methodology for the design of ultrasonic tweezers devices. A general solution for two acoustic wave transmission problems is formulated. The solution to the problem stated by the inhomogeneous Helmholtz equation with transmission boundary conditions, as shown in Figure 2.5, is a well-studied theoretical topic in physical acoustics. In this section, the wave propagation through an enclosed cylindrical boundary is solved to model devices where the known sources lie on the outside such as the acoustic manipulator proposed here. The position of the source relative to the physical boundary, that is inside or outside it, determines the domain in which the incident wave is defined. The solution is defined on either side of the boundary regardless of the positioning of the source. For an incident wave defined in Ω_e the transmitted wave is defined in Ω_i, as in a scattering problem shown in Figure 2.5(a). In a room acoustic problem the incident wave is defined in Ω_i and the transmitted wave in Ω_e, as shown in Figure 2.5 (b). This leads to more general boundary conditions in terms of acoustic field parameters

$$\begin{aligned} v_- - v_+ &= 0 \\ p_- - p_+ &= 0, \end{aligned} \tag{2.11}$$

where the subscripts $(-)$ and $(+)$ denote the boundary data (v, p) in the negative and positive direction of the normal vector. Equations 2.11 covers a more general both by the pressure and velocity continuity irrespective of the incident wave. As discussed in Chapter 1, the internal and external incident wave is used to solve for both the analysis and synthesis of the pressure field, respectively.

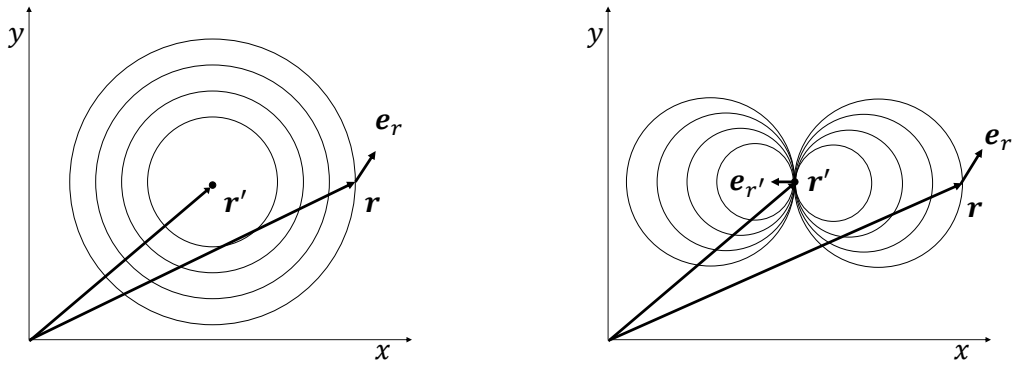

FIGURE 2.6. Schematic representation of the free-space response to a radiating line source as wave-fronts and the arbitrary directions at both source and field positions for monopole and dipole. Unit vectors $\mathbf{e}_{r'}$ and $\mathbf{e}_r$ are defined at source $\mathbf{r}'$ and field $\mathbf{r}$ positions, respectively. (a) Monopole and (b) dipole responses are represented schematically by closed wave-fronts (—) emerging from source position $\mathbf{r}'$.

Further on, an analytical solution to the circular cylinder case is presented which is defined as a common reference for comparing with all subsequent solutions obtained by the models discussed in the following chapters. This analytical solution is regarded as a reference for comparison and is not part of the modelling framework for designing MUTD, shown in Figure 1.2, as discussed in Chapter 1.

2.2.1 Green's function

The response definition of an unperturbed system to a line source, as shown in Figure 2.6 is an important step to solve both the free-space and thus transmission problems. A line source radiates into unbounded external domain satisfying an outgoing Sommerfeld radiation condition. Considering the wave equation in Equation 2.12 stated for homogeneous Helmholtz problem and replacing the right-hand side by a two-dimensional line source $\delta(\mathbf{r}')$ and the potential Φ by a solution G, called Green's function, then a radiation problem is given by

$$\left(\nabla^2 + k^2\right) G(\mathbf{r}', \mathbf{r}) = -4\pi\delta(\mathbf{r}' - \mathbf{r}), \quad \text{on } \Omega \tag{2.12}$$

where $\mathbf{r}'$ and $\mathbf{r}$ are the source and field point coordinates respectively. The corresponding solution for this radiation problem is the space dependent Green's function $G(\mathbf{r}', \mathbf{r})$ for outgoing-wave from an arbitrary source position in a two-dimensional unbounded isotropic homogeneous domain and is given by

$$G(\mathbf{r}', \mathbf{r}) = -\frac{i}{4} H_0^{(1)}(k\left|\mathbf{r}' - \mathbf{r}\right|) \tag{2.13}$$

where $H_0^{(1)}$ denotes the zero-order Hankel function of the first kind. Whilst the free-space Green's function as presented in Equation 2.13 is a fundamental solution to the inhomogeneous Helmholtz equation, the function $G(\mathbf{r}',\mathbf{r})$ can generally be used for solving boundary value problems to any boundary conditions and body shape.

From this fundamental solution and the pressure definition (Equation 2.2) given at field point the pressure field in domain Ω due to a line source can be derived. From the particle velocity definition (Equation 2.12) and the spatial derivative of $G(\mathbf{r}',\mathbf{r})$ with respect to the field position the velocity field due to a line source can be similarly derived, as in

$$\frac{\partial G(\mathbf{r}',\mathbf{r})}{\partial e_r} = \frac{ik}{4} H_1^{(1)}(k|\mathbf{r}'-\mathbf{r}|)\frac{(\mathbf{r}'-\mathbf{r})\cdot\mathbf{e}_r}{|\mathbf{r}'-\mathbf{r}|} \tag{2.14}$$

where $H_1^{(1)}$ denotes the first-order Hankel function of the first kind and $\mathbf{e}_r$ is the arbitrary directions at the source position, as shown in Figure 2.6(a). The Green's function and its gradient with respect to the field point $\mathbf{r}$ are the pressure and velocity response to a monopole source being of great importance to the derivation of solutions for the wave equation. The normal component of the particle velocity v at $\mathbf{r}$ as in Equation 2.3 can be obtained in terms of the derivative in Equation 2.14 by substituting $\mathbf{e}_r$ for $\mathbf{n}$. These functions in Equations 2.13 and 2.14 are used to find the solution for the wave equation in the ESWS model.

The Green's function gradients with respect to the source position $\mathbf{r}'$ represent the acoustic field response to a dipole. The dipole is the result of substituting the line source in Equation 2.12 by a body force term oriented according to $\mathbf{e}_{r'}$, as shown in Figure 2.6(b), then

$$\left(\nabla^2 + k^2\right) p = 4\pi \mathbf{e}_{r'} \cdot \nabla\delta(\mathbf{r}'-\mathbf{r}), \quad \text{on } \Omega \ , \tag{2.15}$$

and the pressure field p for a dipole in an unbounded fluid becomes

$$\frac{\partial G(\mathbf{r}',\mathbf{r})}{\partial e_{r'}} = \frac{ik}{4} H_1^{(1)}(k|\mathbf{r}'-\mathbf{r}|)\frac{(\mathbf{r}'-\mathbf{r})\cdot\mathbf{e}_{r'}}{|\mathbf{r}'-\mathbf{r}|}. \tag{2.16}$$

All gradients assume the source and field points are not collocated (i.e. $\mathbf{r}' \neq \mathbf{r}$). In terms of acoustic parameters, these derivatives express the velocity response to a monopole source in Equation 2.14 and the pressure response to a dipole source in Equation 2.16. The double-gradient with respect to both the source and field point is given by

$$\begin{aligned}\frac{\partial G(\mathbf{r}',\mathbf{r})}{\partial e_r \partial e_{r'}} = &-\frac{ik}{4} H_1^{(1)}(k|\mathbf{r}'-\mathbf{r}|)\left(-\frac{\mathbf{e}_{r'}\cdot\mathbf{e}_r}{|\mathbf{r}'-\mathbf{r}|} - 2\frac{\left((\mathbf{r}-\mathbf{r}')\cdot\mathbf{e}_r\right)\left((\mathbf{r}'-\mathbf{r})\cdot\mathbf{e}_{r'}\right)}{|\mathbf{r}'-\mathbf{r}|^3}\right) \\ &+ \frac{ik^2}{4} H_0^{(1)}(k|\mathbf{r}'-\mathbf{r}|)\frac{\left((\mathbf{r}'-\mathbf{r})\cdot\mathbf{e}_{r'}\right)\left((\mathbf{r}-\mathbf{r}')\cdot\mathbf{e}_r\right)}{|\mathbf{r}'-\mathbf{r}|^2}.\end{aligned} \tag{2.17}$$

which represents the velocity response to a dipole source.

The equations from 2.13 to 2.17 are used in the implementation of a transfer matrix that computes the propagation of pressure field into domain Ω_i from a given boundary data on Γ. The propagator matrix is used in both the ESWS and VSFE model developed in Chapter 3 and 4, respectively. Pressure and velocity response to monopole is applied to the analysis protocol to compute the incident internal field as well as the boundary data needed for solving for the internally scattered field. The monopole source implemented for the analysis protocol represents an equivalent test function to experimentally investigate the response of a device boundary by setting an internal omnidirectional source and measuring the total pressure field. On the other hand, pressure and velocity response to dipole is applied to the synthesis protocol to compute the transmitted internal field as well as the boundary data needed for solving for the externally incident field. The dipole source implemented for the synthesis protocol represents an equivalent applied function to experimentally investigate the radiation of a device boundary by setting an external normal force and measuring the transmitted pressure field.

2.2.2 Analytical solution

Here an analytical solution for the scattering problem shown in Figure 2.7 is demonstrated as a reference for further solutions developed hereafter. As a particular case, the wave field in a circular cylindrical cavity for an incident wave field completely defined in the exterior domain is solved given a line source radiating from $\mathbf{r}'$. Figure 2.7 depicts the problem of a source located outside the boundary of the penetrable object with radius a which is defined as the traditional scattering problem and solved for a reference case to illustrate the solution using the analytical method. The solution for the reference case problem presented below assumes the incident pressure field p^o due to a line source and is given by

$$p^o(\mathbf{r}) = p_0 G(\mathbf{r}', \mathbf{r}). \tag{2.18}$$

Using Fourier series, widely applied to boundary value problems, Equation 2.18 can be expanded as an infinite series based on cylindrical wave functions. The incident pressure field p^o is expressed by a series of cylindrical harmonics as in

$$p^o(\mathbf{r}) = \begin{cases} S\dfrac{i}{4}\displaystyle\sum_{n=-\infty}^{\infty} J_n\left(k|\mathbf{r}'|\right) H_n^{(2)}\left(k|\mathbf{r}|\right) e^{in\phi} & \mathbf{r} > \mathbf{r}' \\ S\dfrac{i}{4}\displaystyle\sum_{n=-\infty}^{\infty} H_n^{(2)}\left(k|\mathbf{r}'|\right) J_n\left(k|\mathbf{r}|\right) e^{in\phi} & \mathbf{r} < \mathbf{r}', \end{cases} \tag{2.19}$$

where J_n and $H_n^{(2)}$ denotes the n-order Bessel function and Hankel of the second kind, respectively. The scattered p^s and transmitted p^t pressure field are the result of the interaction between the incident field p^o and the obstacle, as shown in Figure 2.7. The solution can be derived by taking

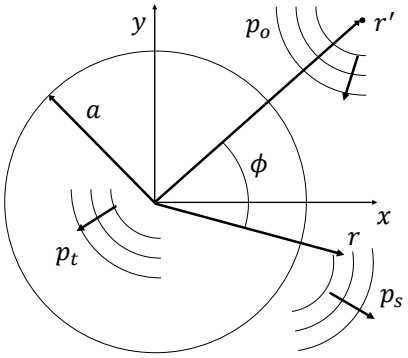

FIGURE 2.7. Representation of wave scattering problem by a circular cylindrical object showing of incident p^o, scattered p^s and transmitted p^t wave for a line source located outside a penetrable object. The object is an infinite cylinder with radius a, the line source is positioned at $\mathbf{r}'$, the field point at $\mathbf{r}$ with angle ϕ relative to the source

the results for Maxwell equations [Harrington, 1961] and adapting for the acoustic problem

$$p^s(\mathbf{r}) = p_0 \frac{i}{4} \sum_{n=-\infty}^{\infty} a_n J_n\left(k|\mathbf{r}|\right) J_n\left(k\left|\mathbf{r}'\right|\right) e^{in\phi} \tag{2.20}$$

$$p^t(\mathbf{r}) = p_0 \frac{i}{4} \sum_{n=-\infty}^{\infty} b_n H_n^{(2)}\left(k_o|\mathbf{r}|\right) J_n\left(k\left|\mathbf{r}'\right|\right) e^{in\phi} \tag{2.21}$$

where k_o is the object characteristic wave number and the coefficients a_n and b_n are found by matching the transmission boundary conditions at $\mathbf{r} = a$, as in $p^t = p^o + p^s$ and $v^t = v^o + v^s$:

$$a_n = -\frac{J_n\left(ka\right)}{H_n^{(2)}\left(ka\right)} c_n \tag{2.22}$$

$$b_n = -\frac{J_n\left(ka\right)}{J_n\left(k_o a\right)} \left[1 - a_n\right] \tag{2.23}$$

where ka is the non-dimensional wavenumber, c_n is given by

$$c_n = \frac{Z_r J_n^{'}\left(k_o a\right)/J_n\left(k_o a\right) - J_n^{'}\left(ka\right)/J_n\left(ka\right)}{Z_r J_n^{'}\left(k_o a\right)/J_n\left(k_o a\right) - H_n^{(2)'}\left(ka\right)/H_n^{(2)}\left(ka\right)}. \tag{2.24}$$

The Equations 2.20 and 2.21 are the solutions for the system of equations 2.10 where $p_e = p^s$ and $p_i = p^t$ given an external source at $\mathbf{r}'$. The Sommerfeld's radiation condition for both scattered and incident field is attained in the unbounded external domain when $\mathbf{r} \to \infty$. Truncation is

intrinsic to the computational process as the solution is given by an infinite series. The number of terms n_t which provides a convergent solution is determined by the non-dimensional wavenumber ka and usually being equal to $n_t = ka + 10$. A further discussion based on a convergence study in terms of the ratio n_t can be found in Section 3.3.1.

As already mentioned, the above expression solves the scattering problem for an incident wave generated by a line source located in the external domain Ω_e. Further formulation is needed to generalise this solution for an arbitrary incident wave and it is not the scope of this thesis. The solution for the case where the source is located inside the boundary and the incident wave is defined only in the interior domain can be found in Appendix C from Equations C.2 and C.3.

Note the solution using this cylindrical wave expansion approach is only stated here for a circular cylinder fluid-filled boundary and given the incident field is defined in the exterior domain. An interesting case from the application point of view is that of the special case of plane wave incidence ($\mathbf{r}' \to \infty$) which can be found for spheres and circular cylinders [Lax and Feshbach, 1948], fluid spheroids [Tobocman, 1984], axisymetric shapes [Seybert et al., 1986], arbitrary cylindrical shapes [Seybert et al., 1986]. An alternative formulation of the scattering problem for general incident wave, using a spherical partial wave basis can be found elsewhere [Waterman, 1969]. For future work, further development in the cylindrical wave expansion is needed for matching the boundary conditions on different curves other than the circular. The reader may refer to Bowman et al. [1987] for an advanced topic on acoustic scattering by simple shapes.

2.3 Kirchhoff-Helmholtz Integral

The KHI equation states that the pressure field is completely defined by the acoustic pressure and the normal velocity on the boundary surface in addition to any acoustic force inside the bounded domain. Hence, given an internal domain Ω_i bounded by a surface Γ defined by an arbitrary curve, as shown in Figure 2.8, the pressure p_+ at any point $\mathbf{r}$ within the domain Ω_i is given by the KHI [Morse, 1954]:

$$p_+(\mathbf{r}) = \int_\Gamma \left[p_i(\mathbf{r}_\Gamma) \frac{\partial G(\mathbf{r}, \mathbf{r}_\Gamma)}{\partial n} + \frac{\partial p_i(\mathbf{r}_\Gamma)}{\partial n} G(\mathbf{r}, \mathbf{r}_\Gamma) \right] d\Gamma + \int_{\Omega_i} q(\mathbf{r}_i) G(\mathbf{r}, \mathbf{r}_i) \, d\Omega_i. \tag{2.25}$$

The pressure p at any point $\mathbf{r}$ within the domain Ω_i is obtained by integrating the dipole response plus the monopole response weighted by the pressure $p(\mathbf{x}_\Gamma)$ and its normal derivative on the surface Γ, respectively, in addition to any primary source of volume injection $q(\mathbf{r}^o)$ within the domain Ω_i. The vectors $\mathbf{r}$, $\mathbf{r}_\Gamma$ and $\mathbf{r}^o$ denotes the coordinates of the point where the pressure is being evaluated, the coordinates of the point on the surface and the coordinates of the source within the domain Ω_i.

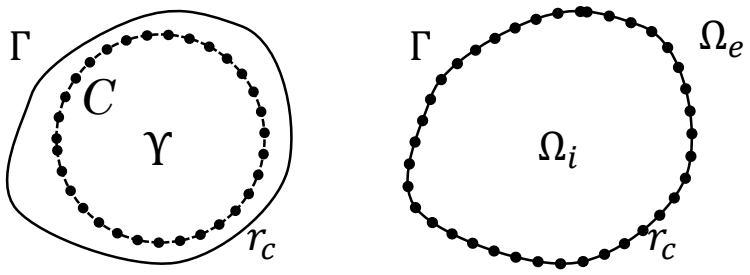

(a) (b)

Figure 2.8: Schematic of geometry for the formulation of KHI used to solve the boundary value problem. (a) Domain Υ surrounded by the contour C inside the physical boundary Γ. (b) Extending contour C to the physical boundary Γ. The position of the co-located points are shown as $\mathbf{r}_c$.

2.3.1 Discrete formulation of KHI

First, a discrete formulation of the KHI is considered. The main feature is to define any practical acoustic field approximately as an equivalent linear superposition of solutions based on secondary sources located on any closed boundary Γ. Figure 2.8 shows a set of points $\mathbf{r}_c$ where the secondary sources are placed at. The pressure field p_i in Ω_i is given by

$$p_+(\mathbf{r}) = \sum_{j=1}^{n_p} \left[p_i(\mathbf{r}_{c_j}) \frac{\partial G(\mathbf{r},\mathbf{r}_{c_j})}{\partial n} + \frac{\partial p_i(\mathbf{r}_{c_j})}{\partial n} G(\mathbf{r},\mathbf{r}_{c_j}) \right] \Gamma_j, \tag{2.26}$$

where $\mathbf{r}_c = (\mathbf{r}_{c_1}, \mathbf{r}_{c_j}, \ldots, \mathbf{r}_{c_{n_p}})^t$ is the co-located points set, Γ_j is the length of each discretized segment of Γ and n_p is the number of points distributed along Γ. Assuming no sources within the boundary $q(\mathbf{r}^o) = 0$, the Equation 2.26 implies the acoustic field in Ω_i due to a limited set of sources outside the boundary Γ being completely determined by the normal velocity and the pressure on the boundary. The application of secondary sources on C using the KHI with a theoretically determined Green's function is employed to emulate virtual sources either inside or outside C is denoted here as the VS method. The VS method is implemented in combination with the FEM in order to build the tuning model for studying the boundary behaviour on piezoelectric devices.

Any set of external sources that produce the identical conditions of pressure and normal velocity on the contour C also produces the same pressure field within the domain Ω_i. This can be demonstrated by making the observation points tend to the surface C (i.e., $\mathbf{r} \to \mathbf{r}_c$). In this case, the Equation 2.25 has only two unknown variables the pressure and the velocity on Γ. If the surface velocity on the physical boundary is known a priori then a set of source located outside the boundary can be determined in order to produce a similar velocity on the boundary hence a similar pressure field within the boundary. This approach is the basis of the ESM explained in the next subsection.

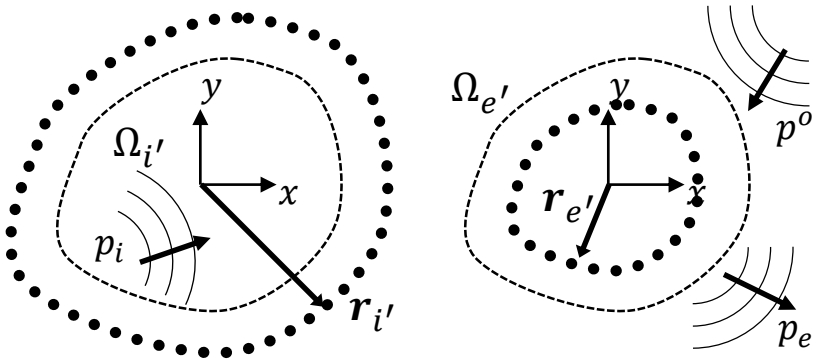

(a) (b)

Figure 2.9: Schematic of geometry for the ESM showing the set of equivalent line sources radiating into equivalent domains relative to the physical boundary. (a) Equivalent interior and (b) equivalent exterior system with $\mathbf{r}_{i'}$ or $\mathbf{r}_{e'}$ line sources positioned relative to Γ (- -) radiating internal p_i or external p_e pressure field located in equivalent interior $\Omega_{i'}$ or exterior $\Omega_{e'}$ domain.

2.3.2 Equivalent source method

The ESM approximates the solution for the internal p_i and external p_e pressure field via linear superposition of fundamental solutions defined by equivalent sources. The basis for the fundamental solution is that of generated by discrete sources on equivalent domains matching the boundary conditions at collocated points. Figure 2.9 shows the equivalent domain concept and the equivalent source points located in equivalent domains which replaces the original system shown in Figure 2.5(a) solved for circular cylindrical boundary as in Figure 2.7. In the equivalent system, the external field p_e in the external domain Ω_e is simulated by the field generated by a set of linear sources placed inside the boundary Γ at $\mathbf{r}'_e$. They are treated as sources radiating in an unbounded domain Ω'_e equivalent to Ω_e. On the other hand, the internal field p_i in the internal domain Ω_i is simulated by the field generated by a set of linear sources placed outside the closed boundary Γ treated as sources radiating an unbounded domain Ω'_i equivalent to Ω_i, as shown in Figure 2.9(a). The field due to the internal line sources is an approximation of the internal domain field in the original system. Similarly, p_i represents the acoustic field due to linear sources and p^o is the incident wave field, as shown in Figure 2.9(b). In the original system, the total field $p_e + p^o$ is an approximation of the field in the external domain. The location and complex amplitude strengths for these linear sources will be determined later on. This method avoids singularities due to wave field on the boundary Γ being evaluated for line sources placed at the boundary in Equation 2.26.

A similar approach can be derived to formulate the pressure field in the exterior domain Ω_e by applying Equation 2.25 to the external domain and following the discrete formulation as in

$$p_e(\mathbf{r}) = \sum_{j=1}^{n_p} \left[p_e(\mathbf{r}_{c_j}) \frac{\partial G(\mathbf{r}, \mathbf{r}_{c_j})}{\partial n} + \frac{\partial p_e(\mathbf{r}_{c_j})}{\partial n} G(\mathbf{r}, \mathbf{r}_{c_j}) \right] \Delta\Gamma. \tag{2.27}$$

By applying the equivalent procedure the external field can be simplified to

$$p_e(\mathbf{r}) = \sum_{j=1}^{n_p} q(\mathbf{r}_{e'_j}) G(\mathbf{r}, \mathbf{r}_{e'_j}), \tag{2.28}$$

where $\mathbf{r}_{e'}$ are the positions of the equivalent exterior source points. The same equivalent procedure may be applied to simplify the interior field by using equivalent interior source points at $\mathbf{r}_{i'}$. Given an incident pressure wave p^o at $\mathbf{r}$ defined by physical, primary sources, the boundary conditions in Equation 2.11 are then used to calculate the strengths q of a set of internal and external sources defined in equivalent domains $\Omega_{i'}$ and $\Omega_{e'}$, respectively, as in

$$p^o(\mathbf{r}) = \sum_{j=1}^{n_p} q(\mathbf{r}_{i'_j}) G(\mathbf{r}, \mathbf{r}_{i'_j}) + \sum_{j=1}^{n_p} q(\mathbf{r}_{e'_j}) G(\mathbf{r}, \mathbf{r}_{e'_j}), \tag{2.29}$$

where the equivalent sources are positioned at $\mathbf{r}_{e'}$ (internal sources) and $\mathbf{r}_{i'}$ (external sources).

The $2n_p$ set of coefficients $q(\mathbf{r}_{i'_j})$ and $q(\mathbf{r}_{e'_j})$ are found by matching the transmission boundary conditions at the n_p co-located points set $\mathbf{r} = \mathbf{r}_c$. Similarly to the pressure continuity, the normal component of velocity for an incident wave v^o at $\mathbf{r}$ is given in terms of the strengths

$$v^o(\mathbf{r}) = \sum_{j=1}^{n_p} q(\mathbf{r}_{i'_j}) \frac{\partial G(\mathbf{r}, \mathbf{r}_{i'_j})}{\partial n_r} + \sum_{j=1}^{n_p} q(\mathbf{r}_{e'_j}) \frac{\partial G(\mathbf{r}, \mathbf{r}_{e'_j})}{\partial n_r}, \tag{2.30}$$

which may configure a linear system for a total number $2n_p$ equations and $2n_p$ number of coefficients to be solved for. The development of a matrix formulation An interested reader may refer to Doicu et al. [2000] for a review of discrete source methods for both acoustic and electromagnetic scattering problems. In particular, a review on the use of ESM in various acoustic problems can be found elsewhere [Lee, 2017].

2.4 Reproduction using inverse filtering

This section describes the formulation of an inverse filter designed in the frequency domain applied to acoustic field reproduction for creating a specified acoustic field given an externally applied incident wave field. The inverse filter formulation is developed to determine what arrangement of external sources should be used to best achieve a user-defined target acoustic field pattern in the device. The filtering technique is applied over the entire spatial region within an ultrasonic manipulator to control a maximized area for the region of interest. The inverse problem in the scattering theory is a well-established type of problem and particular attention has been paid to inferring characteristics of an otherwise unknown obstacle [Colton and Kress, 2012].

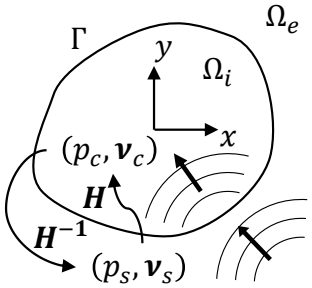

FIGURE 2.10. Schematic representation of the reproduction of a desired pressure field using inverse filtering by applying a source field transmitted from the exterior to the interior domain through a closed interface. The source field (p_s, v_s) in the exterior domain Ω_e is transmitted through Γ by the transfer function $\mathbf{H}$ and gives the control field (p_c, v_c) in the interior domain Ω_i. An inverse filter $\mathbf{H}^{-1}$ represents the function to obtain the source field given a desired control field.

The inverse filter technique has traditionally been used in sound field reproduction by means of ambisonics [Nelson, 1994] and more recently in acoustic holography [Maynard et al., 1985]. Early work on sound field reproduction inside a control region based on the KHI equation was achieved by controlling the pressure and its normal derivative over the control surface [Berkhout et al., 1993].

The application of this principle to sound reproduction by using general two-dimensional sources within a reverberant room to control the interior sound field has been studied using inverse control [Betlehem and Abhayapala, 2005] and using external sound cancellation [Poletti and Abhayapala, 2011]. On the other hand, the sound field has been controlled by multiple sources distributed on a cavity surface [Greenhall et al., 2016] so that a certain region within an enclosure has a desired complex sound pressure [Asano and Swanson, 1995]. A similar approach has been taken by Grinenko et al. [2012] to obtain transducer parameters for a circular array transducer. In their work, a transfer function was defined between the electrical potential applied to the electrodes of the transducer and the pressure on any control surface outside the control region in order to generate the required pressure landscape.

In this section, the inverse filter technique is briefly presented as it is applied to sound field reproduction based on the KHI, i.e. the problem is modelled over the physical boundary. The reproduction of a specified spatial distribution of a pressure field is reviewed by using the inverse filter technique. In Figure 2.10, the transfer function $\mathbf{H}$ is defined for a continuous system so that the pressure p_c and normal velocity v_c of the control field on the boundary Γ in interior domain Ω_i is determined by the pressure p_s and normal velocity v_s of the source field on the boundary Γ in exterior domain Ω_e. The control field should approximate the desired field on the surface bounding the reproduced region which is exactly the interior domain Ω_i in this implementation. This transfer function in terms of a BIE is defined as a continuous operator. In particular, in

the case of the transmission problem this operator is called a Calderon projector [Costabel and Stephan, 1985] since the proposed function projects the source boundary data (p_s, v_s), the so-called Cauchy data on Γ, onto the control boundary data (p_c, v_c), as shown in Figure 2.10.

This model-based transfer function is then inverted numerically to obtain $\mathbf{H}^{-1}$ and determine the pressure and normal velocity of the source field (p_s, v_s) to synthesize a desired pressure field pattern given the control field (p_c, v_c). In the least squares sense the reproduced field is the best field capable of being produced by the source data. The application of the KHI on the reproduction which defines the pressure and its gradient as the key properties. The realization of this principle is defined as the boundary surface control principle and is described as the interior control problem [Ise, 1999].

As an example, the direct transmission problem is solved numerically using a discrete source method (described later in Section 3.1), a discrete version of the transfer function $\mathbf{H}$ can be defined using a matrix formulation

$$\mathbf{b}_c = \mathbf{H}\mathbf{b}_s, \tag{2.31}$$

where $\mathbf{b}_c = \left[\boldsymbol{v}_c, \mathbf{p}_c\right]^t$ denotes the boundary data for the internal field at the control points x_c and $\mathbf{b}_s = \left[\boldsymbol{v}_s, \mathbf{p}_s\right]^t$ the boundary data for the incident field at the source points x_s. The source boundary data can be readily obtained by means of the inversion above mentioned

$$\mathbf{b}_s = \mathbf{H}^{-1}\mathbf{b}_c. \tag{2.32}$$

Numerically small errors in that data produce very large errors in the reconstructed results hence the solution for the inversion does not depend continuously on the data. To avoid this problem, a Singular Value Decomposition (SVD) is applied to the matrix $\mathbf{H}$ before the inversion [Stewart, 1993],

$$\mathbf{H} = \mathbf{U}\boldsymbol{\Sigma}\mathbf{V}^t, \tag{2.33}$$

where $\mathbf{U}$ and $\mathbf{V}^t$ are orthogonal matrices that contains the singular vectors and $\boldsymbol{\Sigma}$ is a diagonal matrix with singular values $\sigma_1 \geqslant \cdots \sigma_p > 0$, with p the total number of singular values. From Equation 2.33 the Moore-Penrose inverse is then applied which defines $\mathbf{H}^+$ the inverse filter

$$\mathbf{H}^+ = \mathbf{V}\boldsymbol{\Sigma}^+\mathbf{U}^t, \tag{2.34}$$

where $\boldsymbol{\Sigma}^+$ is the inverted reduced rank version of $\boldsymbol{\Sigma}$ with singular values $\sigma_1^{-1} \leqslant \cdots (\sigma_0\sigma_1)^{-1}, 0 \cdots 0$, with σ_0 as the relative threshold. The pseudoinverse is used to obtain the inverse filter $\mathbf{H}^+$. An interesting theoretical compilation of problems involving active control of scattered acoustic fields can be found in Kiyono et al. [2016]. This technique is applied to the acoustic field reproduction problem treated here in both ESWS and TPFE models. For the control data set, the refracted field is always considered on the boundary immediately inside the cavity. In the ESWS case, the transfer function is computed using a matrix propagator (a discrete projector) which accounts

for the transmission of waves across the physical boundary. The source data is obtained as the Cauchy data (pressure and derivative) on the boundary immediately outside the acoustic cavity. Lastly, the transfer function in the TPFE model is obtained by solving using FEM for a set of individually addressable electrical sources.

2.5 Electroelastic wave equation

The theory of electroelasticity investigates the relationship between the stress T, strain S, electric field E and electric displacement D in electroelastic materials. The piezoelectric effect can be described by such relationship and was discovered, by Curie and Curie [1880], for certain materials such as sphalerite, topaz, and quartz. This effect was evidenced as the formation of two electric poles of opposite charges generating positive charges when such material is compressed and in the opposite direction generating negative charges when decompressed. Piezoelectricity has since been reviewed and is now regarded as a form of energy conversion [Ikeda, 1996] that entails the physical property by which a particular device develops surface charge under mechanical stress or vice versa. The linear, piezoelectric constitutive relations [Tiersten, 1963b] are given by

$$\mathbf{T} = c^E \mathbf{S} - \mathbf{e}\mathbf{E} \tag{2.35}$$

$$\mathbf{D} = \mathbf{e}^t \mathbf{S} + \varepsilon^S \mathbf{E}, \tag{2.36}$$

where $\mathbf{e}^t$, ϵ^S, c^E are the piezoelectric coupling, the relative permittivity and the stiffness tensor at constant electric field, respectively. An electroelasticity wave equation based on the above equations and other Maxwell equations can be formulated in a coupled field system of equations [Tiersten, 1963a]

$$c^E \nabla^2 u + \mathbf{e}\nabla^2 \varphi = \rho \frac{\partial^2 u}{\partial t^2} \tag{2.37}$$

$$\mathbf{e}^t \nabla^2 u - \varepsilon^S \nabla^2 \varphi = 0. \tag{2.38}$$

where u is the displacement and φ is the electrical potential fields.

Although discrete numerical modelling is a common choice in order to solve for the electroelasticity wave equations a Green's function solution can be formulated for specific cases [Berndt and Sevostianov, 2015]. The FEM is a versatile volumetric numerical method appreciated as being long developed and widely used among design practitioners to solve real engineering problems. Pre-calculated expressions based on general forms of spatial dependent material properties are developed in commercial software and very little study is required by the user towards the governing equations. Solving practical problems in a convenient matrix formulation primarily requires an understanding of both differential equations of physical phenomena and continuum approximations of material properties. Well-established mathematical techniques are employed

to derive integral formulations for the former, such as the Galerkin scheme and variational principle which is the topic of the following sections. The latter is often achieved by experimental measurements and studies on piezoelectric characterization can be found elsewhere [Kiyono et al., 2016; Li et al., 2013]. The goal of this section is to review established development on electroelasticity based on the variational principle to allow further simplifications to be applied to wave propagation behaviour of piezoelectric media.

2.5.1 Variational principle for electroelasticity

The variational principle is applied to variational calculus to determine integral equations from differential equations and boundary conditions. Hamilton's principle states that work is done by external forces when the displacement varies. Hence, there is a variation of the integral determined by the difference between total kinetic energy and potential energy of deformation taken between fixed initial and final values for time [Love, 1906], termed the Lagrangian function for elastic systems. A system's dynamics is determined by applying the variational principle to the Lagrangian function. This principle determines how the variables of a system evolve with time according to the excess of virtual work due to external loads. In other words, if the virtual work due to external loads is integrated within a specified time interval, say t_1 and t_2, then it is included in the integral of the Lagrangian function.

The excess of virtual work due to external loads is given by the product of the point load $\mathbf{F}_P$ and a small virtual change in the displacement $\mathbf{u}$. The Lagrangian function for elastic systems can be defined as the difference between kinetic energy and the enthalpy

$$\mathscr{L} = \int_V \left(\mathscr{T} - \mathscr{E}\right) dV. \tag{2.39}$$

By integrating by parts the variational of the kinetic energy term over the specified interval, the variational of the product displacement by particle velocity $\dot{\mathbf{u}}$ integrated over the time interval vanishes in such a way that the kinetic energy term is only a function of the displacement, the acceleration $\ddot{\mathbf{u}}$ and the mass density ρ. The enthalpy for the non-piezoelectric media is defined as the elastic potential energy and is given by the product of the strain tensor $\mathbf{S}$ by the stress tensors σ. The stress tensor on the hand is defined by the linear elasticity relation as the product of stiffness tensor c^E by the strain tensor.

By applying the variational operator δ, denoting the first-order variation, over a specified volume V and given the virtual work definition then the equilibrium equation may be expressed as

$$\int_V \left(-\delta\mathbf{u}^t \rho \ddot{\mathbf{u}} - \delta\mathbf{S}^t c^E \mathbf{S}\right) dV = -\delta\mathbf{u}^t \mathbf{F}_P. \tag{2.40}$$

In order to include piezoelectric effects into the Hamilton principle, an extension has been formulated to the variational principle [Tiersten, 1967]. In regard to the excess of virtual work due

to external loads, previously discussed for elastic materials, an electrical analogue is given by the product of the point charge $\mathbf{Q}$ and the small virtual change in electrical potential φ. Furthermore, for electroelasticity the Hamilton principle is derived again and the electric enthalpy has a contribution from the product of the electric displacement $\mathbf{D}$ by a small virtual change in the electric field $\mathbf{E}$. By substituting the new enthalpy definition into the Lagrangian formulation in Equation 2.39 and applying the variational operator both the electrical potential and the terms can be handled likewise. If the stress-charge form of the piezoelectric constitutive equations (Equation 2.36) is then taken into account an alternative equilibrium equation may be expressed in the same form as Equation 2.40 by

$$\int_V \left(-\delta\mathbf{u}^t\rho\ddot{\mathbf{u}} - \delta\mathbf{S}^t(c^E\mathbf{S} - \mathbf{e}^t\mathbf{E}) + \delta\mathbf{E}^t(\mathbf{e}^t\mathbf{S} + \varepsilon^S\mathbf{E})\right)dV = -\delta\mathbf{u}^t\mathbf{F}_P + \delta\varphi^t\mathbf{Q}. \tag{2.41}$$

Lastly, by separating the terms multiplying the variation in displacement and strain from the ones which multiply the variation in electrical potential and electrical field a system of equation is given by

$$\begin{cases} \int_V \left(\delta\mathbf{u}^t\rho\ddot{\mathbf{u}} + \delta\mathbf{S}^t(c^E\mathbf{S} - \mathbf{e}^t\mathbf{E})\right)dV & = \delta\mathbf{u}^t\mathbf{F}_P \\ \int_V \left(\delta\mathbf{E}^t(\mathbf{e}^t\mathbf{S} + \varepsilon^S\mathbf{E})\right)dV & = \delta\varphi^t\mathbf{Q} \end{cases}. \tag{2.42}$$

2.5.2 Finite element for electroelasticity

In order to solve the equilibrium in Equations 2.40 and 2.42 using FEM, the problem domain is divided into several finite elements. By approximating each continuum variable with an appropriate form, or test, function and taking each term of these equations separately, each of which solves the differential equations only locally with potentially good approximation rates. It can be shown convergence to a discrete solution is achieved given a fixed problem domain without singularities for an increasing number of nodes by which these elements are defined [Zienkiewicz and Cheung, 1967]. A converged solution to the exact solution is commonly verified by comparison with known analytical solutions in a case by case manner when applicable.

Here the resulting variational principle is stated in matrix notation as has been derived elsewhere [Allik and Hughes, 1970]. The continuum displacement inside each element may be replaced by an approximation given by its nodal value multiplied by a form function $\left[\mathbf{N}_u\right]$. Furthermore, the in-plane strain tensor is defined as the gradient of the displacement field which can also be approximated in terms of a form function, $\left[\mathbf{B}_u\right]$, which is related to $\left[\mathbf{N}_u\right]$ by derivation operator matrix. By taking the definition of in-plane strain on a continuum media, and approximating by nodal variables, it is possible to write nodal displacement and strain variable in a vector form $\mathbf{U_e} = \left[\mathbf{N}_u\right]\left\{\mathbf{U}\right\}_e$ and $\mathbf{S_e} = \left[\mathbf{B}_u\right]\left\{\mathbf{U}\right\}_e$ respectively. The shape functions definitions $\left[\mathbf{N}_u\right]_e$ and $\left[\mathbf{B}_u\right]_e$ depend on the element type and are calculated by each element local coordinate system as to interpolate the dependent variable solved for. For example, the shape functions for a

simple one-dimensional linear element are defined as $\left[\mathbf{N}_u(\epsilon)\right]_e = \frac{1}{2}\left[(1-\epsilon),(1+\epsilon)\right]$ for a natural coordinate system based in ϵ and $\left[\mathbf{B}_u(\epsilon)\right]_e = \frac{1}{2}\left[-1,1\right]$. The equilibrium in Equation 2.40 may be rewritten taking into account these approximated nodal variables. The resulting system of equations must be valid for any arbitrary variation on displacement $\{\delta\mathbf{U}\}_e$. For this reason, these arbitrary coefficients may be left out from the equations which are reassembled into an element matrix based equation

$$\left[\mathscr{M}\right]_e \left\{\ddot{\mathbf{U}}\right\}_e + \left[\mathscr{K}_{uu}\right]_e \{\mathbf{U}\}_e = \{\mathbf{f}\}_e, \tag{2.43}$$

where $\left[\mathscr{M}\right]_e$ is the element mass matrix, $\left[\mathscr{K}_{uu}\right]_e$ is the element stiffness matrix and $\{\mathbf{f}\}_e$ is the force vector. This system of equations may be found elsewhere [Zienkiewicz and Cheung, 1967].

In order to solve the appended system of equations 2.42 using FEM, the electrical potential field is considered as an additional independent variable. This variable is defined in piezoelectric domains and may be replaced by an approximating form function inside each element multiplied by a nodal vector $\{\boldsymbol{\varphi}\}_e$. By taking the definition of the electrical field in a continuum media, it is possible to write these variables in vector form based on a form function $\varphi_e = \left[\mathbf{N}_\varphi\right]_e \{\boldsymbol{\varphi}\}_e$ and $E_e = \left[\mathbf{B}_\varphi\right]_e \{\boldsymbol{\varphi}\}_e$. The aforementioned equilibrium in Equation 2.42 may be reconsidered with the added piezoelectric effects. Similarly, the appended system of equations must also be valid for any arbitrary variation on electric potential $\{\delta\boldsymbol{\varphi}\}_e$. For this reason, these arbitrary coefficients can be left out of the equation which is reassembled into an element matrix based equation

$$\begin{cases} \left[\mathscr{M}\right]_e \left\{\ddot{\mathbf{U}}\right\}_e + \left[\mathscr{K}_{uu}\right]_e \{\mathbf{U}\}_e + \left[\mathscr{K}_{u\varphi}\right]_e \{\boldsymbol{\varphi}\}_e &= \{\mathbf{f}\}_e \\ \left[\mathscr{K}_{\varphi u}\right]_e \{\mathbf{U}\}_e + \left[\mathscr{K}_{\varphi\varphi}\right]_e \{\boldsymbol{\varphi}\}_e &= \{\mathbf{q}\}_e \end{cases} \tag{2.44}$$

where $\left[\mathscr{K}_{\varphi u}\right]$ and $\left[\mathscr{K}_{u\varphi}\right]$ are the piezoelectric 'stiffness' matrices, $\left[\mathscr{K}_{\varphi\varphi}\right]$ is the dielectric 'stiffness' matrices and $\{\mathbf{q}\}_e$ the point charge vector. The matrices defined in Equation 2.44 are computed by integrating the form functions over the volume of each element which depends on local material properties and form functions. It is worth noting that boundary conditions considered for this review only account for special cases of loads applied to the nodes of elements. Additional electroelastic vectors including the definitions of body and surface forces and charges necessary for comprehensive interpretation of the variational principle can be found in Allik and Hughes [1970].

All domains are characterized by the element mass matrix $\left[\mathscr{M}\right]_e$ defined by

$$\left[\mathscr{M}\right]_e = \int_{V_e} \left[\mathbf{N}_u\right]_e^t \rho \left[\mathbf{N}_u\right]_e dV. \tag{2.45}$$

The general formula for the element stiffness matrix is

$$\left[\mathscr{K}_{uu}\right]_e = \int_{V_e} \left[\mathbf{B}_u\right]_e^t \left[\mathbf{c}^E\right] \left[\mathbf{B}_u\right]_e dV, \tag{2.46}$$

where c^E is the elastic tensor which is defined by the material model. For piezoelectric media, the piezoelectric effect is modelled by considering additional material coefficients as in

$$\left[\mathcal{K}_{u\varphi}\right] = \int_{V_e} \left[\mathbf{B}_u\right]^t [\mathbf{e}]^t \left[\mathbf{B}_\varphi\right] dV \tag{2.47}$$

$$\left[\mathcal{K}_{\varphi u}\right] = \int_{V_e} \left[\mathbf{B}_\varphi\right]^t [\mathbf{e}] \left[\mathbf{B}_u\right] dV \tag{2.48}$$

$$\left[\mathcal{K}_{\varphi\varphi}\right] = -\int_{V_e} \left[\mathbf{B}_\varphi\right]^t \left[\varepsilon^S\right] \left[\mathbf{B}_\varphi\right] dV. \tag{2.49}$$

A globally assembled system of equations is derived from each individual element and both the displacement and the electric potential fields in the piezoelectric domain can then be solved from a global system of equations using inversion methods. Further derivation of FEM principles based on structural analysis can be found in textbook elsewhere [Zienkiewicz and Cheung, 1967]. Although electroelasticity is not covered in this book, a brief introduction to finite element analysis of piezoelectric transducers can be found elsewhere [AC. and B., 2008].

2.6 Acoustic radiation force

Acoustic radiation force or acoustic radiation pressure is commonly regarded as the resulting force on a particular scatterer due to an incident pressure landscape [Beyer, 1978]. The radiation force is a second order effect resulting from a momentum transfer between particle and incident wave. Early studies quantifying acoustic radiation force applied on rigid particles were validated with experimental results [King, 1934]. Moreover, some authors have found good agreement between theoretical and experimental results involving such phenomena in elastic spheres [Hasegawa, 1979; Hasegawa and Yosioka, 1969]. This effect has also been investigated on bubbles larger than resonance size, i.e. driven above resonance [Asaki and Marston, 1994]. Furthermore, the associated acoustic scattering problem can be rewritten to evaluate the acoustic radiation potential for a fluid host in the presence of elastic spheres. Scattering coefficients are obtained through applying appropriate boundary condition at the interface then solving the wave equation as in Section 2.2 and can be found elsewhere [Mitri and Fellah, 2006].

In general, the velocity potential Φ of an acoustic field[1] in the presence of a scatterer can be expressed in a linear approximation as the sum of an incident term Φ^o and a scattering Φ^s term

$$\Phi = \Phi^o + \Phi^s, \tag{2.50}$$

[1]The acoustic field here is defined as Φ expressed in terms of scalar potential, as opposed to the pressure p (see 2.2) to differentiate radiation pressure (force) applied on particles from pressure field within acoustic cavities, but they are interchangeable in the development of acoustic wave equation.

where a factor of $e^{-i\omega t}$ is assumed but not expressed. The scattering term can be determined by solving a flow problem in an inviscid fluid around a compressible particle of radius $R << \lambda$ [Landau and Lifshits, 1959]. Thus, the velocity potential of the scattered wave can be defined as

$$\Phi^s = -\frac{R^3}{3\rho_s r}\dot{p}^o f_1 - \frac{R^3}{2} f_2 \nabla\left(v^o \frac{1}{r}\right), \tag{2.51}$$

where ρ_s is the sphere's density, v^o is the incident particle velocity, $\dot{p}^o$ is the time derivative of the incident pressure and r is the radial distance between the sphere's centre and the point at which the velocity potential is calculated. The factors f_1 and f_2 are the monopole and dipole coefficients given by

$$f_1 = 1 - c_f^2 \rho_f / \rho_s c_s^2, \quad f_2 = 2(\rho_s - \rho_f)/(2\rho_s + \rho_f), \tag{2.52}$$

where f and s denote the fluid and the particle properties respectively. An expression for the time-averaged acoustic radiation potential U_a due to a sphere, the Gor'Kov potential [Gor'Kov, L P, 1962], is given by

$$U_a = 2\pi R^3 \left(\frac{\langle p^{o^2} \rangle}{3\rho_f c_f^2} f_1 - \frac{\rho_f \langle v^{o^2} \rangle}{2} f_2 \right), \tag{2.53}$$

where $\langle p^{o^2} \rangle$ and $\langle v^{o^2} \rangle$ are the mean square of the incident pressure and particle velocity, respectively. The acoustic energy density is defined in order to extract the acoustic radiation force from Equation 2.53. The energy carried by an acoustic wave through a fluid medium can either be in the form of potential, U_p, or kinetic energy, U_k. By substitution into Equation 2.53 of the acoustic energy density expressions and considering the sphere's volume, $V_s = \frac{4\pi R^3}{3}$, the acoustic radiation potential can be rewritten in the form

$$U_a = V_s \left(U_p f_1 - \frac{3}{2} U_k f_2 \right). \tag{2.54}$$

The components of the acoustic force $\mathbf{F}_a$ are determined from the gradient of this potential field

$$\mathbf{F}_a = -\nabla U_a. \tag{2.55}$$

Substituting Equation 2.54 into Equation 2.55, the force is given by

$$\mathbf{F}_a = V_s \left(\frac{3}{2} \nabla U_k f_2 - \nabla U_p f_1 \right). \tag{2.56}$$

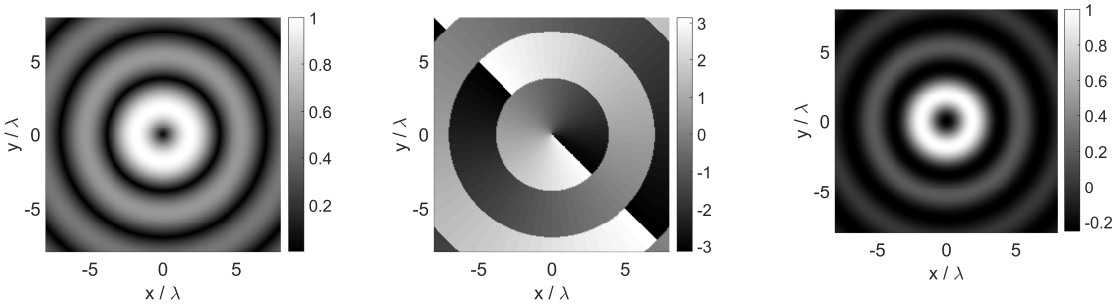

(a) (b) (c)

FIGURE 2.11. Simulated radiation potential shape of a first-order Bessel-shaped function acoustic vortices. (a) Normalized pressure magnitude , (b) phase field and (c) normalized acoustic radiation potential which is calculated using Equation 2.54 considering $f_1 = 0.6$, $f_2 = 0.62$

Evidently, the resulting radiation force acts by pushing an immersed particle into a region of minimum acoustic radiation potential. Acoustic particle manipulation devices capitalized on practical wave field with phase singularities called acoustic vortex which is an on-going research topic. Acoustical vortices are Bessel functions with topological charge have been found effective in manipulating relatively small particles ($ka < 1$) with positive contrast factor. Their applications in acoustic tweezers have seen an increase due to their stable lateral, or transverse, energy gradient at their centre [Baresch et al., 2016; Hong et al., 2015; Kang and Yeh, 2010; Riaud et al., 2014] but prove unstable in exceptional cases [Thomas and Marchiano, 2003]. In this case, the radiation potential generated by an acoustic vortex becomes a trap based on a potential well because its gradient acts as a restoring force pushing the particles towards the centre as shown in Figure 2.11. The complex pressure amplitude p^u of a Bessel beam with topological charge $m = 1$ is given by

$$p^u(\mathbf{r}) = p_0 \frac{i}{4} J_1\left(k|\mathbf{r}|\right) e^{i\phi}. \tag{2.57}$$

Analytic expressions for radiation forces on rigid spheres along the axis [Mitri, 2009] and off-axis [Mitri and Silva, 2011], and on soft spheres [Marston, 2009] of an ideal high-order Bessel beam. More recently a theoretical study has been published towards the analytic derivation of the acoustic radiation force using partial-wave approach and applied by acoustic beam with arbitrary wavefronts [Silva, 2011] and standing waves [Marston, 2017]. Acoustical vortex has been extensively studied experimentally [Hong et al., 2015] which has opened up opportunities for developing new manipulation devices [Franklin et al., 2017]. For this reason, acoustical vortices

are solely studied in this thesis as a manipulation mechanism and applied to reproduction of desired pressure field in Chapters 3, 4 and 5.

Note the force field given by Equation 2.56 is only due to gradients of acoustic pressure and particle velocity in standing and propagating wave fields. In general, the particle's equilibrium position does not occur in the region where the radiation force is exactly zero owing to other forcing mechanisms affecting particles, such as gravitational forces [Glynne-Jones and Hill, 2013] and particle to particle interaction [Silva and Bruus, 2014]. If viscous forces are not neglected, acoustic streaming occurs due to fluid flow generated by acoustic waves and may also be considered into the net force equilibrium. Furthermore, bulk streaming may occur in confined space within manipulation devices and studies have shown this effect can be actively controlled [Riaud et al., 2014] or reduced passively [Bernassau et al., 2014]. Although all these effects are acknowledged their analysis and applications are not covered in this thesis.

2.7 Summary

This chapter presented the literature review about the topics on transmission, reproduction and generation of sound waves and their application in ultrasonic particle manipulation. The wave transmission occurs from the outer to the inner media via the physical boundary and is characterized by the transmitted and scattered waves. The incident wave studied can be generated by either theoretically via acoustic sources or practically via an electrical field in piezoelectric transducers. The wave reproduction is formulated using the inverse filtering technique. The collection of these wave phenomena is essential to prove the working principle of the ultrasonic kerfless transducer for application on in-plane ultrasonic tweezers.

The understanding of the general problem of wave transmission through a fluid-fluid boundary in a bounded obstacle is covered in the first section. It also provided a discussion on numerical methods that have been applied to solve the problems for the following wave phenomena leaving comments on ones not been contemplated in the modelling framework developed in this thesis. The theoretical wave field solution for the arbitrary, externally located point source was presented in the second section to demonstrate the modelling principle for MUTD and was provided as a referencing solution for the physics-based models developed in this thesis.

In the second a brief review of an analytical solution is presented for the transmission problem given an incident field defined by a line source located in the exterior domain. The definition of the response to a line source in free space is expressed in a closed form. Further reference for the formulation of the solution for a point source located in the interior domain was indicated. This solution based on cylindrical wave expansion is applied to validate the physics-based models for a circular boundary in Chapters 3, 4 and 5. An overall description was given regarding the implementation of the functions involved and the application cases developed in this thesis were discussed.

The third section describes the KHI equation which gives the pressure field in a bounded domain in terms of pressure and its derivative defined on the closed boundary. A discrete form of this integral is employed to emulate acoustic virtual sources which is implemented in the VSFE model. A general formulation of equivalent domains is presented for reviewing the equivalent source method which implemented in the ESWS model. These methods only account for theoretical acoustic sources and are essential for developing models for general incident acoustic waves.

The fourth section presents a mathematical model by means of inverse filter formulation for pressure field reproduction. The inverse filter technique is used to solve inverse problems based on transfer functions to impose the boundary conditions necessary to generate the target pressure field. This formulation is applied to the ESWS model in terms of theoretical acoustic sources and to the TPFE model in terms of practical electrical potential.

In the fifth section reviews the electroelastic wave equation which governs the physics of piezoelectric transducers. The finite element formulation implemented in commercially available software is presented based on the variational principle for electroelasticity. The resulting global system of equations is presented as a reference for identifying relevant element matrices and load vectors. These mathematical entities are important parameters for the definition of the material properties and boundary conditions, hence the solution for both the VSFE and TPFE models.

The last section reviews the acoustic radiation force and presents the classical expression used for calculating the acoustic radiation potential. It draws attention to the restoring force characteristics a potential well applied to acoustic tweezers by showing the general format of the transverse section of a Bessel beam. The Bessel beam is used as a basic target field in the formulation of the pressure field reproduction applied to the physics-based models.

CHAPTER 3

THE EQUIVALENT SOURCE WAVE SCATTERING MODEL

This chapter is dedicated to the formulation of the ESWS model based on a scattering problem of an arbitrary shaped fluid inclusion in a fluid host. The aim is to compute a good approximation for the scattering problem and compare the numerical solution with the analytical solution described in Appendix C. The proposed model is part of the modelling approach to design of Kerfless Ultrasonic Tweezers Devices and is regarded as the first most simplistic model among the three physics-based models studied as shown in Figure 3.1. This model determines the acoustic pressure and velocity field on the internal boundary within a closed device of specified geometry with approximated material properties due to an incident

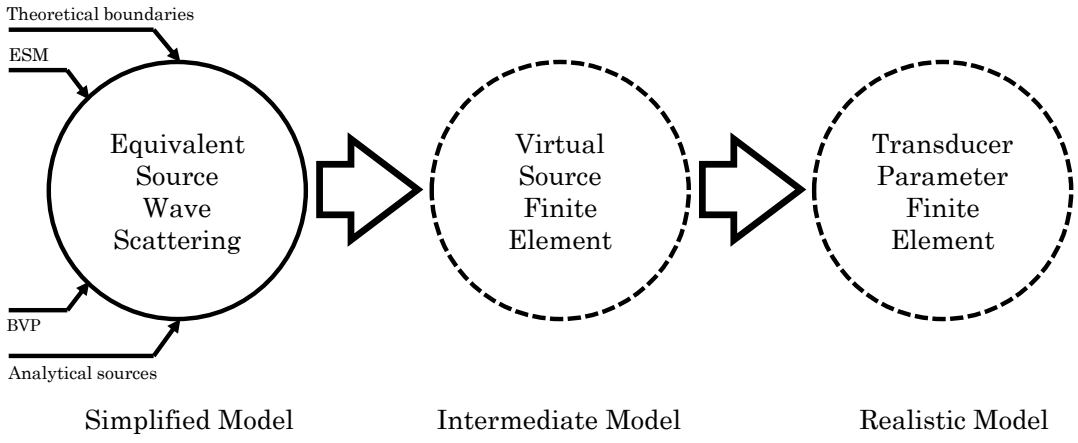

FIGURE 3.1. Schematic diagram for physics-based modelling methodology highlighting the simplified model (ESWS) and main features. Preceded by the realistic and tuning models, the ESWS considers BVP as a analytical input source and ESM as a theoretical boundary formulation.

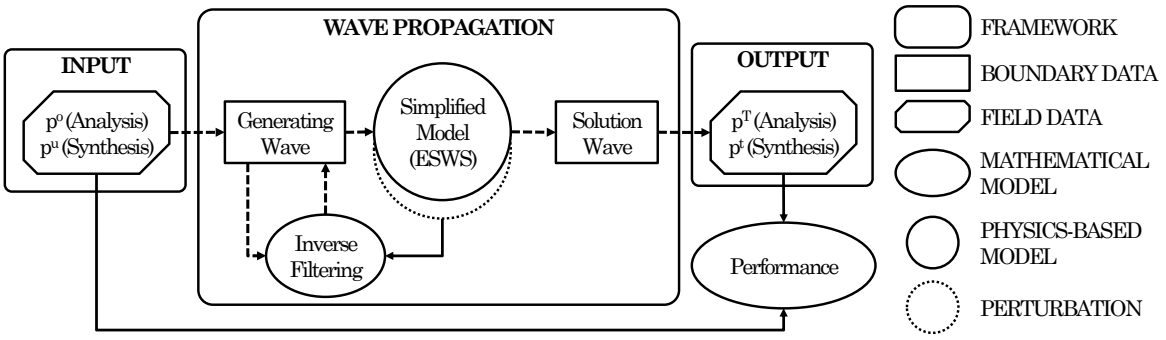

FIGURE 3.2. Schematic diagram of the modelling framework applied to the simplified model. Diagram indicates both the analysis and synthesis output are computed using the ESWS results.

field either determined by an internal monopole line source for the analysis protocol or obtained from a target field using an equivalent set of monopole line sources in equivalent domains for the synthesis protocol. The chapter is devised into the development of the ESWS presenting the linear system of equations solved for followed by the application of a numerical method and the validation for the analysis of pressure field on a circular shaped inclusion. Figure 3.2 shows the schematic diagram for the overview methodology applied in the wave propagation study associated with the ESWS model. The sections of this chapter are summarised below.

Section 3.1 describes the ESWS model based on the ESM via a matrix formulation. The discretization of the physical boundary and the distribution of collocation points along this interface is explained. Two transfer matrices which takes into account the overall effects of the boundary behaviour and the free-space wave propagation are defined. The inverse filter technique applied to the reproduction of pressure field based on the ESWS model is presented.

The Section 3.2 describes two numerical methods applied to solve a common system of linear equations for the acoustic transmission problem. The first one is an iterative method which attempts to resolve the solution for the scattering problem into multiple locally reflected and propagated waves defined by a convergent series of point source strengths. The second applied method is a direct approach which solves the resulting system of equations employing a block matrix inversion procedure.

The Section 3.3 analyses the solution obtained using this simplified model. The parameters space studied and validating the solution field against the analytical method for a circular shape is defined. The results for hexagonally shaped boundaries are investigated.

Section 3.4 presents numerical experiments which determines spatial-dependent performance parameters for analysis and synthesis of pressure field based on the ESWS model.

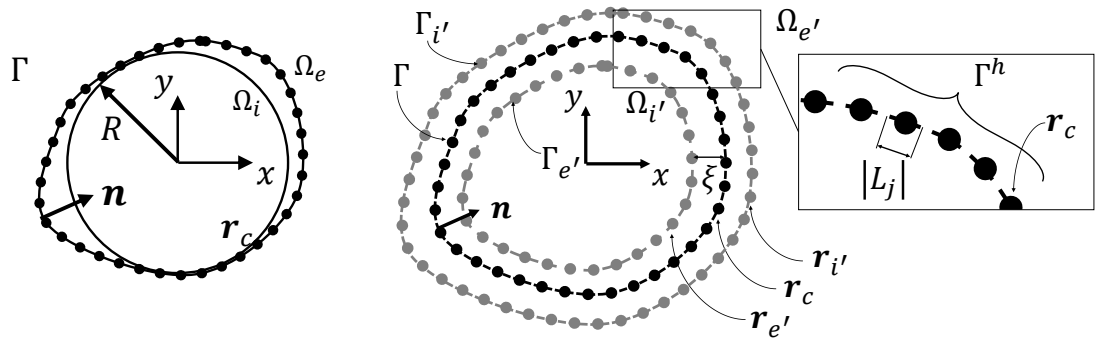

(a) (b)

Figure 3.3: Equivalent source distribution showing the original and co-located points on the physical boundary and the equivalent set of external, internal line sources on surfaces defined on equivalent domains. (a) The original system is shown for a physical boundary Γ circumscribed by a circle with radius R.(b) The equivalent system distribution showing the co-located points $\mathbf{r}_c$ and set of points for external $\mathbf{r}'_e$, internal $\mathbf{r}'_i$ sources at a distance ξ away from the physical boundary Γ. Inset shows details on discretized boundary Γ^h each segment with length $\left|L_j\right|$

3.1 Simplified model development

This section is dedicated to describe the development of the ESWS model in order to solve for the acoustic transmission problem in fluid-fluid media interface. As a simplified model the generation of sound is approximated by a theoretical, arbitrary incident wave that defines the boundary conditions of a boundary value problem. Then it solves the transmission problem based on the ESM which defines two sets of sources in separate unbounded equivalent domains and matches the boundary conditions at co-located points. This method solves for a system equivalent to one defined by strictly internal and external domains. The solution is based on fundamental solutions for the wave equation in these equivalent domains and can be found by solving a system of linear equations using a matrix formulation.

Firstly, the distribution of equivalent monopole line sources are defined relative to the fluid-fluid interface. Then the equations for the boundary conditions are assembled in a matrix form and a transfer function for the transmission of pressure field is defined. Lastly, in order to find the solution two alternative numerical methods are presented. A direct method is employed to solve the resulting system directly via block matrix inversion.

3.1.1 Equivalent source distribution

The geometrical configuration of the equivalent point sources $\mathbf{r}'_e$ and $\mathbf{r}'_i$ are defined according to the co-located points $\mathbf{r}_c$ and follows a simple geometrical transformation, as shown in Figure 3.3(b). The surface Γ is approximated by a discretized curve Γ^h, composed by n_p curvilinear segments

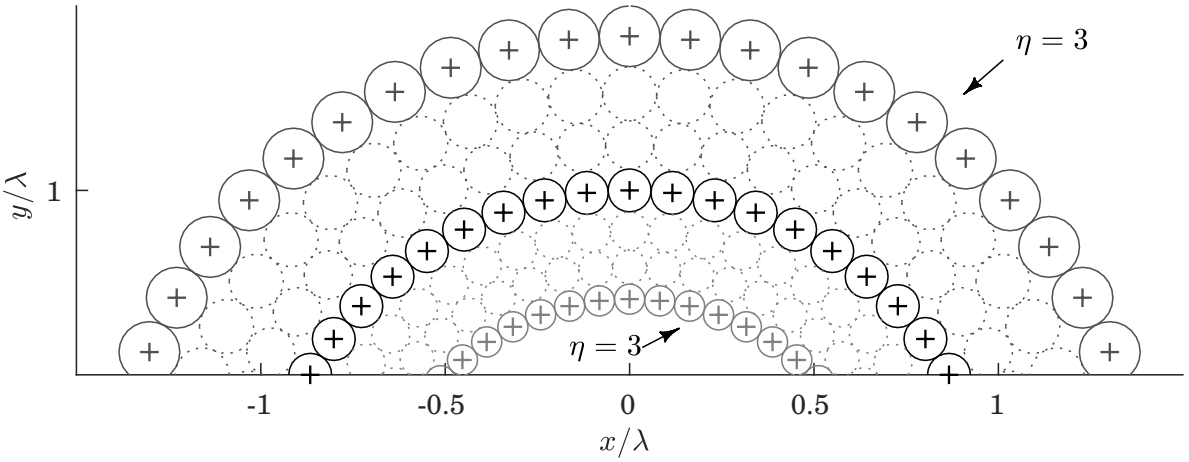

Figure 3.4: Circular packing rule example of placement for the equivalent source distribution relative to the collocation points. Crosses mark the location of each point; Solid lines (—) represent the mathematical bounding circumference; Dotted (.....) represent adjacent layers. Black is the set r_c, dark gray the $r_{e'}$ and light gray the $r_{i'}$. Points generated for $R = 1\lambda$, parametrized curve $\Gamma = r_6^0$ and $n_p = 54$.

L_j, with length $\left|L_j\right|$. Each segment comprises of a middle point $\mathbf{r}_c$ where the pressure p_j and the normal particle velocity v_j must be continuous. A set of equivalent sources is distributed on auxiliary internal $\Gamma_{i'}$ and external $\Gamma_{e'}$ surfaces each with distance ξ_+ and ξ_- away from Γ. Each auxiliary surface contains a set of points $\mathbf{r}_{e'}$ and $\mathbf{r}_{i'}$ placed at a distance along the normal to the surface Γ^h from $\mathbf{r}_c$ where the monopole sources are placed.

The interface is defined by a parametrized curve $\Gamma = r_N^\varepsilon$ in Appendix A. The normal direction $\mathbf{n}$ is calculated using equation A.3 and the length $\left|L_j\right|$ is determined by an integral expression A.4. The distance ξ is defined in terms of a circular packing rule based on a circumscribed circle calculated using the expression below.

$$\xi_+ = R\left|1 - \left(d\left(n_p\right)\right)^{\eta}\right|, \tag{3.1}$$

$$\xi_- = R\left|1 - \left(d\left(n_p\right)\right)^{-\eta}\right|, \tag{3.2}$$

where d_λ is given by

$$d\left(n_p\right) = \frac{1 - 2\sin\left(\pi/n_p\right)}{1 + \sin\left(\pi/n_p\right)}, \tag{3.3}$$

R is the radius of the circumscribed circle and n_p is the total number of collocation points. As shown in Figure 3.4, the parameter η (the number of adjacent layers) is fixed to $\eta = 3$ for all

simulations. The geometrical rule defined by Equation 3.2 is based on successive circumferential packing layers so the distance ξ scales with the number of collocation point per wavelength. Then, for a set of collocation points $\mathbf{r}_c = (\mathbf{r}_{c_1}, \cdots, \mathbf{r}_{c_{n_p}})$ there is a set of equivalent points $\mathbf{r}_{i'} = (\mathbf{r}_{i'_1} \cdots \mathbf{r}_{i'_{n_p}})$ and $\mathbf{r}_{e'} = (\mathbf{r}_{e'_1} \cdots \mathbf{r}_{e'_{n_p}})$ which is computed using the following expression,

$$\mathbf{r}_{e'} = \mathbf{r}_c + \xi_+ \mathbf{n}_c, \tag{3.4}$$

$$\mathbf{r}_{i'} = \mathbf{r}_c - \xi_- \mathbf{n}_c. \tag{3.5}$$

3.1.2 The matrix formulation

Once the geometrical configuration of the ESWS model is defined, the system of Equation 2.10 may be developed using a matrix formulation. According to the ESM the pressure and the normal particle velocity generated by equivalent point sources must match boundary condition at a set of collocation points. If a sufficiently large number of co-located points is carefully chosen then the acoustic wave field within the boundary may be defined with high accuracy. For a general formulation irrespective of which equivalent domain the field is modelled, let q be the strength of a line source at any point $\mathbf{r}'$ then the pressure p at $\mathbf{r}$ in any equivalent domain is given by

$$p(\mathbf{r}) = -\frac{i}{4} H_0^{(1)}(k|\mathbf{r}' - \mathbf{r}|)\, q(\mathbf{r}'). \tag{3.6}$$

From the pressure-velocity relation, the normal component of particle velocity v_n for a given direction $\mathbf{n}$ at the same point $\mathbf{r}$ is possible computed as in

$$v_n(\mathbf{r}) = \frac{1}{4\rho c} H_1^{(1)}\left(k|\mathbf{r}' - \mathbf{r}|\right) \frac{(\mathbf{r}' - \mathbf{r}) \cdot \mathbf{n}_{r'}}{|\mathbf{r}' - \mathbf{r}|}\, q(\mathbf{r}'). \tag{3.7}$$

From these equations both pressure and normal particle velocity may be computed as a linear superposition of responses and strengths of a finite set of equivalent point sources in a vector form

$$p(\mathbf{r}) = \mathbf{C}\mathbf{q} = \sum_{j=1}^{n_p} -\frac{i}{4} H_0^{(1)}\left(k|\mathbf{r}_j - \mathbf{r}|\right) q_j, \tag{3.8}$$

$$v_n(\mathbf{r}) = \mathbf{M}\mathbf{q} = \sum_{j=1}^{n_p} \frac{k}{4\rho c} H_1^{(1)}\left(k|\mathbf{r}_j - \mathbf{r}|\right) \frac{(\mathbf{r}_j - \mathbf{r}) \cdot \mathbf{n}_j}{|\mathbf{r}_n - \mathbf{r}|} q_j, \tag{3.9}$$

where $\mathbf{C} = (C_1, \cdots, C_{n_p})$ is the pressure response vector, $\mathbf{M} = (M_1, \cdots, M_{n_p})$ is the particle velocity response vector and $\mathbf{q} = (q_1, \cdots, q_{n_p})^t$ the point source strength vector with $q_j = q(\mathbf{r}_j)$. A pressure response matrix $[\mathbf{C}]$ is defined to expand this principle to compute the Equations 3.8 and 3.9 at the collocation points located at $\mathbf{r_c}$. The element C_{mn} on the m-th column and the n-th row of $[\mathbf{C}]$ is computed by using the free space Green's function and given by:

$$C_{mn} = G(\mathbf{r}_m, \mathbf{r}_n) \tag{3.10}$$

where $\mathbf{r}_m$ is the position of the m-th collocation point on the surface Γ and $\mathbf{r}_n$ is the position of the n-th equivalent point source. Whereas, the matrix which relates the normal particle velocity to the strength of the equivalent sources is given by $[\mathbf{M}]$ which may also be calculated by using the free space Green's function:

$$M_{mn} = \frac{i}{\rho c} \frac{\partial G(\mathbf{r}_m, \mathbf{r}_n)}{\partial n_m} \tag{3.11}$$

where $\mathbf{n}_m$ is the direction normal to the interface Γ at the m-th collocation point. If the point sources are set in either equivalent domains the response vectors carries the propagation properties of the respective domain.

In order to match the boundary conditions, the pressure at the co-located points $\mathbf{r}_c$ on either side of the boundary Γ, is given by the $\mathbf{p}_-$ and $\mathbf{p}_+$ as

$$\begin{aligned} \mathbf{p}_- &= \mathbf{p}^o + [\mathbf{C}_i]\,\mathbf{q}_i \\ \mathbf{p}_+ &= [\mathbf{C}_e]\,\mathbf{q}_e \end{aligned} \tag{3.12}$$

where $\mathbf{p}^o = (p_1^o, \cdots, p_{n_p}^o)^t$ is given by the incident wave on the interface and the subscripts e and i refers to the equivalent exterior and interior parameters, respectively. The normal particle velocity $\boldsymbol{v}$ on the boundary may be similarly defined by

$$\begin{aligned} \boldsymbol{v}_- &= \boldsymbol{v}^o + [\mathbf{M}_i]\,\mathbf{q}_i \\ \boldsymbol{v}_+ &= [\mathbf{M}_e]\,\mathbf{q}_e \end{aligned} \tag{3.13}$$

where $\boldsymbol{v}^o = (v_1^o, \cdots, v_{n_p}^o)^t$ is given by the incident wave on the interface. The Equations 3.12 and 3.13 represent a fundamental solution which satisfies both the inhomogeneous Helmholtz equation in the inside and the homogeneous Helmholtz equation and the Sommerfeld radiation condition at infinity in the outside. It is noteworthy, the Hankel function is undefined at the origin therefore if evaluated at the position of line sources therefore equations 3.12 and 3.13 yield defined pressure and normal velocity field elsewhere. The acoustic field on both media and hence the unknown sources $\mathbf{q}_e$ and $\mathbf{q}_i$ are determined by imposing the homogeneous boundary conditions of continuity of pressure and normal particle velocity across the surface Γ at the collocation points, as in Equation 2.11.

The boundary conditions for an internal incident wave may be rewritten in the form

$$\begin{aligned} [\mathbf{M}_e]\,\mathbf{q}_e - [\mathbf{M}_i]\,\mathbf{q}_i &= \boldsymbol{v}^o \\ [\mathbf{C}_e]\,\mathbf{q}_e - [\mathbf{C}_i]\,\mathbf{q}_i &= \mathbf{p}^o \end{aligned} \tag{3.14}$$

and assembled into the following matrix form

$$[\mathbf{A}]\,\mathbf{q} = \mathbf{b}^o, \tag{3.15}$$

where $[\mathbf{A}]$ is defined as

$$[\mathbf{A}] = \begin{bmatrix} \mathbf{M}_e & -\mathbf{M}_i \\ \mathbf{C}_e & -\mathbf{C}_i \end{bmatrix} \tag{3.16}$$

and $\mathbf{q} = [\mathbf{q_e}; \mathbf{q_i}]^t$ and $\mathbf{b}^o = [\boldsymbol{v}^o; \mathbf{p^o}]^t$. For the analysis protocol, the incident boundary data $\mathbf{b}_o$ is that of the generating wave defined by monopole sources as in the Equation C.7. For the synthesis protocol, the incident boundary data $\mathbf{b}^o = [-\boldsymbol{v}^o; -\mathbf{p^o}]^t$ is obtained from a generating wave defined by Bessel beam as in the Equation C.8.

The Equation 3.15 forms the basic system of equation to solve for the unknown strengths given an arbitrary incident wave using the ESWS. Now the behaviour and propagation matrix are defined in order to express the solution for both the analysis study using internally reflected wave and synthesis study using externally generated wave.

3.1.3 Boundary behaviour $[\mathbf{B}]$ and propagation $[\mathbf{P}]$ matrices

Given an incident boundary data $\mathbf{b}^o$, a behaviour matrix $[\mathbf{B}]$ is defined such that

$$\mathbf{b} = [\mathbf{B}]\,\mathbf{b}_o, \tag{3.17}$$

where $\mathbf{b}$ is any affected boundary data on either side of the interface Γ. A behaviour matrix is a transfer function that accounts for the incident wave being affected by the boundary behaviour caused by the interface Γ. Conversely, given an affected boundary data $\mathbf{b}$, a propagation matrix $[\mathbf{P}]$ is defined such that

$$\mathbf{p} = [\mathbf{P}]\,\mathbf{b}, \tag{3.18}$$

where $\mathbf{p}$ is any propagated pressure field on either domain Ω. The propagation matrix is a transfer function from a boundary data defined on the domain where the pressure field is computed without being affected by any boundary behaviour.

The system of equations in 3.15 solves for the unknown source strengths $\mathbf{q}$ of equivalent sources so the pressure field is well defined on either equivalent domains. A further step is taken to compute any boundary data on the interface (either $\mathbf{b}_i$ or $\mathbf{b}_e$) and directly relate it with the incident boundary data $\mathbf{b}^o$. The behaviour matrix is developed to implement both analysis and synthesis protocols using the ESWS model. The propagation matrix is a more general transfer function being developed to compute any pressure field within a domain enclosed by a surface.

Boundary behaviour matrix

The computation of the following matrices is straight forward because the boundary data is defined at the exact location of the collocation points. We define $[\mathbf{O}]$ as an inverse matrix taken from the Equation 3.15 which gives the solution for the source strengths $\mathbf{q}$ in terms of the incident wave $\mathbf{b}_o$ as follows

$$[\mathbf{O}] = \begin{bmatrix} \mathbf{O}_{ep} & \mathbf{O}_{ev} \\ \mathbf{O}_{ip} & \mathbf{O}_{iv} \end{bmatrix} = [\mathbf{A}]^{-1}, \tag{3.19}$$

where the superscript p and v refers to the data type each sub-matrix is related to. Then both the interior behaviour matrix $[\mathbf{B}_i]$ such that the internal boundary data obtained from $\mathbf{b}_i = [\mathbf{B}_i]\mathbf{b}_o$ may be defined as

$$[\mathbf{B}_i] = \begin{bmatrix} \mathbf{M}_i \\ \mathbf{C}_i \end{bmatrix} \begin{bmatrix} \mathbf{O}_{ip} \\ \mathbf{O}_{iv} \end{bmatrix}^T \tag{3.20}$$

and the exterior behaviour matrix $[\mathbf{B}_e]$ such that $\mathbf{b}_e = [\mathbf{B}_e]\mathbf{b}_o$ as in

$$[\mathbf{B}_e] = \begin{bmatrix} \mathbf{M}_e \\ \mathbf{C}_e \end{bmatrix} \begin{bmatrix} \mathbf{O}_{ep} \\ \mathbf{O}_{ev} \end{bmatrix}^T. \tag{3.21}$$

It may be demonstrated from the general boundary conditions in Equation 2.11 that these two matrices are related to each other by the identity matrix and one can be expressed in terms of the other. Without further development this relation for any given incident wave field is provided below

$$[\mathbf{B_e}] = \mathbf{I} + [\mathbf{B_i}], \tag{3.22}$$

where $\mathbf{I}$ is the identity matrix. The equations 3.20 and 3.21 give the behaviour matrices for both incident wave cases regardless of the domain it is defined on. Considering the interaction with the interface Γ, the matrices $[\mathbf{B_i}]$ and $[\mathbf{B_e}]$ either accounts for internally scattered and externally transmitted wave,respectively, if the incident wave is defined in domain Ω_i or for externally scattered and internally transmitted, if defined in domain Ω_e.

Propagation matrix

The propagation matrix $[\mathbf{P}]$ is a transfer function that computes the pressure field that propagates into the domain where the boundary data is defined. This formulation of the propagation matrices is based on the discrete integral (see Section 2.3.1) which causes pressure singularities to occur close to the collocation points. The propagation matrices are implemented not only with response matrices due to a monopole but also to a dipole source. The pressure response matrix $\left[\mathbf{C}^d\right]$ and a normal particle velocity response matrix $\left[\mathbf{M}^d\right]$ to a dipole source is defined similarly to the

response matrices due to monopole source. The element C^d_{mn} on the m-th column and the n-th row of $\left[\mathbf{C}^d\right]$ is computed using the Green's function gradients with respect to the source position in the equation 2.16 and given by:

$$C^d_{mn} = \frac{\partial G(\mathbf{r}_m, \mathbf{r}_n)}{\partial \mathbf{n}_n}. \tag{3.23}$$

The matrix which relates the normal particle velocity to the strength of the equivalent sources is denoted by $\left[\mathbf{M}^d\right]$ calculated using the double-gradient of the Green's function in the Equation 2.16 and given by:

$$M^d_{mn} = \frac{i}{\rho c} \frac{\partial^2 G(\mathbf{r}_m, \mathbf{r}_n)}{\partial n_{r_n} \partial n_{r_m}}. \tag{3.24}$$

From these two dipole response matrices $\left[\mathbf{M}^d\right]$ and $\left[\mathbf{C}^d\right]$ the propagation matrix $[\mathbf{P}]$ is computed using the discrete formulation of KHI in Equation 2.26 defined as in

$$[\mathbf{P}] = \left[\mathbf{C}^d\mathbf{L} \quad \mathbf{CL}\right], \tag{3.25}$$

where $\mathbf{L}$ is a diagonal matrix containing the lengths $\left|L_j\right|$ of each curvilinear segment the collocation point $\mathbf{r}_l$ is placed on.

The scattered field p^s examined for the analysis protocol and the transmitted field p^t for the synthesis protocol are computed using a composed internal behaviour and propagation matrix. In general the internal pressure field p_i is given by

$$p_i = [\mathbf{P}]\,[\mathbf{B}_i]\,\mathbf{b}_o. \tag{3.26}$$

On the other hand, synthesis of pressure field is determined by the application of the inverse filtering technique into a perturbed behaviour matrix and then reapplied using the unperturbed behaviour matrix as in Equation 3.26.

3.1.4 Pressure field reproduction using analytical sources

To investigate the synthesis of pressure field, an arbitrary incident pressure p^o and velocity v^o field on the external side of the boundary is solved for given a target pressure p^u and velocity v^u field on the internal side of the boundary using the inverse filter technique (see Section 2.4). The formulation of the inverse filter is achieved by defining a transfer function between the boundary data on any source surface outside the interface Γ and the boundary data on any control surface inside the interface.

The behaviour matrix $[\mathbf{B}]$ is proposed as the transfer function between control and source data to implement the inverse filter. In the least squares sense the reproduced field is the best

field capable of being produced by the arbitrary incident wave field. The transfer function $[\mathbf{T}_{ES}]$ is defined as the solution for all harmonic responses in a matrix form

$$\mathbf{T}_{ES} = \begin{bmatrix} \mathbf{T}_{pp} & \mathbf{T}_{pv} \\ \mathbf{T}_{vp} & \mathbf{T}_{vv} \end{bmatrix} = \mathbf{B}_i, \tag{3.27}$$

where the first and second superscripts refer to the data type in the source and control data, respectively. For instance, $\mathbf{T}_{pv}$ denotes the transfer function between pressure as source data and normal particle velocity as control data. In this case, the reproduction problem is formulated from the direct transmission solved numerically using Equation 3.20. The transfer function is assembled into a matrix equation given by

$$\mathbf{T}_{ES}\mathbf{b}^o = \mathbf{b}^u, \tag{3.28}$$

where $\mathbf{b}^o$ is the incident boundary data and $\mathbf{b}^u$ is given by the desired boundary data on the interface as in Equation C.8. This ES-based transfer function is then inverted numerically to determine the incident wave that best synthesize a desired pressure field pattern.

The inversion defined by Equation 2.32 gives the solution for the $\mathbf{b}^o$ in terms of the $\mathbf{b}^u$ which is computed using Singular Value Decomposition (SVD) based MATLAB codes. The solution for $\mathbf{b}^o$ is then given by

$$\mathbf{b}^o = \mathbf{T}^+_{ES}\mathbf{b}^u, \tag{3.29}$$

where $\mathbf{T}^+_{ES}$ is the inverse filter transfer function based on the ESWS model. For a given incident boundary data the transmitted wave may be computed using the Equation 3.26. If the inverse filter transfer function is computed for a perturbed system using $Z'_r = (1-\gamma)Z_r$ then the transmitted pressure field p^t after reproduction is given by

$$p^t = [\mathbf{P}]\,\mathbf{T}_{ES}(Z_r)\mathbf{T}^+_{ES}(Z'_r)\mathbf{b}_i. \tag{3.30}$$

3.2 Numerical method for solving simplified model

This section is dedicated to solving the system of equation in 3.15 for the unknown strengths given a known incident boundary data achieved with a numerical method based on a direct solution using block inverse matrix.

3.2.1 Block inversion method

This section presents a direct method developed for solving the ESWS model. Considering the block matrix $[\mathbf{A}]$ in equation 3.16 then the inverse matrix $[\mathbf{O}]$ may be determined by a

Frobenius-Schur inversion as in

$$[\mathbf{O}] = [\mathbf{A}]^{-1} = \begin{bmatrix} \mathbf{M}_e & -\mathbf{M}_i \\ \mathbf{C}_e & -\mathbf{C}_i \end{bmatrix}^{-1},$$

then

$$[\mathbf{O}] = \begin{bmatrix} \left(\mathbf{M}_e - \mathbf{M}_i\mathbf{C}_i^{-1}\mathbf{C}_e\right)^{-1} & \left(\mathbf{C}_e - \mathbf{C}_i\mathbf{M}_i^{-1}\mathbf{M}_e\right)^{-1} \\ \left(\mathbf{M}_i - \mathbf{M}_e\mathbf{C}_e^{-1}\mathbf{C}_i\right)^{-1} & \left(\mathbf{C}_i - \mathbf{C}_e\mathbf{M}_e^{-1}\mathbf{M}_i\right)^{-1} \end{bmatrix}. \tag{3.31}$$

The solution to the Equation 3.15 may be directly obtained from the boundary conditions expressed in terms of the behaviour matrices in Equation 3.16. The internal behaviour matrix $[\mathbf{B_i}]$ is given by

$$\begin{aligned}[\mathbf{B_i}] &= \begin{bmatrix} \mathbf{M}_i\left(\mathbf{M}_i - \mathbf{M}_e\mathbf{C}_e^{-1}\mathbf{C}_i\right)^{-1} & \mathbf{M}_i\left(\mathbf{C}_i - \mathbf{C}_e\mathbf{M}_e^{-1}\mathbf{M}_i\right)^{-1} \\ \mathbf{C}_i\left(\mathbf{M}_i - \mathbf{M}_e\mathbf{C}_e^{-1}\mathbf{C}_i\right)^{-1} & \mathbf{C}_i\left(\mathbf{C}_i - \mathbf{C}_e\mathbf{M}_e^{-1}\mathbf{M}_i\right)^{-1} \end{bmatrix} \\ &= \begin{bmatrix} \left(\mathbf{I} - \mathbf{Z}_e^{-1}\mathbf{Z}_i\right)^{-1} & \left(\mathbf{Z}_i - \mathbf{Z}_e\right)^{-1} \\ \left(\mathbf{Z}_i^{-1} - \mathbf{Z}_e^{-1}\right)^{-1} & \left(\mathbf{I} - \mathbf{Z}_e\mathbf{Z}_i^{-1}\right)^{-1} \end{bmatrix},\end{aligned} \tag{3.32}$$

where $[\mathbf{Z}] = \left[\mathbf{C}\mathbf{M}^{-1}\right]$ for either external or internal subscripts. Similarly, the external behaviour matrix $[\mathbf{B_e}]$ is given by

$$[\mathbf{B_e}] = \begin{bmatrix} \left(\mathbf{I} - \mathbf{Z}_i^{-1}\mathbf{Z}_e\right)^{-1} & \left(\mathbf{Z}_e - \mathbf{Z}_i\right)^{-1} \\ \left(\mathbf{Z}_e^{-1} - \mathbf{Z}_i^{-1}\right)^{-1} & \left(\mathbf{I} - \mathbf{Z}_i\mathbf{Z}_e^{-1}\right)^{-1} \end{bmatrix}.$$

The block inversion method is chosen as the only method applied in the simulations presented hereafter as it does not depend on a convergent solution.

3.3 Simplified solution field

This section presents numerical simulations which demonstrate the solution field obtained using the simplified model. The pressure field results are presented in the acoustic chamber, i.e. in the internal domain Ω_i and obtained using both the analysis and synthesis protocols. In the analysis protocol, the internally scattered pressure field p^s is obtained due to an internal incident line source defined by

$$p^o = -p_0\frac{i}{4}H_0^{(1)}(k|\mathbf{r}_o - \mathbf{r}|). \tag{3.33}$$

where $\mathbf{r}_o$ is the line source position and $\mathbf{r}$ is the field position. A simplified approach to this protocol approximates the boundary behaviour of a piezoelectric device by testing the response of a fluid-fluid interface with a theoretical source. In the synthesis protocol, the internally

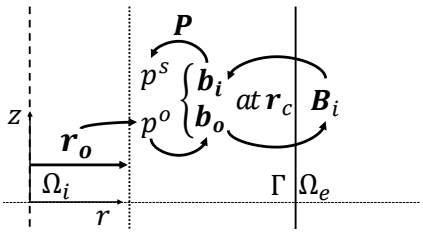

FIGURE 3.5. Schematic system with domains cross-section for ESWS model validation with exact solution in the analysis protocol. The line source at $\mathbf{r}_o$ inside internal domain Ω_i radiates incident p^o which scatters back from the interface Γ producing the scattered p^s.

transmitted wave due to an external incident source obtained from target acoustic vortex defined by

$$p^u = p_0 \frac{i}{4} J_1\left(k|\mathbf{r}_o - \mathbf{r}|\right) e^{i\phi}. \tag{3.34}$$

where ϕ is the angle between $\mathbf{r}_o$ and $\mathbf{r}$. The simplified approach to the synthesis protocol estimates the resulting applied acoustic vortex considering the desired pressure field is reproduced by setting secondary sources on a perturbed fluid-fluid boundary behaviour. Figure 3.6 shows a flow diagram with the sequence of calculation for both the analysis and synthesis protocols for the ESWS model.

For this solution the internal fluid is set with acoustic properties equal to that of liquid water at room temperature, i.e. $\rho_f = 997\ \mathrm{kg\,m^{-3}}$ and $c_f = 1482\ \mathrm{m\,s^{-1}}$ [John D. Cutnell and Johnson, 2014], and the external fluid is characterized by a fictitious material with acoustic properties relative to that of water, density ratio $\rho_r = 7.5$ and speed ratio $c_r = Z_r/\rho_r$ with Z_r the impedance ratio. The size of the interfaces Γ in terms of wavelength was set to $R = 2\lambda$, or $kR = 4\pi$.

3.3.1 Validation with analytical solution for circular shapes

This section is dedicated to validate the solution for the scattered pressure field p^s obtained with ESWS model for the analysis protocol. A cross-section of the system solved in this section is depicted in Figure 3.5. This is achieved by comparing solution using Equation 3.26 with one using a truncated solution from the analytical model obtained from Equation C.2 given by

$$p^s(\mathbf{r}, \mathbf{r}_o) = p_0 \frac{i}{4} \sum_{n=-n_t}^{n_t} a_n J_n\left(k|\mathbf{r}|\right) J_n\left(k\left|\mathbf{r}_o\right|\right) e^{in\phi}, \tag{3.35}$$

where n_t is the number of truncation terms, $\mathbf{r}_o$ is the distance to the source from the centre of the domain and a_n are the coefficients solved for the boundary conditions. The validation results are studied using a two-step process. The first step is to analyse the effect of the area within the interface in which validation is performed on the approximation error $\varepsilon(r_o)$ (see Appendix B

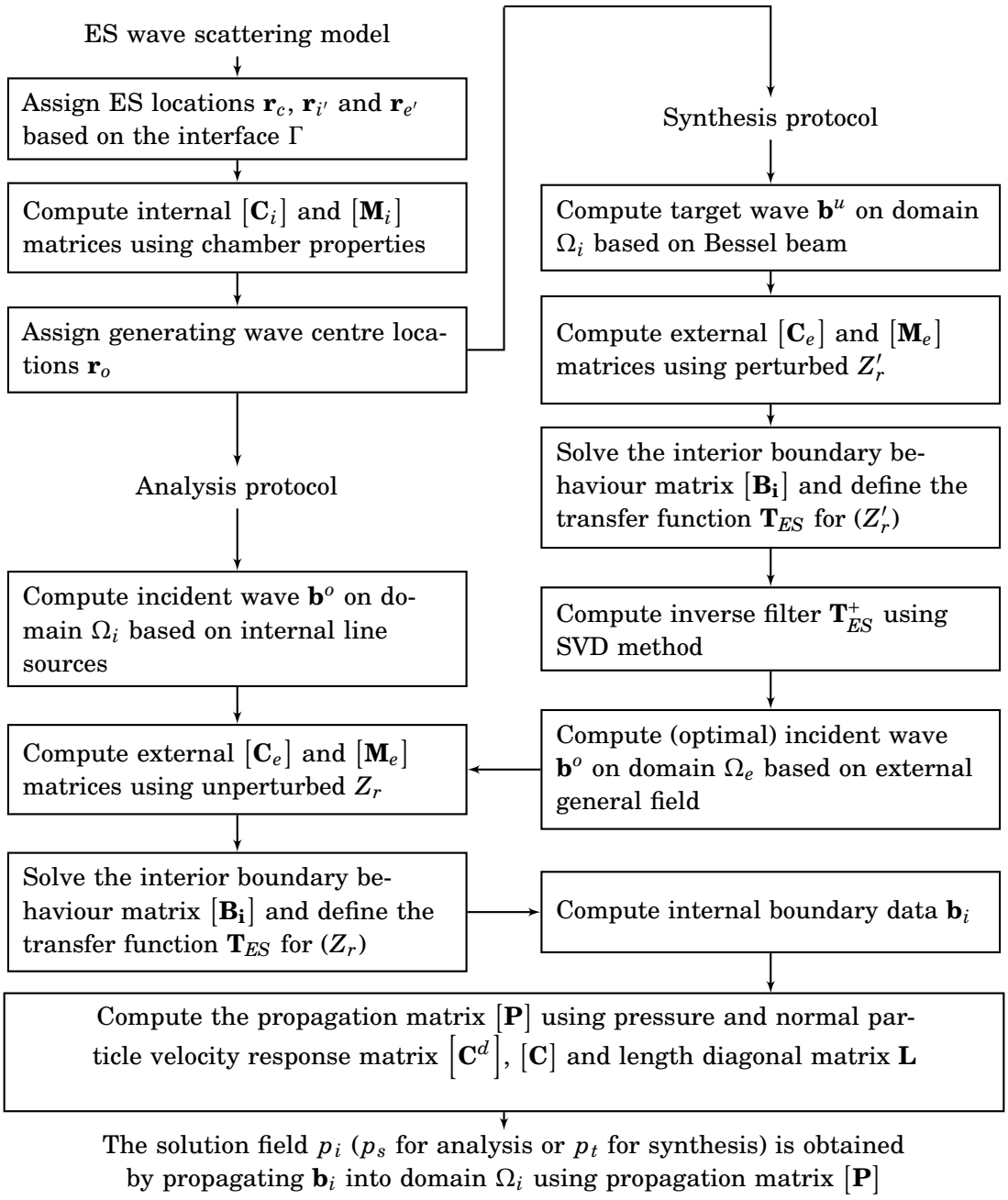

Figure 3.6: The ESWS model flow diagram showing the logic sequence of calculations. The process stages on both the analysis and the synthesis protocols are computed using a common mathematical model of transfer functions $\mathbf{T}_{ES}$ calculated from the matrices obtained based on the equivalent sources.

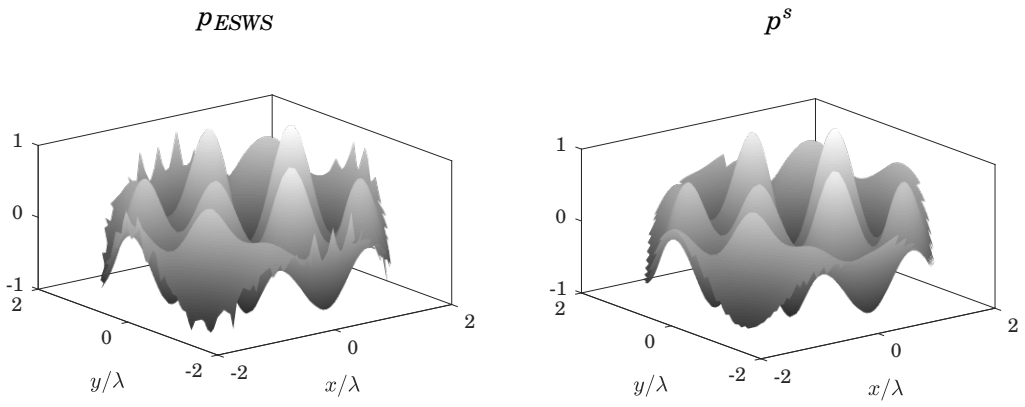

FIGURE 3.7. Example of simulated ESWS-based compared with analytical analysis field. Results for $kR = 4\pi$, $Z_r = 15$, boundary shape defined by a circular curve $\Gamma = r^0$ and distance to source from the centre of domain $r_o = \lambda$. Pressure field is normalized inside validation region for a distance $\xi_a = 4\pi^2/3k$ away from Γ, shown truncated between -1 and 1 and for $\langle |L| \rangle = \lambda/3$.

for more details), then investigate how the validation area affects the convergence study. Furthermore, the analytical solution is a summation of an infinite series which approximates the solution and may present errors as such if truncated at insufficient number of modes. For this reason, convergence is also examined against inaccurate analytical solution.

Firstly, a side by side comparison of the scattered field obtained from the ESWS model for the analysis protocol, or ESWS-based analysis field p_{ESWS}, is compared with the exact solution, or analytical analysis field p_s, for an off-centred line source $\mathbf{r}_o$ inside a circular boundary $\Gamma = r^0$, as shown in Figure 3.7. The graphs show both pressure field over a validation region for an area determined by an internal boundary Γ' at a distance $\xi_a = 4\pi^2/3k$ away from the interface Γ in the normal direction obtained from Equation A.7. Results are normalized and shown truncated between -1 and 1. An approximation error is defined as

$$\varepsilon = \frac{p_{ESWS} - p_s}{max\left(p_s\right)}. \tag{3.36}$$

The first step, the number of collocation points is fixed to $n_p = 54$ hence the resulting segmented contiguous curve has an average arc length $\langle |L| \rangle \approx \lambda/3$ (see Appendix A for details). The greater n_p is the more accurate the solution which generally contributes to convergence. As shown in Figure 3.8, each circular graph contains the real value [1] of pressure for incident p_o, scattered p^s and total $p^T = p_o + p^s$ field followed by the approximation error ε and is presented in rows for a varying off-centred distance r_o for the point source indicated by a white cross. Graphs

[1] The real value of pressure field only partially represents the solution and phase is taken into account for further calculations.

in the last column show increasing errors towards the interface is an overall behaviour for all off-centre distances. The ESWS model achieves better accuracy away from the collocation points mainly due to the propagator matrix formulation of the reflected field caused by singularities, as shown in Figure 3.7.

There is a strong correlation between incident and total field for a centred point source (a) and the $\varepsilon(r_o)$ is low throughout the chamber. At $r_o = 0.5\lambda$ (b) these fields are more dissimilar compared to (a) suggesting lower correlation with higher errors. It can be seen at $r_o = \lambda$ (c) and 1.5λ (d) the reflected and total pressure field are similar, but with opposite sign which indicates that a single mode dominates the response in this region. The results at $r_o = 1.5\lambda$ (d) shows the response to point source approaching the physical boundary which produces the less accurate results.

The second step of validation is based on Figure 3.9 and determines the number of collocation points n_p and the validation area that produces reasonably accurate results. This step is demonstrated by a series of convergence plots for the error $\log \varepsilon_{rms}(r_o)$ with linearly varying average arc length from $\langle |L| \rangle \approx \lambda$ to $\lambda/4$, for three values of ξ_a for the radius of the validation area. Moreover, two analytical solution approximations according to the number of truncated terms n_t (see Section 2.2.2 for details).

The results confirm not only the accuracy of the solution generally decreases with increasing radius of validation area as discussed previously but also presents lower convergence rates. However, if the validation area considered stretches to the entire domain ($r = 2\lambda$) convergence is fast but errors are high $\log \varepsilon_{rms}(r_o) > -1$ for any off-centre distance. In terms of the analytical solution the errors for low $n_t = kR - 4$ reaches a spatial dependent threshold and for $n_t = kR + 10$ converges equally from the centre until $r_o = 1.5$. In conclusion, this study shows the approximation error is $\log \varepsilon_{rms}(r_o) < -3$ for an average arc length $\langle |L| \rangle \approx \lambda/3$ and solution is accurate enough for the field analysed at a distance of $\lambda/2$ away from the interface Γ.

3.3.2 Solution for hexagonal shapes

The solutions for the analysis and synthesis protocols are demonstrated for hexagonal shapes. In order to assess the effect of the chamber corner ς on the solution field, two distinct hexagonal shapes r_6^{ς} are studied, namely a smooth r_6^{65} and sharp r_6^{145} (see Appendix A for boundary shape details). Results are presented in pairs of response and total pressure field for analysis and desired and transmitted pressure field for synthesis, as shown in Figure 3.10 and 3.12, in a similar format to the ones presented in the validation section.

Analysis of pressure field

The analysis of pressure field based on the simplified model for non-dimensional wavenumber $kR = 4\pi$ and impedance ratio $Z_r = 15$, as shown in Figure 3.10, is discussed here. The effect of the boundary behaviour is less expressive for the centred point source (a) where incident p_o and total

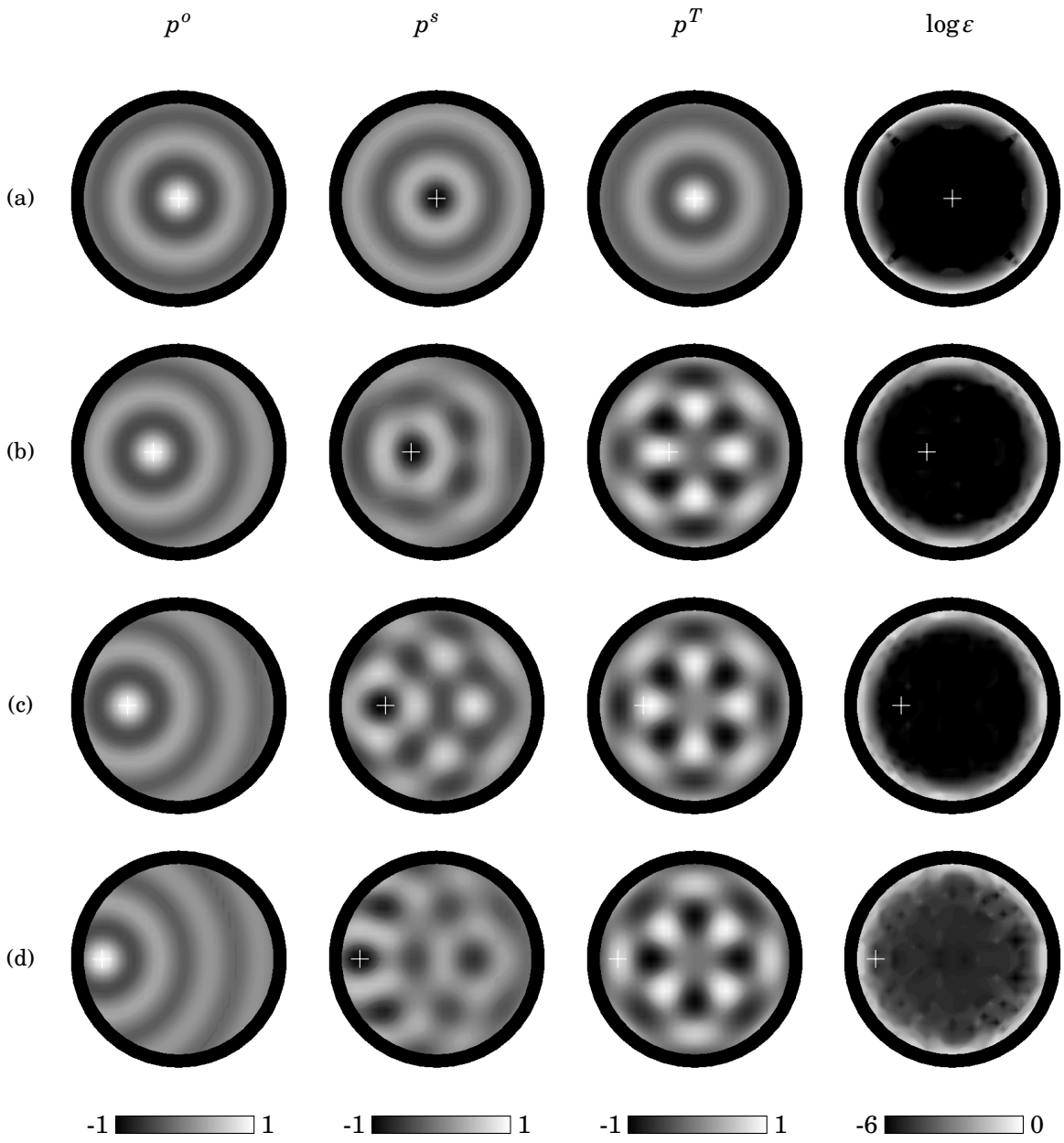

FIGURE 3.8. Simulated ESWS-based analysis field for the circular shape with off-centred point source compared with analytical model. Real value of incident field p^o, scattered field p^s, total field p_T and approximating error ε in log scale from Equation 3.36 for $r_o = 0$ (a), 0.5 (b), 1 (c),1.5 (d). Results shown for $kR = 4\pi$ and $Z_r = 22.5$.

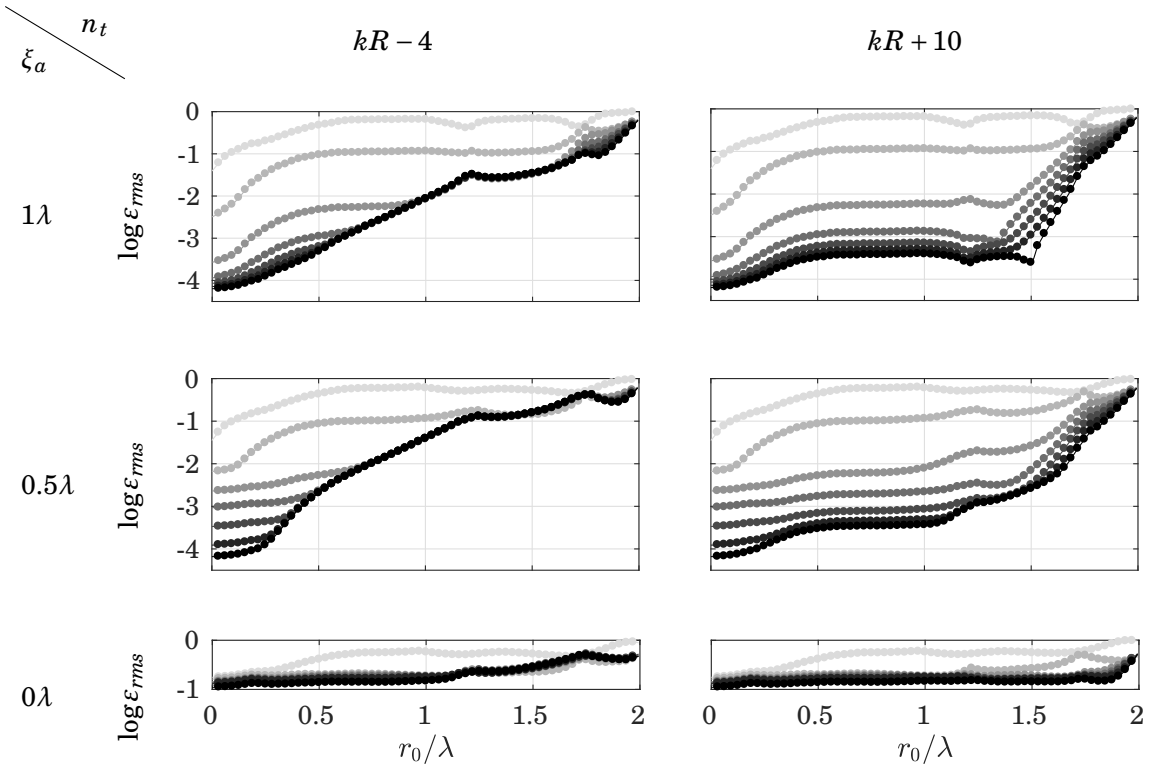

FIGURE 3.9. Simulated ESWS-based approximation error $\log \varepsilon_{rms}(r_o)$ in terms of source off-centred distance for the analysis field. Dotted lines(•••) show results for average arc length $\langle |L| \rangle$ decreasing from λ to $\lambda/4$ in shades from bright to dark. Results for circular shape (r^0) are in log scale and computed for $kR = 4\pi$ and impedance ratio $Z_r = 22.5$.

p^T field are highly correlated as for the circular shape. Even though response field for hexagonal shapes are dissimilar the total field is not much affected due to its low magnitude. For a distance $r_o = \lambda/2$ (b), despite the response seems to equally disturb the total field p^T for both shapes, their affect on the correlation is apparently higher compared to the centred. The comparison between shapes for the last two rows differs from the first two. In the smooth case although the scattered field p^s is strongly influenced by a resonant mode with high amplitude close to the boundary as in the circular case and its contribution to the total field is minimal at $r_o = \lambda$ (c) and more visible at $r_o = 1.5\lambda$ (d), suggesting lower correlation at the latter. In the sharp case at $r_o = \lambda$ (c) both the total p^T and the scattered p^s field differs in shape compared to (d), which is more similar to (b), and their linear relation to p^o are comparable.

To summarise, by investigating the shape of the total field it is evident despite comparable interfaces the sharpness of their corners changes the overall response to a internal line source hence the analysis of pressure field. Thus, there is an indication the linear relationship between the incident and total pressure field is lower due to high discrepancies in the overall shape of the scattered pressure field for the smooth hexagonal shape. Next section presents in more details

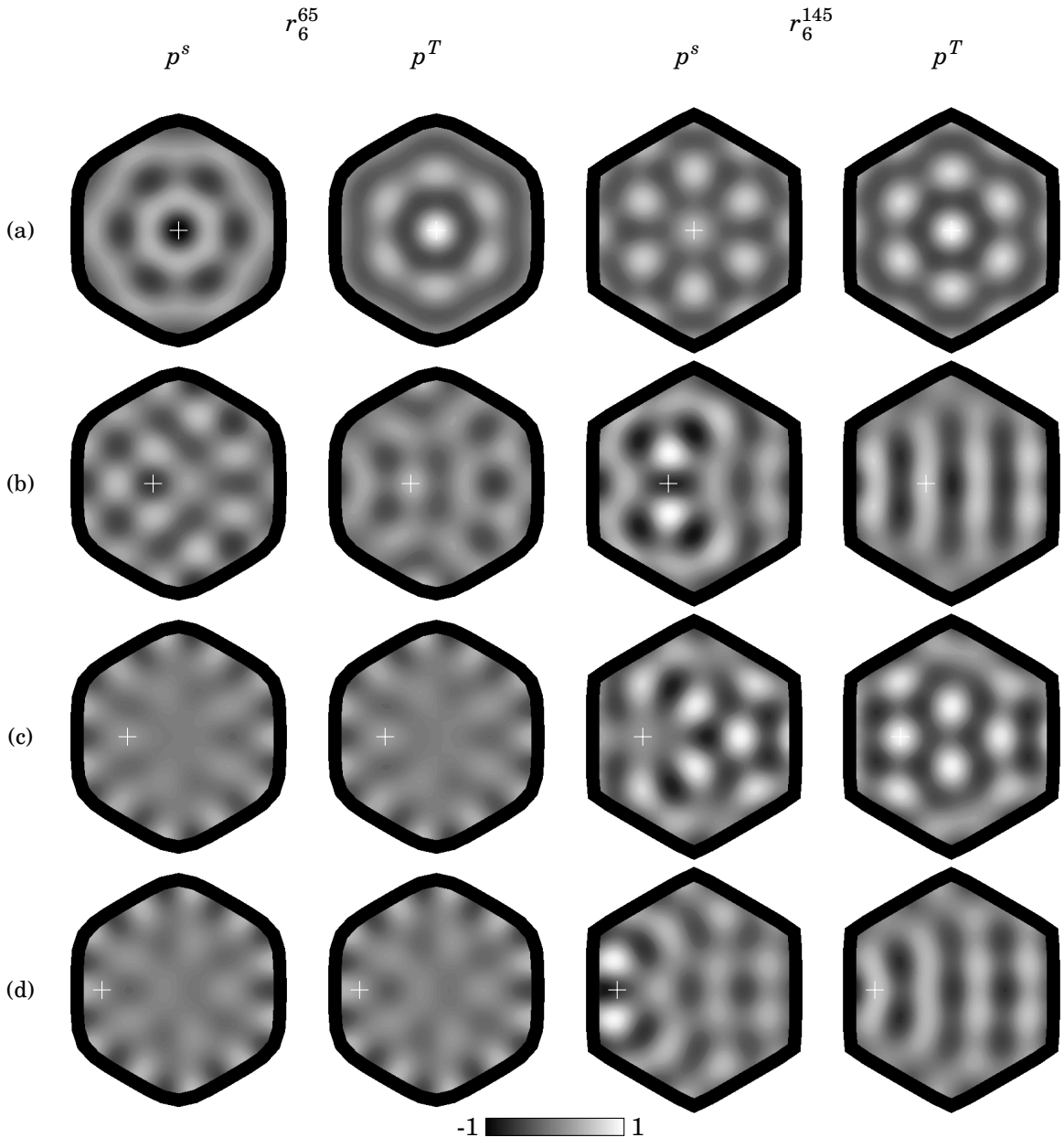

FIGURE 3.10. Simulated ESWS-based analysis field for the hexagonal shapes with off-centred point source. Real value of response field p^s and total field p_T for smooth r_6^{65} and sharp r_6^{145} hexagonal shapes and for $r_o = 0$ (a), 0.5 (b), 1 (c),1.5 (d). Results shown for non-dimensional wavenumber $kR = 4\pi$ and impedance ratio $Z_r = 15$.

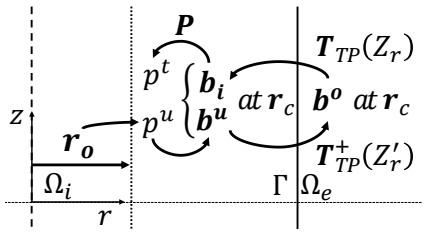

FIGURE 3.11. Schematic system with domain cross-section for ESWS model investigation of the transmitted pressure field in the synthesis protocol. The target p^u centred at $\mathbf{r}_o$ inside internal domain Ω_i is reproduced by external incident p^o through the interface Γ.

these results and introduces a study for synthesis of pressure field.

Synthesis of pressure field

The synthesis protocol based on the simplified model is discussed here. A target wave based on Bessel beams is reproduced by computing a corresponding optimal incident external field using an inverse transfer function for specified impedance ratio. According to Figure 3.6, a sequence of computing steps follows as in the analysis protocol to obtain the solution field in the internal domain by multiplying the incident boundary data by the behaviour and propagation matrices. Throughout this investigation a relative difference of 20% between the applied Z_r and specified Z'_r impedance ratio is considered, that is a perturbation factor of $\gamma = 20\%$. A cross-section of the system solved in this section is depicted in Figure 3.11. Figure 3.12 shows desired field p^u, transmitted field p^t for the smooth hexagonal shape for off-centred point sources.

The reproduction error between p^u and p^t are shown in real value $p_a = p^u - p^t$ and in logarithmic scale $\varepsilon = (p_a)/max(p^u)$. The desired pressure field p^u that of a Bessel beam and is given by Equation 2.57. The results show good agreement between desired and transmitted pressure field for a centred point source (a) with a symmetric error distribution. Both results for intermediate distances (b)-(c) the errors present no apparent symmetry with the transmitted field $p^t(r_o = \lambda)$ slightly more interfered than the $p^t(r_o = \lambda/2)$. The synthesis of near boundary focused acoustic vortex at $r_o = 3\lambda/2$ (d) exhibits higher interference compared to the more central ones caused by a symmetric disturbance. The spatially averaged Root Mean Squared (RMS) reproduction error is found $\langle \log \varepsilon_{RMS} \rangle \approx -0.8$. These synthesis results present no evident relation with the analysis results shown in Figure 3.10.

To further investigate any association between the analysis and the synthesis loading scenario a performance study is proposed. This study is intended to summarise the solution field results and provide a global assessment of this boundary behaviour response. The next section covers simplified performance study based on which a discussion about robust pressure response is drawn.

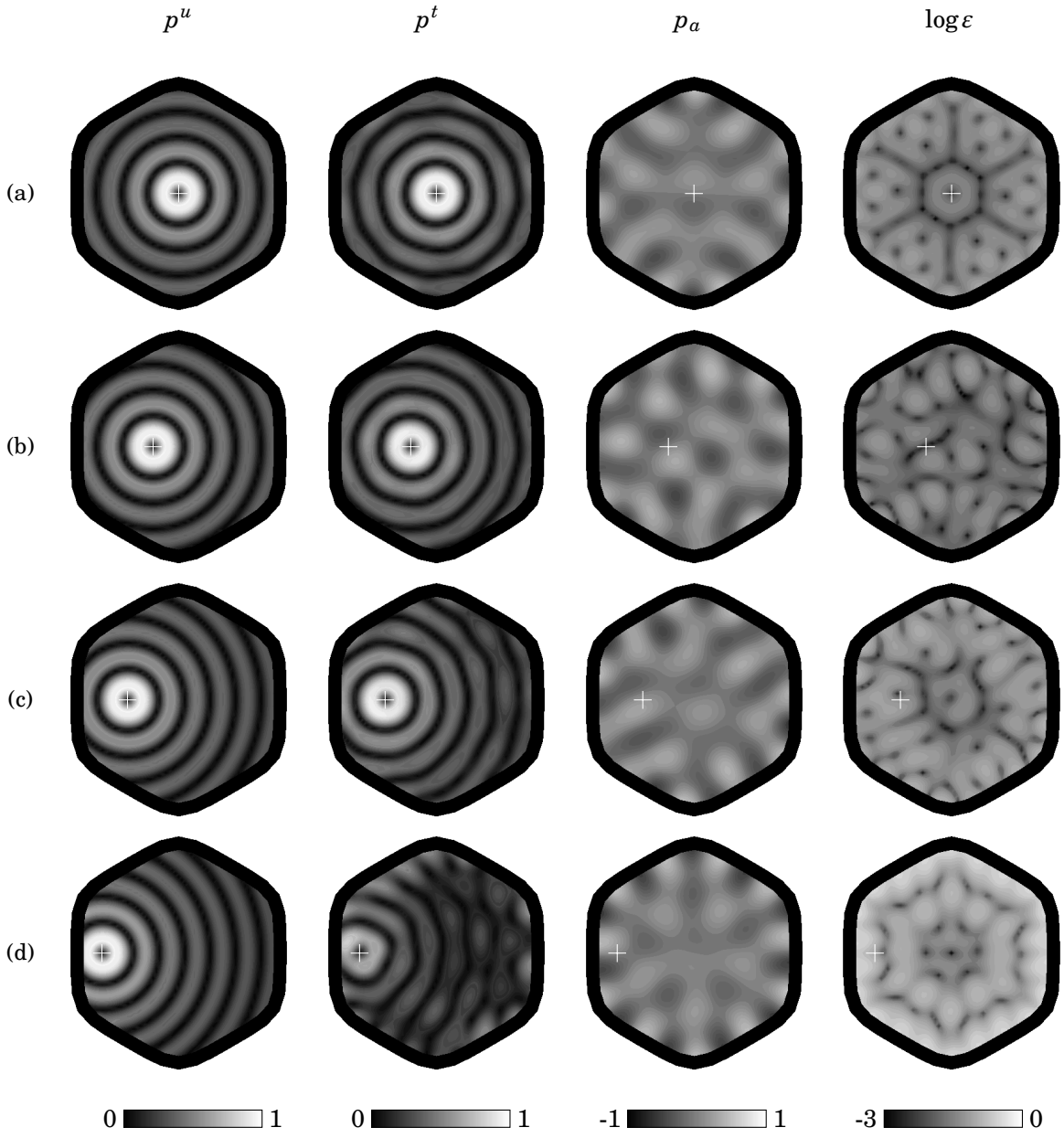

FIGURE 3.12. Simulated ESWS-based synthesis field for the hexagonal shapes with off-centred target wave for a perturbed system. Absolute value of desired field p^u, transmitted field p^t and reproduction error p_a (real value) and $\log\varepsilon$ for smooth r_6^{65} hexagonal shape and off-centre distance of $r_o = 0$ (a), 0.5 (b), 1 (c),1.5 (d). Results shown for non-dimensional wavenumber $kR = 4\pi$ and impedance ratio $Z_r = 15$ and perturbation factor $\gamma = 20\%$.

3.4 Simplified performance study

This section presents numerical experiments which determine spatial-dependent performance parameters for the analysis and synthesis protocols on a fluid-fluid interface based on the ESWS model. Performance of a fluid in an external fluid domain investigate characteristics of a simplified boundary system where pressure waves are the only form of field disturbance in the medium composing ultrasonic tweezers devices. The analysis performance measures how much a testing function based on internal monopoles remains undisturbed upon wave scattering. The synthesis performance measures how much a target function based on internal vortices remains accurate upon wave reproduction. The performance parameter is computed using a shape correlation parameter between either the incident p^o or the desired p^u pressure field as the input and either the total p^T or the transmitted p^t field as the output (see Appendix B for details on analysis and synthesis performance). This parameter study assumes higher values indicates better design.

The results presented here are shown in spatially mapped performance graphs with values in terms of the position of the generating wave centre. These graphs are symmetric due to the interface symmetry hence the performance parameters are mapped in a unique section of the domain and rotated accordingly.

3.4.1 Simplified analysis performance

The analysis performance $\psi_a(\mathbf{r}_o)$ is a correlation parameter that relates the incident pressure field due to a internal line source with the total pressure field which takes into account the internally scattered wave. This parameter quantifies the discrepancy in shape between a total field p^T and a given internal incident wave field p^o hence the efficiency of the device interface in withstanding an incident wave defined by a monopole line source. The mapped analysis performance $\psi_a(\mathbf{r})$ is presented for the circular ($\Gamma = r^0$) and hexagonal ($\Gamma = r_6^{65}, r_6^{145}$) boundary shapes and the effect of the impedance ratio Z_r is studied, as shown in Figure 3.13. The spatially averaged $\langle \psi_a \rangle$, shown in Figure 3.14, is then suggested as a parameter to measure the global disruption in total field caused by the reflected wave hence the efficiency of the interface in withstanding an arbitrary internal incident wave. The Simplified Analysis Performance (SAP) is evaluated at $r_o = (r_o^{(1)}, r_o^{(2)}, \ldots, r_o^{(M)})$ in equidistant rectangular grid over the internal domain and averaged as in

$$\langle \psi_a \rangle_f (T_d) = \frac{1}{M} \sum_{n=1}^{M} \frac{\left| p^T(T_d, r_o^{(n)})^\dagger p^o(r_o^{(n)}) \right|^2}{\left| p^T(T_d, r_o^{(n)}) \right|^2 \left| p^o(T_d, r_o^{(n)}) \right|^2}, \tag{3.37}$$

where $T_d = \left(kR, r_N^{\varsigma}, Z_r \right)$ is the transducer design parameters with $0 < \langle \psi_a \rangle < 1$. The parameter study presents several features of the mapped analysis performance $\psi_a(\mathbf{r}_o)$ for both circular and hexagonal shapes. The analysis performance preserves both the radial and reflection symmetry properties of the interface shape. The main results featured in all correlation maps is that the

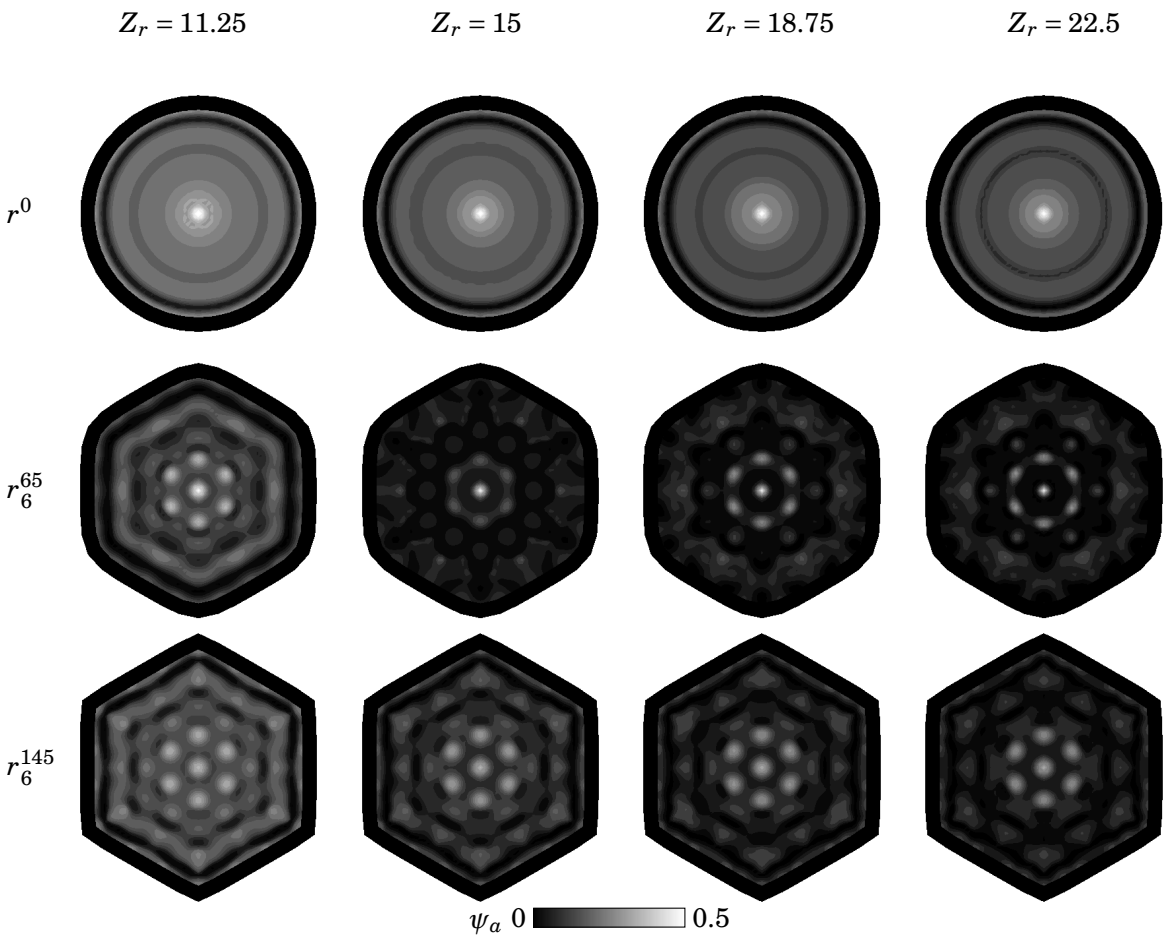

FIGURE 3.13. Simulated ESWS-based spatially mapped analysis performance $\psi_a(\mathbf{r})$ for the circular and hexagonal shapes. Parameter study for impedance ratio Z_r ranging from 11.25 to 22.5 with a fixed density ratio $\rho_r = 7.5$ and boundary shapes for r^0, r_6^{65} and r_6^{145}. Results shown for non-dimensional wavenumber $kR = 4\pi$.

analysis performance is always maximum at the central region, generally decreases with higher impedance ratio and mostly minimum at a distance $\approx 0.3\lambda$ off the boundary. It also shows the circular and sharp hexagonal shape are more robust to changes in the impedance ratio Z_r in terms of the analysis performance if compared to the smooth hexagonal shape over the range studied. This means that the response field p^s due to a varying incident field p^o in terms of the point source location is less affected by the material properties in those shapes. The difference between robustness of each shape is more evident for $Z_r = 15$ where dark regions (low $\psi_a(\mathbf{r})$) in the smooth hexagonal shape becomes lighter (high $\psi_a(\mathbf{r})$) for both $Z_r = 11.25$ and $Z_r = 18.25$. This correlation pattern is confirmed by the results for the solution for hexagonal shapes shown in Figure 3.10 where a resonant mode is strongly responsive to point source located close to the interface $r_o > \lambda$.

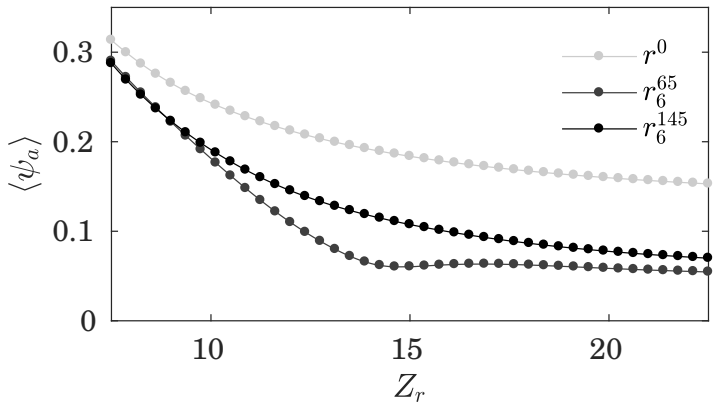

FIGURE 3.14. Simulated ESWS-based spatially averaged analysis performance $\langle \psi \rangle_a$ for the circular and hexagonal shapes in terms of acoustic impedance ratio.

Further investigation is done using the averaged analysis performance $\langle \psi_a \rangle$ as shown in Figure 3.14. For this example with mass density ratio $\rho_r = 7.5$, maximum SAP $\langle \psi_a \rangle = 0.31$ is found for speed of sound ratio $c_r = 1$ in circular shape. The analysis performance is shown a strictly decreasing function of the impedance ratio for circular and sharp hexagonal shapes. For a smooth hexagonal shape a resonant mode results in a minimum analysis performance close to $Z_r = 15$ which is restored for higher impedance ratio. However, the performances for both the hexagonal shapes are virtually identical for low impedance ratio indicating a possible asymptotic behaviour for hexagonal shapes. On the other hand, better analysis performance can be seen for high impedance ratio for the circular compared to hexagonal shape.

3.4.2 Simplified synthesis performance

The Simplified Synthesis Performance (SSP) ψ_s is a shape correlation parameter that relates the desired pressure field with the transmitted pressure field which takes into account a perturbation to the optimal incident boundary data $\mathbf{b}_o$. First, the mapped synthesis performance $\psi_s(\mathbf{r})$ is presented for smooth hexagonal shape ($\Gamma = r_6^{65}$) as shown in Figure 3.15 and the effect of the impedance ratio is studied. The spatially averaged $\langle \psi_s \rangle$ is then suggested as a parameter to measure the global disruption in reproduced field, as in

$$\langle \psi_s \rangle_f (T_d, \gamma) = \frac{1}{M} \sum_{n=1}^{M} \frac{\left| p^u(r_o^{(n)})^\dagger p^t(Z_r', r_o^{(n)}) \right|^2}{\left| p^u(r_o^{(n)}) \right|^2 \left| p^t(Z_r', r_o^{(n)}) \right|^2}. \tag{3.38}$$

This parameter quantifies the discrepancy in shape between a transmitted field p^t and a given target wave field p^u hence the efficiency of reproduction in the synthesis protocol for a specified interface with perturbed impedance ratio properties. Both results show the synthesis

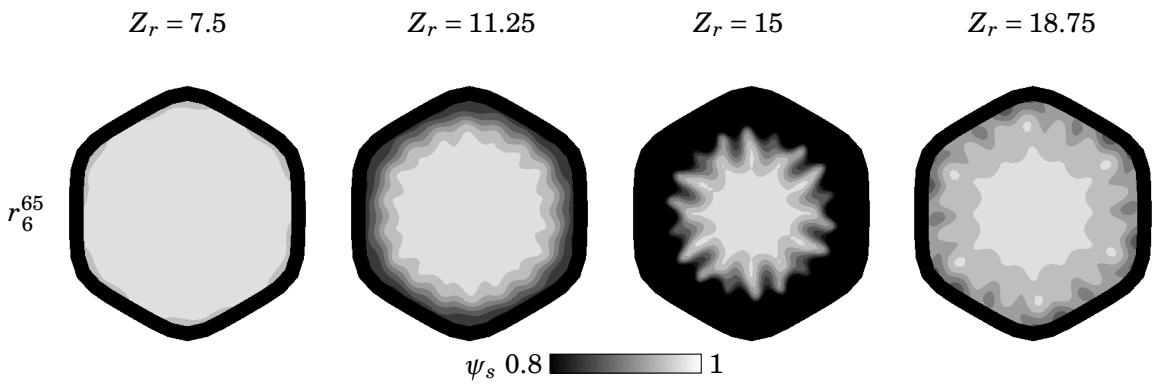

FIGURE 3.15. Simulated ESWS-based spatially mapped synthesis performance $\psi_s(\mathbf{r})$ for the smooth hexagonal shape. Parameter study for impedance ratio Z_r ranging from 7.5 to 18.75, ρ_r fixed to 7.5, interface shape r_6^{65} and specified impedance ratio perturbation $\gamma = 0.8$. Results shown for non-dimensional wavenumber $kR = 4\pi$. High synthesis performance $\psi_s(\mathbf{r}_o) \approx 1$ is considered to generate high-fidelity traps whereas $\psi_s(\mathbf{r}_o) < 0.8$ low-fidelity reproduction both of which the transmitted pressure field can be seen from Figure 3.12(a)-(d).

performance for a perturbation parameter $\gamma = 20\%$. This means the impedance ratio used in computing the inverse filter differs by a factor of -0.2 compared to the impedance ratio of the applied system.

It can be seen from Figure 3.15 that the synthesis, in contrast with analysis performance, preserves the radial symmetry but not the reflection symmetry. This may be explained by the fact Bessel beam as desired wave field carries orbital angular momentum hence the gradient of the mapped synthesis performance is not symmetric in opposite angular directions. By investigating the effect of the impedance in quantifying this parameter it is evident the map at $Z_r = 15$ exhibits a local minimum, particularly around the edges of the smooth hexagon. This is clearly a direct result of the local resonance examined in the analysis performance. The results for lower Z_r reveals a maximised synthesis performance over the domain whereas the analysis performance varies linearly on the same range. This suggests the analysis performance plays an important role in determining the synthesis performance.

Further parameter study is demonstrated in Figure 3.16 showing the spatial average synthesis performance $\langle \psi_s \rangle$. The results may be classified in two groups resonant and non-resonant interfaces. This synthesis response behaviour is expressed quantitatively with regards to the magnitude of disturbance in the analysis of a perturbed system which contributes to the predicting error of the incident wave necessary to accurately synthesize a desired wave field in a non-perturbed system. This explains the linear relation of rate of change in both the synthesis and analysis performance.

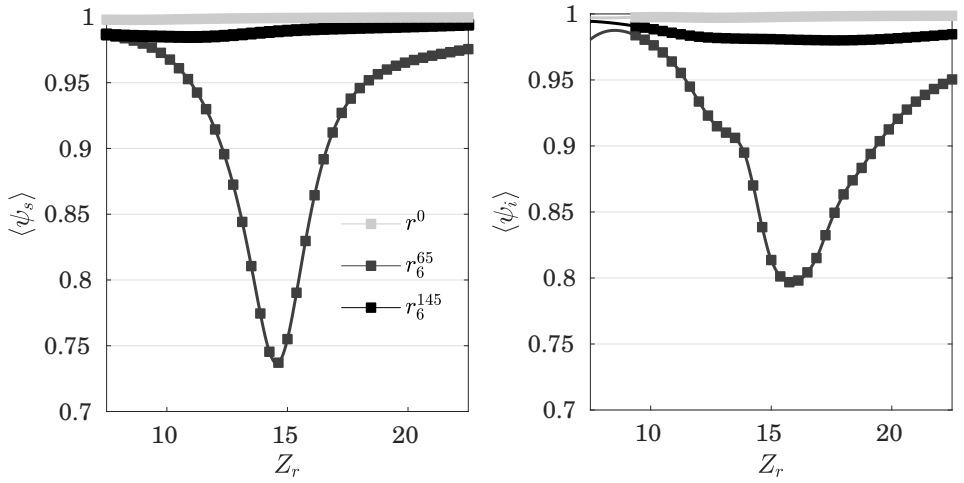

FIGURE 3.16. Simulated ESWS-based spatially averaged synthesis $\langle\psi_s\rangle$ and inferred $\langle\psi_i\rangle$ performance for the circular and hexagonal shapes in terms of impedance ratio and inferred perturbation $\gamma = 0.8$. Synthesis and inferred performances are given by Equations 3.38 and 3.39, respectively. Results shown for non-dimensional wavenumber $kR = 4\pi$. Dots are strictly obtained and solid lines are interpolated

3.4.3 Simplified inferred performance

The synthesis performance has been suggested to relate to the analysis performance. This association is referred to as the inferred performance, denoted by ψ_i, and gives an estimate to the synthesis performance obtained by simply computing the spatially average shape correlation between analysis performances. The goal is to predict a performance parameter based on the solution to an inverse problem (i.e synthesis) by examining the solution to a direct problem (i.e. analysis). The inferred performance is given by

$$\langle\psi_i\rangle_f(T_d,\gamma) = \frac{1}{M}\sum_{n=1}^{M}\frac{\left|\psi_a(r_o^{(n)})^{\dagger}\psi_a(Z_r',r_o^{(n)})\right|^2}{\left|\psi_a(r_o^{(n)})\right|^2\left|\psi_a(Z_r',r_o^{(n)})\right|^2}. \tag{3.39}$$

This performance takes into account the correlation between the analysis performance obtained from a perturbed system $\psi_a(Z_r')$ and from an unperturbed system $\psi_a(Z_r)$. Then, this parameter quantifies the statistical association between analysis performances of perturbed transducer designs. Figure 3.16 shows both $\langle\psi_s\rangle$ and $\langle\psi_i\rangle$ performances for perturbation parameter $\gamma = 0.8$. The inferred performance predicts the synthesis performance with maximum 14.3% error for the smooth hexagonal shape and with maximum 0.2% error for the circular shape.

The process of obtaining the synthesis performance only needs one correlation parameter calculation whereas the inferred performance needs one additional for each of the two analysis performance required. However, the synthesis protocol requires an exclusive step for computing

the inverse filter $\mathbf{T}_{ES}^{+}$. The computation of a transfer function for the synthesis protocol depends on how the external incident wave is defined on the physics-based model. Moreover, measuring real system transfer functions for external incident wave and computing its inverse filter is hypothesised to require experimental methods based on non-acoustic inputs compared with internal incident wave. Thus, one could benefit from investigating analysis rather than synthesis parameters to predict device efficiency on reproduction and justify reduced accuracy of inferred parameters.

3.5 Conclusion

The boundary behaviour of arbitrary shaped fluid-fluid interfaces with characteristic non-dimensional wavenumber $kR = 4\pi$ and impedance mismatch was investigated for the acoustic radiation and transmission problems, as in analysis and synthesis respectively. The purpose of the investigation was to quantify the association between generating and solution waves for both internal and external sources. A simplified model using the ESM was developed to solve for both radiation and transmission problems. The pressure response to an internal source in a circular interface was found in good agreement with an analytical model based on cylindrical wave expansion for an average arc length of $\langle |L| \rangle \approx \lambda/3$. This boundary behaviour has been studied by a shape correlation between total and incident pressure field, as in analysis performance, for hexagonal shapes with rounded corners and circular interfaces. The study has found the analysis performance decreases monotonically with the impedance ratio only in non-resonant systems and has local minimum otherwise. This relationship reflects on the shape correlation between transmitted and desired pressure field, as in synthesis performance. Moreover, the synthesis performance can be predicted by an inferred association based on analysis performance. That is, an impedance ratio perturbation causes the spatially average synthesis performance to be equivalent to the shape correlation between resulting analysis performances. This concludes that coupled resonances in fluid-fluid interfaces exhibits correlated effects on both the acoustic radiation and the transmission phenomenon.

CHAPTER 4

THE VIRTUAL SOURCE FINITE ELEMENT MODEL

The goal of this chapter is to describe the proposed VSFE model in order to solve the wave propagation in acoustic chambers using a virtual source method (see Section 2.3.1) based on FEM. The VSFE is a intermediate model which links both simplified (ESWS) and realistic models (TPFE). This model is an intermediate step to aid the design of MUTD. As represented in the schematic shown in Figure 4.1, this intermediate model considers realistic physical boundaries by employing the FEM and still features theoretical sources as input data. Preliminary results for the problem of a fluid-fluid interface are validated with an analytical solution (see Section 2.2.2) for a circular physical boundary and with a semi-analytical model (see

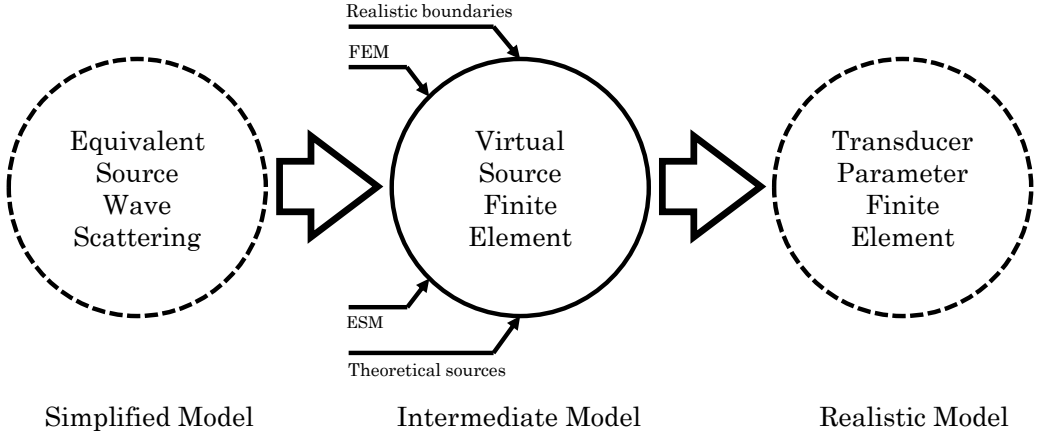

FIGURE 4.1. Schematic diagram for physics-based modelling methodology highlighting the intermediate model (VSFE) and main features. Preceded by the simplified model and followed by the realistic model, the VSFE considers VS method as a theoretical input source and FEM as a realistic boundary formulation.

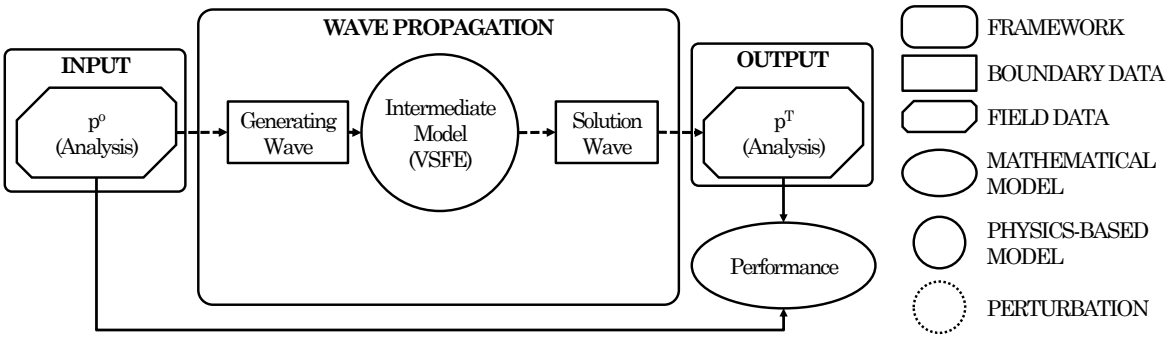

FIGURE 4.2. Schematic diagram of the modelling framework applied to the intermediate model indicating the analysis output is computed using the VSFE-based results.

Chapter 3) for hexagonal physical boundaries. The VSFE model is then applied to solve for the pressure response in acoustic chambers surrounded by a piezoceramic in the analysis protocol and obtain performance parameters, as shown schematically in Figure 4.2. The inputs and output of the VSFE model for the analysis protocol are exactly as previously defined for ESWS. The inputs are incident wave is based on internal line sources and the outputs are scattered wave which solution depends on the transducer parameters.

The VSFE model uses the FEM to solve the problem of acoustic transmission through an enclosed space and is presented as an alternative to the ESWS model. The implementation of the VSFE comprises the definition of the finite elements and material properties over each domain and the boundary conditions. The aim is to replace the outer fluid domain with a piezoelectric material model. The application of a virtual source method imposes an incident pressure field without any singularity in the solution domain. This ensures the analysis of the pressure field is composed only by the wave field internally scattered off the physical boundary.

In the MUTD, transducers are represented by a piezoelectric active layer which confines the acoustic chamber. The piezoelectric effects on such layer due to a radiating acoustic field are more accurately modelled by an electroelastic material modelling than by an ideal fluid modelling. Therefore, material models based on an intermediate level of complexity are investigated by gradually approximating the propagation phenomena to examine the mismatch between the two extremes. This is detailed by presenting the equations solved for the coupled electroelastic wave propagation problem in piezoelectric crystals. The focus is on the simplifying assumptions applied to the material coefficients in order to solve an equivalent problem and compare the response field and performance parameters with the ESWS model. Further comparison for each material modelling is examined in the Appendix D which presents a numerical relationship for a set of practical design cases.

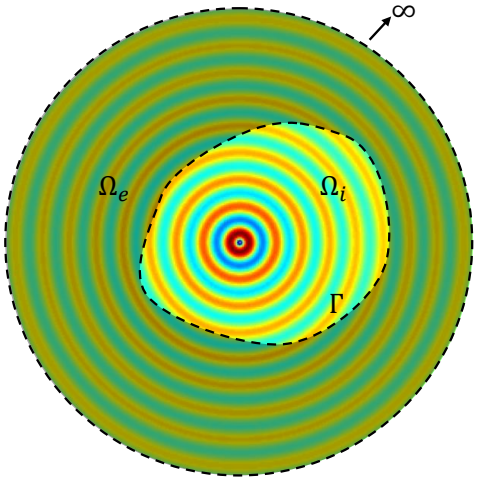

FIGURE 4.3. The conceptual problem to be solved for an internally radiating wave highlighting an infinite outer domain and solution field for a given physical boundary Γ. Radiating wave due to a line source Ω_i propagates to Ω_e and is transmitted through Γ. Coloured image shows acoustic field completely transmitted as if Ω_i and Ω_e had the same acoustic properties for illustration purpose.

4.1 Discrete formulation of the equation of motion

This section is dedicated to describing a discretized wave equation on the piezoelectric continuum and present simplifications for the system of equation to solve for various equivalent media using the FEM. A variational principle stated in a matrix formulation may be regarded as the base for the FEM. This formulation has been used for building up the electroelastic model as an extension of the elastic model using a common mathematical framework. This theory was reviewed by applying the variational method to the equation of motion for electroelasticity (see Section 2.5). The resulting system is now used for gradually simplifying the physical phenomena modelling breaking down into distinct theoretical unbounded domain scenarios such as piezoceramic transducer, linear elastic structure, and incompressible acoustic material modelling.

The goal is to present the finite element formulation for problems associated with electroelasticity in plane strain state applied to the two-dimensional piezoelectric model. Figure 4.3 shows the concept of the interior Helmholtz inhomogeneous problem to be solved with the VSFE model. Electroelastic material in the outer domain has high contrast with inner domain and result in wave scattering phenomenon. The geometrical representation indicates Ω_i as the acoustic chamber, Ω_e as the surrounded perturbed media, Γ as the surface representing the physical boundary between both media. The aim is to explain how the VSFE is formulated by the FEM so to solve an equivalent differential equation solved by the ESWS model and proceed considering piezoelectric material modelling.

4.1.1 Acoustic and electroelastic domains

In this section, the definition of each domain and their respective FE elements are presented in detail. Using the FEM, each modelled domain is defined by either a direct use of a particular element type and its set of dependent variables or in combination with a multiphysics interfacing coupled field. A coupled field is a term used in the engineering analysis to describe models that include the interaction of more than one physical phenomenon. The fluid acoustic behaviour modelled in the inner domain Ω_i is calculated using acoustic elements which solve the acoustic pressure field within the chamber. The outer medium Ω_e is modelled by solid mechanics in addition to electrostatic elements. The resulting system of equations that solves for the coupled field and further element matrices definition, found in Allik and Hughes [1970], are presented in Section 2.5.2.

A brief description of each element matrix applied to different domains is as follows. The element matrices are computed automatically by the FEM software based on the material configuration and the element type chosen. These matrices are then used to solve the above system equilibrium equation. The material properties are set by the user using either predefined material libraries or manually. The shape functions depend on the element type and are calculated by each element local coordinate system as to interpolate the dependent variable solved for.

The use of isoparametric elements is well-suited to obtain good approximation and solve for the time-harmonic linear acoustic analysis in a two-dimensional space. This type of elements uses shape functions to represent both the dependent parameters and the element's geometry. Modelling arbitrary shaped boundaries requires high spatial resolution changes over short distances. For this reason, the study of arbitrary shapes as general acousto-elastic chambers is best achieved by meshing all domains with unstructured triangular elements.

The VSFE model uses quadratic triangular elements, also termed as the linear-strain triangle, applied to all domains. This element has six nodes along its edges and features quadratic shape functions. The reason for choosing quadratic over linear elements is that it better resolves high stress gradients and may represent curvilinear boundaries more accurately with the same number of nodes [Zienkiewicz, 2005] compared with linear ones. The implementation of virtual sources by using monopoles and dipoles introduces high stress gradients in their vicinity. As the chamber corners get sharper the smaller is the radius of curvature and the more concentrated the loads applied at the corner. Therefore, a higher-order element is well-suited for the implementation of the VSFE.

Each element matrix depends on the assigned material coefficients which reflect on the solution computed using the FE solvers. For the fluid media case, only hydrostatic stress is sustained hence the pressure field p, obtained from displacement is the only relevant dependent variable solved for. For the isotropic elastic case, the longitudinal and transverse strain are related by a constant ratio. For the transverse isotropic case, this relation depends on the direction analysed. For the piezoelectric case, the field solution for structural displacement $\mathbf{u}$

and electric potential φ are coupled and characterized by an electro-elastic wave propagation. Until here, a discussion was drawn about the features already available within FE models for modelling electroelastic media. From now on, further development employed by the VSFE model is described and in particular material models are discussed in the next subsection so alternative material properties approximations are derived.

4.1.2 Wave propagation on simplified media

This subsection presents approximations applied to the material modelling by simplifying the theory of electroelastic waves (see Section 2.5) and highlights the resulting wave propagation characteristics. The goal is to tailor simplified homogeneous material constants for alternative material models which share equivalent pressure-wave speed to that of the piezoelectric material. These approximations are achieved by specializing the more general equilibrium system in Equation 2.44 into four different homogeneous continuum mechanics models, namely piezoelectric, transverse isotropic, isotropic elastic and weakly compressible material.

The propagation of bulk acoustic waves in ideal fluid media occurs exclusively as longitudinal waves in which displacements occur in the direction of propagation. In elastic media due to shear stress an additional transverse wave propagates where displacement is perpendicular to the propagation. For isotropic media, longitudinal waves travel with the phase speed always greater than the transverse waves which are independent on the propagation direction. In anisotropic media, both longitudinal and transverse wave speeds depend on the propagation direction. Furthermore, transversely isotropic material is a type of anisotropy that presents an axis of rotational symmetry hence characterized as isotropic in the transverse plane.

The solution to the harmonic analysis using FE solvers are defined for the plane strain conditions. Under this condition, both the strain and displacement field components are solved for in the plane of domain Ω and are considered zero in the perpendicular direction. However, FEM commercial packages usually require the material models to be set independently of the model parameters conditions. Therefore, the following material models are described for a general 3-dimensional problem and the solution is computed accordingly.

Piezoelectric materials of symmetry class 6 mm exhibit axial symmetry in the polarization direction and are considered transversely isotropic even under piezoelectric effects [Every and McCurdy, 1987]. The material properties of class 6 mm piezoelectric materials poled in direction

$n = (0,0,1)$ are defined in contracted Voigt notation as in Tiersten [1963b] by

$$\begin{bmatrix} c^E & -\mathbf{e}^t \\ \mathbf{e} & \varepsilon^S \end{bmatrix} = \left[\begin{array}{cccccc|ccc} c^E_{11} & c^E_{12} & c^E_{13} & 0 & 0 & 0 & 0 & 0 & -e_{13} \\ c^E_{12} & c^E_{11} & c^E_{13} & 0 & 0 & 0 & 0 & 0 & -e_{13} \\ c^E_{13} & c^E_{13} & c^E_{33} & 0 & 0 & 0 & 0 & 0 & -e_{33} \\ 0 & 0 & 0 & c^E_{44} & 0 & 0 & 0 & -e_{15} & 0 \\ 0 & 0 & 0 & 0 & c^E_{44} & 0 & -e_{15} & 0 & 0 \\ 0 & 0 & 0 & 0 & 0 & c^E_{66} & 0 & 0 & 0 \\ \hline 0 & 0 & 0 & 0 & e_{15} & 0 & \varepsilon^S_{11} & 0 & 0 \\ 0 & 0 & 0 & e_{15} & 0 & 0 & 0 & \varepsilon^S_{22} & 0 \\ e_{13} & e_{13} & e_{33} & 0 & 0 & 0 & 0 & 0 & \varepsilon^S_{33} \end{array}\right], \tag{4.1}$$

where $c^E_{66} = \frac{1}{2}\left(c^E_{11} - c^E_{12}\right)$. For transverse isotropic elastic media, the elastic tensor is defined as

$$\left[c^T\right] = \begin{bmatrix} c^T_{11} & c^T_{12} & c^T_{13} & 0 & 0 & 0 \\ & c^T_{11} & c^T_{13} & 0 & 0 & 0 \\ & & c^T_{33} & 0 & 0 & 0 \\ & & & c^T_{44} & 0 & 0 \\ & \text{sym} & & & c^T_{44} & 0 \\ & & & & & c^T_{66} \end{bmatrix}, \tag{4.2}$$

where T denotes transverse isotropy. Further simplification to the material properties for isotropic elastic media can be expressed in terms of an elastic tensor given by

$$\left[c^I\right] = \begin{bmatrix} c^I_{11} & c^I_{12} & c^I_{12} & 0 & 0 & 0 \\ & c^I_{11} & c^I_{12} & 0 & 0 & 0 \\ & & c^I_{11} & 0 & 0 & 0 \\ & & & c^I_{44} & 0 & 0 \\ & \text{sym} & & & c^I_{44} & 0 \\ & & & & & c^I_{44} \end{bmatrix}, \tag{4.3}$$

where the superscript I denotes isotropic approximation and $c^I_{44} = \frac{1}{2}\left(c^I_{11} - c^I_{12}\right)$. On the other hand, for the weakly compressible material [1] approximation, can be simplified to a solid material as a zero shear modulus inviscid fluid with the stiffness matrix

[1] Elastic isotropic materials which predominantly change shape as a result of applied stress are known to be weakly compressible such as liquids and rubbers[Greaves et al., 2011]

$$\left[c^F\right] = \begin{bmatrix} c_{11}^F & c_{11}^F & c_{11}^F & 0 & 0 & 0 \\ & c_{11}^F & c_{11}^F & 0 & 0 & 0 \\ & & c_{11}^F & 0 & 0 & 0 \\ & & & 0 & 0 & 0 \\ & \text{sym} & & & 0 & 0 \\ & & & & & 0 \end{bmatrix}. \tag{4.4}$$

The equation of motion in Equation 2.43 may be solved using the material properties presented in Equations 4.1 to 4.4 together with the element matrices in Equations 2.45 to 2.49 and the form functions.

Different assumptions are applied to formulate each of the above-mentioned simplifications. For the piezoelectric material, stiffened elastic coefficients may be considered in terms of permittivity and piezoelectric coefficients as well as the normal direction of the elastic waves [Every, 1980], as in

$$c'_{rlsm} = c_{rlsm} + \frac{e_{rlp} n_p e_{smq} n_q}{\varepsilon^S_{rs} n_r n_s}, \tag{4.5}$$

where c'_{rlsm} is the element stiffness 4^{th} order tensor and the summation over repeated indices applies. Nevertheless, the behaviour of a piezoelectric material without piezoelectric effects is simplified to that of a transverse isotropic elastic domain by simply setting the piezoelectric coupling coefficients to $\mathbf{e} = 0$, letting $c^T = c^E$ and not considering the dielectric matrix ε^S. The anisotropic material, in particular, transverse isotropic, may be approximated by an isotropic domain by averaging the anisotropic elastic properties over all possible crystal orientations with constant strain [Hill, 1952]. These coefficients are given by

$$c_{11}^I = \frac{1}{5}\left(3A + 2B + 4C\right) \qquad c_{12}^I = \frac{1}{5}\left(A + 4B - 2C\right) \qquad c_{44}^I = \frac{1}{5}\left(A - B + 3C\right), \tag{4.6}$$

where

$$A = \frac{1}{3}\left(c_{11}^T + c_{22}^T + c_{33}^T\right) \qquad B = \frac{1}{3}\left(c_{12}^T + c_{13}^T + c_{23}^T\right) \qquad C = \frac{1}{3}\left(c_{44}^T + c_{55}^T + c_{66}^T\right).$$

Lastly, for weakly compressible material the element stiffness matrix may be obtained by letting $c_{11}^F = c_{11}^I$. These material model simplifications render the pressure-wave speed c_p to be expressed in terms of the elastic constant c_{11}^F and the material density ρ as in

$$c_p = \sqrt{\frac{c_{11}^F}{\rho}}. \tag{4.7}$$

The elastic tensor $[\bar{c}]$ for a fictitious material model can be obtained by taking $\left[c^E\right]$ from a known piezoelectric material, say PZT-5A. Following each approximation step, one can compute the elastic tensors, including c_{11}^F, and $\bar{c}_{ij}$ for each material model using the following relation

$$\bar{c}_{ij} = \frac{Z_r^2}{\rho_r} c_r c_{ij} \tag{4.8}$$

where Z_r is the acoustic impedance ratio, ρ_r is the mass density ratio and

$$c_r = \frac{\rho_f \omega^2}{c_{11}^F k^2}, \tag{4.9}$$

is the ratio of square of wavespeeds, where ρ_f is the mass density of the fluid, with ω and k being the angular frequency and the wavenumber respectively from the acoustic chamber model. Ratios are defined for parameters on exterior domain Ω_e over the ones on interior domain Ω_i. The aim is to approximate a solid material as a weakly compressible material. Firstly, the pressure-wave speed c_p is computed from Equation 4.7 using the elastics constants c_{11}^F, c_{11}^I and c^T for a specified c^E. Then, the ratio c_r is calculated from Equation 4.9 w.r.t the chamber fluid properties. Lastly, the appropriate approximate stiffness tensor $\bar{c}_{ij}$ is obtained from Equation 4.8 to achieve a specified Z_r and ρ_r.

4.2 Intermediate model implementation

The steps for implementing the VSFE model are presented briefly in this section. These steps can be divided into two groups, the first one is the description of the domains and coordinates of the problem and the second concerns with the definition of the equations and conditions solved for. In order to link the FE modelling according to the design of MUTD some modelling concepts described for the ESWS model in Chapter 3 are only mentioned but not completely described again. The VSFE model was developed using COMSOL Multiphysics 5.1 (Comsol Inc., Burlington, MA), a commercial FEM package.

The geometric extent of the VSFE model includes an external layer for taking the radiation boundary condition into account, as shown in Figure 4.4. Secondary line sources are implemented as applied forces on the acoustic domain and defined as point loads on nodal positions distributed over C. Finite element analysis is performed to solve a frequency domain problem using stationary linear solvers and here is implemented for the analysis protocol. The aim is to simulate a line source inside the inner domain Ω_i and work out an equivalent set of line sources on C and then simulate the field from those sources.

The piezoelectric effect is modelled in Ω_e by setting variables shared by both solid mechanics and electrostatic elements. Both the electric field and electric displacement field from electrostatic elements are set as variables of the solid mechanics elements. The polarization variable from the solid mechanics elements is set as a variable of the electrostatic elements. Furthermore, the interaction between both external and internal domains is modelled by an acoustic-structure using a set of weak contributions defined by the acoustic and displacement field.

An AL is appended to the outer edge of the model, as shown in Figure 4.4, to introduce a far-field radiation condition. An additional boundary Γ^* is considered for the definition of this special absorption domain. The radiation condition is then achieved by making sure the energy propagated outwardly is increasingly damped. The advantage of this technique is that it can

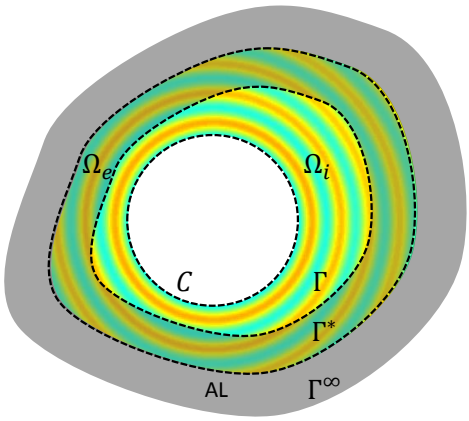

FIGURE 4.4. Conceptual radiation problem to be solved using VSFE highlighting the geometrical representation the domain truncation method and incident pressure field emulation outside the surface C in inner domain Ω_i and transmitted through the surface Γ to the outer domain Ω_e. The boundaries Γ^* and Γ^∞ enclose the AL domain where energy propagated outwardly is damped.

be employed on isoparametric representation of any FEM geometry. By using this approach the domain truncation becomes not limited by a particular implementation of infinite domains, such as Perfectly Matched Layers (PML) or infinite elements that are only defined for a few well-defined shapes [COMSOL AB, 2015].

The second group of steps is dedicated to the equations which define the physics of the problem and conditions solved for. The Absorption Layer with Increasing Damping (ALID) is defined as a viscous damping feature applied to the solid mechanics elements. The magnitude of attenuation in the absorbing region is defined as a function of the distance and the longitudinal wavelength between Γ^* and Γ^∞. A distance equation is solved for the dependent variable defined as the distance away from the surface interfacing the internal and external domains. This is considered a generalized approach to achieve absorption of outwardly propagating waves.

The virtual source method (see Section 2.3) is applied to emulate the radiating pressure field within the inner domain Ω_i, as shown in Figure 4.4. In this approach, a collection of monopoles and dipoles is used to produce an equivalent field outside surface C. On the FE model, these sources are employed by minimizing equations, called weak expressions [COMSOL AB, 2015], and are defined as a linear combination of shape functions for acoustic variables and its source intensities. The emulation of a radiating pressure field is achieved by using a discrete formulation of the KHI described in Section 2.3.1. Such methodology requires the knowledge of geometrical parameters of the surface where the point sources are defined on. The use of secondary sources located on the interface Γ is necessary to directly compare VSFE model results with either the

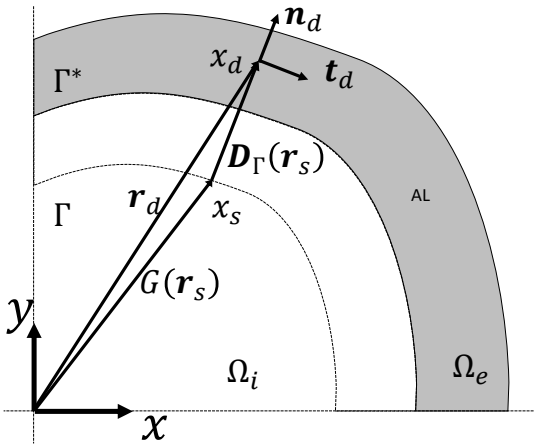

FIGURE 4.5. Schematic of an absorbing layer with increase damping showing the absorbing contour (grey area).

ESWS model or the analytical solution. In the following sections details on each of the discussed modelling steps are presented.

4.2.1 Domain representation

This section is dedicated to the geometrical representation of the external domain Ω_e for the VSFE model. The coordinates for the absorbing layer, the local material properties and the piezoelectric polarization are defined by an implicit distance function. The aim is to configure a built-in function in COMSOL as to calculate the distance between any point in the exterior domain Ω_e to the physical boundary Γ and implement the VSFE based on these geometrical parameters.

Extrusion as a coordinate function

This section presents the equations defined in the exterior domain for calculating the coordinate system from an extrusion feature as a distance function. The general extrusion operator G is a component coupling featured in COMSOL which maps an expression G_s defined on a source domain to an expression G_d evaluated on destination domain [COMSOL AB, 2015]. This operator is used here to calculate distance functions and the local coordinate system.

An operator G that maps destination points $x_d = (r_d, \theta_d)$ in Ω_e and source points $x_s = (r_s, \theta_s)$ on Γ to each to locations $\mathbf{r}_d$ and $\mathbf{r}_s$, respectively, on intermediate coordinate systems. This operator is used to calculate the distance function defined as $\mathbf{D}_\Gamma$, as shown in Figure 4.5. Note the positions of acoustic sources do not regard with the destination and source nomenclature used here as the latter refers to nodal points defined by the FEM software [COMSOL AB, 2015]. The component coupling first evaluates the destination map $G_d(x_d)$ over the domain Ω_e and

carries out a mesh search operation to find the point on the boundary Γ where this evaluation matches the source map $G_s(x_s)$. The source map is evaluated to the physical boundary Γ by setting $G_s(r_s,\theta_s) = (r_N^c(\theta_s),\theta_s)$ (see Appendix A for details). This resolves misplaced finite element nodes x_s on to the parametric curve Γ. Whereas the destination map is defined as the identity function $G_d(r_d,\theta_d) = x_d$. Mapping is achieved by setting the mesh search method to the nearest point using an exhaustive search algorithm. This search method returns one source point at $\mathbf{r}_s$ for a given destination point at $\mathbf{r}_d$ [COMSOL AB, 2015]. The final operation defined as G_Γ is given by a simple minimization of the difference between $\mathbf{r}_d = G_d(x_d)$ and $\mathbf{r}_s = G_s(x_s)$

$$G_\Gamma(x_d) = \mathbf{D}_\Gamma = \mathbf{r}_s - \mathbf{r}_d. \tag{4.10}$$

The distance function can be computed by taking the modulus of the vector field $\mathbf{D}_\Gamma$ as in

$$d_\Gamma = |\mathbf{D}_\Gamma|. \tag{4.11}$$

The resulting scalar field d_Γ is the distance function into the AL. The absorbing rule for the ALID region is defined by the distance function d_Γ and some calibration parameters defined next. However, before defining the absorption rule, a local coordinate system is defined for the implementation of local material properties in the piezoelectric media.

Local coordinate system

The extrusion operator G is employed to calculate a local coordinate system based on the parametric curve r_N^c which defines the interface Γ. The local material properties in the external domain Ω_e are defined by the resulting orthogonal curvilinear coordinates (d_Γ,θ_Γ). The coordinates are θ_Γ along the interface and d_Γ normal to the interface. The unit vectors along the coordinates axes are $\mathbf{n}_d$ and $\mathbf{t}_d$ as shown in Figure 4.5.

Setting up a locally defined coordinate system in COMSOL requires the assignment of the base vectors (x_1,x_2,x_3). The base vector is set in terms of the global Cartesian coordinates (x,y) which can be obtained directly from the expressions below,

$$\begin{aligned} x_1 &= (n_y, 0, -n_x) \\ x_2 &= (0,0,1) \\ x_3 &= (n_x, 0, n_y), \end{aligned} \tag{4.12}$$

where $\mathbf{n}_d = (n_x, n_y, 0)$. Both coordinate functions collectively can be regarded as an example of a special technique called conformal mapping. Conformal transformations are useful in solving partial differential equations on complex domains but are not the focus of this thesis and an interested reader should refer to Thompson et al. [1982] for a review on recent developments and applications of such technique.

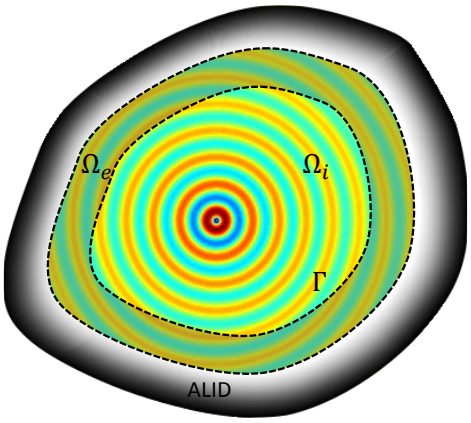

FIGURE 4.6. Conceptual radiation problem to be solved using VSFE highlighting the absorption layer with increase damping. The grayscale gradient patch represents the damping applied which increases from bright to dark.

Absorbing layer using increasing damping

There are several ways to achieve domain truncation if an FE model solves a physics-based problem only in a reasonable region of interest. Furthermore, artificially introducing boundaries to a model may result in additional reflections from its the outer edge. To solve the transducer response of MUTD, a far-field radiation condition is achieved by applying an increasing damping into the outermost layer of the model, as shown in Figure 4.6. This additional layer adds a virtual work to the equilibrium equations to induce viscous effects on the elastic media. For this reason, the damping effects are generated by increasingly varying the damping ratio along the absorbing region causing energy extinction of the wave towards the edge of the model.

This absorption layer is implemented only as a mathematical feature and not intended for realistically represent any physical property apart from the radiation condition. For this purpose, a viscous damping proportional to the mass density is chosen as the applied absorption model whose effect is added directly to the virtual work equation. Damping as a function of mass density is mathematically convenient for the VSFE model because this parameter is constant throughout the external domain Ω_e and does not vary across the implemented material model approximations. This effect is achieved rewriting the Lagrangian function by adding a virtual work δW into the Equation 2.40, as in

$$\delta W = \int_V -\alpha \rho \delta \mathbf{u}^t \dot{\mathbf{u}} dV. \tag{4.13}$$

This contribution is considered in the equilibrium equations in Equation 2.44 rewritten as

$$[\mathscr{M}]_e \left\{\ddot{\mathbf{U}}\right\}_e + [\mathscr{C}]_e \left\{\dot{\mathbf{U}}\right\}_e + [\mathscr{K}_{uu}]_e \{\mathbf{U}\}_e + \left[\mathscr{K}_{u\varphi}\right]_e \{\boldsymbol{\varphi}\}_e = \{\mathbf{f}\}_e \tag{4.14}$$

with the element damping matrix $\left[\mathscr{C}\right]_e$ defined such that $\alpha = \alpha_d b^2$ is a quadratic function of the distance parameter and given by

$$\left[\mathscr{C}\right]_e = \int_{V_e} \left[\mathbf{N}_u\right]_e^t \alpha_d b^2 \rho \left[\mathbf{N}_u\right]_e dV, \tag{4.15}$$

where $\left[\mathbf{N}_u\right]_e$ is the shape function available as a built-in COMSOL function and

$$\alpha_d = K_d \frac{\omega}{2\pi c_r^2}, \qquad b = \frac{d_\Gamma}{l_d}, \tag{4.16}$$

K_d is the calibration damping parameter and l_d is the length of the absorbing region. It is noteworthy, this implementation does not affect the constitutive equations so the stresses and strains are still in phase within the AL.

The AL must absorb radiating energy and should be calibrated by setting up the calibration damping parameter K_d and the length of the absorbing region l_d. Both parameters should be determined to smooth the effect of reflection at a low distance from the interface to limit the total area of the entire model. However, the addition of such a region may induce a gradual impedance change by inappropriately applying domain truncation technique causing collectively spurious reflections [Drozdz et al., 2006]. The approximation error compared to the analytical solution is used as a reference for the calibrating process to quantify the effects of reflections on the total pressure field.

The solution field computed using ALID approach to domain truncation can be readily compared with the results from a standard PML coordinate stretching approach only for a circular cylinder interface. The PML featured in COMSOL is intended for absorbing outgoing wave by stretching the domain into the complex plane in a frequency-domain problem. The ALID calibration process is performed later (see Section 4.3.1) for the circular interface and the results are compared to the ones obtained using PML.

In this work, such absorption region fits the purpose of the methodology used to identify efficient designs for a wide range of shapes. It is worth noting a detailed discussion on the theory and implementation of absorbing regions applied to the propagation of elastic waves in isotropic media can be found in Rajagopal et al. [2012].

4.2.2 Boundary conditions representation

The VSFE model is primarily proposed to implement a set of realistic boundary conditions not covered by the simplified model. The ESWS only considers a fluid-fluid interface between outer and inner domain. Considering electroelastic wave propagation as additional model feature requires the introduction of electrostatics elements and relevant boundary conditions. Although COMSOL Multiphysics defaults most piezoelectric settings, alternative boundary conditions need to be manually defined. The default boundary conditions applied to each domain depend on their geometrical characteristics and the differential equations solved for. In this subsection, the

boundary conditions applied to the VSFE are specified and described in details highlighting the ones not considered by the ESWS model.

To start, an interfacing coupling needs to be modelled to account for the interaction between elastic waves in the solid with pressure waves in the fluid. The implementation of the coupled interface using FEM is achieved by adding an equation for the interaction between pressure load and structure acceleration. This effectively determines the transmission of pressure waves through the elastic structure by setting an internal pressure load in the fluid domain and an external structure acceleration source in the elastic domain over the physical boundary Γ. In the absence of any dipole domain source, an acoustic-structure interaction which introduces a boundary condition is expressed by

$$\begin{aligned} \mathbf{n} \cdot \left(-\tfrac{1}{\rho_c} \nabla p^T \right) &= \mathbf{n} \cdot \ddot{\mathbf{u}} \quad \text{on } \Gamma \\ F_A &= p^T \mathbf{n}, \end{aligned} \tag{4.17}$$

where $\mathbf{n}$ is the surface Γ normal, p^T is the total pressure and F_A is the load per unit area applied to the structure. The acoustic-structure interaction is a multiphysics phenomenon feature in COMSOL AB [2015].

In COMSOL, the boundary condition applied on the edge of the model defaults to free boundary if not overridden by manually specified conditions. However, the implementation of the domain truncation technique (see Section 4.2.1) is needed to achieve the radiation condition for free space problems. The electrostatic boundary conditions are applied on the bounding surfaces of Ω_e where the piezoelectric effects are accounted for. All external domain boundaries default to zero charge boundary condition which translates to the normal component of the electric displacement field to be prescribed to zero.

A zero charge boundary condition is applied to Γ^∞. This condition may be regarded as an idealised electrode with a continuous electrical port placed on the outermost surface of the model, as in

$$\mathbf{n} \cdot D = 0 \quad \text{on } \Gamma^\infty. \tag{4.18}$$

A ground boundary condition is applied to the surface Γ. The ground condition models an ideal electrode with prescribed zero potential across the entire surface.

$$\varphi = 0 \quad \text{on } \Gamma. \tag{4.19}$$

4.2.3 Virtual sources for emulating pressure field

This section presents the implementation of a virtual source method to solve the internal radiation problem. The solution for the problem with an internally placed source may be computed in FE software by simply applying readily defined point load at a point of interest. Conversely, an

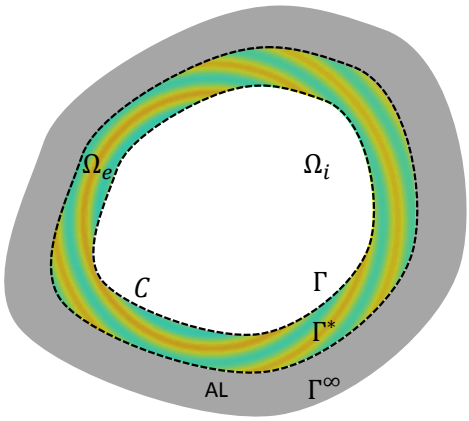

FIGURE 4.7. Conceptual radiation problem to be solved by VSFE using secondary sources by extending the surface C until it reaches Γ.

equivalent surface C defined by the physical boundary Γ is applied to emulate the incident pressure field using secondary point sources, as shown in Figure 4.7. The virtual sources designed to emulate internally incident wave as input to the FE system is applied to calculate both externally transmitted and internally scattered wave using COMSOL solvers which is investigated in the following sections.

The knowledge of the free space Green's function is used for synthesizing the incident pressure field. The distribution of monopoles and dipoles on a continuous boundary for a boundary-value problem is often described as single and double layers, respectively. The intensity of this distribution is also called the source strength density. A similar approach has been applied to an elastodynamic wave model for predicting the complete scattering behaviour of an arbitrary-shaped scatterer embedded in an infinite host medium in frequency-domain [Velichko and Wilcox, 2010; Wilcox and Velichko, 2010] and in time-domain [Shi et al., 2014].

The virtual sources method is an alternative approach to the implementation of the analysis protocol for the developed FE models. The accuracy of approximation of the virtual line sources to a volume discretization method depends on the distribution of secondary sources over the surface C. The response to a virtual source outside C may be calculated using the KHI Equation 2.26. This integral equation is implemented in discrete form for the FE models as defined by the Equation 2.43. If both monopole and dipole sources are applied simultaneously the resulting field outside Γ would be matched with the incident field due to internal virtual sources and vanishes inside Γ if material properties inside were identical to outside, as illustrated in Figure 4.7. However, acoustic contrast on the solid walls of the device causes characteristic boundary behaviour and thus incident wave gets scattered back into internal domain. The implementation of the

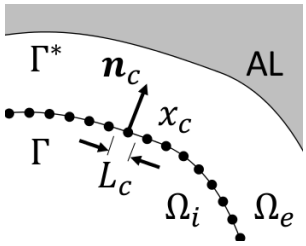

FIGURE 4.8. Secondary source distribution for the implementation of virtual point method applied to the VSFE model showing the set of collocation points x_c located on the physical boundary. Vector $\mathbf{n}_c$ represents normal direction to Γ and L_c is the length of the curvilinear segment.

discrete KHI into the VSFE is achieved in a two-step process. First the secondary line sources are applied as boundary conditions using the FEM software and then the BIE is computed to emulate the specified incident wave field.

The first step is achieved by defining the secondary sources at the nodes x_c over the interface Γ, as shown in Figure 4.8. In COMSOL, weak contributions, or more generally weak form, are the numerical expressions applied to FE for imposing domain and boundary conditions. The right hand side parameters of the equilibrium equation 4.14 corresponds to the applied loads which express the contributions of secondary sources. In terms of monopole and dipole responses defined in Equations 2.12 and 2.15, the pressure field p on an unbounded domain may be obtained as a linear combination of each response as in

$$\left(\nabla^2 + k^2\right) p = 4\pi \left(f_d \frac{\partial \delta(\mathbf{r}^d - \mathbf{r})}{\partial e_d} - f_m \delta(\mathbf{r}^m - \mathbf{r}) \right), \quad \text{on } \Omega \ , \tag{4.20}$$

where f_m and f_d are the strengths of the monopole and dipole sources and $\mathbf{e}_d$ is the orientation of the force term. Similar to the Green's function $G(\mathbf{r}', \mathbf{r})$ which solves the above inhomogeneous Helmholtz equations, the shape functions $\left[\mathbf{N}_u\right]_e^t$ and the corresponding derivative $\left[\mathbf{B}_u\right]_e^t$ are the solutions for the applied weak contributions in the FEM. In that light, the strength of these sources are proportional to the forces applied as point loads implemented by the elements containing the nodes at x_c. The applied force vector $\mathbf{f}_e$ for each element may be written as weak contribution weighted by the strength of these sources as in

$$\mathbf{f}_e = \left[\mathbf{B}_u\right]_e^t \mathbf{F}^d + \left[\mathbf{N}_u\right]_e^t \mathbf{F}^m, \tag{4.21}$$

where $\mathbf{F}^m = \left\{F_i^m\right\}$ and $\mathbf{F}^d = \left\{F_i^d\right\}$ are the monopole and dipole strength vector applied on each element, respectively. Each secondary source is realized by adding an expression corresponding to the terms of the discretized KHI in Equation 2.27.

The second step is to compute the monopole and dipole strengths based on the KHI. The dipole strength is given by

$$F_d(\mathbf{r}_c) = \frac{1}{\rho\omega^2} p(\mathbf{r}_c) L_c \mathbf{n}_c, \tag{4.22}$$

where p_c is the pressure of the incident pressure field and L_c is the length of the curvilinear segment containing the source point at x_c. Similarly, the monopole strength is given by

$$F_m(\mathbf{r}_c) = \frac{1}{\rho\omega^2}\frac{\partial p(\mathbf{r}_c)}{\partial n_c} L_c \mathbf{n}_c, \tag{4.23}$$

where $\frac{\partial p_c}{\partial n_c}$ is the normal derivative of p_c with respect to Γ. Note, the Green's function and its derivative are implemented in the ESWS model for computing the propagation matrix $[\mathbf{P}]$ in Equation 3.25 using the ESM, as described in Section 3.1.3. The application of shape functions $[\mathbf{N}_u]_e^t$ and $[\mathbf{B}_u]_e^t$ are the equivalent Green's function in the FEM and used here to locally emulate the pressure field. In COMSOL the weak contributions applied to the nodes at x_c are automatically distributed over the adjacent elements by setting each contribution as the corresponding shape function weighted by the strength.

The advantage of this virtual source method is that it may be applied to any continuous surface C. Particularly the definition of C as the physical boundary Γ guarantees the applicability of the method within the entire interior domain Ω_i for all interfaces studied. As a consequence, the geometrical parameters which define Γ, such as position, normal direction and curvilinear length defined for the ESWS model may be used to compute the strengths of the secondary sources applied to the VSFE model. See Appendix A for details on these geometrical parameters.

The goal of applying the virtual source method is to make the VSFE correspond with the ESWS both in terms of the solution p^s as an output and the definition of the incident boundary data $\mathbf{b}_o$ as an input. Applying this technique to solve the radiation problem for internal sources directly provides the internally scattered field p^s from the nodal solution for validation with previous models. If the VSFE, the ESWS and the analytical models are solved for the same domain configuration, the internally scattered field may be compared point by point. The next section concerns with the application of this methodology to solve for the response field using the described model as a physics-based intermediate model.

4.3 Intermediate solution field

This section is dedicated to examining the solution field computed using the VSFE model. The goal is to validate a intermediate model and build a minimal FE model for evaluating robust MUTD. The ESWS provided good approximation results with a fluid as the exterior domain compared with the analytical solution for the analysis protocol. It is expected the response to theoretical sources to change significantly as the applied material model represents a realistic device more accurately. Analysing mesh refinement, domain truncation method and the emulation of the incident pressure field are employed here for the fluid and piezoelectric model only. However, the effects of physical parameters on the pressure response for both the isotropic and transverse isotropic material models is investigated in the next chapter. A three-step process is proposed to study the accuracy of the intermediate model.

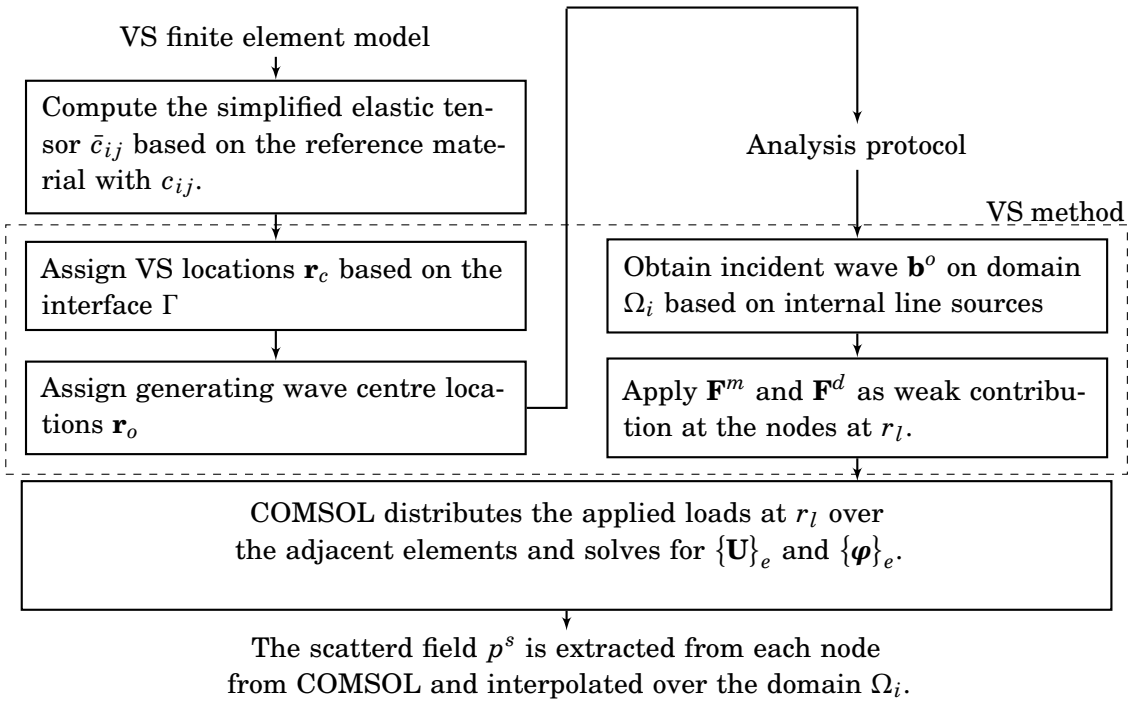

Figure 4.9: The VSFE model flow diagram showing the logic sequence of calculations. The process stages on the analysis protocol is computed using a common mathematical model of transfer functions $\mathbf{T}_{VS}$ calculated from the matrices obtained based on the equivalent sources.

First, a convergence study is performed to quantify the error of the solution for scattered pressure field p^s obtained with VSFE compared with the exact solution. Then, the ALID parameter calibration is carried out to determine acceptable values for the damping parameters that define an efficient absorbing region. The ALID domain truncation method differs from the PML as the latter allows the boundary shape to be defined by any concave surface. Lastly, a preliminary validation study is conducted to analyse the convergence in terms of the number of secondary sources for an arbitrary-shaped boundary. For all investigation, the solution field data was extracted from the nodal solution obtained in COMSOL using interpolation within a rectangular grid consisting of equally spaced coordinates along each Cartesian axis.

Figure 4.9 shows a flow diagram with the sequence of calculation for the analysis protocol and the VSFE model. The first step is achieved by computing the simplified elastic tensor $\bar{c}_{ij}$ as described in Section 4.1.2. The next step is the VS method application for the analysis protocol to calculate the weak contributions at the nodes of the element mesh on the interface. The scattered field p^s is then computed to further investigate the efficiency piezoelectric devices to passively withstand internally testing functions.

Table 4.1 lists the piezoelectric coupling and relative permittivity used for implementing the VSFE model. Table 4.2 the elastic properties for each simplified material model using the

procedure described in Section 4.1.2. The mass density for the material model studied here is fixed to $\rho = 7500\ \mathrm{kg\,m^{-1}}$ despite the fact that the real mass density of PZT-5A is $\rho = 7753\ \mathrm{kg\,m^{-1}}$.

Table 4.1: Piezoelectric coupling and relative permittivity of piezoelectric material implemented on the VSFE.

	$e_{13}(\mathrm{C\,m^{-2}})$	$e_{33}(\mathrm{C\,m^{-2}})$	$e_{15}(\mathrm{C\,m^{-2}})$	ε^S_{11}	ε^S_{22}	ε^S_{33}
PZT5-A	-5.35	15.78	12.29	919.1	919.1	826.6

Table 4.2: Elastic properties of simplified material implemented on the VSFE for different levels of material approximations based on PZT-5A.

	c_{11}(GPa)	c_{33}(GPa)	c_{44}(GPa)	c_{13}(GPa)	c_{12}(GPa)	c_{66}(GPa)
Transverse Isotropic	120.35	110.87	21.053	75.90	75.18	22.573
Isotropic	117.61	117.61	21.349	74.91	74.91	21.349
Weakly Compressible	117.61	117.61	0	0	0	0

4.3.1 Convergence study

For the mesh convergence study, the solution field is solved using the VSFE model for a weakly compressible solid chamber wall, termed VSFE-fluid solution field as a reference to the material modelling approximation. The present study is employed to verify the convergence of the solution field with respect to the element size. The convergence seeks the minimum threshold for the maximum element size necessary to achieve converged solution using standard domain truncation and input source methods. Figure 4.10 presents the schematic geometry showing the system of boundaries solved for this convergence study viewed as the cross-section of the system's domains. The z axis is perpendicular to the plane defined by the radial axis r where the solution field is modelled. The PML domain truncation method is applied to solve for the total field $p^T = p^s + p^o$ due to a monopole source defined by Equation 4.21 inside a circular interface. This modelling step

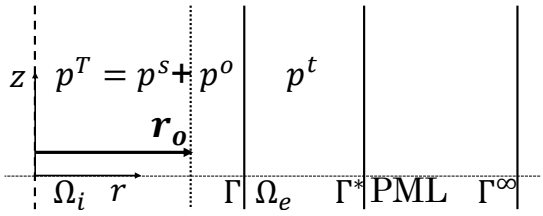

FIGURE 4.10. Schematic system with domain cross-section for VSFE model convergence study using standard PML truncation method and real physical internal incident wave in a circular boundary. The line source at $\mathbf{r}_o$ inside internal domain Ω_i radiates incident pressure field which propagates through the interface Γ into the external domain Ω_e and through Γ^* into the PML where it gets absorbed completely before reaching the boundary Γ^∞.

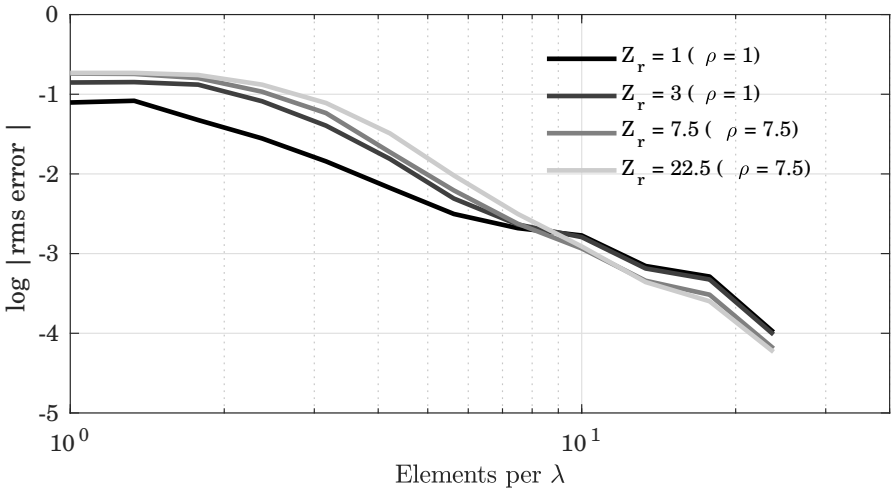

FIGURE 4.11. Convergence as a function of the number of elements per wavelength for preliminary VSFE results using PML truncation method to the solution of an internal real source radiation problem. The non-dimensional wavenumber is $kR = 4\pi$. The analytical solution is from Equation 3.35. The $\log \varepsilon_{rms}$ is shown for $Z_r = 1, 3, 7.5, 22.5$.

is a simplified version of the VSFE model considering prescribed boundary conditions as a line source defined at the physical position of the line sources and studied for verification purposes. Particularly, the study is carried out with the line source positioned at an off-centred distance $r_o = \lambda$ from the origin of the coordinate system.

The analytical pressure field on a fluid-fluid acoustic interface is obtained using cylindrical harmonics expansion (see Appendix C for details) and calculated as a truncated series given by

$$p^T(\mathbf{r}) = \begin{cases} p_0 \frac{i}{4} \sum_{n=-n_t}^{n_t} J_n\left(k|\mathbf{r}_o|\right)\left[H_n^{(2)}\left(k|\mathbf{r}|\right) + a_n J_n\left(k|\mathbf{r}|\right)\right] e^{in\phi} \mathbf{r} > \mathbf{r}_o \\ p_0 \frac{i}{4} \sum_{n=-n_t}^{n_t} J_n\left(k|\mathbf{r}|\right)\left[H_n^{(2)}\left(k|\mathbf{r}_o|\right) + a_n J_n\left(k|\mathbf{r}_o|\right)\right] e^{in\phi} \mathbf{r} < \mathbf{r}_o \end{cases}, \tag{4.24}$$

where n_t is the number of truncation terms and a_n are the coefficients found by matching the transmission boundary conditions at Γ in Equation C.4. An approximation error is computed over internal domain Ω_i except at $\mathbf{r}_o$ between the VSFE and the analytical solution is defined as

$$\varepsilon = \frac{p_{VSFE} - p^T}{max\left(p^T\right)}. \tag{4.25}$$

The RMS error of the pressure field as a function of the element size for various impedance ratio and the free space problem ($Z_r = 1$) is shown in Figure 4.11. The convergence plot shows that the VSFE-fluid with PML for the free space problem achieves accurate results with the lowest number of elements per wavelength between all convergence investigated. It is noteworthy,

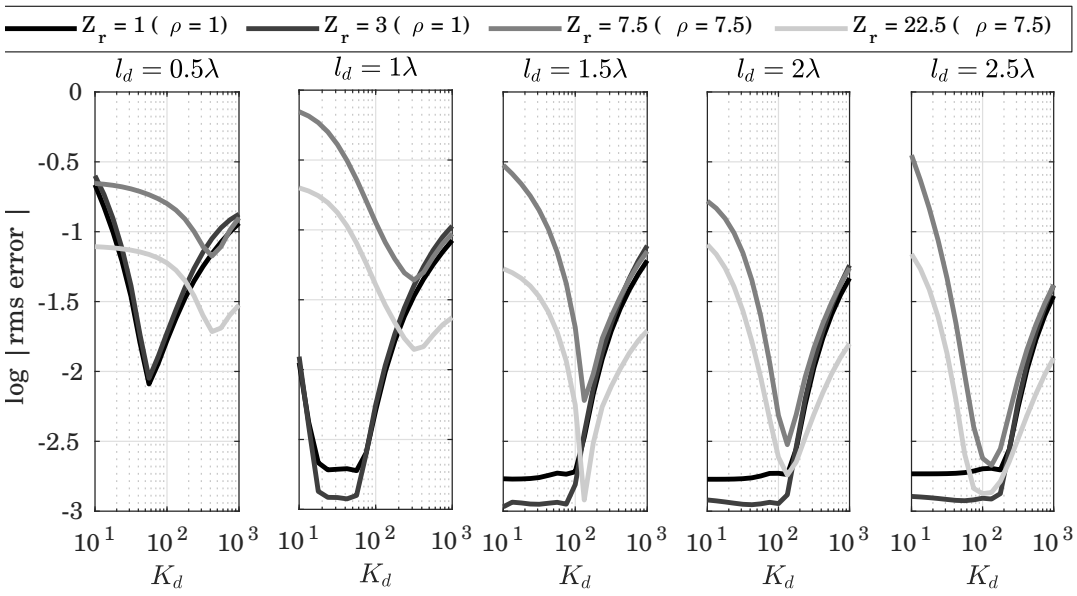

FIGURE 4.12. Convergence as function of the damping parameter K_d and ALID layer length l_d for preliminary VSFE results using ALID truncation method to the solution of an internal real source radiation problem. The non-dimensional wavenumber is $kR = 4\pi$. The analytical solution is from Equation 3.35. The $\log \varepsilon_{rms}$ is shown for $Z_r = 1, 3, 7.5, 22.5$.

COMSOL uses the pressure-wave speed defined by Equation 4.7 to calculate the longest wavelength and set the stretch functions for the PML [COMSOL AB, 2015]. The number of elements necessary to achieve the same level of accuracy increases with increasing impedance ratio. All impedance ratio studied cases attains good agreement ($\log \varepsilon \approx -3$) with the analytical solution beyond 10 elements per wavelength. Note convergence rate is influenced mainly by the order of the elements and for higher orders may result in different convergence rate.

ALID calibration study

The ALID method is employed as an alternative to the geometrically restricted PML method. The calibration of the damping parameter K_d and the length l_d into the ALID layer is presented for the parameters solved previously using PML method. The accuracy of the ALID method is studied by examining the convergence of the RMS error compared with the analytical solution. An accurate solution is obtained if the number of elements per wavelength is set to 10 according to previous convergence results. The line source is again positioned at an off-centred distance $r_o = \lambda$. A series of convergence plots is shown in Figure 4.12 with varying ALID layer length l_d from 0.5 to 2.5λ.

In general, the convergence pattern is mainly determined by the speed of sound ratio $c_r = Z_r/\rho_r$ as a function of the length l_d. The approximation errors for the free space ($Z_r = 1$) problem

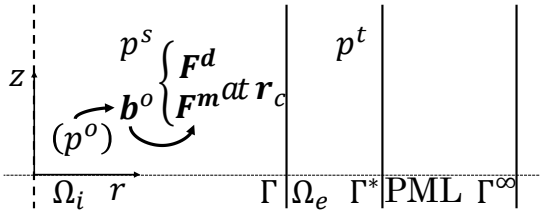

FIGURE 4.13. Schematic system with domain cross-section for VSFE model verification study using virtual sources as internal incident wave and PML truncation method in a circular boundary. The incident $\mathbf{b}^o$ boundary data is computed from the incident p^o and the load $\mathbf{F}^m$ and $\mathbf{F}^d$ is applied as weak contribution at the nodes at $\mathbf{r}_c$. Both the scattered p^s and transmitted p^t pressure field are computed using FE solvers.

indicate the minimum length necessary to accurately compute the reflected pressure field is between $\lambda/2 > l_d > \lambda$. For speed of sound ratio $c_r = 3$, the minimum length is equal three times this value and determined as $l_d = 2.5\lambda$. It is noteworthy the free space problem convergence as a function of the l_d indicates the approximation error reaches a minimum determined by the number of elements per wavelength, as shown in Figure 4.11. Furthermore, a similar trend for the free space ($Z_r = 1$) is expected for the high impedance ratio ($Z_r = 22.5$) problem, as the former results with $l_d = \lambda/2$ approach the latter with $l_d > 2\lambda$.

Nevertheless, the damping parameter is calibrated for $l_d = 2.5\lambda$ which yield a calibration damping parameter of $K_d \approx 10^2$ for minimum approximation error. All results investigated show that above certain calibration threshold the larger K_d the higher the error. This may be interpretation as an excess of absorption leading to numerical reflection due to increased rate of change of the damping parameters between adjacent elements. The convergence study shows calibration threshold depends on model parameters such as speed of sound ratio c_r, impedance ratio Z_r, layer length l_d. It is hypothesized, this threshold is also a function of source position and boundary shape but just the influence of parameters cited above on the approximation error suffice for the calibration study.

This investigation has shown the VSFE-fluid solution field using the ALID method to be in good agreement with the analytical solution. The application of this domain truncation method to solve for piezoelectric material properties is essential to progress further in the development of the solution for the realistic transducer response.

4.3.2 Verification for the virtual sources

A set of numerical simulations is analysed to verify the solution field obtained using the virtual source method. The virtual source verification goal is to assess the accuracy of the solution field in terms of the number of virtual sources by comparing it against the analytical solution. The verification study represents the first step which employs the VS method to investigate

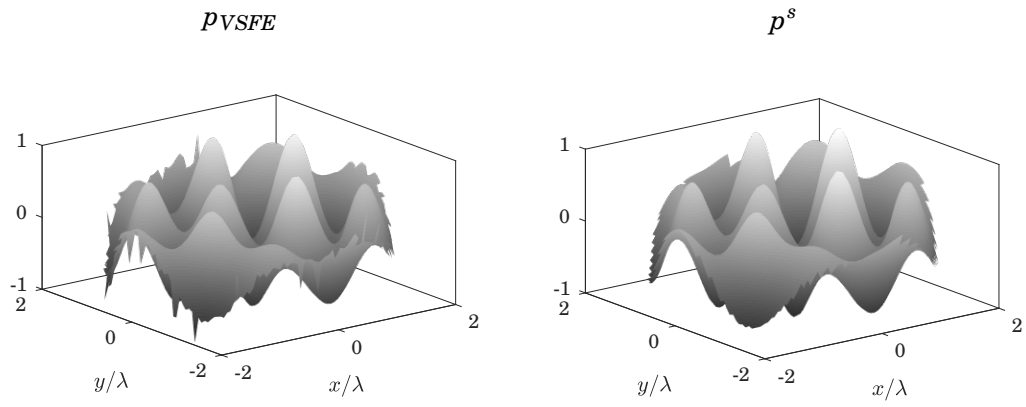

FIGURE 4.14. Example of simulated VSFE-based compared with analytical analysis field for an off-centred virtual source $r_o = \lambda$. Results for $kR = 4\pi$,$\Gamma = r^0$ and $Z_r = 11.25$. The pressure field is normalized with the maximum magnitude inside validation region for a distance $\xi_a = 4\pi^2/3k$ away from Γ, shown truncated between -1 and 1 and for $\langle |L| \rangle = \lambda/3$.

the use of monopoles and dipoles to emulate the incident field applied in the internal domain. Figure 4.13 shows the system with domain cross-section which obtains the scattered field p^s extracted directly from COMSOL solvers. Figure 4.9 shows the sequence of steps required to solve the system. Firstly, a side by side comparison for an example of p_{VSFE} is compared with the exact scattered field p^s for an off-centred line source, as shown in Figure 4.14.

Convergence plots for the approximating error $\log \varepsilon$ as a function of source off-centred distance for various impedance ratios, as shown in Figure 4.15. For all results, the error for virtual source close to the interface is higher compared with a centred one at least in two orders of magnitude. The analysis field for free space problem ($Z_r = 1$) converges with less number of secondary sources than for the impedance mismatch cases ($Z_r > 1$). The error exhibits a pattern in the off-centred distance axis which follows the spatially mapped analysis performance discussed in Section 3.4.1 (e.g. see Figure 3.13). For speed of sound ratio $c_r = 3$, the convergence rates are lower than for $c_r = 1$. In conclusion, this study shows the approximation error is $\log \varepsilon_{rms}(r_o) < -2$ for an average arc length $\langle |L| \rangle \approx \lambda/3$.

4.3.3 Validation for VSFE-fluid

The solution for the scattered pressure field in the analysis protocol is demonstrated for hexagonal shapes using the VSFE model. The validation step represents the last step before investigating boundary behaviour for piezoelectric material as device modelling. In order to assess the accuracy of the solution field in terms of the chamber corner ς, two distinct hexagonal shapes r_6^{ς} are studied, namely a smooth r_6^{65} and sharp r_6^{145} (see Appendix A for boundary shape details). The

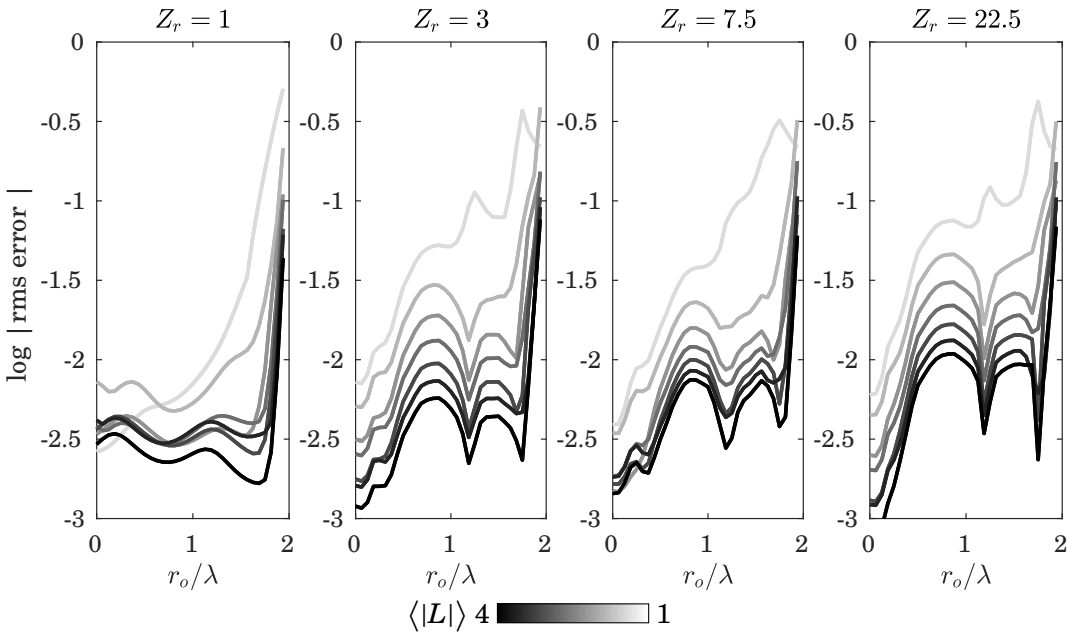

FIGURE 4.15. Simulated VSFE-based approximation error $\varepsilon(r_o)$ in terms of source off-centred distance for the analysis field. Solid lines(—) show error for average arc length $\langle |L| \rangle$ ranging from λ to $\lambda/4$ with the number of secondary sources per wavelength increasing linearly from 1 to 4. Results for $kR = 4\pi, \Gamma = r^0$ and $Z_r = 1, 3, 7.5, 22.5$.

following results are presented in pairs of response field and approximation error using both the p_{VSFE} and the p_{ESWS}. All simulations are run for the same number of discretization points over the physical boundary previously defined for $\langle |L| \rangle = \lambda/3$. The ESWS pressure field is obtained using the equivalent source method (see Section 3.1 for details) and calculated as the matrix product of transfer matrices given by

$$\mathbf{p}_{ESWS} = [\mathbf{P}]\,[\mathbf{B}_i]\,\mathbf{b}_o, \tag{4.26}$$

where $\mathbf{b}_o$ is the incident boundary data obtained, $[\mathbf{P}]$ and $[\mathbf{B}_i]$ are the propagator and the internal boundary behaviour matrices. The sequence of calculations for the ESWS model, including boundary data and matrices, are presented in Figure 3.6 following the analysis protocol.

The approximation error ε is defined as

$$\varepsilon = \frac{p_{VSFE} - p_{ESWS}}{max\left(p_{VSFE}\right)}. \tag{4.27}$$

An example of validation result for a centred virtual source and impedance ratio $Z_r = 11.25$ is shown in Figure 4.16. Pressure singularities in the vicinity of the interface Γ are present on both results. This is due to the implementation of secondary sources for emulating the incident pressure field in the VSFE model. This effect also appears in the ESWS solution with opposite

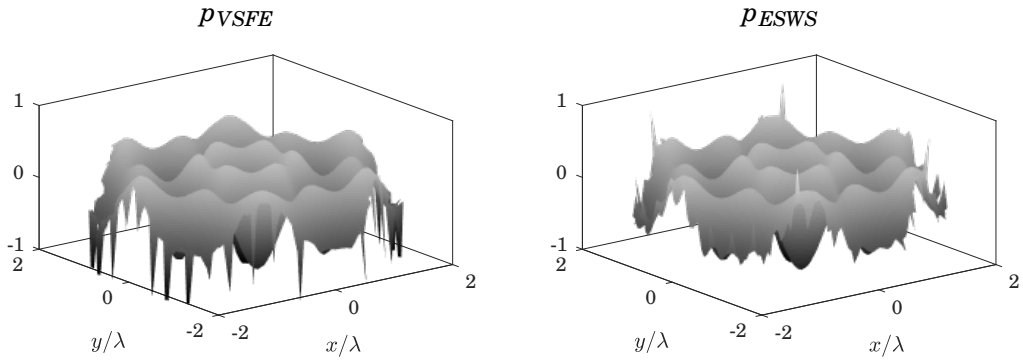

FIGURE 4.16. Example of simulated VSFE-based model compared with the ESWS-based scattered field for a centred virtual source. Results for $kR = 4\pi$,$\Gamma = r_6^{65}$, $Z_r = 11.25$ and $\langle |L| \rangle = \lambda/3$. The pressure field is normalized with the maximum magnitude inside the validation region for a distance $\xi_a = 4\pi^2/3k$ away from Γ, shown truncated between -1 and 1 and for $\langle |L| \rangle = \lambda/3$.

sign as a result of emulating the response pressure field using the propagator matrix. For this reason, the error between the solutions outside the validation region obtained using both methods is greater than the error of each method compared with the analytical result.

Figures 4.17 to 4.19 show validation results for various off-centred distance and two different impedance ratios. These results confirm errors are high in the vicinity of the interface in all cases, particularly more evident for the circular shape in Figure 4.17. The smooth shape, shown in Figure 4.18, presents a small decrease in the overall accuracy as the virtual point source gets away from the centre. For the sharp shape, shown in Figure 4.19, the error is more uniformly distributed over the chamber regardless of the off-centred distance r_o. Higher impedance ratio results ($Z_r = 15$) are shown in Figure 4.16. There is no significant change in accuracy for the sharp shape compared with the low impedance case. However, errors are higher compared with the lower impedance for the smooth shape where the chamber exhibits a resonance mode.

To further examine the accuracy of the VSFE-fluid solution field, the RMS error is computed as a function of both the point source distance and the impedance ratio. Figure 4.20 shows the RMS error for both the smooth and sharp hexagonal shapes in addition to that for the circular shape. Note that errors surfaces are only evaluated over the partially mapped domain obtained for r_o in a radial section of Ω_i (see Appendix B for details). It can be seen that for the hexagonal shapes the accuracy between both methods is not lower for virtual sources close to the interface ($r_o \approx 2\lambda$) than for elsewhere. For the circular case, this error pattern does not happen as the comparison between VSFE and ESWS reflects the error pattern of each method (see Figure 3.9 for ESWS and Figure 4.14 for VSFE). This suggests the errors within the validation region on both methods are equivalent as a result of virtual source emulation in polygonal shapes.

The results indicate that the response of the sharp hexagonal shape is computed with good agreement between methods throughout the analysed parameter space. For the smooth shape,

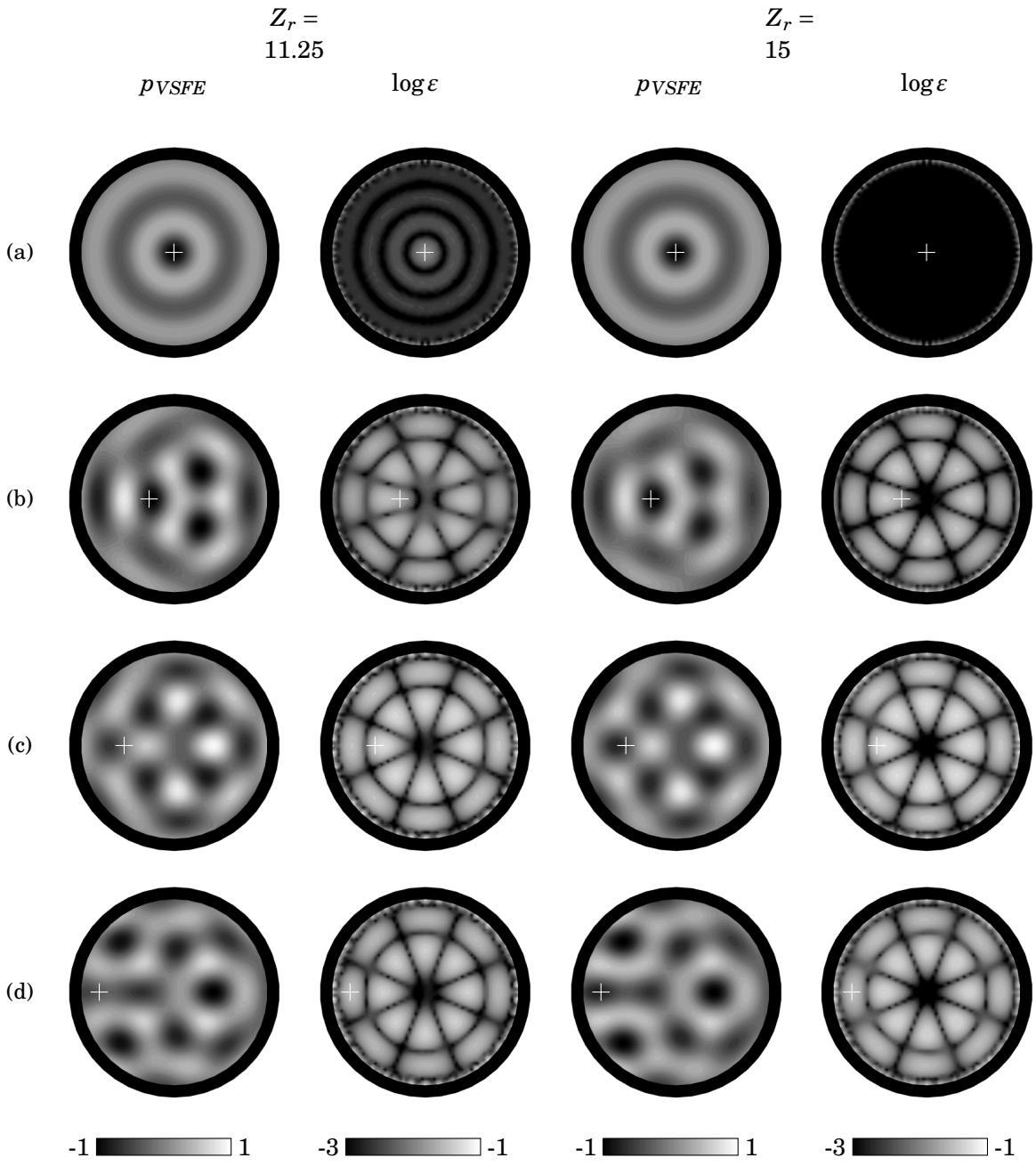

FIGURE 4.17. Simulated VSFE-based analysis field using fluid-like material properties with off-centred point source and for circular interface r^0 compared with the ESWS-based model. Real value of response field p^s and error $\log\varepsilon$ for $r_o = 0$ (a), 0.5 (b), 1 (c),1.5 (d). Results are shown for non-dimensional wavenumber $kR = 4\pi$ and $\langle |L| \rangle = \lambda/3$.

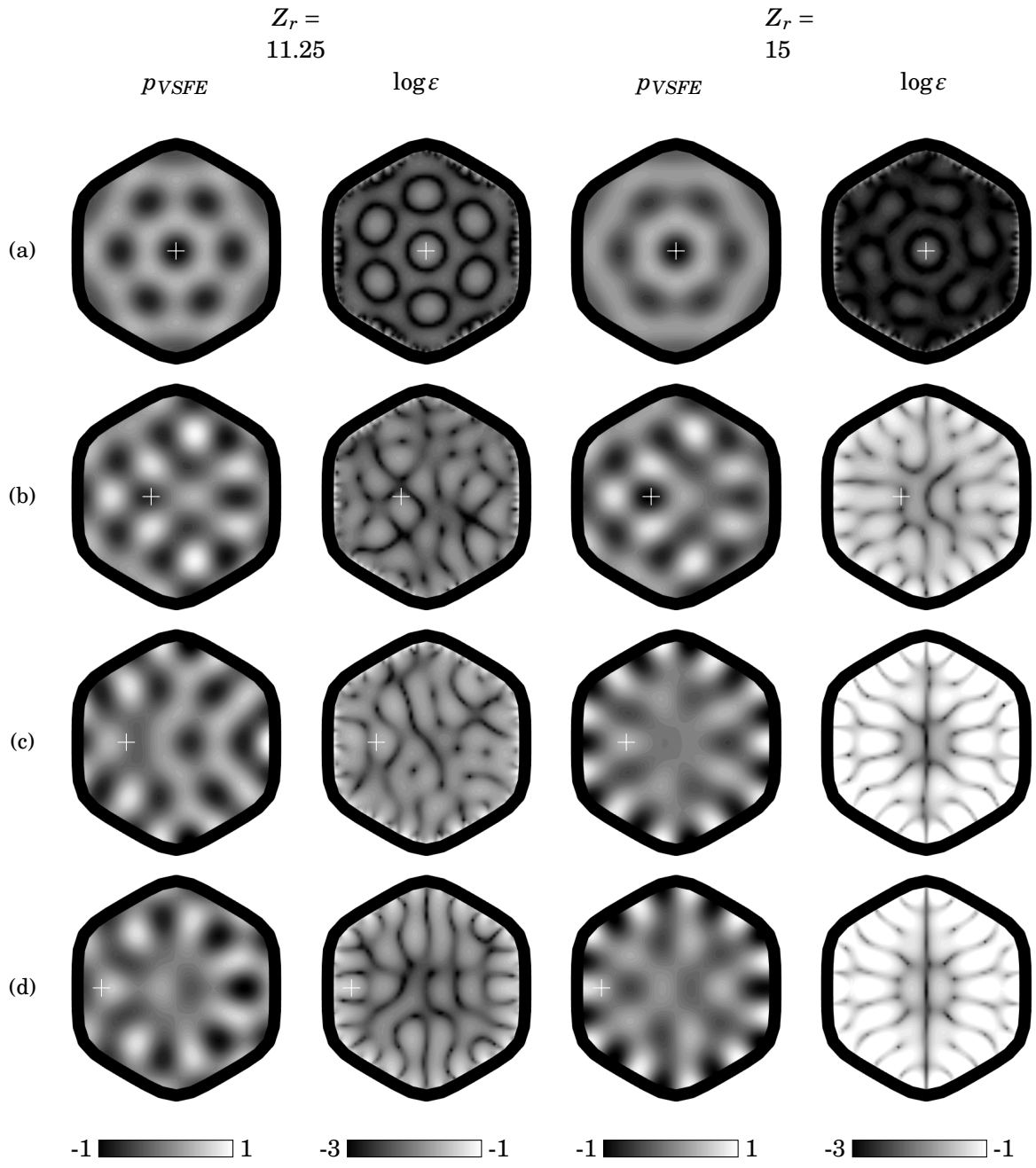

FIGURE 4.18. Simulated VSFE-based analysis field using fluid-like material properties with off-centred point source and for smooth hexagonal interface r_6^{65} compared with the ESWS-based model. Real value of response field p^s and error $\log\varepsilon$ for $r_o = 0$ (a), 0.5 (b), 1 (c),1.5 (d). Results are shown for non-dimensional wavenumber $kR = 4\pi$ and $\langle |L| \rangle = \lambda/3$. (Same as in Figure 4.17)

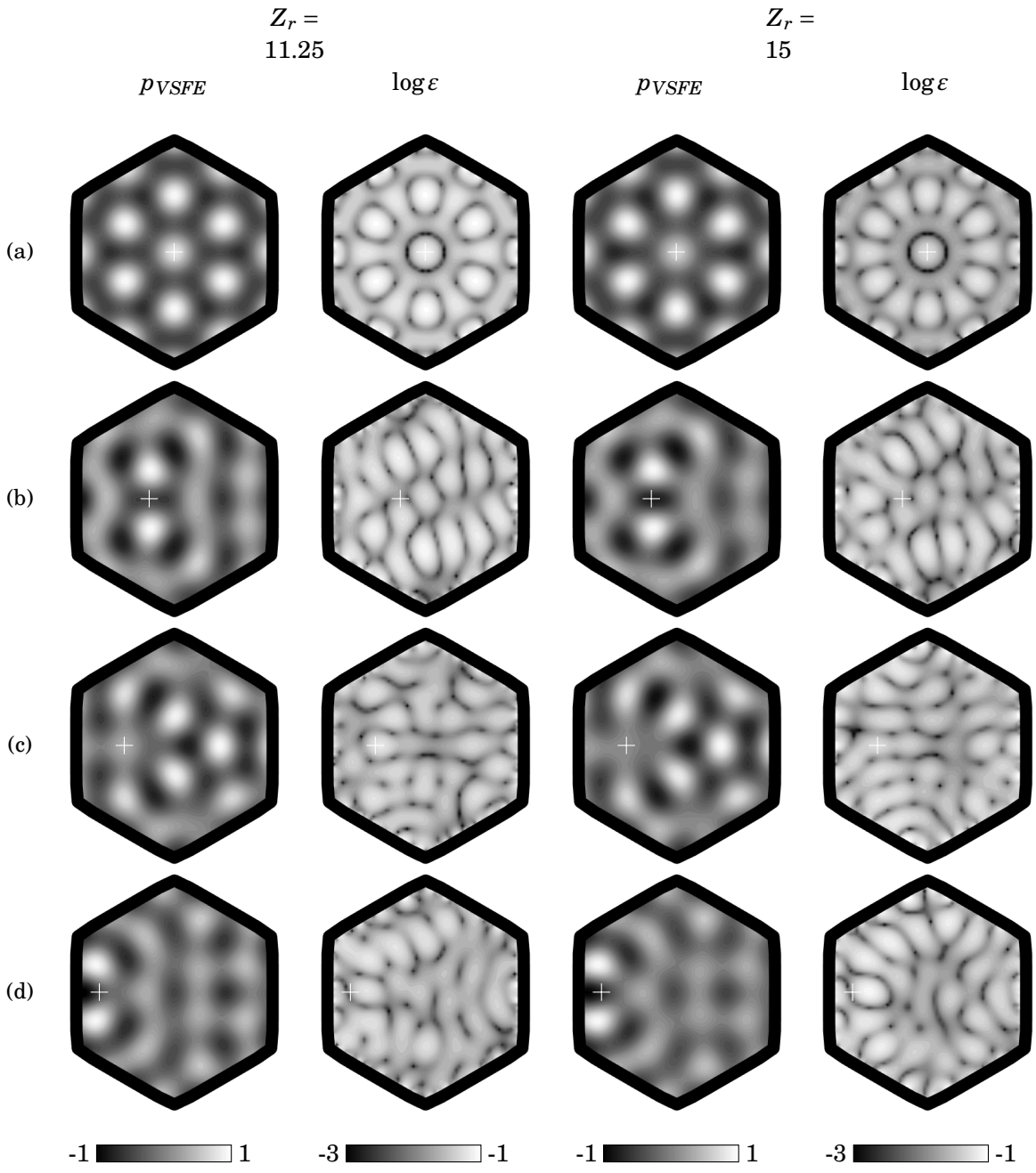

FIGURE 4.19. Simulated VSFE-based analysis field using fluid-like material properties with off-centred point source and for sharp hexagonal interface r_6^{145} compared with the ESWS-based model. Real value of response field p^s and error $\log\varepsilon$ for $r_o = 0$ (a), 0.5 (b), 1 (c),1.5 (d). Results are shown for non-dimensional wavenumber $kR = 4\pi$ and $\langle |L| \rangle = \lambda/3$.. (Same as in Figure 4.17)

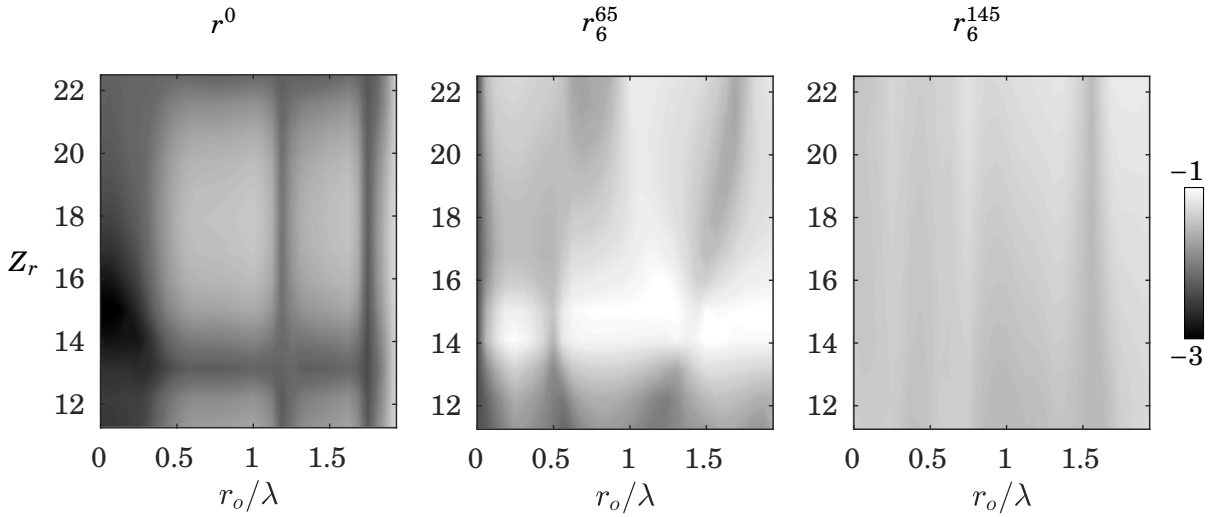

FIGURE 4.20. Simulated VSFE-fluid approximation error $\log \varepsilon_{rms}(r_o)$ of the analysis field for circular and hexagonal shapes in terms of the impedance ratio and off-centred point source distance. Results are shown for non-dimensional wavenumber $kR = 4\pi$ and are truncated between -3 and -1 in log scale.

significant variation in the errors is due to the chamber's resonance around $Z_r = 15$ which results in approximating error $\log \varepsilon > -1$. There is no strong evidence as to why very high accurate results for centred virtual sources only occurs for the smooth shape in contrast with the sharp shape. This could be because of the FE inability to resolve concentrated loads applied at corners with a small radius of curvature.

To summarise, the intermediate model was validated by comparing results from the VSFE-fluid with the ESWS model. The model is accurate enough to predict the boundary behaviour within a wide validation region due to an internal point source radiation except for resonant chambers. The next section is dedicated to investigating how the piezoelectric material properties affect the scattered field based on the analysis protocol.

4.3.4 Comparison for VSFE-piezo

This section presents a study of the scattered field solved for the piezoelectric material using VSFE model, termed as VSFE-piezo solution field. This solution is investigated against the semi-analytical solution assuming fluid material approximation using ESWS model. The goal of this study is to examine the accuracy of the intermediate model in approximating the scattered field due to virtual sources emulating an internal monopole. This approximation is based on setting the material properties in the outer domain in the FE model to the material constants defined in Equation 4.6 and 4.1. The pressure wave speed of the piezoelectric material defined in Equation 4.7 is selected as the physical parameter that tunes the material model. In this

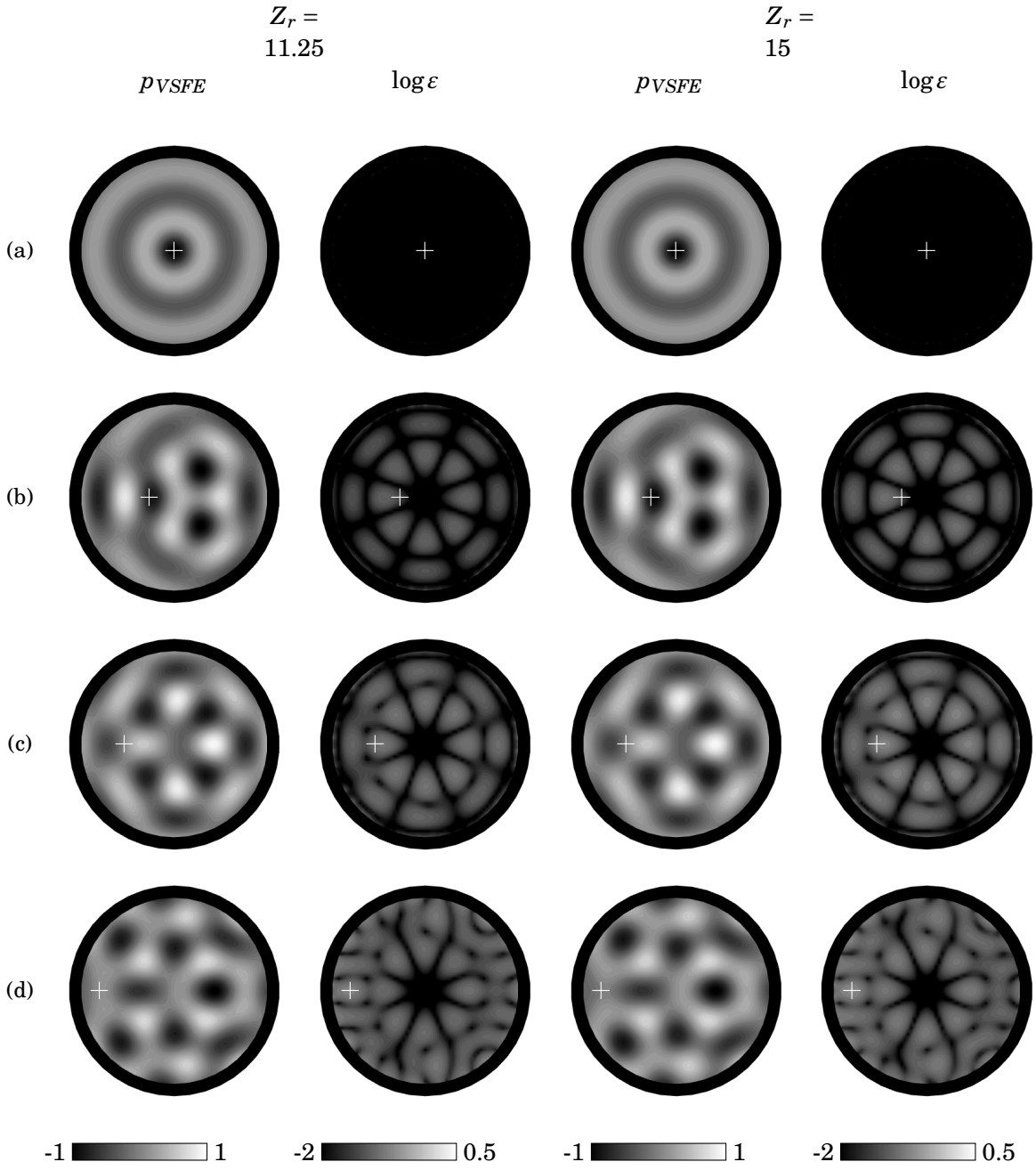

FIGURE 4.21. Simulated VSFE-based analysis field using piezoelectric material properties with off-centred point source and for circular interface r^0 compared with ESWS-based model. Real value of response field p^s and error $\log\varepsilon$ for $r_o = 0$ (a), 0.5 (b), 1 (c),1.5 (d). Results shown for non-dimensional wavenumber $kR = 4\pi$. (Same as in Figure 4.17)

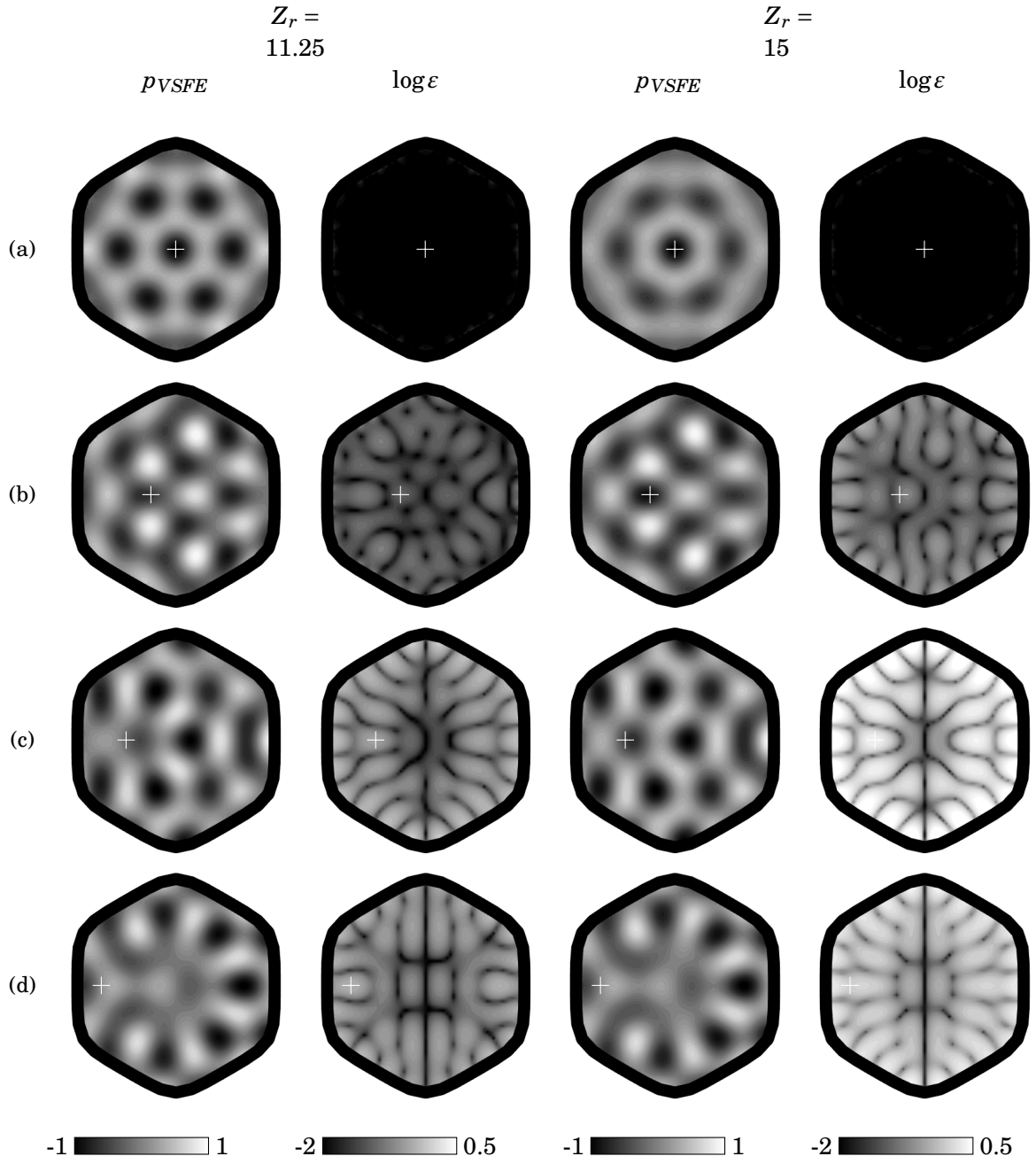

FIGURE 4.22. Simulated VSFE-based analysis field using piezoelectric material properties with off-centred point source and for smooth hexagonal interface r_6^{65} compared with ESWS-based model. Real value of response field p^s and error $\log\varepsilon$ for $r_o = 0$ (a), 0.5 (b), 1 (c),1.5 (d). Results shown for non-dimensional wavenumber $kR = 4\pi$. (Same as in Figure 4.17)

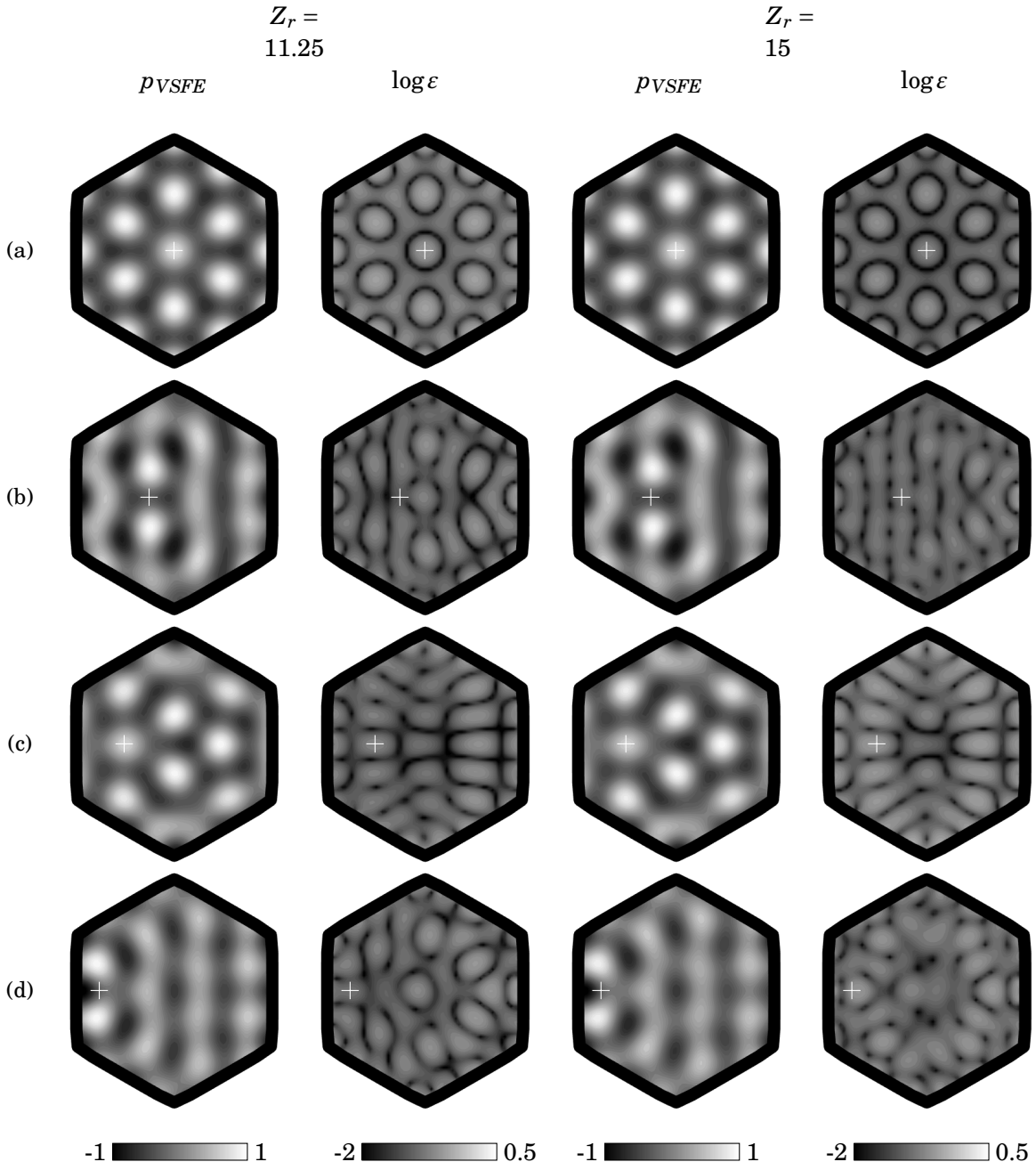

FIGURE 4.23. Simulated VSFE-based analysis field using piezoelectric material properties with off-centred point source and for sharp hexagonal interface r_6^{145} compared with ESWS-based model. Real value of response field p^s and error $\log\varepsilon$ for $r_o = 0$ (a), 0.5 (b), 1 (c),1.5 (d). Results shown for non-dimensional wavenumber $kR = 4\pi$. (Same as in Figure 4.17)

investigation, the ESWS-based solution field and approximation error are computed using the Equations 4.26 and 4.27, respectively.

The VSFE-piezo solution field on three different interfaces is investigated for each one at four off-centred source distance and for two different impedance ratios, as shown in Figures 4.21 to 4.23. Impedance ratio is defined w.r.t. the pressure-wave speed in piezoelectric material over the speed in internal fluid. In this investigation, the lower the error the better the fluid material approximates piezoelectric material model as surrounding media.

For the circular interface, as shown in Figure 4.21, the comparison indicates no significant difference for the error in terms of the impedance ratio. The response field is overall insensitive to the impedance ratio. The field shape compares well with the VSFE-fluid solution field except in Figure 4.17(d) for $r_o = 1.5\lambda$. Furthermore, the error is very low all over domain Ω_i for centred source and at the chamber's centre for any off-centred source distance.

For the smooth hexagonal, as shown in Figure 4.22, the overall response field presents low sensitivity to the impedance ratio. The response to a centred source results in low approximation error throughout the chamber. This means a good agreement between the two models is found for the symmetric analysis field which may be confirmed if compared to the VSFE-fluid solution field presented in Figure 4.18(a). Moreover, errors are high for $r_o > \lambda$ and may not represent the equivalent solution, in particular for the impedance ratio $Z_r = 15$ and $r_o = \lambda$ which results in errors mostly greater than $\log\varepsilon > 0.5$.

On the other hand, the error does not vary significantly with both the impedance ratio and the virtual source position for the sharp hexagonal, as shown in Figure 4.23. The interface response is overall insensitive to the impedance ratio and the results compares well with the VSFE-fluid solution field except for $r_o = \lambda$ in Figure 4.19(c). Although the analysis of the solution field for the sharp hexagonal interface presents similarity with the circular one, the RMS error is no less than $\log\varepsilon_{rms} > -0.85$ in the former and no more than $\log\varepsilon_{rms} < -0.95$ in the latter.

To summarise, the approximation error for various off-centred distance and impedance ratio are shown in Figure 4.25. The VSFE-fluid is in good agreement with the VSFE-piezo solution field with errors up to $\log\varepsilon_{rms}(r_o) \approx 10^{-2.3}$ for virtual sources in the central region except in the sharp hexagonal interface, with errors up to $\log\varepsilon_{rms}(r_o) \approx 10^{-0.7}$. Overall, the solution field VSFE-fluid is less accurate when compared with the results from the VSFE-piezo in the smooth hexagonal interface for impedance ratio close to $Z_r \approx 15$. Therefore, the impedance ratio is a non-sensitive parameter to the approximation error within the impedance ratio range analysed except in the smooth hexagonal interface. This may be justified by the fact that the this specific fluid-fluid interface is highly resonant (see Figure 3.10) whereas in the piezoelectric case it is not (see Figure 4.22). Furthermore, it is hypothesized, a calibration study should reveal alternative threshold for the K_d parameter needed to minimize numerical reflection in the piezoelectric domain.

A simple verification of the VSFE-piezo solution field is done for the circular interface ($\Gamma = r^0$)

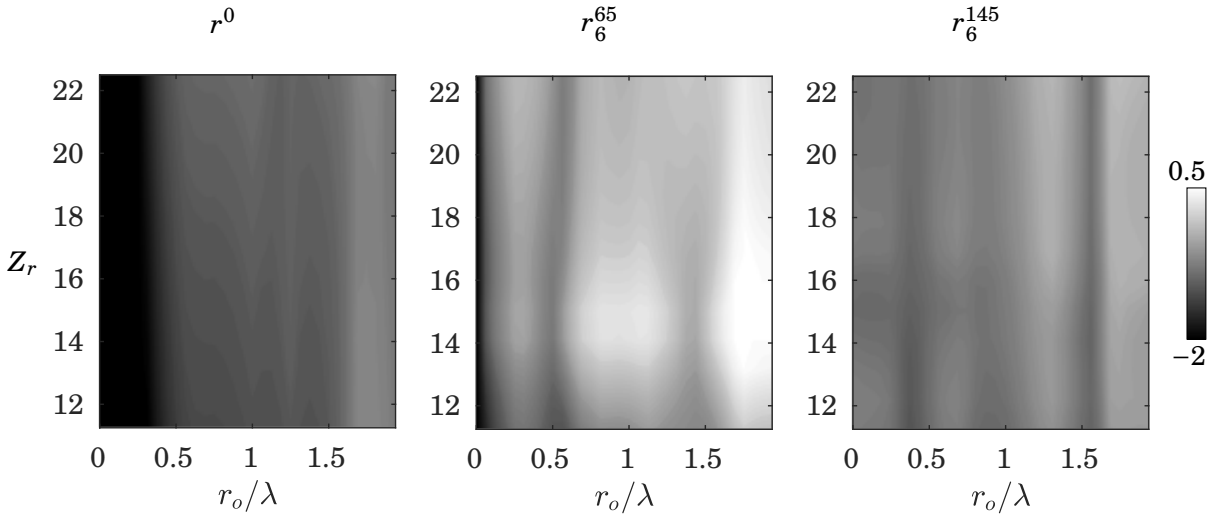

FIGURE 4.24. Simulated VSFE-piezo approximation error of the analysis field for various shapes in terms of the impedance ratio and off-centred point source distance. Results are shown for non-dimensional wavenumber $kR = 4\pi$ and are truncated between -2 and 0.5 in log scale.

to examine the accuracy of the applied ALID truncation method against the standard PML method. For an off-centred virtual source $r_o = \lambda$ and impedance ratio $Z_r = 22.5$, the results yielded an approximation error $\log \varepsilon_{rms} = -1.3$ which is 2.5 times lower than the error compared with the ESWS solution.

These results highlight the current state in the tuning model development. The VSFE-fluid analysis field has been shown to approximate quite well the VSFE-piezo for a centred virtual source and smooth interfaces. Since the goal is to investigate the robustness of these acoustic chambers, a performance rather than an accuracy study is better suited to examine this model further. The next section covers a performance measure of how much a testing function based on internal monopoles remains undisturbed upon wave scattering by using the intermediate model.

4.4 Intermediate performance study

This section presents numerical experiments which determine spatially-dependent performance parameters for the analysis protocol in both fluid-fluid and piezoelectric-fluid interface based on the VSFE model. In the analysis protocol, performance quantifies the effects of confinement geometry in the total field pattern due to a testing function based on internal monopoles. The analysis performance is a mathematical model parameter computed by comparing p^o as the input with the total pressure field $p^T = p^o + p^s$ as the output, where the generating wave is defined by the radiating pressure field p^o and the solution wave is the internally scattered pressure field p^s, as described in Figure 4.2. The intermediate model allows the study of performance for

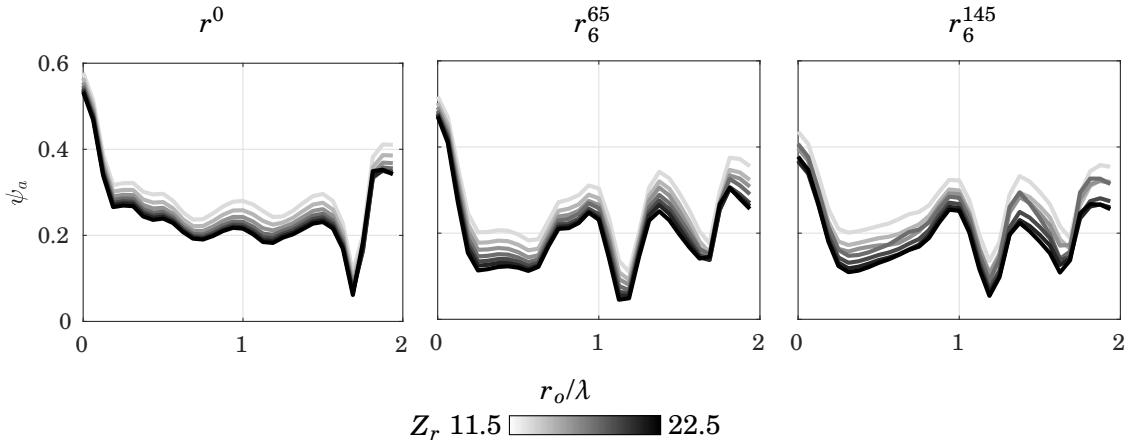

FIGURE 4.25. Simulated tuning analysis performance using piezoelectric material properties for circular and hexagonal shapes in terms of off-centred point source distance. Results are shown for non-dimensional wavenumber $kR = 4\pi$.

alternative material property approximation by adjusting the physical coefficients. The goal of this study is two-fold. First, it examines how the effects of piezoelectric material characterization on the pressure response affects the performance parameters. Them, it quantifies the accuracy of predicting how much a testing function based on internal monopoles remains undisturbed upon wave scattering on fluid-fluid interfaces obtained from VSFE compared with the ESWS for circular and hexagonal shapes.

4.4.1 Intermediate analysis performance

The analysis performance $\psi_a(r_o)$ is defined as the shape correlation between the incident p^o and the total p^T pressure field due to a virtual point source centred at r_o (see Appendix B for details on performance parameters). This performance is a function of the non-dimensional wavenumber, interface shape and acoustic impedance ratio, collectively denoted by the transducer design $T_d = \left(kR, r_N^{\varsigma}, Z_r\right)$ and is given by

$$\psi_a(T_d, r_o) = \frac{\left|p^T(T_d, r_o)^{\dagger} p^o(r_o)\right|^2}{\left|p^T(T_d, r_o)\right|^2 \left|p^o(r_o)\right|^2}. \tag{4.28}$$

The partially mapped analysis performance is obtained by computing this parameter over a radial section of the acoustic chamber in Ω_i. Figure 4.25 shows the asymptotic behaviour of the Intermediate Analysis Performance (IAP) as $Z_r \to \infty$ for each interface shape. This performance parameter measures the mismatch between the shape of the incident and the total pressure field. The lower the analysis performance the more the shape of p^T is altered by the internally reflected field compared with p^o.

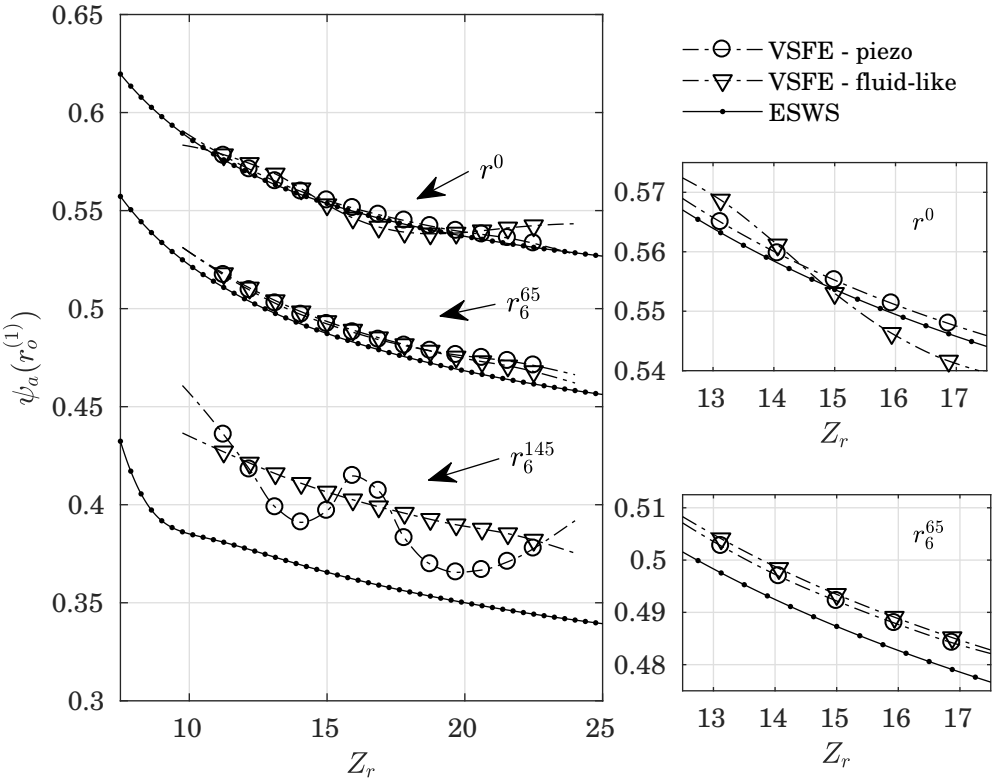

FIGURE 4.26. Simulated VSFE-based analysis performance evaluated at $r_o^{(1)} = 0$ ($\psi_a(r_o^{(1)})$) compared with the ESWS for the circular and hexagonal shapes in terms of acoustic impedance ratio. Inset top right is subfigure for circular r^0 and bottom right for smooth hexagonal r_6^{65} shapes.

The IAP is globally maximum at the centre $r_o = 0$ and locally minimum at $r_o \approx 1.7\lambda$. In this case, maximum and minimum performances are due to constructive and destructive interference between incident and reflected pressure field. This behaviour may also be appreciated on the fluid-fluid interface. In terms of the analysis performance, the circular and smooth hexagonal shape are more robust to changes in the impedance ratio Z_r if compared to the sharp hexagonal shape over the impedance ratio range studied. The IAP derivative with respect to impedance ratio is maximised for the sharp hexagonal shape at $Z_r = 11.5$ and $Z_r = 17.5$ indicating high sensitivity to change of the interface response.

A comparison between the IAP and SAP, obtained from the ESWS model, for a centred virtual point source is shown in Figure 4.26. It is noteworthy the resulting incident pressure field for centred sources ($r_o = 0$) has rotation symmetry for all shapes. Solution field for these results are shown in Figures 4.17(a), 4.18(a), 4.19(a), 4.21(a), 4.22(a), 4.23(a). The results show excellent agreement between IAP and SAP for the circular and smooth hexagonal shape with $\log \varepsilon_{rms} < -2$.

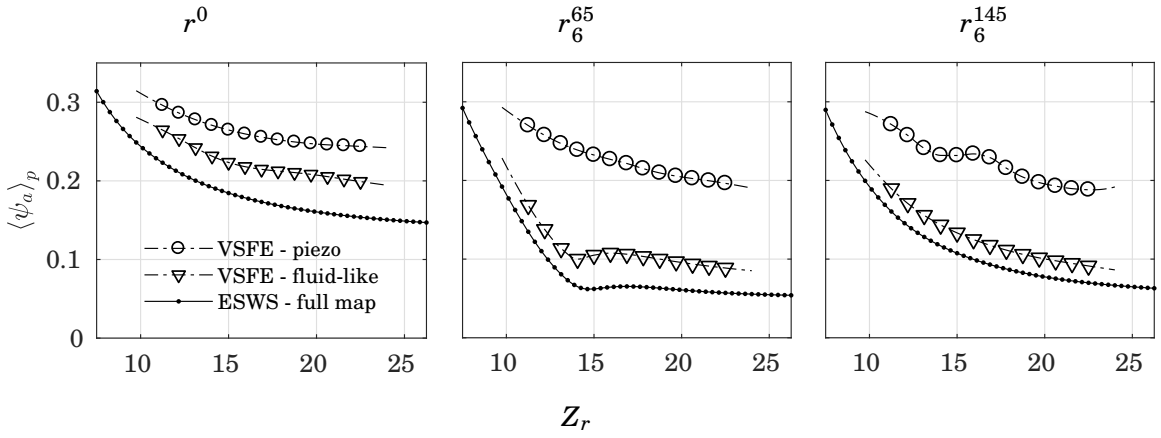

FIGURE 4.27. Simulated VSFE-based spatially averaged analysis performance $\langle \psi \rangle_a$ compared with the ESWS for the circular and hexagonal shapes in terms of acoustic impedance ratio.

For the sharp hexagonal shape the IAP oscillates around the VSFE-fluid analysis performance with $\log \varepsilon_{rms} = -1.4$.

The spatially averaged SAP was suggested as a parameter to measure the efficiency of the interface in withstanding an arbitrary internal incident wave (see Section 3.4.1 for details on SAP). The spatially averaged IAP $\langle \psi_a \rangle$ is given by

$$\langle \psi_a \rangle_p (T_d) = \frac{1}{M} \sum_{n=1}^{M} \psi_a(T_d, r_o^{(n)}) \tag{4.29}$$

and compared against alternative analysis performances as shown in Figure 4.27.

For low impedance ratio, all analysis performances for both hexagonal shapes are very similar indicating a possible asymptotic behaviour. The averaged IAP is showing a strictly decreasing function of the impedance ratio for circular and smooth hexagonal shapes. For a sharp hexagonal shape, a resonant mode results in a local minimum close to $Z_r = 14.75$. However, the SAP does not predict such a resonant mode for r_6^{145} as much as the IAP also does not reflect the local minimum for r_6^{65} at $Z_r = 14.75$.

Some discrepancy on the general behaviour between SAP and IAP is a direct effect of the response field and hence the wave propagation for each material model. The extent of similarity between both models was investigated by examining the accuracy of the simplified model for the centred and off-centred incident field. On the other hand, further study on how much the analysis field is affected by each material model approximation is devised in the Appendix D. This study confirms that each approximation is characterized by an unique pressure field response which cannot be singled out only by analysing their relative differences. Nevertheless, the IAP study suggests that higher VSFE-piezo analysis performance compared with SAP for a given transducer design is due the simplification of the local boundary behaviour by not considering the effects of

incident wavefront direction. One can observe from Figure 4.26 that accurate performance level is obtained for centred point sources. For the off-centred position the acoustic impedance ratio in the VSFE model is over-estimated, as shown in Figure 4.27. This may be because the effective speed of sound in the external domain for oblique incidence is lower than for normal incidence.

4.5 Conclusion

The boundary behaviour of arbitrary shaped piezoelectric-fluid interfaces with characteristic non-dimensional wavenumber $kR = 4\pi$ and impedance mismatch was investigated for the acoustic radiation problem. A intermediate model using a combination of VS and FE methods was developed to solve for acoustic chambers with realistic boundaries. The wave propagation phenomenon was simplified by tuning the coefficients of a piezoelectric material model to that of an equivalent media with similar pressure-wave speed properties. The simplified VSFE-fluid response solution was found to be in good agreement compared to the analytical solution with errors $\log\varepsilon \approx -3$ for 10 elements per wavelength by using standard PML domain truncation and real input source methods. A custom ALID truncation method was developed for dealing with arbitrarily shaped interfaces and calibrated for minimum approximation error which yielded layer length of $l_d = 2.5\lambda$ and absorbing parameter of $K_d \approx 10^2$. A verification for the virtual source method was found to be in good agreement with an analytical model with approximation error of $\log\varepsilon_{rms}(r_o) < -2$ for an average arc length $\langle |L| \rangle \approx \lambda/3$. A validation for virtual sources in the central region has found the VSFE-fluid solution field to be in good agreement with the realistic VSFE-piezo for smooth interfaces but rendered on average low accuracy for the sharp hexagonal interface. For virtual sources elsewhere, the impedance ratio within the studied range was found to be a sensitive parameter to the approximation error only for the smooth hexagonal shape which exhibits resonance on fluid-fluid but not on the piezoelectric-fluid interface. A intermediate performance study revealed while the VSFE-fluid response predicts to some degree the robustness of realistic boundary behaviour, few results need further addressing. For sharp hexagonal interface, an oscillating IAP for centred virtual source as well as local minimum spatially averaged IAP was found with respect to the impedance ratio. These results suggest chamber resonances predicted for alternative material modelling, such as piezoelectric and weakly compressible material are not always correlated.

CHAPTER 5

MONOLITHIC ULTRASONIC TWEEZER DEVICE

In this chapter, the design of the proposed Monolithic Ultrasonic Tweezer Devices (MUTD) is studied by means of realistic model used for simulating the pressure field required for particle manipulation applications. The *kerfless* device concept is presented based on the physical representation of the wave scattering problem solved by the simplified model (see Chapter 3). The herein described TPFE model is proposed as the realistic model (see Figure 5.1) defined by extending the FEM features implemented in the intermediate model (see Chapter 4). Compared with the previous VSFE model, the TPFE allows more control over the electromagnetic field in the piezoelectric layer by setting electric potential on multi-electrodes and therefore

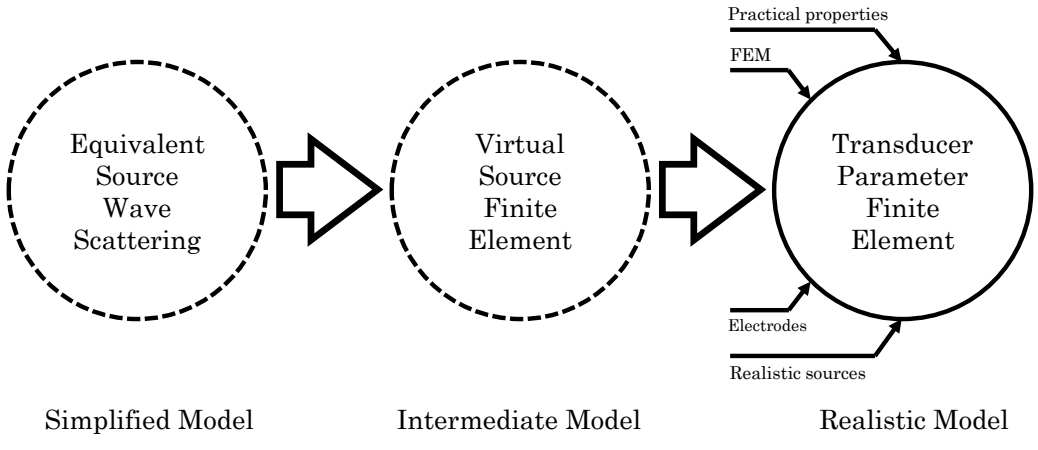

FIGURE 5.1. Schematic diagram for physics-based modelling methodology highlighting the realistic model (TPFE) and main features. Preceded by both the simplified and interface models, the TPFE considers electrodes as an input source and FEM as a boundary formulation.

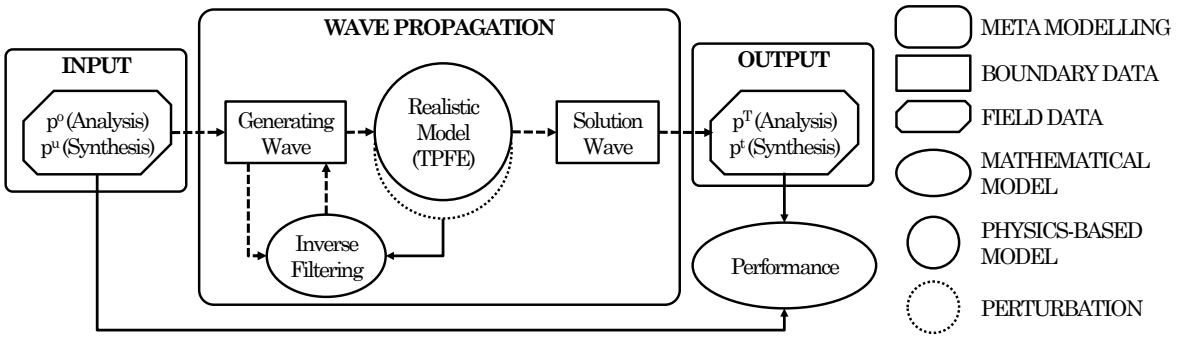

FIGURE 5.2. Schematic diagram of the modelling framework applied to the realistic model. Both the analysis and synthesis protocols are investigated using the realistic model

the generation of target field using more realistic sources. A schematic diagram representing an overview of the methodology applied in the wave propagation study is shown in Figure 5.2 which indicates that both the analysis and synthesis protocols are applied using the TPFE model. According to this diagram, a performance parameter quantifies the correlation of field data by comparing an incident p^o with total p^T field for the analysis protocol whereas the synthesis based performance compares a target p^u with transmitted p^t field upon wave propagation in the device. The analysis protocol studies the theoretical response of a device based on the radiation of internal, single-input source field. The synthesis protocol studies the reproduction of specialized wave fields on a device based on the application of external, multiple-input source field.

A detailed description of this chapter is as follows. Under the physics-based modelling framework represented in the schematic shown in Figure 5.1, the TPFE includes realistic transducer-based sources and practical piezoelectric domain properties. In the analysis protocol, the scattered field inside acoustic chamber is obtained considering external electrical potential as an additional electromagnetic boundary condition which responds to the incident field. Transducer parameters are applied by modelling multiple electrodes based on surface prescribed electric potential boundary conditions. For the synthesis protocol the necessary externally applied electrode voltage is obtained to create a specified acoustic field inside manipulation devices using a TPFE-based inverse filtering formulation (see Section 2.4).

This chapter aims at reducing sensitivity error for high-fidelity, acoustic traps reproduction to perturbation of specified material properties. The search for a robust design of two-dimensional, closed, and piezoelectric devices capitalises on fast solution computed using the simplified model of a wide range but limited set of design cases. The design of feasible ultrasonic fields benefits from the study of robust devices for particle manipulations. Ultrasonic tweezing model is applied to the design of user-defined acoustic field using a novel specialised linear superposition of

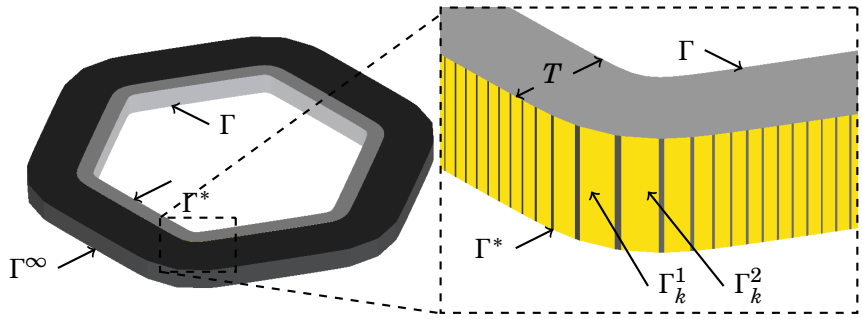

FIGURE 5.3. Design concept of the MUTD. Physical representation showing backing layer (dark grey), piezoceramic material (light grey), electrodes (yellow). The surface Γ represents the interface between transducer and acoustic chamber, Γ^{∞} the external edge of the device, Γ^{*} the boundary between active and backing layer where electrodes are placed on and (Γ_k^1, Γ_k^2) the pair of electrodes.

well-know acoustic vortices.

The outline of this chapter is as follows. The first section is dedicated to explaining the concept of the proposed design and to describing in detail the modelling approaches used to achieve more realistic input data representation. The following section provides preliminary results on the transfer function of the device for a limited range of transducer parameters and the implementation of inverse filtering for the application in the synthesis protocol. The third section presents a performance study on realistic model responses of acoustic chambers for both analysis and synthesis protocols to support the robust design of *kerfless* devices applied to ultrasonic tweezers. Lastly, a closed expression is presented for a proposed user-defined field to spatially extends manipulation capabilities and applied to the TPFE model to assess the performance of large-scale transducer designs .

5.1 The *kerfless* device concept

In this section the claimed features of the MUTD design concept are presented, some preliminary results of pressure field analysis and synthesis shown, and further modelling aspects not covered here are discussed. The MUTD design is proposed an extension of the multi-electrode array transducers for particle manipulation [Kozuka et al., 1996], and as an alternative to the more complex transducer design for ultrasonic particle manipulation based on a circular multi-element array [Grinenko et al., 2012]. The ultrasonic manipulator construction using *kerfless* concept capitalises on a moving radiated sound field over a single element by switching in a controlled manner between activated electrical ports of a multi-electrode transducer, shown in Figure 5.3. These devices are fabricated without mechanically decoupled elements as opposed to the *kerfed* ultrasonic arrays such as the ones for non-destructive evaluation [Drinkwater and Wilcox, 2006].

Many aspects of this novel design including practical boundary conditions, reasonable material

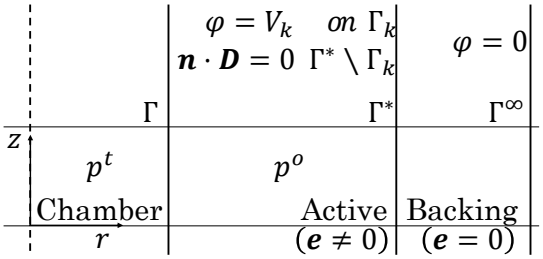

FIGURE 5.4. Schematic system with domain cross-section for the kerfless device concept. The device chamber confines the transmitted pressure field p^t, the active layer generates the incident pressure field p^o by applying the voltages V_k on the electrodes which partially cover the external boundary Γ^* and letting free electrical potential otherwise, the backing layer where only mechanical waves propagates and gets absorbed completely before reaching the boundary Γ^∞.

property representation and device geometry have already been studied in this thesis. However, the lack of practical input sources still needs to be addressed to ensure high-fidelity representation of its transfer function for prototyping purposes. The developed physics-based model assumes a 2D system which does not consider any effect normal to the plane (see Section 2.1) and the MUTD design is proposed as a practical full space representation of such system. Figure 5.3 shows the schematic of the physical representation of the device modelled in this Chapter.

The *kerfless* transducer structure corresponds to the active piezoceramic layer which encloses the fluid chamber. The multi-electrode design is illustrated by the individually addressable electrodes arranged over the external face of the active layer. The internal chamber is filled with aqueous medium with acoustic properties considered similar to liquid water. An absorbing material is located outside the active layer characterized by an increasing damping feature [Drozdz et al., 2006](see Section 4.2). An AL method (ALID) is used in FE-based models for theoretically simulating wave scattering in unbounded media which acts as a backing material in the MUTD designed to avoid spurious resonant modes. Figure 5.4 shows a cross-section of the device representing the layers, pressure field and electrical boundary conditions. The acoustic-structure interaction between the acoustic chamber and the active layer are implied and accounts for the interaction between the elastic waves in the piezoelectric layer with the pressure waves in the fluid layer on the interface Γ (see details on Section 4.2.2).

The transducer depth and wall thickness are relevant design parameter in practical devices based on bulk wave propagation. The depth of the piezoelectric transducer is equal to that of the acoustic chamber which is sealed top-bottom, as in practical devices [Courtney et al., 2013]. Devices with transducer depth greater than the acoustic wavelength can exhibit three-dimensional acoustic streaming mechanism and cause disturbance to particle manipulation [Bernassau et al., 2014]. The dimension in the vertical direction is left undefined for the purpose of not modelling any physics behaviour in the direction perpendicular to the transversal plane (vertical direction).

Limitations to this approach would be that practical devices are not capable of holding particles against gravity [Courtney et al., 2011] or any non-negligible fluid dynamics phenomenon due to lateral effects. The thickness T of the active layer, as shown in Figure 5.3, is kept constant throughout the development of the TPFE model. The wall thickness resonant frequency, given by the longitudinal wave speed over the thickness, is often used as a piezo ceramic parameter for defining the operating frequency. In terms of off-the-shelf piezoelectric ceramics standards the closest shape and application case to the proposed MUTD are tubes operating at wall thickness frequency.

The construction of electrical ports in MUTD is based on individually connecting each addressable electrode placed on the outer surface of active layer. Details on the placement of the electrodes are highlighted in Figure 5.3 showing each electrode extending perpendicularly top to bottom on the surface between the active and passive layer. In the TPFE, the electrodes characteristic is attained by representing them as boundary conditions applied to a set of segmented curves defined on the outer surface of active layer. The next subsection is dedicated to describing in detail these boundary conditions by comparing it with the ones defined in the tuning model (see Chapter 4).

5.1.1 Boundary conditions representation

This section describes in detail the boundary condition representation and the transducer parameter conversion method applied to TPFE model. High-fidelity numerical modelling using FEM is an on-going research topic in engineering science whereby a compromise is sought between accuracy and computational speed. As the goal is to develop the closest agreement for the response characteristics of a practical device, this section is dedicated to describing the development of boundary conditions applied on electrodes featured in MUTD. The multi-electrode for array transducers is the core strategy adopted in the *kerfless* design. The developed geometrical features and input data aims at robust design modelling approach to design of ultrasonic tweezers devices.

The electrical characteristics of practical electrodes defined for FE analysis is a specialized field of study in coupled field systems that bridges the boundary representation in piezoelectric devices. Some simplified definitions of electrode modelling has already been discussed in this thesis (see Section 4.2.2) which provides the basis for understanding the role this type of electrical port has in transducers. However, to describe it as an input for transduction and further radiation into the acoustic field it is paramount to define its physical representation and the electrical potential as a source load. The geometrical extent of each separate electrode shown in Figure 5.3 is described as a parametrized ratio over the boundary Γ as defined by Equation A.6 in Appendix A.

The physics in the active layer is governed by electroelastic medium which is responsible for producing an acoustic field if an electric potential is applied, and vice versa (see Sections 2.5.2 and 4.1.1 for details on electroelasticity). The generated acoustic field is transmitted to the adjacent layers through each of its boundaries Γ and Γ^*. The pressure field propagated into the fluid

chamber, termed as transmitted field p^t, is the output of the synthesis protocol which aims to match with a target field p^u by applying the computed electrical potential over the electrodes. The pressure field propagated into the backing layer gets absorbed where only mechanical waves propagate. This is implemented in the outermost layer between Γ^* and Γ^∞ by setting the piezoelectric coupling parameter in the material modelling to zero $\mathbf{e} = 0$, as shown in Figure 5.4, effectively approximating it to transverse isotropic (see Section 4.1.2).

The mathematical aspect of the electrode modelling applied on the TPFE model which is based on the terminal approach differs from the configuration adopted in the VSFE. In VSFE, the electrical port is defined as a zero charged surface whereas for the TPFE the terminal is configured as a floating potential or voltage input. The floating potential allows the electrical potentials to vary as independent parameters for the electrical ports defined along the boundary which is determined by the FE model in response to the pressure field of an internal source. The voltage input configuration allows the electrical potential to be prescribed as input sources for each electrical port along the boundary. This applied boundary condition extends the previous approach by one dimension from a singular point to a segment of a curve in space. In the following, the method applied to describe the input data that accounts for the area of influence under which the electrical input is defined.

The aim of representing the transducer's boundary conditions is to define a source load for the TPFE as the equivalent acoustic point source implemented in the VSFE (see Section 4.2.3). The goal of this realistic model is to derive a relationship between both source types which provides pressure field results similar to the VSFE model. The sources of the MUTD are defined in terms of the applied voltage on the electrical ports as a boundary condition. A simple linear rule is proposed as a converting method between pressure and its derivative into electrical potential. The applied methodology is not exhaustive as much of the focus of this chapter is on developing a realistic model for practical acoustic radiation and not to compare different methods for achieving best accuracy. Representing these above mentioned conditions in a closed expression using an equivalent source method based on the electroelastic Green's function requires further research. An interested reader may refer to Berndt and Sevostianov [2015] for expressing electromechanical fields in closed form in terms of point electric charge and point force.

A terminal boundary condition is applied to a segmented boundary set Γ_k and provides an electrical connection which corresponds to the ideal electrode placed externally on the transducer surface. For initially building the TPFE model, this terminal is set to a floating potential group which assigns a unique potential to each group of contiguous boundary segments [COMSOL AB, 2015]. The floating potential group configuration is eventually substituted with a prescribed voltage condition which specifies the applied electrical potential on the electrode for the application of the transducer parameters. This terminal boundary condition is applied in addition to the already defined electrostatic boundary conditions in the solution of the VSFE model (see Equation 4.18).

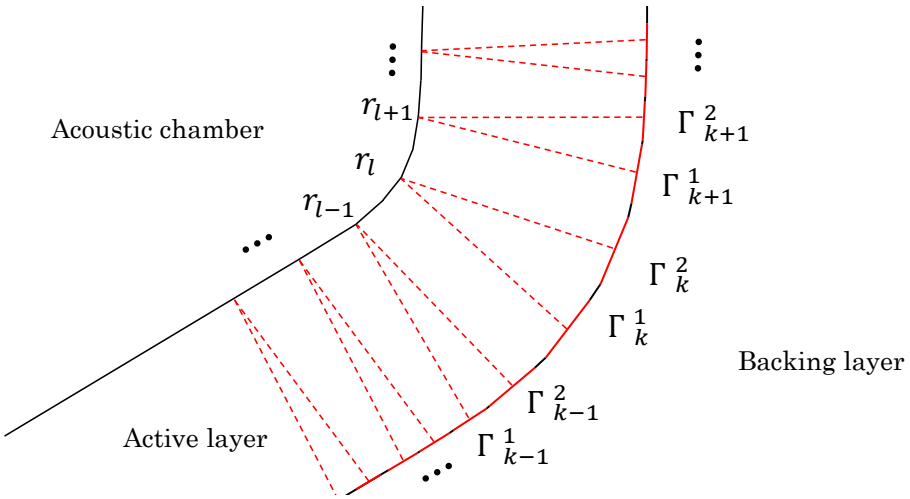

FIGURE 5.5. Segmented boundary set Γ_k highlighting the dual terminal approach. A pair of electrodes (Γ_k^1, Γ_k^2) (red continuous line) on the Γ^* is represented for each co-located point r_l on the boundary Γ. Dashed red lines represent the geometrical relationship between the electrodes and co-located points.

To summarise, in the VSFE a zero charge was applied on the boundary Γ and zero potential on Γ^∞, as shown in Figure 5.4. On the other hand, in the TPFE the zero charge boundary condition is only applied on segments which are not covered by the electrodes (i.e. $\Gamma^* \setminus \Gamma_k$) whilst ground is applied on Γ and the floating potential on Γ_k. The equations regarding all electrostatic boundary condition in the solution of the MUTD model is as follows

$$\varphi = \begin{cases} 0 & \text{on } \Gamma^\infty \\ V_k & \text{on } \Gamma_k, \end{cases} \tag{5.1}$$

and

$$\mathbf{n}\cdot\mathbf{D} = 0 \qquad \text{on } \Gamma^* \setminus \Gamma_k, \tag{5.2}$$

where φ is the electric potential and V_k are the electrode potentials. The Equation 5.1 defines the set of boundary condition that comprises the first step to achieve the realistic modelling. This floating potential boundary condition can be regarded as an added electrical potential sink effect that allows additional disruption to the radiation problem. The MUTD model is almost ready for simulation of practical operating devices as it features this boundary segmentation approach, not present in previous models, but lacks setting a prescribed value for the electrode potentials.

A dual terminal approach applied to the boundary Γ_k^n, for $n = 1,2$ is shown as segmented electrodes in Figure 5.5. For each acoustic point load defined at r_l two side-by-side electrodes are defined on the TPFE. The dual approach is used to achieve equal number of independent sources in all three developed physics-based models. That is, for each pair of secondary sources (i.e. one monopole and one dipole) collocated on the boundary of the cavity there are two electrodes

confined within the segment of influence defined by each source. Such terminal configuration complies with the converting method used in the transducer parameter application. This dual configuration of the boundary conditions is defined as the pair $V_k^n = (V_k^1, V_k^2)$ on either segment Γ_k^n differing from single terminal approach by considering a gap of zero electric charge between the two individually addressable electrodes.

The dual terminal approach differs from the zero electric charge because the electrodes act as a source of electrical discharge whose strength depends on the applied set of secondary sources. According to the FE solution in Equation 2.44, the reaction charge $\{\mathbf{q}\}_e$ acting over each electrode are solved for so the electrical potential V_k^n on the segmented boundaries Γ_k^n are constant through each segment. The TPFE-based response for the scattered pressure field is now computed for the analysis protocol to illustrate how the solution field is affected by the dual terminal boundary condition.

5.1.2 Realistic model validation

The realistic model validation consists of a series of comparisons between the scattered pressure field p^s for the analysis protocols computed using both the TPFE and VSFE models. The goal is to compare quantitatively the realistic model results against the tuning model. The analysis of pressure field is achieved by solving the FE-based response to a virtual internal point source defined inside the acoustic chamber (see Section 4.2.3). To identify the effect of the electrical potential terminals in the analysis of pressure fields each solution using the realistic model is shown accompanied by their correspondent incident field and approximation error compared with the tuning model. The approximation error is defined as

$$\varepsilon = \frac{p_{TPFE} - p_{VSFE}}{max\left(p_{TPFE}\right)}. \tag{5.3}$$

The error between responses computed using TPFE and VSFE as a result of the electrical potential noise in the active layer owing to the terminals. A partially mapped parameter is assessed within a line segment between the origin of the coordinate system and the closest boundary (see Appendix B) using the spatial average $\langle\varepsilon\rangle$ for each solution comparison in terms of the virtual source positioning. This approximation error is expected to result in the same order of magnitude compared to the ones presented in the intermediate model validation (see Section 4.3.3). To illustrate the realistic model validation numerical experiments are conducted for an acoustic impedance ratio[1] of $Z_r = 22.5$, for fixed mass density ratio $\rho_r = 7.5$, and two different design shapes Γ, namely circular r^0 and sharp hexagonal r_6^{145}. The wall thickness of the active layer is fixed to $T = 1.35\ c_f/f$, for an excitation frequency $f = 2.625$ MHz and $c_f = 1482$ m s^{-1} [John D. Cutnell and Johnson, 2014] is the pressure-wave speed of the fluid, for this example and all subsequent simulations.

[1]The acoustic impedance ratio is defined as $Z_r = \rho_r c_r$ in terms of the mass density ratio ρ_r and pressure-wave speed ratio c_r between acoustic chamber and active layer (see Section 4.1 for details) and not to be confused with electrical impedance at resonant frequency.

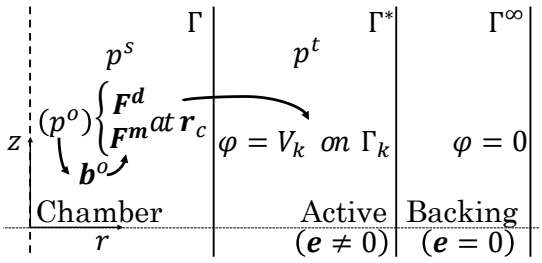

FIGURE 5.6. Schematic of the system with domain cross-section for the analysis protocol on the TPFE model using virtual sources as internal incident wave. The incident $\mathbf{b}^o$ boundary data is computed from the incident p^o and the load $\mathbf{F}^m$ and $\mathbf{F}^d$ is applied as weak contribution at the nodes at $\mathbf{r}_c$. The scattered p^s and transmitted p^t pressure field, and the piece-wise constant electrical potentials V_k on Γ_k are computed using FE solvers.

Figure 5.6 shows the system set up for the analysis protocol employed on the TPFE model. This cross-section shows schematically how the voltages V_k for the electrodes on Γ_k responds to the applied monopoles $\mathbf{F}^m$ and dipoles $\mathbf{F}^d$ and therefore to the virtual sources for a given incident pressure field p^o. The simulation of the device operation, described as synthesis in the next section, is implemented using the modelling framework step described as the synthesis protocol (see Figure 5.2). In operation, the applied voltages are indirectly considered as sources of acoustic radiation whereas in the analysis step the voltage responses are considered the reverse effect.

A flow diagram is presented in Figure 5.7 showing the logic sequence of calculations for the analysis protocol implemented for the validation of the realistic model. COMSOL applies the necessary monopole and dipole load from the VS method to reproduce the incident wave at the co-located points $\mathbf{r}_l$ and computes the scattered field p^s and the voltages responses V_k. An example of pressure field comparison between p_{TPFE} and p_{VSFE} for an off-centred point source in a circular boundary is shown in Figure 5.8. The results show that the pressure response to an internal point source using both models are in good agreement. The electric field radiates in unbounded media outside Γ for the p_{VSFE}, whereas for the p_{PTFE} it is confined within the active layer with electrodes on Γ^* acting as electric potential sink. These electrical boundary conditions affect the analysis field by generating acoustic noise back into the acoustic chamber due to piezoelectric effects.

Figure 5.9 shows TPFE-based analysis field for the circular and hexagonal shape. These figures show a series of solutions in terms of the distance of the applied point source alongside the respective approximation error. The validation region is determined by $\mathbf{g}_N^{\zeta}(\xi_a)$ for a distance $\xi_a = 4\pi^2/3k$ away from the boundary Γ (see Equation A.7). The response field may be compared with results from the ESWS model in Sections 3.3 and the VSFE model in Section 4.3. It can be seen from the results that approximation errors for response to sources in the centre (a) are generally lower for circular than compared with sources elsewhere and present no relevant trend

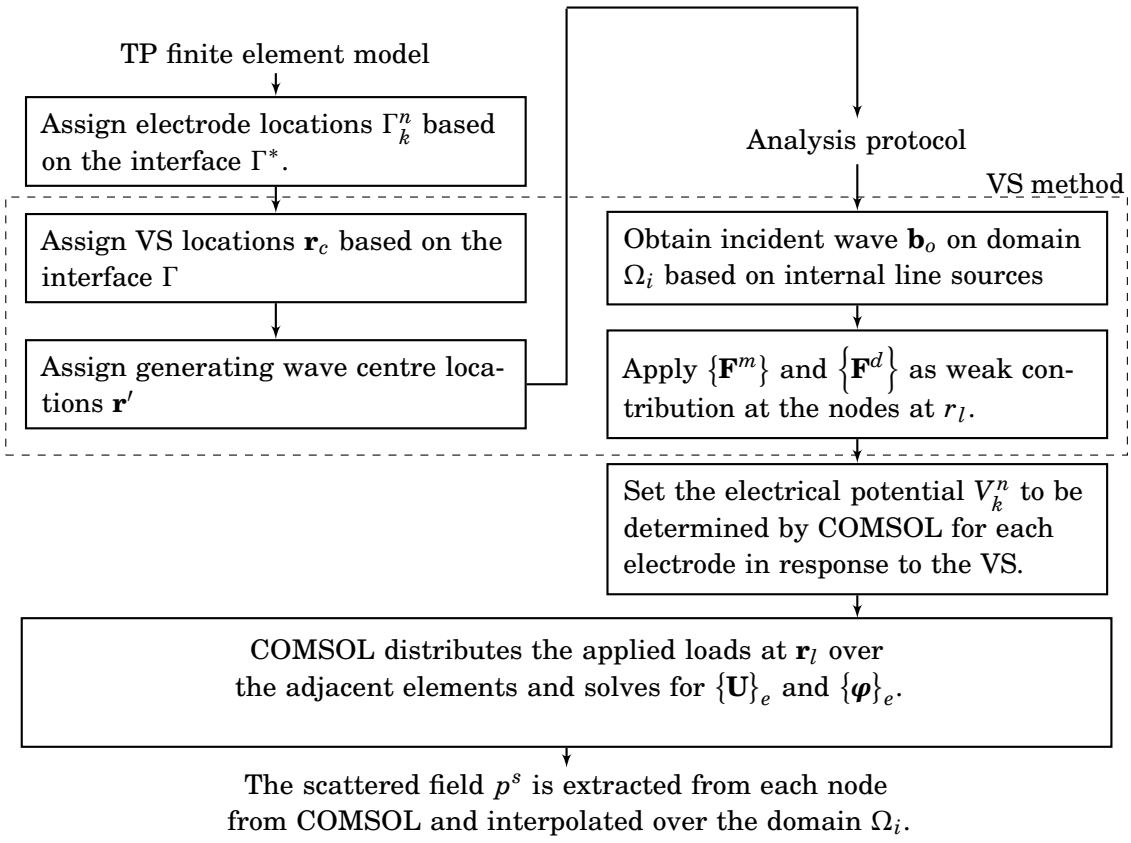

Figure 5.7: The TPFE model flow diagram showing the logic sequence of calculations for the analysis protocol. The process stages on the analysis protocol is computed using a common mathematical model of the VS method implemented in the VSFE model. COMSOL applies the loads at the co-located points and computes the scattered field and the voltages responses.

for the hexagonal boundary. The effects of the terminals on the response in a central area are minimal for circular and indifferent for the hexagonal boundary.

The approximation error as a function of the virtual source distance r_o for the considered VSFE is shown in Figure 5.10. The results show the approximation errors are reasonably low ($-2 < \langle\varepsilon\rangle < -1$) for the majority of the domain analysed. The VSFE model is in excellent agreement with the TPFE across the central region $r_o < 0.125$ of circular shape where errors are lower than $\langle\varepsilon\rangle < -2$. Errors above $\langle\varepsilon\rangle > -1$ can be seen in both hexagonal and circular shape with source distance close to the chamber interface ($r_o > 1.75$). The overall effect of the electrodes on disturbing the analysis of pressure fields depends on the spatial gradient of the incident boundary data. Furthermore, it was demonstrated (see Section 3.5) that the more the analysis performance varies the more the pressure field reproduction is disturbed with system perturbation. This suggests that the more the analysis performance varies due to electric potential sink phenomenon the less robust the corresponding transducer design could become.

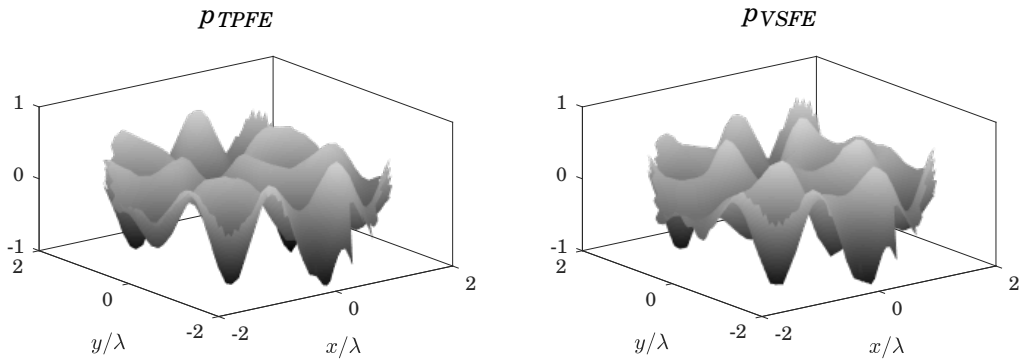

FIGURE 5.8. Example of simulated TPFE-based compared with the VSFE-based analysis field for an off-centred virtual source $r_o = 1.5\ \lambda$. Results for $kR = 4\pi$,$\Gamma = r^0$ and $Z_r = 22.5$. The pressure field is normalized with the maximum magnitude inside the validation region for a distance $\xi_a = 4\pi^2/3k$ away from Γ, shown truncated between -1 and 1 and for $\langle |L| \rangle = \lambda/3$.

5.1.3 Further model evaluation

This section presents a discussion of features of the TPFE model such as boundary condition representation and practical design assessment that needs further investigation.

The backing layer present in the MUTD, modelled using the ALID method, is a feature in the FE models intended to render radiating solutions by satisfying the Sommerfeld radiation condition (see Section 2.1). However, this theoretical condition is not necessarily satisfied by a practical backing layer since an anisotropic absorbent material requires a complex manufacturing process. A practical solution is suggested as a backing material out of tungsten-loaded epoxy. While one of the goals of this thesis is to investigate the realistic model approach to design MUTD, practical material absorption modelling for transducer manufacturing is a topic of research of its own.

Another major concern is to model electromagnetic boundary conditions so the noise due to the dual terminal configuration is minimized and a good agreement between electromagnetic fields on both intermediate and realistic models is obtained. Currently, in the TPFE model, the inner and outer surface of the active layer are both modelled using ground and floating potential boundary conditions whereas the in the VSFE they are set to zero charge and continuous through the outer layer, respectively. This means that a real device would only be best approximated to simple models if such boundary conditions were imposed by design and not just due to simplifying assumptions.

Additionally, in the VSFE coupled electroelastic waves are modelled within the absorbent layer whereas in the TPFE only mechanical waves propagate in the outermost layer. In that sense, a suitable methodology would be setting the domain configuration for the intermediate model as defined in the realistic model but keeping the virtual sources as boundary condition

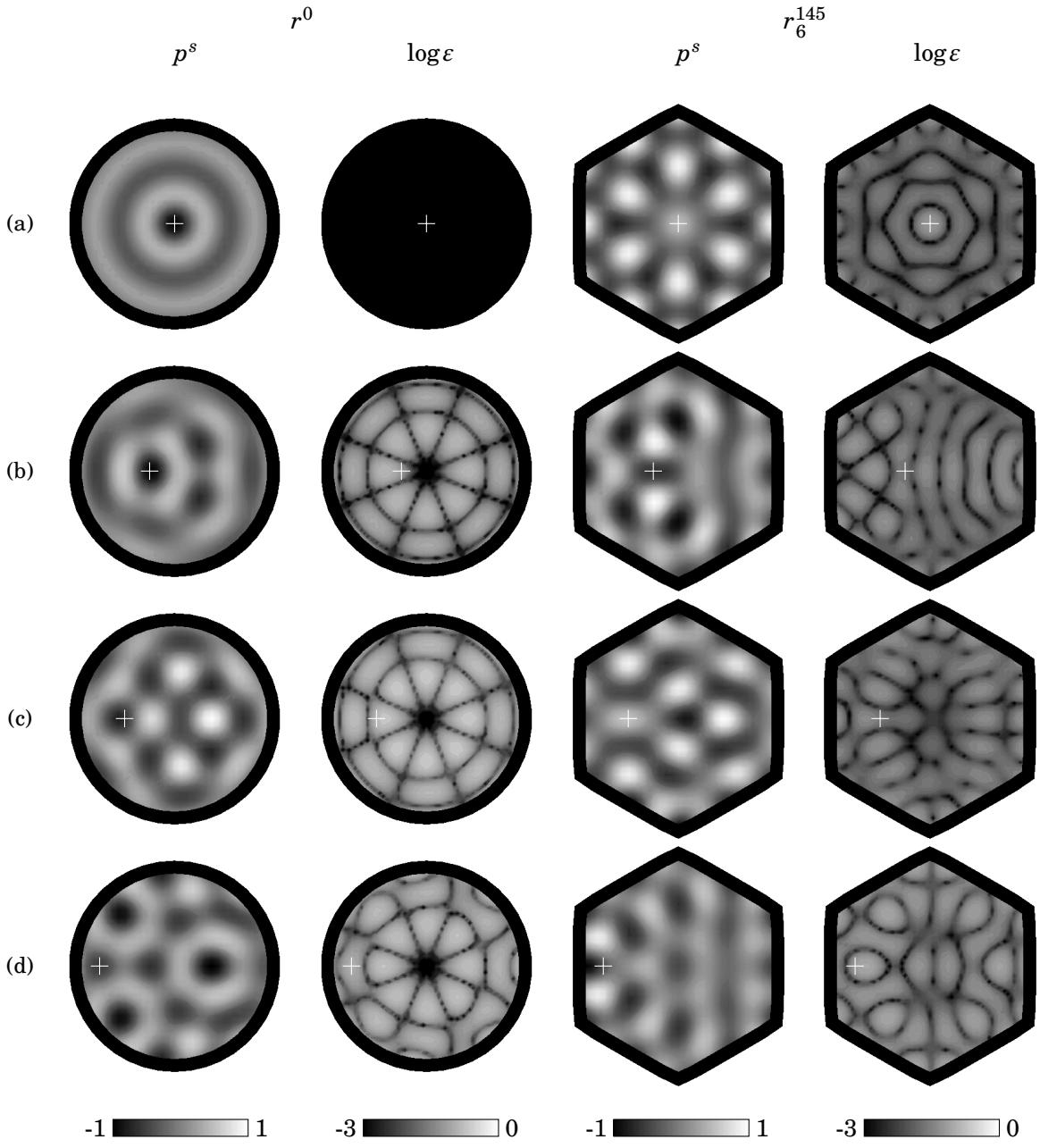

FIGURE 5.9. Simulated TPFE-based analysis field both the circular and hexagonal shapes with off-centred point source compared with VSFE model. Real value of scattered field p^s obtained from TPFE and approximating error $\langle\varepsilon\rangle$ for $r_o = 1.5$ (a), 1 (b), 0.5 (c),0 (d). The approximating errors ε obtained from Equation 5.3 are shown in log scale. White cross represents the line source position r_o

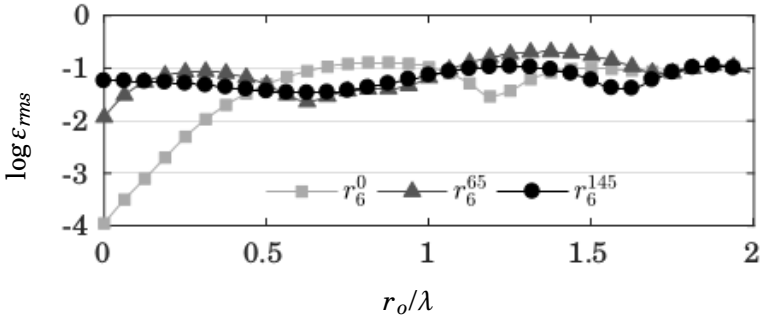

FIGURE 5.10. Simulated TPFE-based approximation error $\log \varepsilon_{rms}$ for the analysis field for two hexagonal shapes (r_6^{65} and r_6^{145}) and circular (r^0) shape for acoustic impedance ratio $Z_r = 22.5$. The RMS of the approximation error ε obtained from Equation 5.3 is plotted in log scale.

approach. This would require further studies on the effects of partially coupled electroelastic domains over both the parameter and performance extraction techniques developed here.

5.2 Transducer parameter application

In this thesis, the transducer excitation is defined as the applied complex harmonic electrical potential V_k^n and considered as an operating independent variable. For the multi-electrode array concept, this definition assumes the transducer acoustic response is dependent on the whole system dynamics hence the need for solving the realistic model of MUTD.

The pressure field reproduction using the TPFE model in combination with the inverse filter technique (see Section 2.4) where the transducer excitation V_k^n are indirectly considered sources of acoustic radiation and the harmonic excitation response on the interface are the control data. A transfer function is defined between the electrical potential applied to the electrodes of the transducer and the pressure and derivative on any control surface outside the control region in order to generate the desired pressure landscape. The transducer transfer function T_{kl}^n from the source data to the control data is computed that relates V_k^n applied on the segments Γ_k^n to the boundary data at the points $\mathbf{r}_l$. An approximation to the transmitted pressure field with smallest average squared error is solved to reproduce a target pressure field as a linear superposition of the response of each individually excited transducer parameter. It is noteworthy the transfer function $\mathbf{T}^n$ of transducers placed along the boundary exhibits rotation symmetry due to the interface symmetry and time-reversal symmetry due to the dual terminal configuration. These symmetries reduces the number of simulations required to compute all components of the transfer function from $2n_p$ to n_p/N.

The applicability of transducer excitation in the radiation of transmitted pressure field p^t into the acoustic chamber Ω_i is demonstrated for the design shapes r_6^{145} and r_5^{145} and for the acoustic

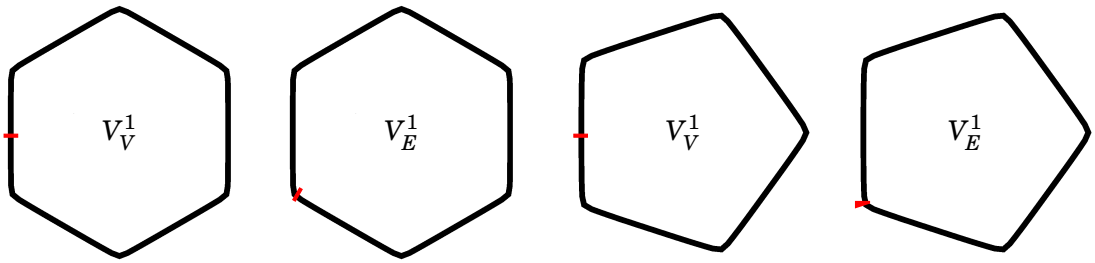

FIGURE 5.11. Diagram showing electrode labelling depending on the relative positioning of its effective area around the boundary for two symmetric boundaries. Position of vertex and edge subscripted V_V and V_E are depicted by a red patch on the active layer for the hexagonal r_6^{145} and pentagonal r_5^{145} design shapes.

impedance ratio $Z_r = 21$ and $Z_r = 25.6$. In these simulations the total number of electrode pairs and control points is set to approximately three times the number of wavelengths around the circumscribed circle $n_p \approx 3kR$. Note the size of the transducer in this example is given by the non-dimensional wavenumber $kR = 10\pi$ and therefore $n_p = 96$, which has a circumscribed circle of radius $R = 4.9$ mm, for an excitation frequency $f = 2.625$ MHz and the speed of sound in water $c_f = 1482\ \mathrm{m\,s^{-1}}$.

The brief description of this Section is as follows. The transfer function is obtained by applying single transducer parameter using the TPFE model. The transmitted pressure field is recreated based on the boundary data obtained from FE in order to investigate the accuracy of the forward TPFE model. The inverse filter is defined based on the computed transfer function of a perturbed system and the equation for the synthesized pressure field is derived. The synthesis protocol is formulated applied to synthesize acoustic vortices and further investigate the effect of tolerances in the matrix inversion process. Lastly,

5.2.1 Transducer transfer function

The transfer function is computed by solving each transfer function individually such that both the pressure p and normal derivative v at $\mathbf{r}_c$ are thus given by a summation as in

$$p(\mathbf{r}_c) = \sum_{k=1}^{N} \left(T_{kl}^{1p} V_k^1 + T_{kl}^{2p} V_k^2 \right) \tag{5.4}$$

$$v(\mathbf{r}_c) = \sum_{k=1}^{N} \left(T_{kl}^{1v} V_k^1 + T_{kl}^{2v} V_k^2 \right), \tag{5.5}$$

where the superscript p and v relates to their respective field parameters. Figure 5.11 shows the configuration for two key transducer parameter V_V^1 and V_E^1 where E stands for "edge" with $k = 1$ and V for "vertex" with $k = n_p/(2N)$. The Equations 5.4 and 5.5 are then assembled into a matrix

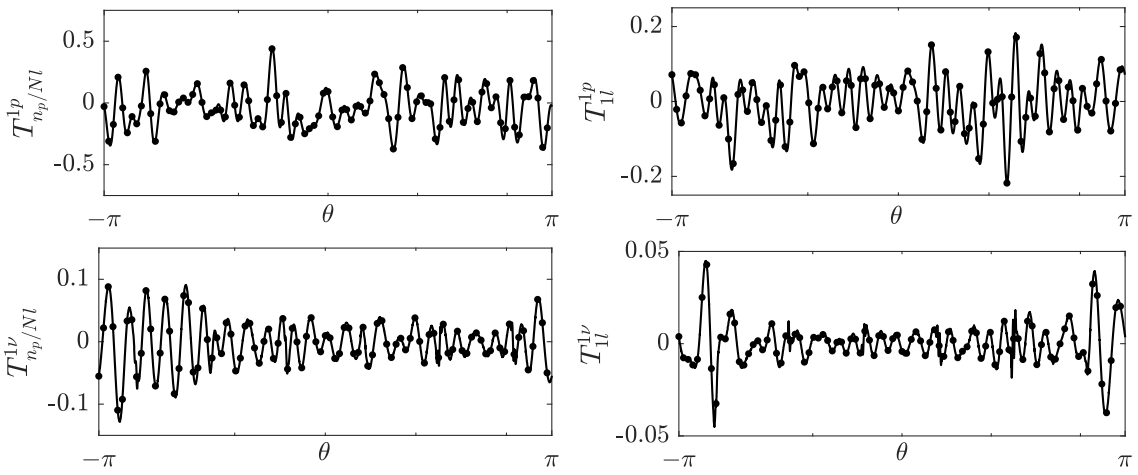

FIGURE 5.12. TPFE-based simulation of transfer functions obtained from the transmitted field at the interface due to a transducer excitation at the vertices and edges of the hexagonal shape. Lines represent data extracted from interface and dots are the elements of vectors T^{1p}_{El}, T^{1p}_{El},$T^{1\nu}_{Vl}$, and $T^{1\nu}_{Vl}$ for transducer design ($kR = 10\pi, r_6^{145}, Z_r = 25.6$).

equation given by

$$\mathbf{b}_i = \begin{bmatrix} \mathbf{T}^{1\nu} & \mathbf{T}^{2\nu} \\ \mathbf{T}^{1p} & \mathbf{T}^{2p} \end{bmatrix} \times \begin{bmatrix} \mathbf{V}^1 \\ \mathbf{V}^2 \end{bmatrix}, \tag{5.6}$$

where each $\mathbf{T}^{np}$ and $\mathbf{T}^{n\nu}$ represents the transfer functions in the matrix form between the vectors $\mathbf{V}^n$ and the pressure $\mathbf{p}$ and the derivative $\boldsymbol{\nu}$, respectively. A matrix $\mathbf{T}_{TP}$ in general form is defined for the application of inverse filtering technique where Equation 5.6 can be rewritten into the equation to consider any number of electrodes per control points

$$\mathbf{b}_i = \mathbf{T}_{TP} \times \begin{bmatrix} \mathbf{V} \end{bmatrix}, \tag{5.7}$$

where $\mathbf{V}$ is the generalized transducer parameter vector. One can recreate the transmitted pressure field in the internal domain Ω_i by multiplying the boundary data by the propagator matrix as in

$$p^t = [\mathbf{P}]\,\mathbf{T}_{TP}\mathbf{V}, \tag{5.8}$$

where p^t is the transmitted pressure field and $[\mathbf{P}]$ is a propagation matrix given by Equation 3.25 which computes the pressure field that propagates into the domain Ω_i from the internal boundary data $\mathbf{b}_i$. Figure 5.12 shows the transfer functions in terms of θ over the extracted on the interface Γ due to excitation of a single electrode with $\mathbf{V} = (V_V^1, 0, \ldots, 0)$ and $\mathbf{V} = (0, V_E^1, \ldots, 0)$.

Figure 5.14 shows a series of graphs representing p^t based on the radiated solution obtained using Equation 5.8 and the approximation error ε^* with respect to the solution obtain directly

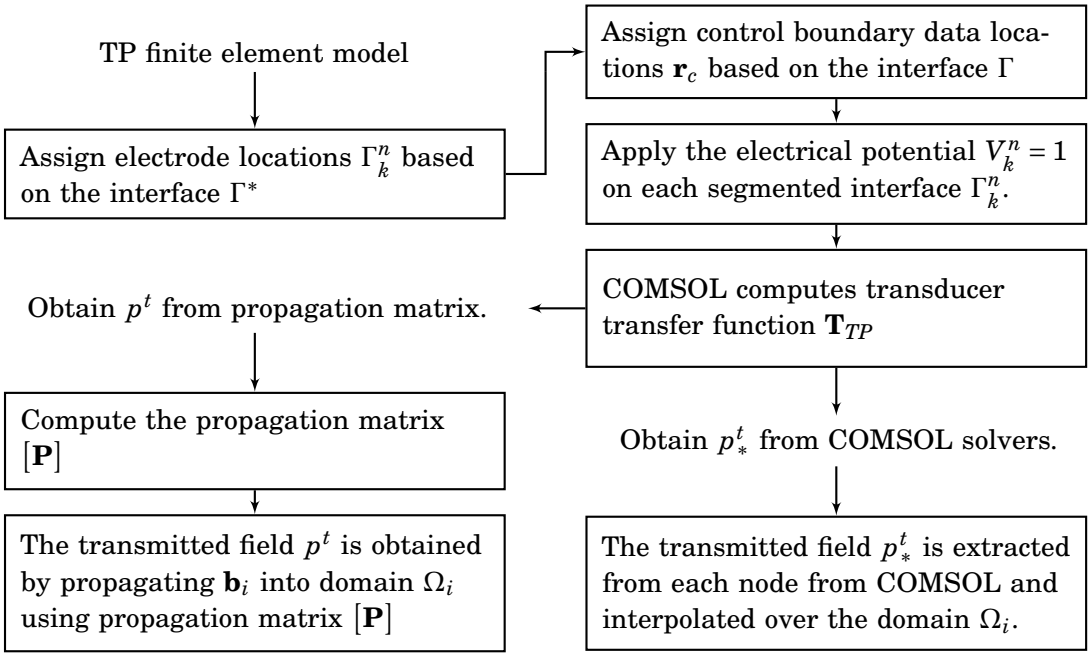

Figure 5.13: The TPFE model flow diagram showing the logic sequence of calculations for recreation of the transmitted pressure field using both FE solvers and propagation matrices. This process shows the difference between the two methods is in how the data is extracted from the FE to obtain p^t either by propagating the boundary data $\mathbf{b}_i$ or extracting field directly from the FE domain.

from FE solver defined as

$$\varepsilon^* = \frac{p_*^t - p^t}{max\left(p^t\right)}. \tag{5.9}$$

where p_*^t is transmitted pressure field. Variation to the pressure amplitude between transducer responses is not appreciated in these results but may be examined from Figure 5.12. These results show the TPFE-based transfer function $\mathbf{T}_{TP}$ propagates the transmitted pressure field in good agreement with the FE solver. Low accuracy in propagation is seen close to the interface due to the point source singularities and in high-pressure regions. The impedance ratio plays an important role in defining the transfer functions especially because the thickness of the transducer is fixed to half wavelength for $Z_r = 21$.

The accuracy investigation for a single excitation is paramount to the reproduction of target pressure field p^u which is that of a Bessel beam and is given by Equation 2.57. The inverse filtering technique introduces numerical error relative to the propagation of a single transducer which is a topic of the next subsection.

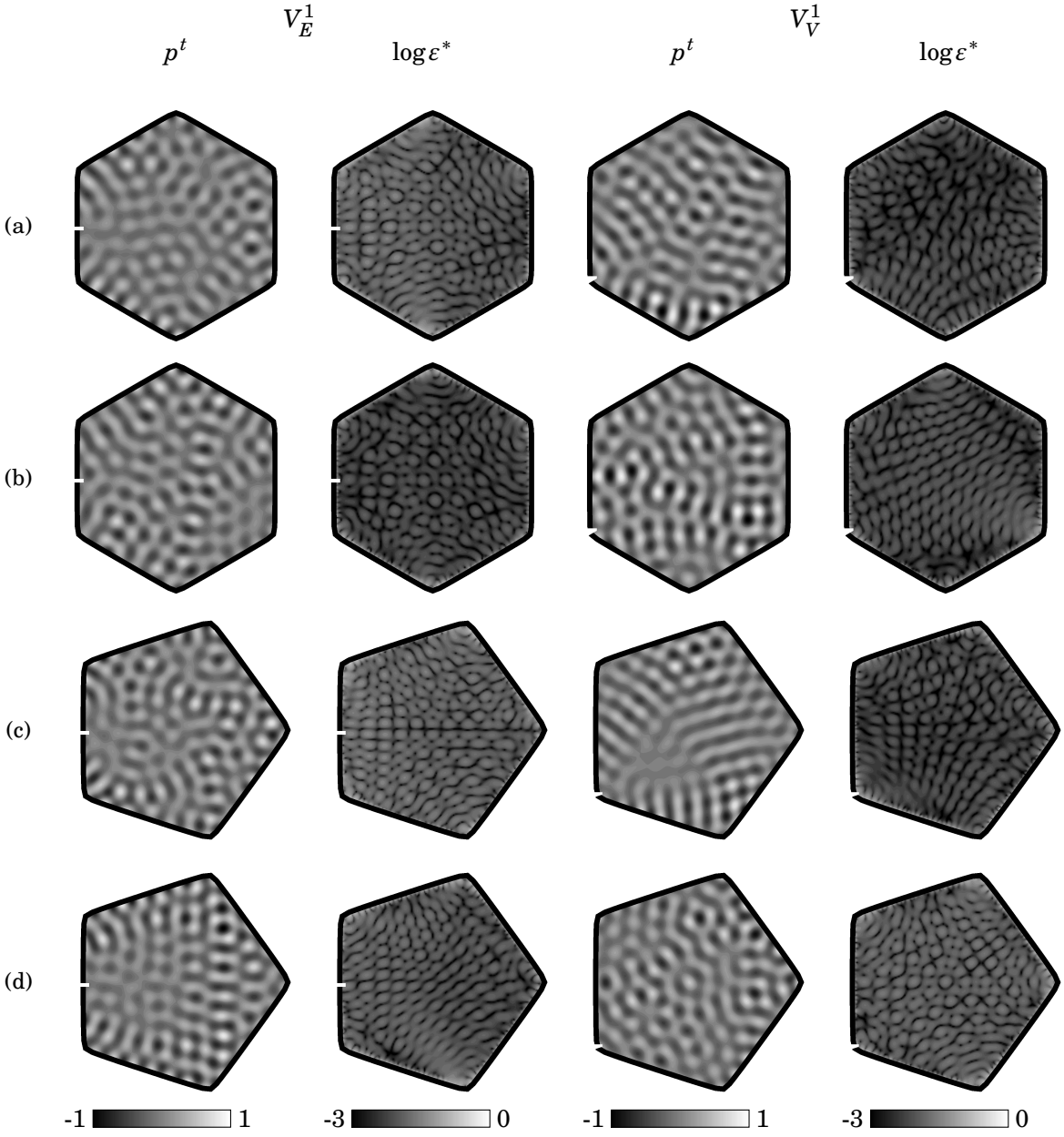

FIGURE 5.14. TPFE-based simulation of the transmitted pressure field p^t inside MUTD chamber and corresponding approximating error $\log\varepsilon^*$ (Equation 5.9). Activated electrode placed on the edge (V_1^1) and at the vertex ($V_{n_p/N}^1$) as depicted by a white patch. Real valued pressure field is normalized from -1 to 1 and approximation error range from -3 to 0. Results shown for boundary shape and acoustic impedance ratio (a) r_6^{145}, $Z_r = 21$, (b) r_6^{145}, $Z_r = 25.6$, (c) r_5^{145}, $Z_r = 21$ and (d)r_5^{145}, $Z_r = 25.6$.

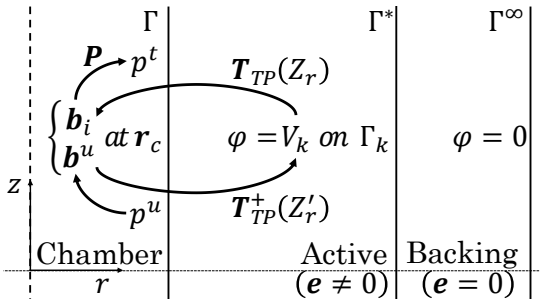

FIGURE 5.15. Schematic geometry viewed as the cross section of domains for inverse filtering technique using the FE-based transfer function to obtain the transmitted pressure field from a target boundary data given a user-specified pressure field based on Bessel beams.

5.2.2 Inverse filtering

The inverse filtering technique is applied on the realistic model for a transfer function solved using the FE solver. These FE-based transfer functions are then inverted numerically to determine the amplitude and phases of the transducer parameters to synthesize a target pressure field pattern in the acoustic chamber. The inversion defined by Equation 2.32 is applied to solve for the transducer parameters V_k^n in terms of the boundary data $\mathbf{b}^u$ for a target wave field, which is given by

$$\mathbf{V} = \mathbf{T}_{TP}^{+}\mathbf{b}^u, \tag{5.10}$$

where $\mathbf{T}_{TP}^{+}$ is the inverse transfer function computed using pseudoinverse based on SVD. Similar to the simplified model (see Section 3.1.4), the transmitted pressure field p^t within the acoustic chamber is reproduced by a combined multiplication of the inverse filter $\mathbf{T}_{TP}^{+}(Z_r')$, the transfer function $\mathbf{T}_{TP}(Z_r)$ and the propagator matrix $\mathbf{P}$. The pressure field p^t is given by

$$p^t = [\mathbf{P}]\,\mathbf{T}_{TP}(Z_r)\mathbf{T}_{TP}^{+}(Z_r')\mathbf{b}^u. \tag{5.11}$$

Figure 5.15 shows in a schematic the Bessel beam p^u inside the chamber is used to compute the internal boundary data $\mathbf{b}^u$ which gives the voltages V_k^n needed after multiplied by the inverse filter $\mathbf{T}_{TP}^{+}(Z_r')$ for a perturbed system and then reapplied back inside the chamber to give the transmitted pressure field p^t after multiplication by the transfer function $\mathbf{T}_{TP}(Z_r)$ for a specified system and the propagation matrix $\mathbf{P}$.

The MATLAB's built-in *pinv* algorithm uses a tolerance greater than which the singular values are treated as zeros. By reducing the rank the TPFE-based transfer function approximation errors in the reproduction problem are expected. The application of full-rank inversion solves the inverse problem by means of least squares as in the ESWS model (see Section 5.2).

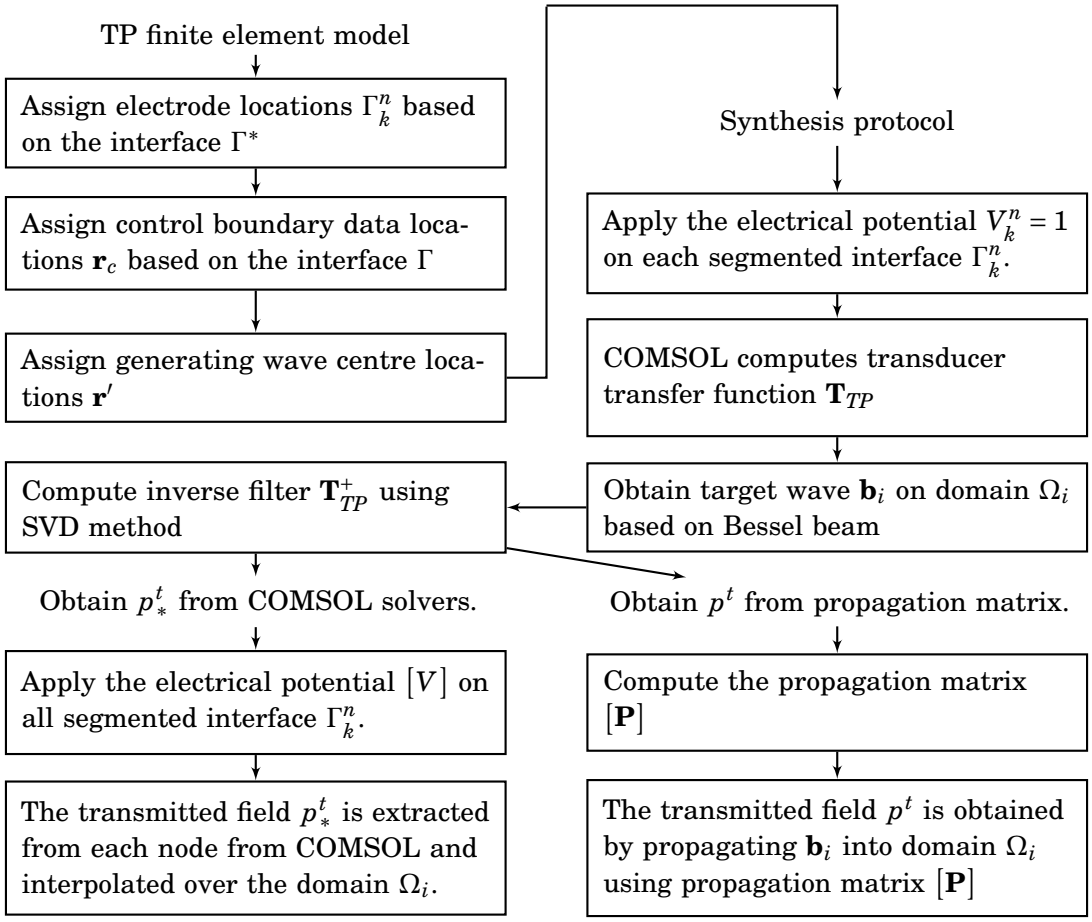

Figure 5.16: The TPFE model flow diagram showing the logic sequence of calculations for the synthesis protocol using both FE solvers and propagation matrices.

5.2.3 Synthesis of pressure fields

In this section, a simple solution is presented to illustrate the application of TPFE on the reproduction of first-order Bessel-shaped function using the inverse filtering technique for the unperturbed system. The FE solution based on high tolerance values is prone to singularity errors caused by prescribed localized high gradient electric potential on discretized boundaries. For this reason, a series of simulations varying the relative tolerance σ_0 in terms of the largest singular value σ_1. The greater the relative tolerance the higher the rank of the matrix used for approximating the inverse filter. Figure 5.17 shows the effect of the SVD relative threshold value σ_0 on the transmitted pressure field obtained using both the transfer function $\mathbf{T}_{TP}$ and the FE solver with the transducer parameters V_k^n as a function of the angle θ. The sequence of calculations for this synthesis protocol is described in the diagram in Figure 5.16

In synthesizing an off-centred acoustic vortex it is evident that the relative tolerance σ_0

affects the reproduction error on both reproduction methods. The higher the threshold value the lower the number of singular values considered in the inverse filtering technique. Even though the transfer function method achieves high-fidelity traps for low threshold, as shown in Figure 5.17(a), the FE solvers compute spurious solutions due to the high spatial gradient of the transducer parameters. For an intermediate threshold $\sigma_0 = 5e^{-4}$, the results show lower relative reproduction accuracy for p^t and higher for p^t_*. By setting a high threshold, the resulting singular values is reduced to a number where reproduction is not accurate in the transfer function method hence the FE solver method. A good compromise for a wide reproduction area is found by minimizing the approximating errors for both methods and setting the spatial average over the internal domain Ω_i of the RMS value of the transducer parameters to $\langle \mathbf{V}_{RMS} \rangle_f \geqslant 1$ V .

Figure 5.18 shows the effects of the off-centre distance on the synthesis of pressure field for both the circular and the hexagonal shapes. A tolerance of $\sigma_0 = 2.9e^{-3}$ is obtained on average for a wide-area high-fidelity reproduction for the circular shape. The reproduction errors for the FE solver method ε^* obtained from Equation 5.9 and the transfer function method ε compared with p^u given by

$$\varepsilon = \frac{p^t - p^u}{max\left(p^u\right)}. \tag{5.12}$$

are shown on the right of each transmitted pressure field. Both reproduction errors are demonstrated not to be spatially related with r_o. However, the circular interface exhibits a well-defined $\log\varepsilon$ that disturbs transmission in a regular pattern affecting more the shape correlation of the field and hence synthesis performance compared to the hexagonal one.

To summarize, the inverse filtering technique applied to transducer parameter is demonstrated to reproduce wide-area high-fidelity traps for an unperturbed perturbed system. The simulations presented in this section only demonstrate this result for a selected set of the target pressure field and transducer designs. Nevertheless, there is good agreement between the pressure field for the synthesis loading cases obtained with the FE-only solvers and the $\mathbf{T}_{TP}$ transfer function method. Hereafter, the investigation of the TPFE model for the realistic performance is carried out using the $\mathbf{T}_{TP}$ transfer function method.

5.3 Realistic performance study

This section presents a parameter study on realistic model responses of acoustic chambers to support the robust design of *kerfless* devices applied to ultrasonic tweezers. The study concerns both the analysis and synthesis performance obtained using realistic model responses. This realistic performance is obtained by solving the spatially mapped shape correlation using the $\mathbf{T}_{TP}$ transfer function method. The analysis of the realistic model has been shown to resolve elastic and electromagnetic waves with added acoustic noise due to electrical potential terminals (see ε in Figure 5.9). The simplified model responses based on fluid-fluid interface are regarded as an

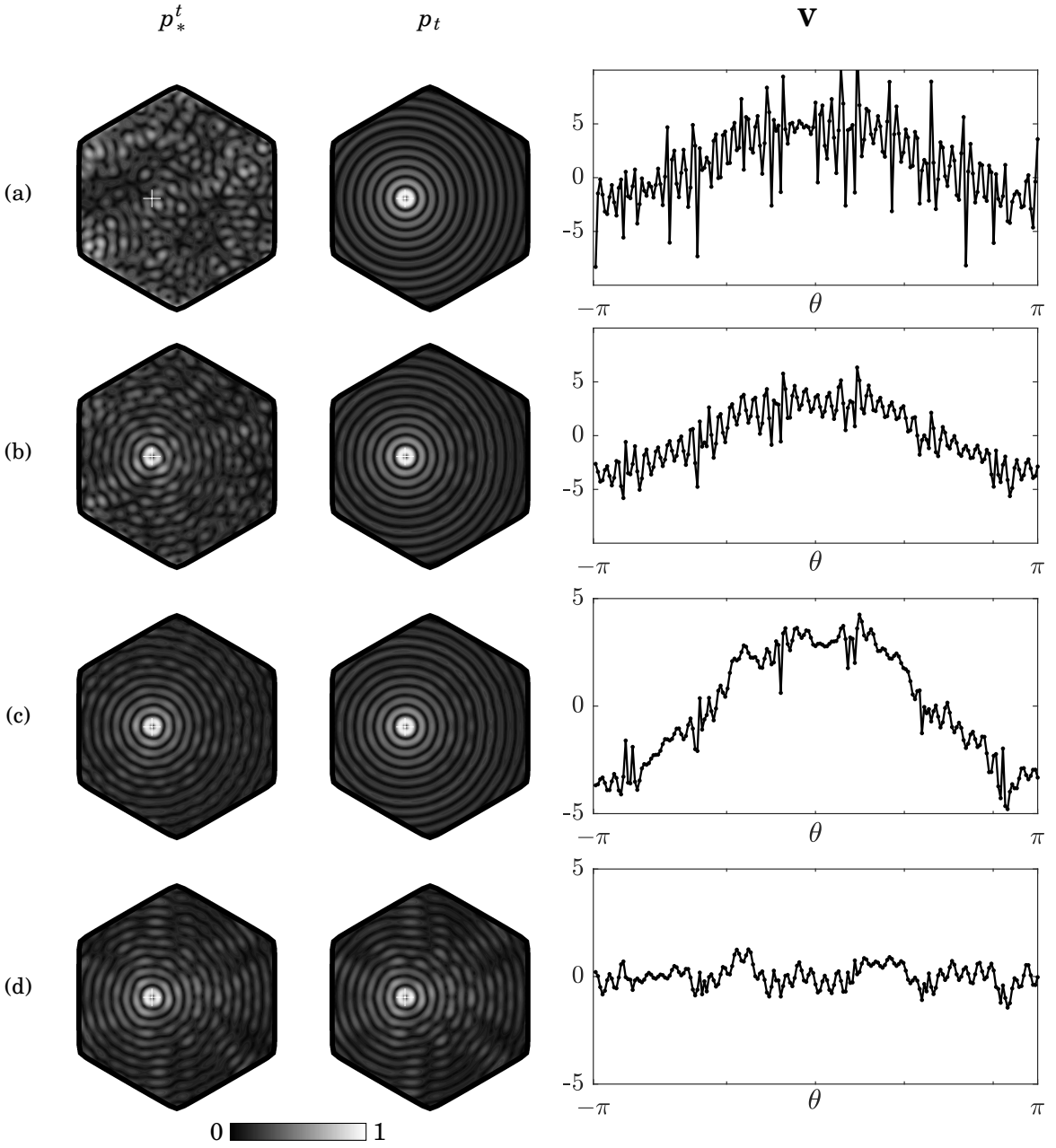

FIGURE 5.17. TPFE-based simulation for the transducer parameters $\mathbf{V}$ and the reproduction of target pressure field p^u in terms of relative tolerance σ_0 in a hexagonal shape. Transmitted pressure field obtained with FEM p_*^t and TPFE p^t are shown with respective real valued transducer parameters $\mathbf{V}$ for an unperturbed system and increasing relative tolerance σ_0 of $5e^{-5}$ (a), $5e^{-4}$ (b) and $5e^{-3}$ (d). A tolerance $\sigma_0 = 3.8e^{-3}$ (c) is obtained on average for a wide-area high-fidelity reproduction. Amplitude of pressure field is normalized from 0 to 1. Results are for transducer design ($kR = 10\pi, r_6^{145}, Z_r = 21$) and $r_o = R/4$.

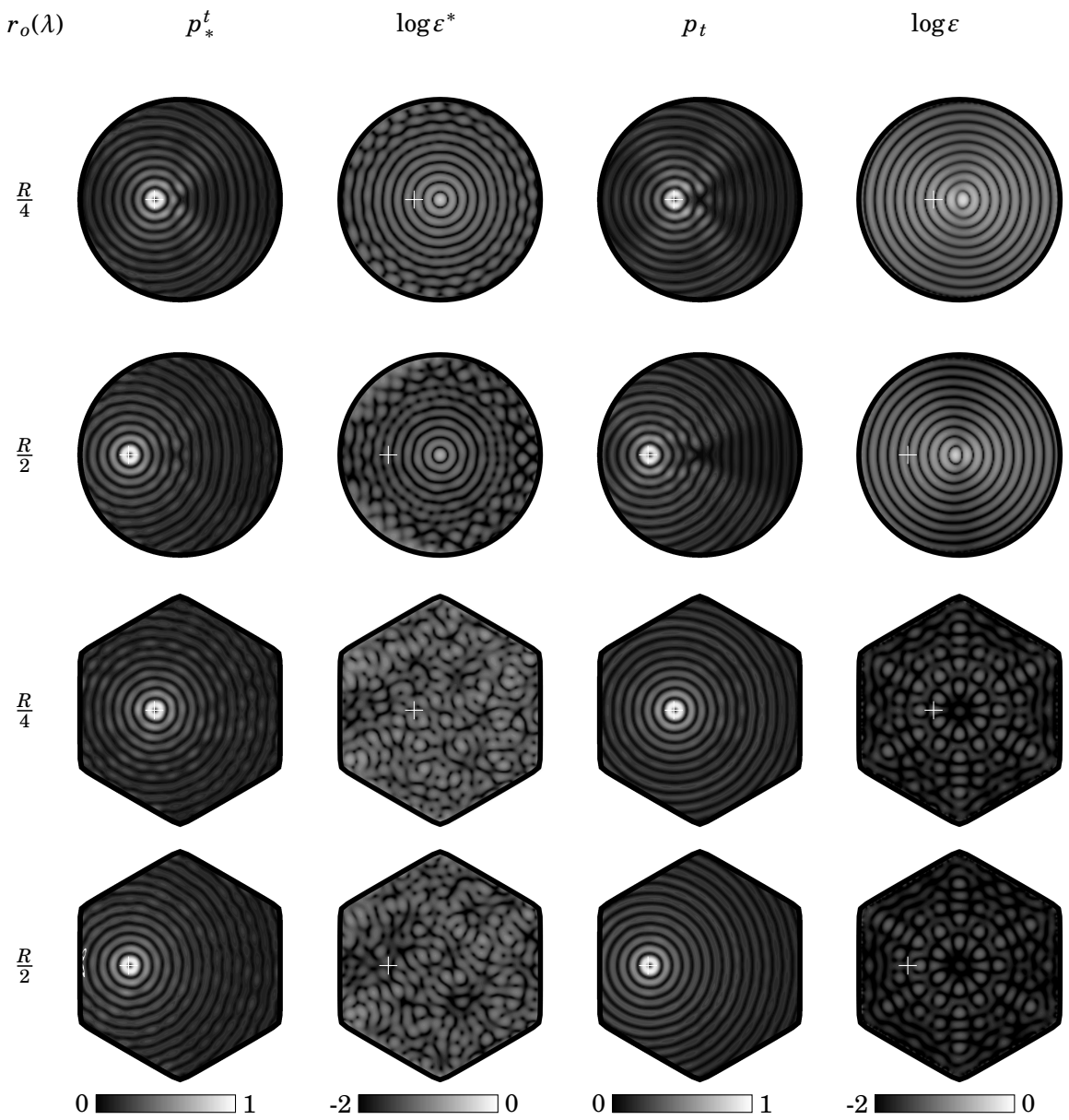

FIGURE 5.18. TPFE-based simulation for the reproduction of target pressure field p^u in terms of the off-centre distance r_o for the circular and hexagonal shapes. Results are for transducer design ($r^0, Z_r = 21$) and ($r^{145}, Z_r = 21$). Amplitude of FEM-based p_*^t and TPFE-based p^t transmitted pressure field are normalized from 0 to 1 and approximating errors $\log\varepsilon^*$ (Equation 5.9) and $\log\varepsilon$ (Equation 5.12) range from -2 to 0.

approximate solution to the realistic ones. Realistic performance of robust *kerfless* devices for synthesis of pressure field is evaluated and compared against performance obtained using both the simplified and tuning model.

Analysis and synthesis performances are both computed using shape correlation coefficient between generating (input) and solution (output) pressure field (see Figure 5.2 for schematic). The realistic analysis performance is directly obtained by implementing the analysis protocol to the realistic model using virtual sources (see Section 5.1.2). On the other hand, realistic synthesis performance is implemented based on electrical terminals as sources of incident pressure field where the source data is obtained by computing the inverse filter based on the transducer parameters (see Section 5.2.3).

According to the simplified performance study (see Section 3.4), synthesis performance was demonstrated to be inferred by the analysis performance in terms of perturbed impedance ratio. Robustness in synthesis performance may be regarded as the ability to withstand variation in the impedance ratio and maintain high shape correlation between desired and applied pressure field. A parameter space based on design variables is defined to allow an exhaustive study of analysis performance. The aim is to explore the parameter space and search for a set of parameters that results in a minimum gradient of Simplified Analysis Performance (SAP) with respect to the impedance ratio. Then relate simplified to realistic analysis performance and study their effects on the synthesis performance.

5.3.1 Preliminary parameter study

This section describes the design variables on the parameter space explored for the analysis performance study and presents preliminary results based on the simplified analysis performance for boundaries with sizes commonly found in practical applications. The design variables are chosen to comply with practical device application, such as geometries and material properties restrict the parameter space to the number of sides N, chamber corner ς, and the acoustic impedance ratio Z_r, as shown in Figure 5.19. The range studied for these parameters are wide enough to identify significant variation in the analysis performance. Each range is discussed separately according to practical applications of in-plane ultrasonic manipulation devices. The sampling strategy adopted was to compute the surface response for a set of design points uniformly distributed over the design space.

The parameter which gives an estimate for the area of interest of in-plane manipulators in terms of the wavelength is the non-dimensional wavenumber. For a typical particle trapping application, a non-dimensional wavenumber of $kR = 10\pi$ and number of co-located points $n_p = 54$ was fixed to the same as in the transducer parameter application section (see Section 5.2). Such parameter defines a device that allows at least 10 wavelengths across the transversal plane. For an operating frequency of $f = 2.625$ MHz the wavenumber in water at room temperature is $\lambda \approx 564$ µm and renders a device of with approximately 5.64 mm in diameter. It is noteworthy a

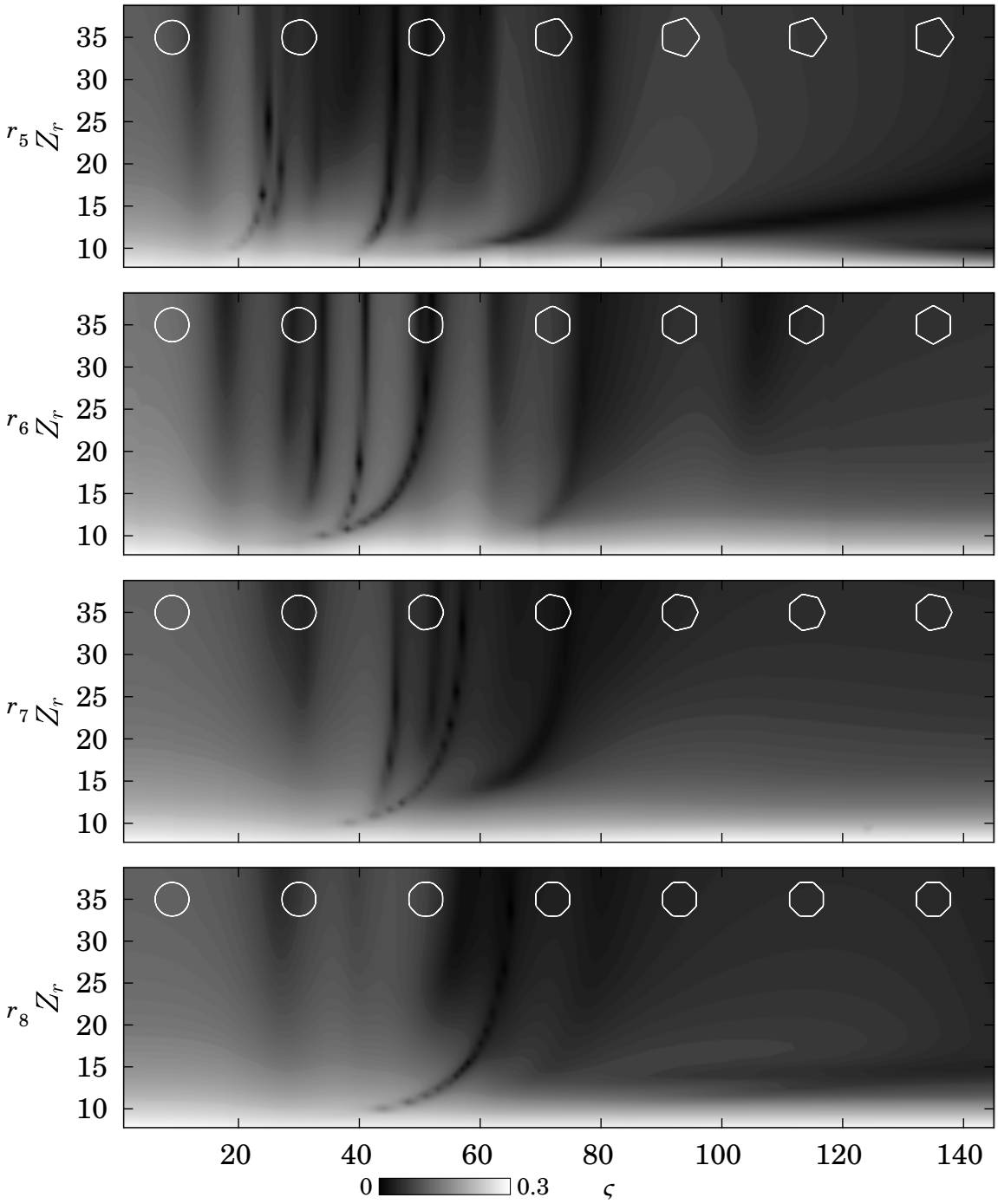

FIGURE 5.19. ESWS-based analysis performance $\langle \psi_a \rangle$ for various shape families in terms of impedance ratio Z_r and chamber corner ς. Results shown for transducer designs $T_d = \left(kR = 10\pi, r_{5\ldots8}^{1\ldots145}, Z_r = 7.75\ldots38.65\right)$. The SAP surface response is a shape correlation parameter computed using Equation 5.13, shown ranging from an uncorrelated $\psi_a = 0$ to $\psi_a = 0.3$. Perfect correlation $\psi_a = 1$ is obtained for $Z_r = 1$ with $\rho_r = 1$ where there is no reflected waves due to an internal incident wave. White drawings represent boundary shapes r_N^{ς}.

similar parameter study has been done for a relatively less spatially extensive model ($kR = 4\pi$, $n_p = 54$) in previous chapters and a large-scale application model ($kR = 20\pi$, $n_p = 192$) is dealt with in the next section. Lead Zirconate Titanate (PZT) piezoceramic was used for designing a piezoelectric actuator can be found in a wide range of material properties. The only exception to this is the theoretical mass density which spans in a narrow range around $\rho = 7600 \pm .15$ kg m^{-1} where typical PZT-5A material presents the density of $\rho = 7750$ kg m^{-1}. A discussion on the other electromechanical coefficients can be found in Section 4.1.2 for PZT-5A and varies in wider range according to the PZT type chosen for each application.

The SAP is exhaustively examined within the above-mentioned parameter space in order to identify the general boundary behaviour of a practical interface size. This analysis performance $\langle \psi_a \rangle_f$ (see fully mapped parameter in Appendix B) is defined by the mean of the shape correlation between the total p^T and the incident p^o pressure field due to an point source at $\mathbf{r}_o$ inside the chamber as in

$$\langle \psi_a \rangle_f (T_d) = \frac{1}{M} \sum_{n=1}^{M} \frac{\left| p^T(T_d, r_o^{(n)})^\dagger p^o(r_o^{(n)}) \right|^2}{\left| p^T(T_d, r_o^{(n)}) \right|^2 \left| p^o(r_o^{(n)}) \right|^2}, \tag{5.13}$$

where the transducer design is $T_d = \left(kR, r_N^\varsigma, Z_r\right)$. The centres $\mathbf{r}_o^{(n)}$ spans over the validation region defined by an internal boundary $g_N^\varsigma(\xi_a)$ at a distance $\xi_a = 4\pi^2/3k$ in normal direction from Γ into internal domain Ω_i (see Equation A.7). The analysis performance spans within $0 < \langle \psi_a \rangle < 1$ where the lower the value the more the scattered wave p^s disturbs the shape of the incident wave p^o. The simplified performance is computed using the Equivalent Source Wave Scattering (ESWS) model which simplifies the transfer function to that of a fluid-fluid interface (see Figure 3.5 for a schematic of the system). Figure 5.19 presents surface response showing the SAP for all shape families $r_{5\ldots8}$. All surface responses show in the left edge ($\varsigma = 1$) the SAP for near circular shapes and in the right edge ($\varsigma = 145$) for the shape with the sharpest corners of each family. The SAP has a higher concentration of local minimum for the family r_5 and lower concentration for the family r_8 as the more sides of a polygon the more similar it is to a circular shape.

High SAP gradient has been related to low performance in the reproduction of traps on systems under perturbation (see Section 3.4). The tuning performance study has demonstrated low SAP due to some resonant modes that are not present on the tuning model because the piezoelectricity affects the propagation of wave on the active layer (see Section 4.4.1). However, further investigation is needed to understand how the electrodes affect the realistic performance for the transducer designs examined in this preliminary studies. For this reason, the next subsections are dedicated to studying the realistic performance by running the TPFE model for both analysis and synthesis protocols.

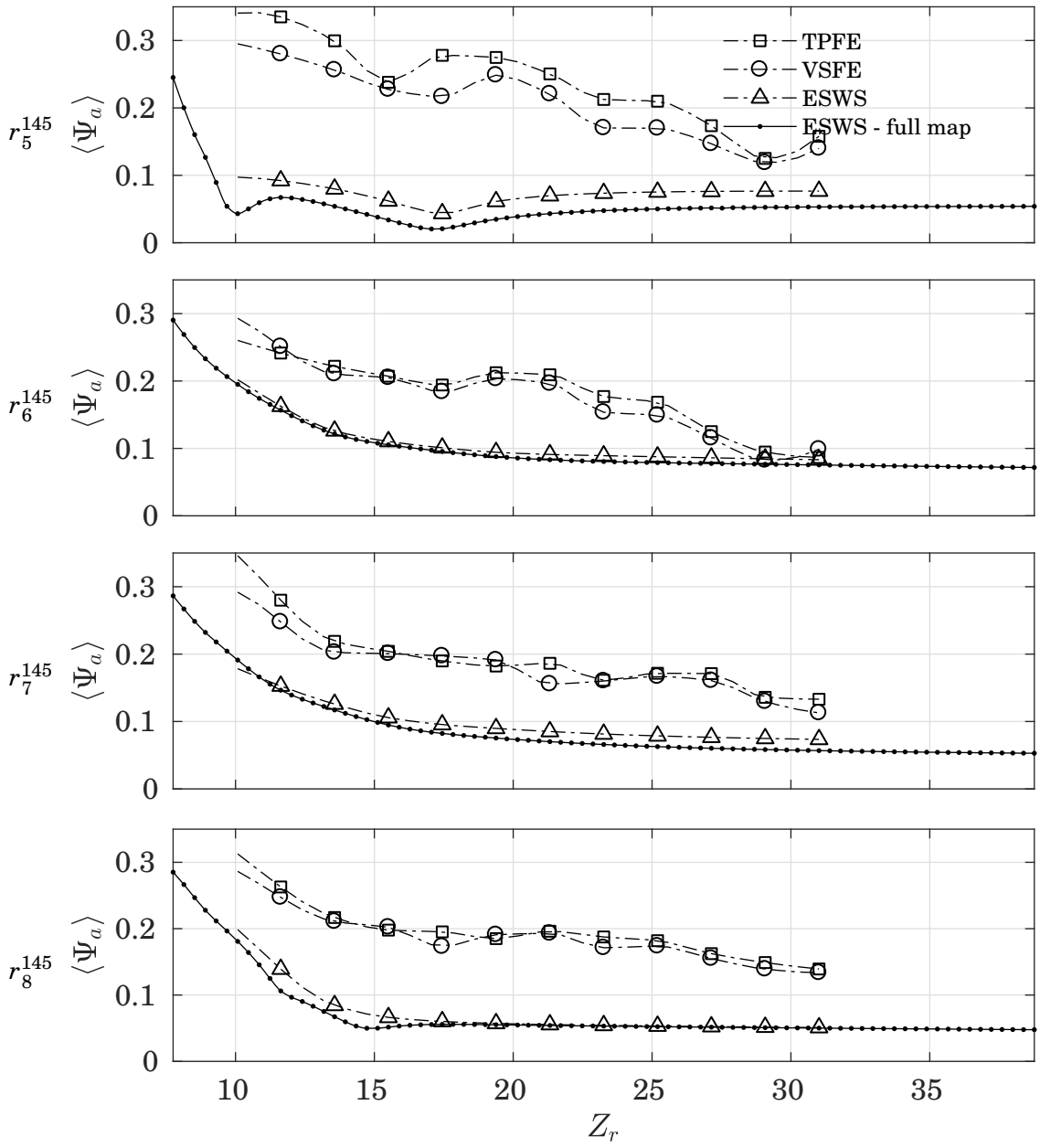

FIGURE 5.20. TPFE-based analysis performance $\langle \psi_a \rangle$ compared with VSFE and ESWS models in terms of impedance ratio for various sharp polygonal shapes. Lines represent interpolated data; Dashed (- - -) is obtained from partially mapped domain and solid (——) from fully mapped domain; Markers at data from physics-based model. Results shown for design shapes $r_{5\ldots8}^{145}$ and non-dimensional wavenumber $kR = 10\pi$. The analysis performance is computed using Equation 5.13, where for $\psi_a = 0$ total pressure p^T and incident p^o field are uncorrelated and $\psi_a = 1$ there is perfect correlation.

5.3.2 Realistic analysis performance

This section studies Realistic Analysis Performance (RAP) over the parameter space of *kerfless* devices for ultrasonic tweezers. This study capitalises on the computationally cheap response function computed using the simplified model (ESWS) to predict trends in the RAP. The goal is to search in the design parameter space for robust design of MUTD that results in minimum sensitivity in analysis performance and hence maximizing synthesis performance.

A comparison between results obtained from all three physics-based models is discussed in this paragraph. The analysis performance is simulated with TPFE, VSFE and ESWS models for design shape with near straight edges and sharp corners, as shown in Figure 5.20. It is noteworthy that results from fully mapped ESWS are also shown in Figure 5.19 on the rightmost edge of each surface response plot. The ES-based results are obtained from fully and partially mapped domain whereas FE-based models are studied only for partial domains being more computationally expensive than the latter (see Apendix B for details on mapped parameters). The approximation error in analysis performance between TPFE and VSFE are in the same order of magnitude of the error between taking the global mean from partially and fully mapped domain for the ESWS model. Furthermore, the relationship between analysis performance obtained from alternative physics-based models differs slightly for each design family studied. Overall both realistic and intermediate analysis performances are demonstrated greater than the simplified one over largely all design parameter studied. This means that the SAP gives a conservative estimate for predicting analysis performance and therefore real systems should be more capable of withstanding internal wave incidence than it would for an equivalent weakly compressible material model.

Furthermore, predicting the behaviour of realistic performance from a simplified model is demonstrated by separately analysing trends on each design shape. First distinguishable fact is the moderately variable response observed in both realistic and simplified models shown in r_5^{145}. Two examples of uniform decay trend in the simplified response can be seen in both r_6^{145} and r_7^{145}, which generally reflects on the realistic counterpart. Lastly, the ESWS response sees an initial steep slope followed by a plateau after $c_r = 2$ as shown in r_6^{145} which renders a similar trend in the TPFE response.

5.3.3 Realistic synthesis performance

This section presents a study on Realistic Synthesis Performance (RSP) based on which the design of robust MUTD is discussed. This synthesis performance $\psi_s(r_o)$ (see Appendix B) is defined by the shape correlation between the transmitted p^t and the desired p^u due to acoustic vortices inside the chamber with centre at r_o as in

$$\langle \psi_s \rangle_f (T_d, \gamma) = \frac{1}{M} \sum_{n=1}^{M} \frac{\left| p^u(r_o^{(n)})^\dagger p^t(T_d(\gamma), r_o^{(n)}) \right|^2}{\left| p^u(r_o^{(n)}) \right|^2 \left| p^t(T_d(\gamma), r_o^{(n)}) \right|^2}, \tag{5.14}$$

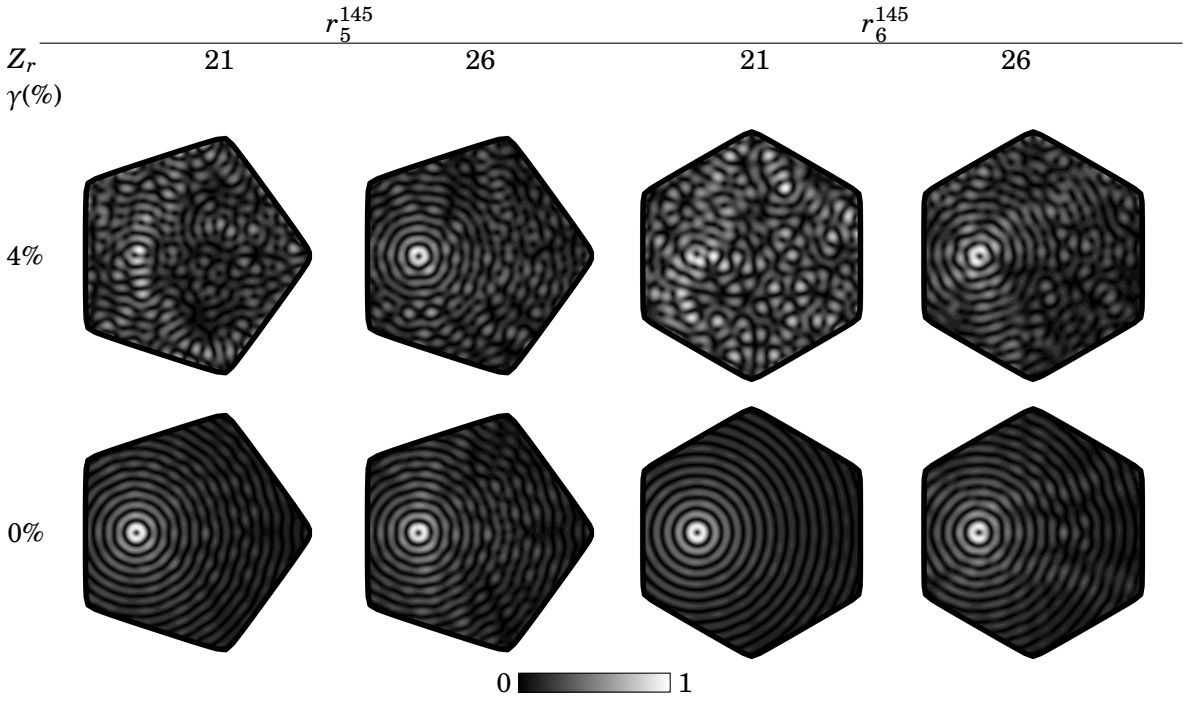

FIGURE 5.21. Simulated TPFE-based transmitted pressure field p^t for synthesis of off-centred acoustic vortices for alternative transducer designs and impedance ratio perturbation. Pressure amplitude is normalised between 0 and 1 for transducer designs $T_d = \left(kR = 10\pi, r_{5\ldots6}^{145}, Z_r = 21, 26\right)$, impedance ratio perturbation $\gamma = (0\%, 4\%)$ and $r_o = R/2$.

where the transducer design is $T_d = \left(kR, r_N^{\varsigma}, Z_r\right)$ and $T_d(\gamma) = \left(kR, r_N^{\varsigma}, (1-\gamma)Z_r\right)$ with $0 < \langle \psi_s \rangle < 1$. The lower the synthesis performance the more the transmitted p^t is disturbed compared to the desired p^u as a result of an specified impedance ratio perturbation γ. The fully mapped performance study is presented for four transducer designs which the RAP has been identified to be dissimilar, as shown in Figure 5.20. Two perturbed cases are considered a standard tolerance $\gamma = 4\%$ and a tight tolerance $\gamma = 2\%$ in addition to the reference case of the unperturbed system $\gamma = 0\%$. The reference results are obtained as presented previously for the synthesis of pressure field in the Section 5.2.3.

This performance parameter is analysed for an acoustic vortex with centre at $\mathbf{r}_o = R/2$ being synthesized by four transducer design in a perturbation scenario, as shown in Figure 5.21. The shape of each transmitted pressure field determines the performance level $\psi_s(\mathbf{r}_o)$. It is apparent that acceptable reproduction of acoustic traps is obtained in all four transducer for the unperturbed case. Some transducer designs reproduces the required pressure field better than others for the perturbed cases. The RSP encompasses this analysis by mapping this level of acceptance over the acoustic chamber. Figure 5.22 shows the mapped RSP for the transducer

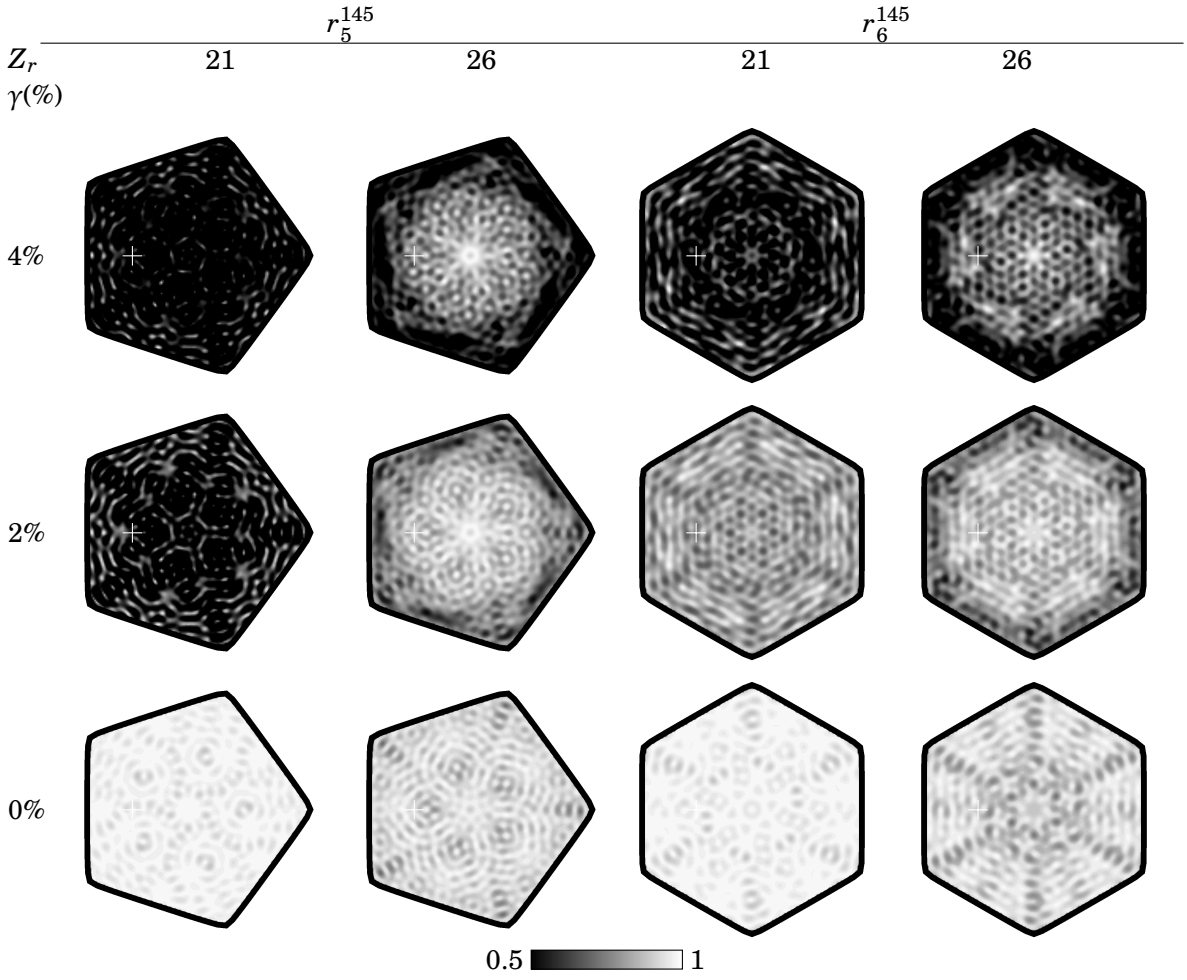

FIGURE 5.22. Simulated TPFE-based spatially mapped synthesis performance $\psi_s(\mathbf{r}_o)$ for the sharp pentagonal and hexagonal shape. Parameter study for transducer designs $T_d = \left(kR = 10\pi, r_{5\ldots6}^{145}, Z_r = 21,26\right)$, an inferred impedance ratio perturbation $\gamma = (0\%, 2\%, 4\%)$. Performance are shown ranging from a practical minimum acceptable value $\psi_s = 0.5$ to perfect reproduction $\psi_s = 1$. White crosses show $\mathbf{r}_o = R/2$ position at which the transmitted pressure field can be evaluated in Figure 5.21

designs and perturbation cases shown in Figure 5.21. The performance results show not only that each design responds differently in synthesis but also that this parameter has a strong spatial dependence. The practical implication of this parameter study in terms of radiation forces and particle dynamics is not covered here. Nevertheless, graphs in Figure 5.22 show the performance parameter between a suggest minimum and a theoretical maximum levels.

The graphs for the unperturbed results where $\gamma = 0\%$ show the lowest impedance ratio design performs better than the highest impedance ratio and are indifferent between the two boundary shapes. Conversely, for the perturbed cases the transducer designs with an impedance ratio

Table 5.1: Summary of synthesis performances obtained for transducer design ($kR = 10\pi$, $r_{5,6}^{145}$ and $Z_r = 21, 26$) in comparison with the variation in analysis performance due to for perturbation parameters ($\gamma = 0\%, 2\%, 4\%$).

	$\langle \psi_s \rangle_f$				$\Delta \langle \psi_a \rangle_p / \langle \psi_a \rangle_p (\%)$			
	r_5^{145}		r_6^{145}		r_5^{145}		r_6^{145}	
γ	$Z_r = 21$	$Z_r = 26$	$Z_r = 21$	$Z_r = 26$	$Z_r = 21$	$Z_r = 26$	$Z_r = 21$	$Z_r = 26$
4%	0.2846	0.6406	0.3956	0.6481	1.2212	0.4032	0.1545	0.8325
2%	0.3905	0.8171	0.7793	0.8253	0.6312	0.2510	0.0810	0.4934
0%	0.9531	0.9078	0.9877	0.8970	–	–	–	–

$Z_r = 26$ performs better than the $Z_r = 21$. For standard tolerance ($\gamma = 4\%$) the designs with $Z_r = 26$ only partially performs at acceptable levels. Whereas for tight tolerance ($\gamma = 2\%$) all designs performs to an acceptable level expect for the transducer design ($r_5^{145}, Z_r = 21$). It may be noted this worst design also exhibits the greater SAP gradient in terms of impedance ratio, as shown in Figure 5.20.

These RSP results confirm the MUTD robustness may be assessed by both the analysis ψ_a and synthesis ψ_s performances. Table 5.1 shows the results for the RSP and the relative variation of RAP for a perturbation γ. The results for each perturbation γ show that, in the pentagonal shape case, there is a correlation between the relative values of $\langle \psi_s \rangle_f$ for different Z_r examined and the relative variation $\Delta \langle \psi_a \rangle_p / \langle \psi_a \rangle_p (\%)$. However, this correlation is not present in the case of sharp hexagonal shape. It is suggested to implement the realistic inferred performance to further investigate the association between realistic performances. This would require the evaluation of the RAP for both unperturbed and perturbed acoustic impedance ratio and then compute the shape correlation between the spatiality mapped performance parameter (see Section 3.4.3 for details on inferred performance).

5.4 User-defined acoustic radiation potential

This section presents a special treatment of ARP to address the reproduction of user-defined acoustic field and further investigate the applicability of the MUTD design concept. The study of acoustic radiation forces (see Section 2.6) plays an important role in choosing a User-defined Acoustic Radiation Potential (UARP) and achieving general in-plane ultrasonic manipulation. The applied UARP is derived based on a family of functions which is essential to this study. This is followed by establishing a simple case scenario which reflects the interest of a general MUTD user. Lastly, the TPFE model is applied to simulate large-scale devices with a radius of approximately 10 mm for $kR = 20\pi$ and therefore $n_p = 192$, and the partially mapped RSP is investigated.

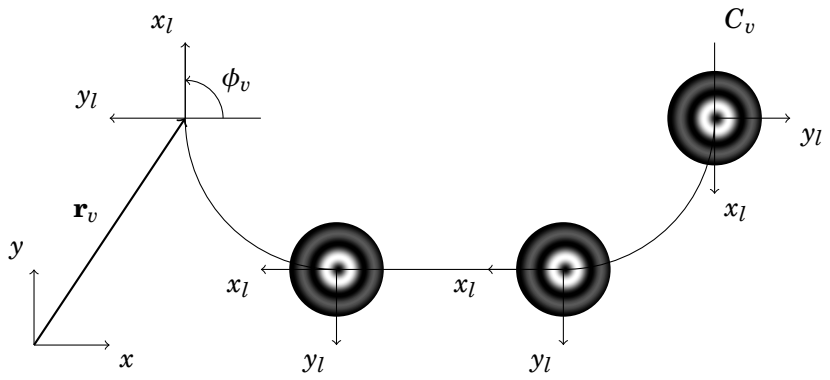

FIGURE 5.23. Simulated sculpting technique for multiple acoustic vortices aligned with C_v. Each acoustic vortex is centred at the origin of their local coordinate which is shifted by $\mathbf{r}_v$ and rotated by ϕ_v.

5.4.1 Design of static field

Dynamic and reconfigurable ultrasonic fields designed for acoustic devices has recently been achieved to manipulate particles to targeted positions as a result of the acoustic radiation force. To trap microparticles inside a region of interest one can apply user-defined ultrasonic field by dynamically activating a series of controlled sources and change the desired pressure field. Once particles are trapped, one can effectively move or manipulate entrapped particles by varying the applied voltage over time [Courtney et al., 2013; Melde et al., 2016]. Whilst the latter application is an interesting research field this section is only concerned with designing ultrasonic field suitable for particle entrapment, that is the design of static field.

The process of identifying the fundamental wave fields required for constructing an acoustic landscape related to a UARP is described hereafter as radiation potential shaping. This strategy capitalizes on a practical pressure field called acoustic vortices (see Section 2.6). These Bessel-shaped functions are characterized by a phase singularity which acts as a potential well, or trap, for acoustic tweezers. An elaborated pressure field as an assemble of multiple traps has been constructed by a linear superposition of shifted-only acoustic vortices elsewhere [Courtney et al., 2011]. This section demonstrates a novel assembly of traps aligned with a designed segment of curve C_v, as shown in Figure 5.23. This special pressure field shaped into a curve segment is determined analytically and demonstrated as a practical MUTD application.

Given such a broad definition of ultrasonic field configuration, this technique is investigated only for a particular implementation of a simple curve segment. Readers interested in optimal acoustic traps are referred to Marzo et al. [2015] for a general implementation using acoustic holography for manipulation of levitated particles. After demonstrating the applied technique, a series of numerical experiments are presented to investigate the implementation of this acoustic field design as a means to arbitrary trap particles inside the device chamber.

This investigation is evaluated quantitatively in a comparison of alternative alignment methods by analysing the shape correlation of the total acoustic radiation potential with respect to a standard function. A partially mapped RSP is presented which studies the ability of a selected transducer design to reproduce a particular UARP pattern in perturbation scenario. The goal for this implementation is to demonstrate the advantages of RSP study in designing MUTD for tailored practical application of particle manipulation. The implementation of such a technique on the reproduction of the desired field is a topic for the next subsection.

5.4.2 Radiation potential sculpting

The application of acoustic vortices as potential wells for particle manipulation purposes is achieved by a simple acoustic landscaping technique hereafter termed radiation potential sculpting. The shape of a scalar field may be characterized by the distribution of the "peaks" and "valleys" that corresponds to local maxima and minima, respectively. Shaping an UARP along a designed curve segment is suggested as a technique to arrange the distribution of the local minima by superimposing a finite set of potential wells. This technique assumes the spatially distributed UARP only interfere locally within a certain length and does not interact with adjacent characteristic segments. In consequence, sculpting is implemented heuristically based on linear superposition by simply adding shifted and rotated acoustic vortices to shape a final acoustic landscape.

The concept of acoustic traps based on potential-well is reviewed in Section 2.6 and defined as Bessel-shaped functions with topological charge or acoustical vortices in Equation 2.57. Shifting the centre of these special functions can be achieved by translating the radius $\mathbf{r}'_v$ as described previously for zeroth order Hankel function (see Section 2.2.1) and for first order Bessel-shaped function (see Section 2.6). Similarly, a rotation is defined as a phase-shifted Bessel-shaped function in terms of a given phase ϕ_v. It is noteworthy high-order Bessel function has also been studied as trapping mechanism. For simplicity, the radiation potential sculpting is only proposed for first order Bessel function. The total pressure field p^u_* is the result of acoustic landscaping by collectively shifting, rotating and superimposing acoustic vortices centred on and aligned with a curve segment which is given by the expression

$$p^u_*(\mathbf{r}) = p_0 \frac{i}{4} \sum_{v=1}^{N_v} J_1\left(k|\mathbf{r}'_v - \mathbf{r}|\right) e^{i(\phi_v - \phi)}, \tag{5.15}$$

where $\mathbf{r}'_v$, ϕ_v are the vortex centre radius vector and phase shift, respectively. The subscript v refers to the vortex index and N_v is the total number of vortices. The phase shift ϕ_v is defined as a linear function of the normal direction of the curve segment.

The sculpting approach is applied to extend these potential-well traps to a potential-valley C shaped by an arbitrary curve. A simple "S" curve segment is used as an example for demonstrating this technique as represented in Figure 5.24. This curve segment C_S is composed of two quarter-circle and three straight line segments each with equal characteristic length l_C intercalated and

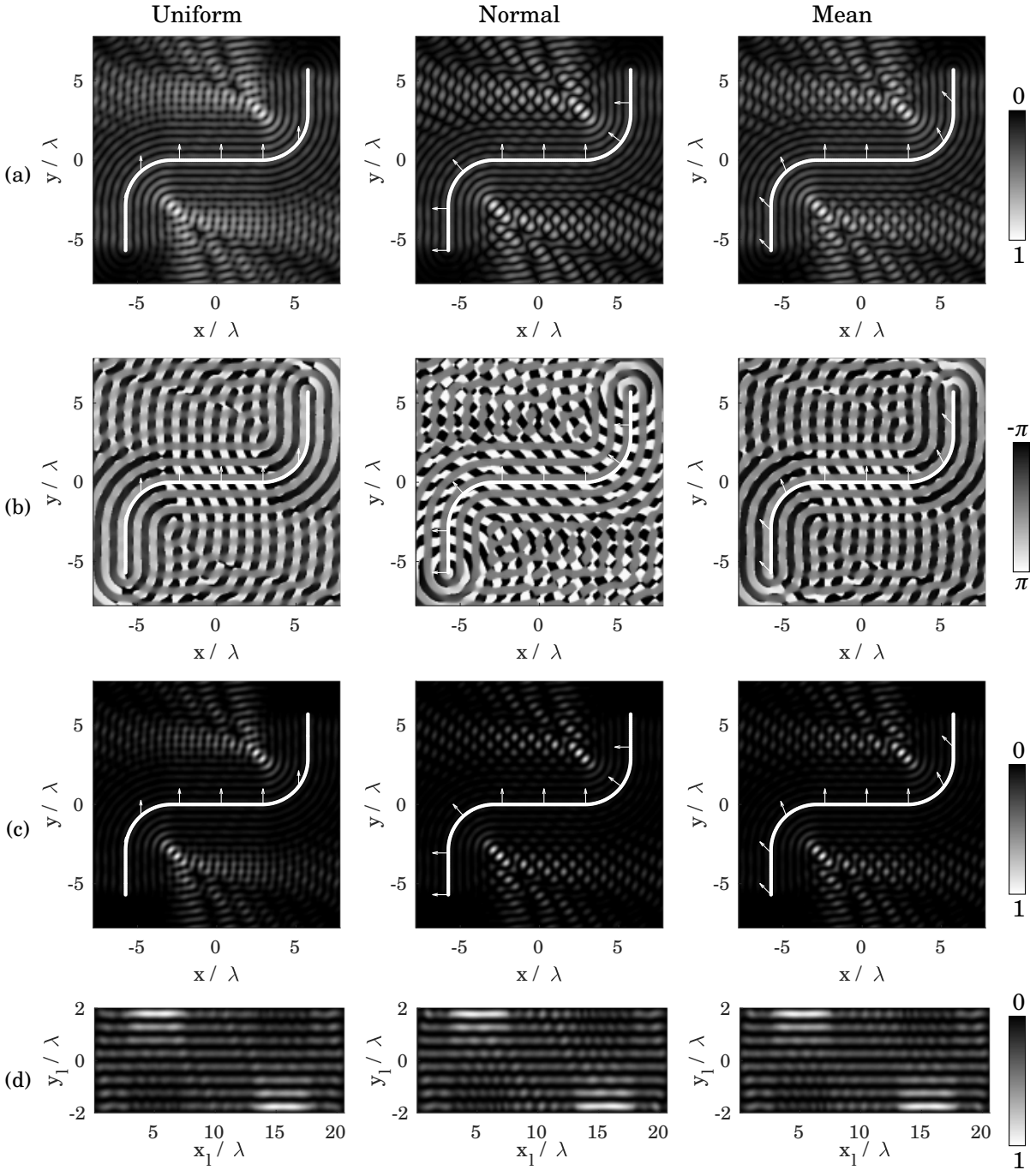

FIGURE 5.24. Simulated sculpting technique for multiple acoustic vortices aligned with a valley C_S analysing alternative phase shift methods. (a) Results of amplitude p_*^u. (b) Phase of the pressure field. (c) Radiation potential in global coordinates $U(x, y)$. (d) Radiation potential in local coordinates $U(x_l, y_l)$. Graphs show results for uniform, normal and mean phase shift method. The white lines represent the C_S with characteristic length $l_C = 2.876\lambda$ and arrows the directional vector for the phase shifts ϕ_v. Pressure amplitude and radiation potential are normalized between 0 and 1.

concatenated to form a continuous valley. To allow fine superposition of potential-wells, a set of uniformly distributed points are positioned along the length of the curve segments and spaced by one-tenth of a wavelength $l_\lambda = \lambda/10$. The total number of points N_v of each valley is given by the greatest integer less than the curve's total length L divided by l_λ.

The UARP produced by the superimposed pressure field $p_*^u(\mathbf{r})$ is computed using the Gor'kov potential U_a presented in Equation 2.54. The acoustic radiation potential U_a^* obtained for the target pressure field $p_*^u(\mathbf{r})$ is defined as

$$U_a^* = U_a(p_*^u). \tag{5.16}$$

The results for UARP are analysed for three alternative phase shift approaches based on uniform, normal, and mean phase shift. These phase shifting approaches depend on the normal angle ϕ_{n_v} at $\mathbf{r}_v$ over C_S and is defined as

$$\phi_v = \begin{cases} \phi_{ref} & \text{for uniform phase} \\ \phi_{n_v} + \phi_{ref} & \text{for normal phase} \\ \frac{1}{2}\left(\phi_{n_v} + \phi_{ref}\right) & \text{for mean phase} \end{cases}, \tag{5.17}$$

where ϕ_{ref} is an arbitrary phase reference. Figure 5.24 shows the amplitude and phase of $p_*^u(x,y)$, the $U_a^*(x,y)$ and their respective potential in local coordinates $U_a^*(x_l,y_l)$ for a comparison between the phase shift approaches. The phase reference for this example is set to $\phi_{ref} = \pi/2$ but any value would produce identical UARP for each phase shift method. The phase shift method affects the phase of each acoustic vortex p^u which changes the shape of p_*^u and hence the resulting potential U_a^*. In order to further investigate quantitatively each phase shift method the potential U_p is benchmarked against a standard function.

The transverse section of the UARP in local coordinates U_l, as shown in Figure 5.24, may be compared to a Standard Acoustic Radiation Potential (SARP), $\tilde{U}$. As shown in Figure 5.25, this potential is identified as piecewise function of either a standing plane wave or a Fractional Bessel Beam (FBB) [Mitri and Silva, 2011] on the straight and the curved parts of C_S, respectively. The standing plane wave is such that the potential minimum lies at the origin of the local coordinates. The FBB is characterized by having its origins at the centre of curvature $\mathbf{r}_q$ of the quarter-circle and a zero at the centre of expansion $\mathbf{r}_v$ of each acoustic vortices. The SARP can be obtained from the standard pressure field defined as

$$\tilde{p} = \begin{cases} A\sin\left(k y_l\right) & \text{for straight segments} \\ B J_m\left(k|\mathbf{r}_q - \mathbf{r}_v|\right) e^{im\phi} & \text{for curved segments} \end{cases}, \tag{5.18}$$

where A and B are arbitrary constants, $1 > m > -1$ is the fractional topological charge obtained such that $\tilde{p} = 0$ at $y_l = 0$ and ϕ the angle between the two vectors $\mathbf{r}_q$ and $\mathbf{r}_v$. Figure 5.26 shows an example of the local U_l (UARP) overlaid with the $\tilde{U}$ (SARP) obtained from Equation 5.18 for both the straight and the curved segments. It is noteworthy the amplitude of the standard potential

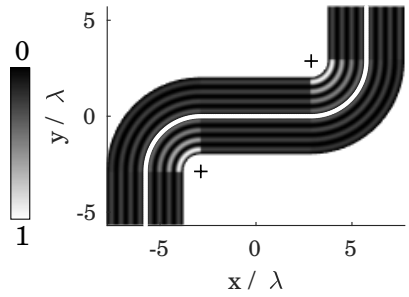

FIGURE 5.25. Example of standard acoustic radiation potential $\tilde{U}$ applied to the curve segment C_S for $l_C = 2.876\lambda$. White line represents the C_S and black cross the centre of curvature $\mathbf{r}_q$ of the quarter-circle.

is set to arbitrary constants as the relevant feature analysed with this technique is the shape reproduction of the valleys along the segment curve. To assess this UARP landscaping technique, a performance parameter ψ_p is defined as the weighted sum of the shape correlation between U_l and $\tilde{U}$ over the segments of C_v. As the points $\mathbf{r}_v$ are equally distributed over C_S, the $\psi_p(C_S)$ can be expressed by a simple summation as in

$$\psi_p(C_S) = \frac{1}{N_v} \sum_{v=1}^{N_v} \frac{\left|U(r_v)^\dagger \tilde{U}(r_v)\right|^2}{(U(r_v)^\dagger U(r_v))(\tilde{U}(r_v)^\dagger \tilde{U}(r_v))}. \tag{5.19}$$

The Potential Sculpting Performance (PSP) ψ_p is further examined for the range of radius of curvature to allow comparison between the alternatives phase shift methods, as shown in Table 5.2. The results show the normal method produces the least value for the performance hence the worst method to synthesize C_S curves for all analysed radius. This is mainly due to interference caused by the superposition of the pressure field generated by the straight segments

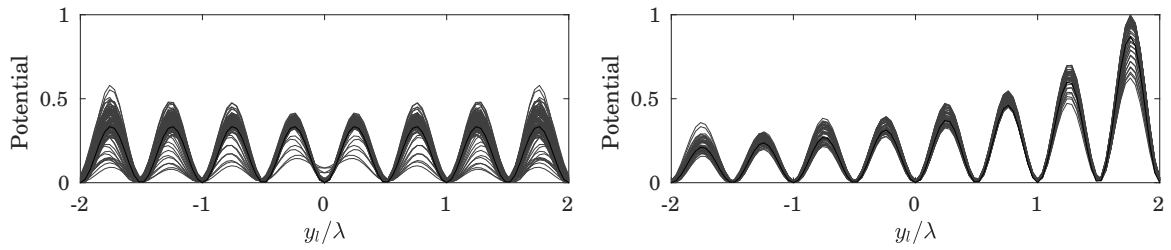

FIGURE 5.26. Example of user-defined acoustic radiation potential in local coordinates U_l (UARP) applied to the curve segment C_S for $l_C = 2.876\lambda$ for the mean phase shift method. The multiple grey lines on each graph are the local U_l centred on each trap centre $\mathbf{r}_v$ and the black lines are the $\tilde{U}$ (SARP).

Table 5.2: Performance of the acoustic potential sculpting technique obtained from Equation 5.19 for various radius of curvature comparing alternative phase shift methods.

	$\psi_p(C_S)$				$\psi_p(C_S)$		
$l_C\,[\lambda]$	Uniform	Normal	Mean	$l_C\,[\lambda]$	Uniform	Normal	Mean
2.2500	0.9346	0.9139	0.9438	3.0000	0.9791	0.9681	0.9805
2.3763	0.9479	0.9427	0.9581	3.1220	0.9743	0.9589	0.9766
2.5000	0.9672	0.9402	0.9626	3.2500	0.9816	0.9681	0.9820
2.6214	0.9675	0.9544	0.9707	3.3759	0.9843	0.9761	0.9849
2.7500	0.9682	0.9494	0.9694	3.5000	0.9783	0.9697	0.9817
2.8761	0.9760	0.9693	0.9808	3.6224	0.9825	0.9727	0.9843

on the ends of C_S with the ones in the middle. The mean method overall performs just better compared to the uniform method except for the case of characteristic length equals to $l_C = 2.5\lambda$.

The results presented in this section demonstrate the feasibility of synthesizing UARP by means of radiation potential landscaping based on a novel superposition alignment of acoustic vortices. This sculpting technique can be regarded as a tool for extending potential wells into potential valleys by shifting and rotating acoustic vortices for generating high-fidelity traps. The best method found for aligning the potential valleys to "S" curve is the mean phase shift which rotates by a phase shift defined as the mean between a phase reference and the normal direction of the curve segment.

5.4.3 Application of high-fidelity traps in MUTD

The potential sculpting technique is implemented with the TPFE model in order to demonstrate the synthesis of high-fidelity potential valleys in large-scale MUTD. The accuracy of the potential valley applied to both unperturbed and perturbed realistic models is investigated using a local RSP measure. This assessment determines whether a particular potential valley is robust for the selected transducer design. Whilst optimizing the transducer design for a designed UARP is an interesting research investigation, this topic is not covered in this thesis.

The first step of the implementation is to present the transmitted pressure field p^t using Equation 5.24 which synthesizes the "S" curve segment from the previous section for an unperturbed system. The applied transducer parameters $\mathbf{V}$ on the electrodes in order to achieve this field pattern is analysed to avoid spurious solutions due to high spatial gradient. Then, a partially mapped RSP is computed along the curve segment C_S for an inferred perturbation of $\gamma = 2\%$. This investigation is based on a low impedance ratio sharp hexagonal large-scale transducer. Figure 5.27 shows the synthesized p^t, the voltages $\mathbf{V}$ and the potential in local coordinates U_l sculpted into the valley C_S with a characteristic length $l_C = 2.876\lambda$.

The performance of pressure field synthesis implemented with the TPFE model, that is the RSP, has the shape correlation association between each pair of generating and transmitted

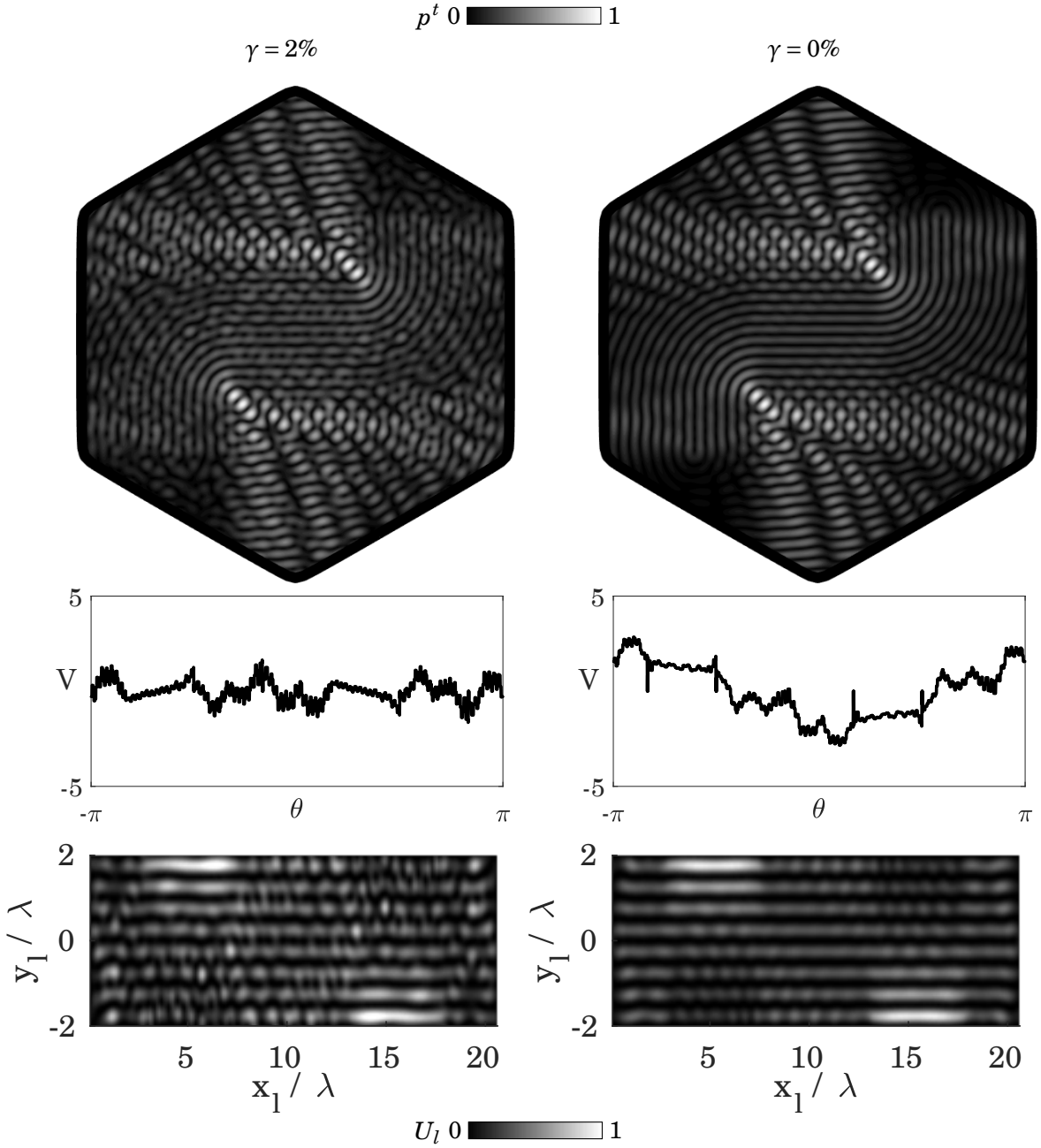

FIGURE 5.27. TPFE-based simulation of the synthesized pressure field inside the MUTD chamber and the acoustic radiation potential in local coordinates for a valley C_S on both perturbed and unperturbed cases. Graphs show the transmitted pressure field p^t (top), the transducer parameters $\mathbf{V}$ and the local UARP U_l (bottom) for $\gamma = 2\%$ (left) and $\gamma = 0\%$ (right). Transducer design is $T_d = \left(kR = 20\pi, r_6^{145}, Z_r = 21\right)$. Fields are normalized between 0 and 1.

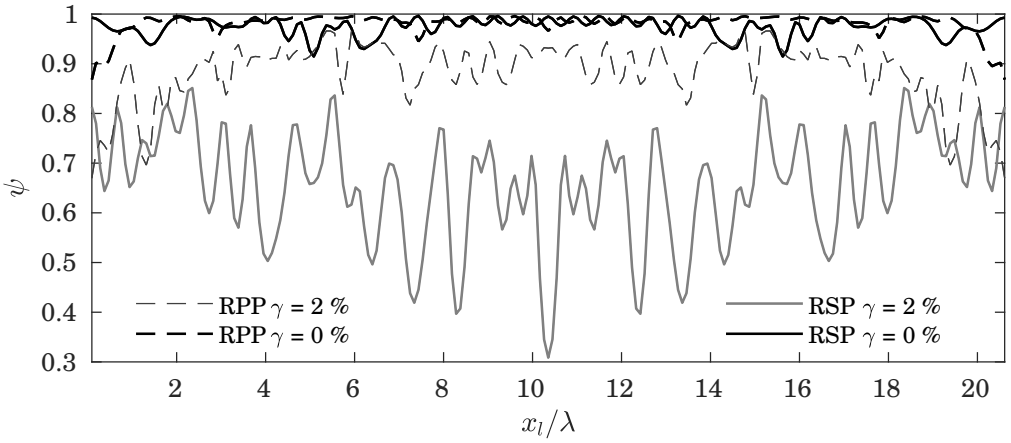

FIGURE 5.28. Simulation of the realistic performances RPP and RSP in local coordinates for a perturbed and unperturbed cases. The RPP and RSP performance parameters are shown in terms of the centres $\mathbf{r}_v$ (or $\mathbf{r}_o$) and computed using Equation 5.14 and 5.19, respectively.

acoustic field in terms of their centre (see Section 5.3). For synthesizing potential valleys, the PSP is defined in this section which compares the UARP from superimposed generating fields to an ideal SARP using the sculpting technique. The combination of these two parameters is defined as the Realistic Potential Sculpting Performance (RPP), ψ_{rp}, which is implemented with the TPFE model and applied to the reproduction of potential valleys.

Figure 5.28 shows the performances RPP and RSP in terms of the local coordinate x_l/λ for a perturbation of $\gamma = 2\%$ compared to the unperturbed response. These realistic performances are computed using the transmitted field and potential U_l in local coordinates as shown in Figure 5.27. The RPP may be regarded as the ability of a MUTD to reproduce high-fidelity potential valleys under material properties perturbation. Realistic results indicate both the potential valley and acoustic vortices are in good agreement with their respective standard version for $\gamma = 0\%$. The corresponding RSP for this transducer design application is greater than $\langle \psi_s \rangle_p > 0.9$ which is comparable with previous studies in Section 5.3.3 therefore this performance measure scales with the size of the model. The potential valley correlates more with its SARP than the acoustic vortices

Table 5.3: Summary of performance parameters obtained for a perturbed ($\gamma = 2\%$) and unperturbed ($\gamma = 0\%$) transducer design ($kR = 20\pi$, r_6^{145} and $Z_r = 26$) applied to reproduction of the potential valley along C_S with characteristic length of $l_C = 2.876$.

γ	$\left\langle \psi_p \right\rangle_p$ (PSP)	$\langle \psi_s \rangle_p$ (RSP)	$\left\langle \psi_{rp} \right\rangle_p$ (RPP)
0%	0.9808	0.9753	0.9808
2%	-	0.6578	0.8846

in the perturbed case. Table 5.3 shows a comparison between alternative performance parameters which summarises all developed associations to assess the accuracy of the reproduction.

5.5 Conclusion

A *kerfless* multi-electrode transducer device for ultrasonic tweezing was theoretically investigated. The aim of the investigation was to assess the performance of transducer designs in synthesizing user-defined acoustic fields required for manipulation of particles. A realistic FE model based on a backed monolithic arbitrarily shaped piezoceramic covered with electrically decoupled terminals to simulate realistic transfer function was developed. This TPFE model was compared to an intermediate FE model which is based on a theoretical representation of an unbounded electrical potential in active domain extended to infinity. The synthesis of pressure field has been demonstrated by using an optimized SVD-based inverse filtering technique applied to wide-area high-fidelity reproduction of acoustic traps. A boundary shape study has found that circular transducer designs produce well-defined symmetric reproduction errors whereas polygonal shapes produces uncorrelated errors. A preliminary performance study based on simplified ES models using analysis loading to obtain boundary behaviour response has helped identify potential transducer designs associated with highly disturbed reproduction field. The effects of the boundary behaviour on the shape disturbance of reproduction field have been assessed by a synthesis performance parameter. This performance parameter was found to relate to robustness of transducers with respect to perturbed impedance ratio. This performance-driven approach was applied to investigate a novel pressure field landscaping technique based on position and phase shifted acoustic vortices. The application of wide-area high-fidelity reproduction of traps in practical devices was examined by a combination of landscaping and synthesis performance study. This study concluded that the shape of reproduced acoustic radiation potential achieves better correlation with a local standard user-defined potential than the shape of reproduced pressure field with respect to global standard acoustic vortices for a particular transducer design.

CHAPTER 6

CONCLUSION AND FURTHER WORK SUGGESTIONS

Acoustic manipulation technology still faces both application and design challenges which opens up room for research on theoretical aspects of such contactless mechanisms. In-plane, closed acoustic manipulators have been studied for more than 20 years and the implementation of high-fidelity, wide-area generation of user-defined manipulation patterns is on-going research. These devices operates with manipulated material contained inside a two-dimensional acoustic chamber which is invaluable technology for many applications in natural science. The level of complexity demanded on these devices for current application needs has made robust modelling a key factor on further development. Acoustic tweezers have proven dexterous in focusing traps and manipulating particles inside an acoustic chamber. A monolithic construction for acoustic manipulators has recently drawn the attention of experimental research owing to their simplifying configuration. An in-plane, closed, monolithic transducer array for particle manipulation was investigated numerically but not experimentally in this thesis. The main motivation of this research was the interest in implementing a robust modelling approach to the design of a micro-scale acoustic manipulator for reproducing high-fidelity and reconfigurable field focused on simplifying both model and device configuration.

6.1 Thesis review

In previous work, the physical representation of practical in-plane acoustic manipulation devices has been historically developed by both simplified and realistic modelling approaches. The proof-of-principle of practical devices and understanding of physical phenomenon inside acoustic chambers was investigated considering simple boundary conditions. Realistic modelling approaches, mostly based on Finite Element Method, have been developed to assess system-wide responses and

confirmed the magnitude of forces on practical devices. In this Thesis, a thorough investigation of approximating assumptions between these two approaches was key to develop a modelling framework to robust design these devices. A comprehensive bottom-up strategy was devised to deal with design problems by using various modelling methods. The developed physics-based models ranged from fluid-fluid interface responses to theoretical acoustic sources up to transducer responses to realistic electrical excitation for generating user-defined acoustic traps in Monolithic Ultrasonic Tweezer Devices.

The present work investigated the application of a modelling approach bridging simplified and realistic models to study the system-wide response of acoustic manipulators. Furthermore, these models were applied to high fidelity reproduction of acoustic traps of a multi-electrode array transducer designed with mechanically coupled elements for ultrasonic tweezing. The *kerfless* design was a device configuration based on a backed monolithic ceramic surrounding a two-dimensional acoustic chamber and modelled by a geometrical representation of single closed physical boundaries. For this reason, the wave field was defined by the boundary behaviour and considered to radiate outwardly in an unbounded domain. The shape design investigation was inspired by dielectric microcavity based on polygonal interfaces with rounded corners which enables engineering of resonant modes. Resonances predicted throughout the thesis are features of these symmetric transducer designs and the potential to eliminate them by proposing arbitrary shapes was not covered here.

This thesis was primarily concerned with numerical simulations of pressure field and the performance of Monolithic Ultrasonic Tweezer Devices with varying shape, size and material properties. Two alternative protocols were studied based on the positioning of primary sources relative to the interface between the acoustic chamber and the ultrasonic transducer. The analysis protocol denoted the propagation of wave due to theoretical sources inside the chamber causing incidence and reflection to take place internally. The synthesis protocol referred to the application of external sources cause scattering and transmission to occur in separate domains. For each protocol, the generating and the solution wave were considered an input-output pair and a performance-based parameter study examined their relationship. Mathematical models were employed to relate data across each problem using shape correlation between pressure field and to pressure field reproduction using inverse filtering technique.

The effects of boundary condition, domain representation and source of radiation on the pressure response was investigated alternatively by a simplified, an intermediate and a realistic model. Each physics-based model was devised to solve for a particular wave phenomenon relevant to the analysis and synthesis of pressure field for in-plane closed acoustic manipulators. The simplified model was based on the Equivalent Source Method and focused on the boundary behaviour aspect of wave propagation through a fluid-fluid closed interface which extended the simplistic "free space" assumption to that of room acoustics or wave scattering problems in the analysis and the synthesis protocols, respectively. The intermediate model was based on the

FEM and studied the effects of the piezoelectric material properties in the chamber response by examining the internally reflected field in the analysis protocol. An Absorbing Layer with Increasing Damping was implemented as a custom truncation method for dealing with arbitrarily shaped interfaces. The realistic model extended the latter by considering patched electrodes as a sink of electrical potential or as a source of acoustic radiation in the analysis and the synthesis protocols, respectively.

A modelling approach provided integration of these protocols with the mathematical and physics-based models which facilitated the identification of limited performance in Monolithic Ultrasonic Tweezer Devices. This thesis claimed a performance-driven method for designing in-plane closed monolithic piezoelectric devices applied to the synthesis of general purpose superimposed acoustic traps. The main contributions of this work summarise the steps taken to achieve this goal. A simplified analysis was inferred from the synthesis performance using shape correlation between the two parameters. A parameter study demonstrated that mapping the analysis performance of piezoelectric devices may be obtained by tuning electromechanical coefficients. High-fidelity reproduction of acoustic traps was achieved using a novel acoustic radiation potential sculpting technique in a realistic model. This study concluded that the examination of analysis of pressure field employing simplified models might avoid designing limited performance Monolithic Ultrasonic Tweezer Devices.

Research on performance of acoustic manipulation techniques has a sparse record of theoretical and experimental work. Analysing the shape of the pressure field and the magnitude of applied forces by tracking manipulated particle have been a common choice for experimentally assessing device performance. Theoretical research has focused on studying mechanical outputs and searching for optimal devices by maximizing applied force field. The association between chamber response to an internal source and field reproduction of acoustic vortices was investigated by employing a performance study based on shape correlation of the pressure field solved using simplified and realistic models. This investigation allowed the implementation of a computationally cheap parametric study of transducer design for analysing the theoretical performance through a realistic model applied to wide-area, high-fidelity reproduction of acoustic traps.

6.2 Summary of findings

The key contributions of this thesis can be categorised by the three physics-based models, namely Equivalent Source Wave Scattering, Virtual Source Finite Element and Transducer Parameter Finite Element; each was developed as a separate study towards modelling the proposed Monolithic Ultrasonic Tweezer Devices. An analytical model based on the cylindrical wave expansion method was implemented for solving wave transmission only through a fluid-fluid circular interface by a simple source internally located using Equations C.2 and C.3 and

employed as a numerical validation tool for all developed models. Convergence was achieved for a number of truncation points $n_t = kR + 10$ in Section 3.3.1 which was fixed throughout the thesis. Unless stated otherwise, discussed results are for small acoustics chambers with non-dimensional wavenumber $kR = 4\pi$ (i.e. 4λ across chamber diameter).

6.2.1 The Equivalent Source Wave Scattering model

The Equivalent Source Wave Scattering model was employed as the simplified model using the equivalent source method to solve for both internal radiation and transmission problems. The pressure response to an internal source in a circular interface was found to be in good agreement with an analytical model in Section 3.3.1 for an average arc length of $\langle |L| \rangle \approx \lambda/3$ between the equivalent sources with errors $\log \varepsilon(r_o) < -3$. An investigation in the synthesis protocol for smooth hexagonal boundary shape found that a perturbation factor of $\gamma = 0.8$ in the acoustic impedance ratio rendered a spatially averaged root mean squared reproduction error of $\log \langle \varepsilon_{RMS} \rangle \approx -0.8$.

The shape correlation study between incident and total pressure field found that the simplified analysis performance using Equation 3.37 ranging between $0 < \psi_a < 1$ decreases linearly with the acoustic impedance ratio only in non-resonant systems and has local minimum otherwise. A maximum spatial average of this performance of $\langle \psi_a \rangle = 0.31$ was found in Section 3.4.1 for circular shape, mass density ratio $\rho_r = 7.5$ and speed of sound ratio $c_r = 1$. This parameter reflects on the shape correlation in spatially averaged synthesis performance. In Section 3.4.2, this study found that the spatially mapped synthesis performance over regular polygonal acoustic chambers only exhibits radial symmetry whereas the analysis performance also shows reflection symmetry.

The simplified synthesis performance using Equation 3.38 was found to generate high-fidelity traps at high values $\psi_s(\mathbf{r}_o) \approx 1$ whereas $\psi_s(\mathbf{r}_o) < 0.8$ to generate low-fidelity ones in Section 3.4.2. Moreover, the spatially averaged synthesis performance was found to be inferred from the spatially average shape correlation between perturbed analysis performances. The performance inference study in Section 3.4.3 showed maximum errors of 14.3% and 0.2% compared to the simplified synthesis performance for smooth hexagonal and circular shapes, respectively.

6.2.2 The Virtual Source Finite Element model

The Virtual Source Finite Element model was employed as the intermediate model using a combination of Finite Element and Virtual Source methods to solve for acoustic chambers surrounded by a piezoelectric media. This transitioning model allowed the investigation of the boundary behaviour from weakly compressible to piezoelectric crystal by tuning the electromechanical coefficient of the material model using Equations 4.6 to 4.9. This model was studied for the fluid-fluid material modelling case in Section 4.3.1 using standard Perfectly Matched Layers domain truncation method and the resulting pressure field was found convergent for 10 elements per wavelength compared to the analytical solution for an off-centred distance with errors of $\log \varepsilon_{RMS}(\lambda) \approx -3$. An Absorption Layer with Increasing Damping was implemented with coefficients defined by

Equations 4.16 as domain truncation method for arbitrarily shaped boundaries and validated in Section 4.3.1 reaching convergence threshold for layer length $l_d = 2.5\lambda$ and damping parameter $K_d \approx 10^2$. Verification for the virtual source method by employing secondary sources whose strengths defined by Equations 4.22 and 4.23. This study found results in good agreement with the analytical solution in Section 4.3.2 with approximation error of $\log \varepsilon_{RMS}(r_o) < -2$ for an average arc length $\langle |L| \rangle \approx \lambda/3$.

In Section 4.3.4 a validation for this intermediate model with virtual sources in the central region found the solution field for the simplified fluid material modelling agreed with the realistic piezoelectric one in smooth interfaces with errors up to $\log \varepsilon_{RMS}(r_o) < -2.3$. The results for the sharp hexagonal interface rendered on average low accuracy with errors up to $\log \varepsilon_{RMS}(r_o) < -0.7$. For virtual sources elsewhere, the impedance ratio within the studied range was found a sensitive parameter to the approximation error only for the smooth hexagonal shape which exhibits resonance on fluid-fluid but not on the piezoelectric-fluid interface.

A Intermediate Analysis Performance study revealed that the Virtual Source Finite Element-fluid performance predicts to some degree the robustness of realistic boundary behaviour. The results for centred virtual source in Section 4.4.1 showed excellent agreement between Intermediate and Simplified Analysis Performances with $\log \varepsilon_{RMS} < -2$ for smooth shapes and $\log \varepsilon_{RMS} = -1.4$ for sharp shapes. The study for off-centred virtual sources suggests that higher Intermediate Analysis Performance compared with Simplified Analysis Performance for a given transducer design is due the simplification of the local boundary behaviour by not considering the effects of incident wavefront direction.

6.2.3 Monolithic Ultrasonic Tweezer Device

The Transducer Parameter Finite Element model was employed as the realistic model using Finite Element Method to represent a backed monolithic piezoceramic covered with electrically decoupled terminals and simulate realistic harmonic responses to transducer excitation. For the analysis protocol, the overall effect of the electrodes on disturbing the analysis of pressure fields compared with the Virtual Source Finite Element model depended on the boundary data smoothness of the incident field. The synthesis of the pressure field computed from Equation 5.11 was applied to wide-area high-fidelity reproduction of acoustic traps inside acoustic chambers with $kR = 10\pi$ by using an optimized inverse filtering technique based on singular value decomposition. A boundary shape study in Section 5.2.3 found that circular transducer designs produce well-defined symmetric reproduction errors whereas polygonal shapes produce uncorrelated errors.

The realistic synthesis performance from Equation 5.14 was found to relate to the robustness of transducers with respect to perturbed acoustic impedance ratio. This synthesis performance was studied in Section 5.3.2 for sharp polygonal shaped boundaries and for standard $\gamma = 4\%$ and tight $\gamma = 2\%$ tolerances. This study found that the performance of pentagonal transducers with $Z_r = 26$ compared to $Z_r = 21$ dropped from $\langle \psi_s \rangle_f = 0.64$ to $\langle \psi_s \rangle_f = 0.28$ and from $\langle \psi_s \rangle_f =$

0.82 to $\langle \psi_s \rangle_f = 0.39$ for standard and tight tolerance, respectively. This rendered high loss on reproduction fidelity compared with a drop from $\langle \psi_s \rangle_f = 0.65$ to $\langle \psi_s \rangle_f = 0.40$ and from $\langle \psi_s \rangle_f = 0.83$ to $\langle \psi_s \rangle_f = 0.78$, for hexagonal transducers under the same conditions.

The application of reproduction of traps in Monolithic Ultrasonic Tweezer Devices was investigated using a novel pressure field landscaping technique based on sculpting acoustic radiation potential. This technique combined position and phase shifting of acoustic vortices with respect to arbitrary curve segments, or valleys, using Equations 5.15 and 5.17. The sculpting technique was applied in Section 5.4.2 to sculpting a "S" curve segment and produced high shape correlation coefficient from 0.944 up to 0.985 between the resulting local and a standard acoustic radiation potential for a characteristic length range of $2.25\lambda < l_C < 3.62\lambda$. The sculpting technique was applied to the reproduction of potential valleys using the Transducer Parameter Finite Element model with $kR = 20\pi$ (i.e. excitation frequency $f = 2.625\ MHz$ and radius $R \approx 10\ mm$). An application example in Section 5.4.3 rendered a partially mapped realistic synthesis performance $\langle \psi_s \rangle_p = 0.658$ and realistic potential sculpting performance $\left\langle \psi_{rp} \right\rangle_p = 0.885$ for a particular transducer design ($kR = 20\pi$, r_6^{145} and $Z_r = 26$), perturbed by $\gamma = 2\%$ and for an "S" valley with characteristic length of $l_C = 2.876$.

6.3 Future work

The areas to be considered for future work are improvements in direct and inverse modelling including considering different boundary geometries, developing models to solve for problems defined by elastic materials and alternative acoustic radiation potential techniques.

The analytical solution for the scattering problem of two-dimensional penetrable circular objects due to internal incident line source was presented and compared with the developed models for the analysis protocol. It would be more beneficial to implement this solution as a simplified model for arbitrary boundary shapes to be able verify the intermediate and realistic model with the exact solution. First, this would need the transmission boundary conditions to be matched on the arbitrary shaped interface in terms of expanded cylindrical functions to solve for the internal radiation problem. Then, expand the acoustic vortices in terms of cylindrical functions in order to apply the inverse filtering technique and obtain the incident wave field necessary for pressure field reproduction. This would allow the further studies on both analysis and synthesis performance using well-formulated analytical expressions.

One can find interesting to implement the Equivalent Source Wave Scattering model using alternative material properties other than the current developed fluid media to further bridge the gap between simplified and realistic model. This would improve the accuracy of the simplified model response compared to the realistic model. The implementation of isotropic elastic point sources is suggested as a first step to achieving better approximation. Elastic sources are directional as the acoustic dipole and an additional set of equivalent sources in the equivalent

external domain is required to solve for acoustic-structure boundary conditions. Anisotropy and piezoelectricity are also advised as material modelling. The more complex the wave propagation model the more point sources are required for solving the boundary conditions. Nevertheless, a compromise between model computational cost and accuracy is of great importance in reasoning extensions to the simplified model.

The study of the synthesis protocol to the intermediate model could be achieved by computing the externally incident wave using the transfer function and the inverse filter from the simplified model then readily applying the resulting source strengths as loads in Finite Element Method. This would allow to study the intermediate synthesis performance using alternative approximation to the material model as a system perturbation parameter. This performance parameter could also be compared with the simplified inferred performance to further investigate quantitatively the ability to predict this important design parameter.

A relevant further implementation of realistic model is to investigate three dimensional models using Finite Element Method to make validation of practical MUTD. The major advantage would be to consider any additional effect normal to the plane studied in this work. Nevertheless, three dimensional models of acoustic manipulators devices has already been studied and should justify the added computational cost as the main feature is to model complex geometries rather than prismatic ones. The major drawback is that adding a third spatial dimension would increase significantly the size of the system of equations solved as well as the number o simulations needed to compute the spatially mapped performance parameters. Any equivalent three dimensional model which implements the simplifying assumptions to further investigate each physical effect separately would have to consider fundamental solutions to the 3D wave equation.

To further evaluate manipulation capabilities of real devices a validation technique could be applied to the realistic model by comparing the electrical impedance of the transducer terminals obtained using FEM. Additional acoustic effects which occurs in the fluid chamber may be studied such as acoustic streaming and absorption, due to particle to particle interaction such as secondary acoustic forces, and particle to wall interaction such as viscous boundary layer. This realistic modelling approaches would be beneficial to the validation against acoustic manipulation experiments commonly addressed using particle manipulation observations. Furthermore, the application of arbitrary shapes in the developed modelling methodology would benefit from a design investigation for a wider range of geometries, for example chaotic chamber such as the stadium shape, i.e. a rectangle capped by semicircles.

APPENDIX

BOUNDARY PARAMETRIC CURVE

The study of different shapes throughout this work was developed based on a single boundary parametric curve. This parametrization has to follow the requirement of meeting at least with second order parametric continuity C^2 to derive continuous expressions for the arc length and radius of curvature. Based on the studies of hexagonal dielectric cavities [Wiersig, 2003a], a common expression was chosen to generate a diverse set of polygons with rounded corners defined by a polar curve $r(\theta)$ in terms of the angle θ. A parametrization of a particular curve $r\left(c,N,\theta\right)$, in terms of polar coordinates determined by two independent parameters N and c reads

$$r\left(c,N,\theta\right)=\left(\frac{N}{2\sum_{n=1}^{N}\sin\left(\frac{\theta}{2}+\frac{n\pi}{N}\right)^{c}}\right)^{\frac{4}{c}}, \tag{A.1}$$

where N is the number of sides of the polygon and c is the chamber corner. By setting $c=2$ the curve $r\left(2,N,\theta\right)$ always degenerates to a circle, whereas $c\to\infty$ gives a polygon with flat sides and sharp corners for any number of sides defined by N. It is noteworthy all curves generated by this parametrization shares the exact same circumscribed unit circle. Furthermore, a maximum curvature radius was adopted as normalization function for the subsets of the curves implemented on this thesis. A specialization of A.1 is defined as a curve classification that describes a unique parametrization $r_N^{\varsigma}=r\left(c,N,\theta\right)$ where c is a function of ς and N and is determined by expression

$$c=\begin{cases}\frac{N^{1.76}}{K(N)}2^{\left(\frac{\varsigma-3}{2}\right)} & \text{for} \quad \varsigma>1\\ 2 & \text{for} \quad \varsigma=0\end{cases}, \tag{A.2}$$

where K is determined by linearisation as an approximation method to the normalization procedure applied to maximum curvature radius. The values obtained using this approximation for $N=\{5,6,7,8\}$ are shown in the table A.1.

Table A.1: Values of K in terms of numbers of sides N.

N	K
5	1.000
6	0.997
7	0.985
8	0.975

From the parametrization in A.1 several functions based on differential geometry of curves can be derived in order to support modelling presented in this thesis, namely normal vector, arc length and radius of curvature. The normal vector $\hat{n}$ is given by

$$\begin{aligned}\hat{n} = &\left[-r_\theta \sin\left(\theta\right) + r\cos\left(\theta\right)\right]\hat{x} \\ &+ \left[r_\theta \cos\left(\theta\right) - r\sin\left(\theta\right)\right]\hat{y},\end{aligned} \tag{A.3}$$

in Cartesian coordinate system. The length of L given by the arc length between points corresponding to θ_a and θ_b such that $0 \leqslant b - a < 2\pi$ is given by the following integral

$$L = \int_{\theta_a}^{\theta_b} \sqrt{r^2 + r_\theta^2}\, d\theta, \tag{A.4}$$

where $r_\theta = dr/d\theta$. The radius of curvature ρ is defined by

$$\rho = \frac{\left(r^2 + r_\theta^2\right)^{3/2}}{r^2 + 2r_\theta^2 - r r_{\theta\theta}}, \tag{A.5}$$

where $r_{\theta\theta} = d^2r/d\theta^2$. The calculations are computed numerically using the following expressions:

$$\begin{aligned}r &= \left(\frac{2b}{N}\right)^{-\frac{4}{c}} \\ r_\theta &= -\frac{4}{c}\left(\frac{2b}{N}\right)^{-\left(\frac{4}{c}+1\right)} \frac{b_\theta 2}{N} \\ r_{\theta\theta} &= -\frac{4}{c}\left(\frac{2b}{N}\right)^{-\left(\frac{4}{c}+1\right)} \left(-\left(\frac{4}{c}+1\right)\left(\frac{2b}{N}\right)\frac{b_\theta^2 c^2}{2N} + \frac{b_{\theta\theta} c}{4}\right)\frac{2}{N},\end{aligned}$$

where the b, b_θ and $b_{\theta\theta}$ are defined by the summation over the number of sides N

$$\begin{aligned}b &= \sum_{n=1}^{N} a^c \\ b_\theta &= \sum_{n=1}^{N} a^{(c-1)} a_\theta \\ b_{\theta\theta} &= \sum_{n=1}^{N} (c-1)a^{(c-2)}a_\theta^2 + a^{(c-1)}a_{\theta\theta},\end{aligned}$$

and a, a_θ and $a_{\theta\theta}$ are simple derivatives of the trigonometric function as in

$$a = \sin\left(\frac{\theta}{2} + \frac{n}{N}\pi\right)$$
$$a_\theta = \cos\left(\frac{\theta}{2} + \frac{n}{N}\pi\right)$$
$$a_{\theta\theta} = -\sin\left(\frac{\theta}{2} + \frac{n}{N}\pi\right).$$

These expressions can be evaluated in the polar coordinate system for a set of n_p coordinates $\theta = (\theta_1, \cdots, \theta_{n_p})$ which are equally spaced and uniformly distributed over the circumscribed circumference. Furthermore, the intermediate angles which defines each piecewise linear boundary (Γ_k^1, Γ_k^2) implemented in the dual terminal representation for the realistic model (see Section 5.1.1) are given by the expression

$$\theta_k^n = \theta_k + (n - \frac{3}{2})\frac{\pi}{n_p}\left[1 + (-A, A)\right], \quad \text{for } k = 0, 1, \ldots, n_p - 1 \quad \text{and} \quad \text{for } j = 1, 2 \quad , \tag{A.6}$$

where $0 < A < 1$ is the fraction between the active and total arcs for each circumference segment centred at θ_k and the nomenclature $(,)$ indicates the start θ_s and θ_e end coordinates of each interval. For instance, each boundary segment Γ_k^n is defined between the pair of coordinates (r_s, r_e) for the coordinates pair $\theta_k^n = (\theta_s, \theta_e)$.

A validation region within the polar curve $r(\theta)$ where field parameters are calculated throughout the thesis is defined by an internal polar curve at a distance ξ_a away from the original curve in the normal direction. This validation curve is given by

$$g_N^\varsigma(\xi_a) = r_N^\varsigma + \xi_a \hat{n}_N^\varsigma \tag{A.7}$$

The integral in Equation A.4 is calculated using Gauss-Legendre quadrature [Press et al., 1992] rules with tolerance attained to 10^{-9} and the Legendre polynominal roots are computed using Newton's method with tolerance attained to 10^{-10} for a initial guess given by Abramowitz [1974] §22.16.6 . Curves are categorized by the number of sides (or symmetry), namely 5, 6, 7, 8-sided for $N = \{5, 6, 7, 8\}$, respectively.

Some results are presented in Table A.2 to A.9 showing the parameters θ_k, r_N^ς, $\hat{n}$, ρ, L for reference. Tables below show a partial set of points because the symmetry of the geometries renders either reflected values or shifted by a fraction of π. It is noteworthy the chamber corner ς determines the minimum curvature ρ of any group r^ς and scales the total length L for any group r_N.

Table A.2: Curve parameters for $N = 5$, $\varsigma = 65$ and $n_p/N = 19$.

k	θ_k	r_5^{65}	$\hat{n}$	ρ	L
1	-2.44713533	1.12102459	0.848266207	0.376235515	0.0750307454
2	-2.38099654	1.10530144	1.01655496	0.555108653	0.075514961
3	-2.31485774	1.08439141	1.12381778	0.920568639	0.0749613124
4	-2.24871895	1.06258031	1.18598426	1.60200315	0.0733913704
5	-2.18258016	1.04263723	1.22038718	2.86309787	0.07138733
6	-2.11644137	1.02600065	1.2388723	5.26807827	0.0694538186
7	-2.05030257	1.01330722	1.24849176	10.107678	0.0678762442
8	-1.98416378	1.00479501	1.25331143	20.1200422	0.0667851245
9	-1.91802499	1.00053286	1.25576586	35.6444398	0.0662314843
10	-1.8518862	1.00053286	1.25750826	35.6444398	0.0662314843
11	-1.7857474	1.00479501	1.2599627	20.1200422	0.0667851245
12	-1.71960861	1.01330722	1.26478236	10.107678	0.0678762442
13	-1.65346982	1.02600065	1.27440183	5.26807827	0.0694538186
14	-1.58733102	1.04263723	1.29288694	2.86309787	0.07138733
15	-1.52119223	1.06258031	1.32728986	1.60200315	0.0733913704
16	-1.45505344	1.08439141	1.38945635	0.920568635	0.0749613124
17	-1.38891465	1.10530144	1.49671917	0.555108643	0.0755149609
18	-1.32277585	1.12102459	1.66500796	0.376235495	0.0750307449
19	-1.25663706	1.1269655	1.88495559	0.322755102	0.0745850996

Table A.3: Curve parameters for $N = 5$, $\varsigma = 145$ and $n_p/N = 19$.

k	θ_k	r_5^{145}	$\hat{n}$	ρ	L
1	-2.44713533	1.17329691	1.20259848	1.18035916	0.0882192098
2	-2.38099654	1.13236167	1.22914048	7.48830012	0.0839677983
3	-2.31485774	1.0976026	1.23842555	9.94988217	0.0792476467
4	-2.24871895	1.06879295	1.24534207	12.7404609	0.0753506981
5	-2.18258016	1.04545755	1.25032357	17.6418821	0.0722156551
6	-2.11644137	1.02721665	1.25361652	27.4134825	0.0697783341
7	-2.05030257	1.01377949	1.25552213	51.2575657	0.0679902187
8	-1.98416378	1.00493529	1.25639415	137.930312	0.0668166484
9	-1.91802499	1.00054697	1.25662803	1221.67776	0.0662353203
10	-1.8518862	1.00054697	1.2566461	1221.67776	0.0662353203
11	-1.7857474	1.00493529	1.25687998	137.930312	0.0668166484
12	-1.71960861	1.01377949	1.25775199	51.2575657	0.0679902187
13	-1.65346982	1.02721665	1.2596576	27.4134825	0.0697783341
14	-1.58733102	1.04545755	1.26295055	17.6418821	0.0722156551
15	-1.52119223	1.06879295	1.26793205	12.7404609	0.0753506981
16	-1.45505344	1.0976026	1.27484857	9.94988217	0.0792476467
17	-1.38891465	1.13236167	1.28413364	7.48830012	0.0839677983
18	-1.32277585	1.17329691	1.31067564	1.18035916	0.0882192098
19	-1.25663706	1.20478715	1.88495559	0.0596803482	0.0829624424

Table A.4: Curve parameters for $N = 6$, $\varsigma = 65$ and $n_p/N = 16$.

k	θ_k	r_6^{65}	$\hat{n}$	ρ	L
1	-2.55254403	1.07800157	0.727336443	0.393549922	0.0712276648
2	-2.48709418	1.06486311	0.875214869	0.62344633	0.0713838944
3	-2.42164434	1.04826331	0.961653832	1.13735689	0.0706347103
4	-2.35619449	1.03202773	1.00679018	2.21506065	0.0692331152
5	-2.29074464	1.0183451	1.02903886	4.4974977	0.067735256
6	-2.2252948	1.00822384	1.03959485	9.46649499	0.0665119777
7	-2.15984495	1.00206358	1.0445264	19.4756191	0.0657359022
8	-2.0943951	1	1.04719755	28.1184891	0.0654719662
9	-2.02894526	1.00206358	1.0498687	19.4756191	0.0657359022
10	-1.96349541	1.00822384	1.05480025	9.46649498	0.0665119777
11	-1.89804556	1.0183451	1.06535624	4.4974977	0.067735256
12	-1.83259571	1.03202773	1.08760492	2.21506064	0.0692331152
13	-1.76714587	1.04826331	1.13274127	1.13735686	0.0706347103
14	-1.70169602	1.06486311	1.21918026	0.623446268	0.0713838939
15	-1.63624617	1.07800157	1.36705884	0.393549819	0.0712276632
16	-1.57079633	1.08312034	1.57079633	0.328142745	0.0709264178

Table A.5: Curve parameters for $N = 6$, $\varsigma = 145$ and $n_p/N = 16$.

k	θ_k	r_6^{145}	$\hat{n}$	ρ	L
1	-2.55254403	1.11153237	1.01712104	1.71094331	0.0796429847
2	-2.48709418	1.0806963	1.0330461	10.7401827	0.0761492495
3	-2.42164434	1.05525946	1.03887664	15.0600332	0.0727635719
4	-2.35619449	1.03496517	1.04285944	22.0094362	0.0700740688
5	-2.29074464	1.01949521	1.04534075	37.0908273	0.0680333867
6	-2.2252948	1.00861035	1.04664157	80.2865024	0.0666023893
7	-2.15984495	1.00214452	1.04712761	313.709937	0.065754222
8	-2.0943951	1	1.04719755	2.21669031e+14	0.0654732161
9	-2.02894526	1.00214452	1.04726749	313.709937	0.065754222
10	-1.96349541	1.00861035	1.04775353	80.2865024	0.0666023893
11	-1.89804556	1.01949521	1.04905436	37.0908273	0.0680333867
12	-1.83259571	1.03496517	1.05153566	22.0094362	0.0700740688
13	-1.76714587	1.05525946	1.05551846	15.0600332	0.0727635719
14	-1.70169602	1.0806963	1.06134901	10.7401827	0.0761492495
15	-1.63624617	1.11153237	1.07727406	1.71094331	0.0796429847
16	-1.57079633	1.13682438	1.57079633	0.0598134737	0.0768295662

Table A.6: Curve parameters for $N = 7$, $\varsigma = 65$ and $n_p/N = 14$.

k	θ_k	r_7^{65}	$\hat{n}$	ρ	L
1	-2.62867957	1.05445525	0.640076366	0.410436682	0.0681431591
2	-2.56456543	1.04315472	0.771046045	0.704285116	0.0681224943
3	-2.5004513	1.02961699	0.840867969	1.42198068	0.0673359597
4	-2.43633716	1.01725344	0.873670714	3.09862791	0.0661618197
5	-2.37222302	1.00779846	0.888154981	7.04959312	0.0650885722
6	-2.30810889	1.00196414	0.894425285	15.6432806	0.0643792231
7	-2.24399475	1	0.897597901	23.6047533	0.0641347026
8	-2.17988062	1.00196414	0.900770517	15.6432806	0.0643792231
9	-2.11576648	1.00779846	0.907040821	7.04959311	0.0650885722
10	-2.05165235	1.01725344	0.921525089	3.09862788	0.0661618197
11	-1.98753821	1.02961699	0.95432784	1.42198061	0.0673359596
12	-1.92342407	1.04315472	1.0241498	0.704284969	0.0681224936
13	-1.85930994	1.05445525	1.15511975	0.410436447	0.0681431564
14	-1.7951958	1.05900274	1.34639685	0.331058229	0.0679261645

Table A.7: Curve parameters for $N = 7$, $\varsigma = 145$ and $n_p/N = 14$.

k	θ_k	r_7^{145}	$\hat{n}$	ρ	L
1	-2.62867957	1.07722418	0.879826956	2.52185329	0.0738152999
2	-2.56456543	1.05295864	0.88973434	15.1315086	0.0709764129
3	-2.5004513	1.03352521	0.893514455	22.8180324	0.0684565065
4	-2.43633716	1.01869906	0.895851148	38.5442165	0.0665412867
5	-2.37222302	1.00826082	0.897075095	83.5614388	0.0651972498
6	-2.30810889	1.00205778	0.897532149	326.813868	0.0644002288
7	-2.24399475	1	0.897597901	6.01729275e+13	0.064136103
8	-2.17988062	1.00205778	0.897663653	326.813868	0.0644002288
9	-2.11576648	1.00826082	0.898120707	83.5614388	0.0651972498
10	-2.05165235	1.01869906	0.899344654	38.5442165	0.0665412867
11	-1.98753821	1.03352521	0.901681347	22.8180324	0.0684565065
12	-1.92342407	1.05295864	0.905461462	15.1315086	0.0709764129
13	-1.85930994	1.07722418	0.915368846	2.52185329	0.0738152999
14	-1.7951958	1.09824274	1.34639685	0.059900075	0.0722863728

Table A.8: Curve parameters for $N = 8$, $\varsigma = 65$ and $n_p/N = 12$.

k	θ_k	r_8^{65}	$\hat{n}$	ρ	L
1	-2.68344372	1.03966471	0.580270892	0.437731325	0.0685362534
2	-2.61799388	1.02913336	0.69713873	0.853606785	0.0683504973
3	-2.55254403	1.01751596	0.751301638	2.00070617	0.0674777636
4	-2.48709418	1.00802629	0.773194015	5.07606467	0.0664562104
5	-2.42164434	1.00203274	0.781628215	12.7788591	0.0657280542
6	-2.35619449	1	0.785398163	21.0291881	0.0654715384
7	-2.29074464	1.00203274	0.789168112	12.778859	0.0657280542
8	-2.2252948	1.00802629	0.797602313	5.07606462	0.0664562104
9	-2.15984495	1.01751596	0.819494694	2.00070605	0.0674777635
10	-2.0943951	1.02913336	0.873657643	0.853606548	0.0683504967
11	-2.02894526	1.03966471	0.990525812	0.437730942	0.0685362503
12	-1.96349541	1.04412476	1.17809725	0.333505656	0.0683652448

Table A.9: Curve parameters for $N = 8$, $\varsigma = 145$ and $n_p/N = 12$.

k	θ_k	r_8^{145}	$\hat{n}$	ρ	L
1	-2.68344372	1.05523404	0.775118631	4.46133891	0.0726033148
2	-2.61799388	1.0349651	0.781054546	21.7873964	0.0700736959
3	-2.55254403	1.01949521	0.783541344	37.0890355	0.0680333859
4	-2.48709418	1.00861035	0.784842186	80.2864801	0.0666023893
5	-2.42164434	1.00214452	0.785328222	313.709936	0.065754222
6	-2.35619449	1	0.785398163	2.46800667e+13	0.0654732161
7	-2.29074464	1.00214452	0.785468105	313.709936	0.065754222
8	-2.2252948	1.00861035	0.78595414	80.2864801	0.0666023893
9	-2.15984495	1.01949521	0.787254983	37.0890355	0.0680333859
10	-2.0943951	1.0349651	0.789741781	21.7873964	0.0700736959
11	-2.02894526	1.05523404	0.795677696	4.46133891	0.0726033148
12	-1.96349541	1.07410615	1.17809725	0.0600359498	0.0719238133

APPENDIX B

SPATIALLY MAPPED PARAMETERS

A validation metric is implemented to assess the wave field solutions presented hereafter. This metric is based on two statistical associations in terms of the pressure field in domain Ω_i, a relative error ε and a shape correlation Ψ. A map of these parameters is defined based on the centre of the expansion r_o of a generating wave which spatially extend the parameter analysis over the internal domain. In the case of the analysis of pressure field the generating wave is that of one produced by a point source with centre r_o as incident wave p^o, whereas in the synthesis of pressure field the generating wave is that of one reproduced by a Bessel beam with centre r_o as transmitted wave p^t. Two alternative functions are defined for the spatial average parameter $\langle\cdot\rangle_f$ for fully and $\langle\cdot\rangle_p$ for partially mapped parameter given by

$$\langle\cdot\rangle_f(p_1,p_2) = \iint_\Omega (\cdot)(p_1,p_2,r_o)d\Omega, \tag{B.1}$$

$$\langle\cdot\rangle_p(p_1,p_2) = \int_l (\cdot)(p_1,p_2,r_o)dl, \tag{B.2}$$

where $\langle\cdot\rangle$ is the mapped parameter, p_1 and p_2 are any pressure field refer by the parameters and l is a curve segment by default $\mathbf{r} = (r,\pi)$ or defined elsewhere, in polar coordinates for $0 \leqslant r < R$ where R is the radius of the circumscribed circle of the physical boundary Γ, hence the scaling factor for r_N^ς (see Appendix A for details).

Relative error

The normalized RMS error (NRMSE) $\langle\varepsilon\rangle$ is used as the relative error to assess the accuracy of a solution fields. The spatially mapped error $\varepsilon(r_o)$ is presented whenever two solution fields obtained from distinct physics-based models are validated.

$$\varepsilon\left(p_1,p_2,r_o\right) = \frac{p_{1i}(r_o) - p_{2i}(r_o)}{p_{1max}(r_o) - p_{1min}(r_o)}. \tag{B.3}$$

Then the RMS error is simply

$$\varepsilon_{rms} = \sqrt{\frac{\sum_{i=1}^{n} \varepsilon^2}{n}}, \tag{B.4}$$

where n is the total number of points in a rectangular grid over internal domain Ω_i. To illustrate the partially mapped approximation rms error is defined below

$$\langle \varepsilon_{rms} \rangle_p (p_1, p_2) = \sum_{r_o=0}^{R} \sqrt{\frac{1}{n} \frac{\sum_{i=1}^{n} (p_{1i}(r_o) - p_{2i}(r_o))^2}{\left(p_{1max}(r_o) - p_{1min}(r_o)\right)^2}} dr_o,$$

where $\varepsilon_{rms}(r_o)$ is averaged over a line from the centre $r_o = 0$ to the closest edge of internal domain Ω_i ($r_o = R$).

Shape correlation

A shape correlation coefficient ψ, also referred to as performance, is used to assess the linear relationship between two distinct modes obtained. This statistical association provides a measure of the least squares deviation of the points from the straight line correlation. The spatially mapped correlation in terms of the centre of the generating wave field is computed whenever two solution fields obtained from distinct pressure field responses are correlated.

$$\psi(p_1, p_2, r_o) = \frac{\left| p_1(r_o)^\dagger p_2(r_o) \right|^2}{(p_1(r_o)^\dagger p_1(r_o))(p_2(r_o)^\dagger p_2(r_o))}, \tag{B.5}$$

where r_o is the centre of the generating wave field. Similar to the MAC, ψ is bounded between zero and unity, it cannot detect scaling errors and it is only sensitive to discrepancies in the overall shape of the pressure field. Three alternatives implementation of the performance is applied to the parameter study, namely ψ_a analysis, ψ_s synthesis and ψ_i inferred performance as given by

$$\psi_a = \psi \left(p^T(Z_r), p^o, r_o \right) \tag{B.6}$$

$$\psi_s = \psi \left(p^t(Z_r), p^t(\gamma Z_r), r_o \right) \tag{B.7}$$

$$\psi_i = \psi \left(p^r(Z_r), p^r(\gamma Z_r), r_o \right), \tag{B.8}$$

where Z_r is the impedance ratio, γ is the perturbation factor. Each performance parameter is defined in domain Ω_i bounded by Γ and scaled to R. Such a local measure is not suitable for evaluating shape response, so a global measure $\langle \psi \rangle$ is defined as a weighted integral in domain Γ defined by the relations in Equations B.1 and B.2.

APPENDIX C

ANALYTICAL PRESSURE FIELD

This appendix presents the equations for calculating the analytical solution for internal point source employed in the analysis and the synthesis loading scenario and the definition of the boundary data (i.e. the pressure and particle velocity) of the generating waves on the physical boundary employed in both the analysis and the synthesis loading scenario.

C.1 Analytical solution for internal point source

The problem stated in Section 2.2 is solved here for a incident wave completely defined in the interior domain Ω. This problem is that of a source laying inside the boundary of the penetrable object, as shown in Figure C.1. The reference case problem is solved in this appendix based on cylindrical wave functions [Harrington, 1961] (see Section 2.2) is adopted as comparison model for verification purposes to the ESWS (see Chapter 3), for the VSFE (see Chapter 4) and for the TPFE (see Chapter 5). The incident pressure field p^o is expressed as a series in terms of cylindrical waves exactly the same as Equation 2.19 e here is repeated for completeness as

$$p^o(\mathbf{r}) = \begin{cases} p_0 \frac{i}{4} \sum_{n=-\infty}^{\infty} J_n\left(k|\mathbf{r}'|\right) H_n^{(2)}\left(k|\mathbf{r}|\right) e^{in\phi} \mathbf{r} > \mathbf{r}' \\ p_0 \frac{i}{4} \sum_{n=-\infty}^{\infty} H_n^{(2)}\left(k|\mathbf{r}'|\right) J_n\left(k|\mathbf{r}|\right) e^{in\phi} \mathbf{r} < \mathbf{r}' \end{cases} . \tag{C.1}$$

where $k = \omega/c$ is the object characteristic wave number , J_n and $H_n^{(2)}$ denotes the n-order Bessel function and Hankel of the second kind, respectively. The solution for the reflected p^s and transmitted p^t wave can be expressed in a similar form as the Equation 2.20 and Equation 2.20, respectively. The analysis can be derived similarly except that the reflected and transmitted

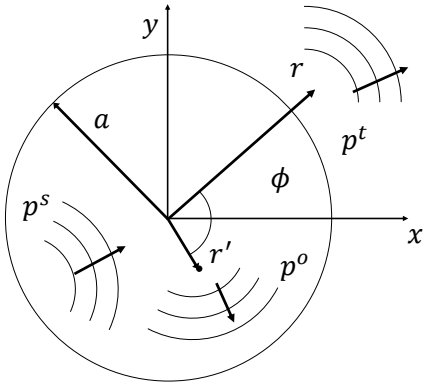

FIGURE C.1. Representation of incident p^o, scattered p^s and transmitted p^t wave for a line source located inside a penetrable object. The object is an infinite cylinder with radius a, the line source is positioned at $\mathbf{r}'$, the field point at $\mathbf{r}$ relative to the source.

waves are defined on alternative domains where the corresponding fields are internal and external respectively with respect to the boundary. From the above analysis it is clear that

$$p^s(\mathbf{r}) = p_0 \frac{i}{4} \sum_{n=-\infty}^{\infty} a_n J_n\left(k|\mathbf{r}|\right) J_n\left(k\left|\mathbf{r}'\right|\right) e^{in\phi} \tag{C.2}$$

$$p^t(\mathbf{r}) = p_0 \frac{i}{4} \sum_{n=-\infty}^{\infty} b_n H_n^{(2)}\left(k|\mathbf{r}|\right) J_n\left(k\left|\mathbf{r}'\right|\right) e^{in\phi}, \tag{C.3}$$

where the coefficients a_n and b_n are found by matching the transmission boundary conditions at $\mathbf{r} = a$, as in $p^t = p^o + p^r$ and $v^t = v^o + v^s$:

$$a_n = -\frac{H_n^{(2)}\left(ka\right)}{J_n\left(ka\right)} c_n \tag{C.4}$$

$$b_n = -\frac{H_n^{(2)}\left(ka\right)}{H_n^{(2)}\left(k_o a\right)} \left[1 - a_n\right], \tag{C.5}$$

where c_n is given by

$$c_n = \frac{Z_r H_n^{(2)'}\left(k_o a\right)/H_n^{(2)}\left(k_o a\right) - H_n^{(2)'}\left(ka\right)/H_n^{(2)}\left(ka\right)}{Z_r H_n^{(2)'}\left(k_o a\right)/H_n^{(2)}\left(k_o a\right) - J_n^{'}\left(ka\right)/J_n\left(ka\right)}. \tag{C.6}$$

where Z_r is the impedance ratio between object over host fluid and $k_o = \omega/c_o$ is the host characteristic wave number. The Equations C.2 and C.3 gives the solution for the system of equations in Equation 2.10 where the external pressure is $p_e \equiv p^t$ and the internal pressure is $p_i \equiv p^s$.

C.2 Boundary data for analysis

The generating wave used in the analysis of pressure field is that of a monopole defined in the internal domain Ω_i. The expressions are obtained from the same equations that defines the fundamental solution used for the ESWS model. Considering $\mathbf{r}'$ and $\mathbf{r}$ are the source and field point coordinates, respectively. In this case, the incident pressure field p^o and the respective normal component of particle velocity v^o may be directly expressed in term of the free space Greens' function in Equations 2.13 and 2.14 and is written in a matrix form as in

$$\mathbf{b}_o = \begin{bmatrix} v^o \\ p^o \end{bmatrix} = \begin{bmatrix} \frac{p_0}{Z}\frac{i}{4}H_1^{(1)}(k|\mathbf{r}'-\mathbf{r}|)\cos\alpha \\ -p_0\frac{i}{4}H_0^{(1)}(k|\mathbf{r}'-\mathbf{r}|) \end{bmatrix}, \tag{C.7}$$

where p_0 is the pressure amplitude, Z is the acoustic impedance and the director cosine is defined between the vectors $\mathbf{r}'-\mathbf{r}$ and the normal $\mathbf{n}_r$ as in

$$\cos\alpha = \frac{(\mathbf{r}'-\mathbf{r})\cdot\mathbf{n}_r}{|\mathbf{r}'-\mathbf{r}|}.$$

C.3 Boundary data for synthesis

The generating wave used in the synthesis of pressure field is that of a first order Bessel beam defined in the internal domain Ω_i. The expressions are obtained from the same equations that defines the fundamental solution used for the ESWS model. Considering $\mathbf{r}'$ and $\mathbf{r}$ are the centre of expansion of the Bessel beam and field point coordinates, respectively. In this case, the internal pressure field p_i and the respective particle velocity v_i may be directly expressed in term of the free space Greens' function as in

$$\mathbf{b}_i = \begin{bmatrix} v_i \\ p_i \end{bmatrix} = \begin{bmatrix} \frac{p_0}{Z}\frac{i}{4}\left(J_2\left(k|\mathbf{r}'-\mathbf{r}|\right)\cos\alpha + i\frac{1}{|\mathbf{r}'-\mathbf{r}|}J_1\left(k|\mathbf{r}'-\mathbf{r}|\right)\sin\alpha\right)e^{i\phi} \\ p_0\frac{i}{4}J_1\left(k|\mathbf{r}'-\mathbf{r}|\right)e^{i\phi} \end{bmatrix}, \tag{C.8}$$

where J_2 is the second order Bessel function and the director sine is defined between the vectors $\mathbf{r}'-\mathbf{r}$ and the normal $\mathbf{n}_r$ as in

$$\sin\alpha = \frac{(\mathbf{r}'-\mathbf{r})\times\mathbf{n}_r}{|\mathbf{r}'-\mathbf{r}|}.$$

APPENDIX D

FURTHER STUDY ON THE TUNING SOLUTION FIELD

This appendix presents further study on the tuning solution field of how the modelling of the propagation phenomena for each material modelling affects the analysis field within the acoustic chamber.

The first step to investigate the effects of simplification of material properties is to quantify the effects of the piezoelectric coefficient on the chamber response to the analysis loading scenario. This approximation is achieved by setting the piezoelectric constants to zero hence suppressing coupling between displacement u and electric potential φ in the active layer. The equivalent material result of disabling this coupling effect of a $6mm$ class piezoceramic is that of one characterized by a transverse isotropic elastic media. For this media, elastic wave propagation is isotropic in planes that are perpendicular to the polarization direction of the piezoceramic. In the VSFE model, polarization of the PZT material is defined by the system of coordinates aligned with physical boundary.

The goal of this section is to investigate the VSFE-piezo analysis field to an internally located point source for some transducer design examples and compare with the response for each material modelling. The incident pressure field is defined by a zeroth order Hankel function centred within the internal domain (see Appendix C for definition). This is achieved by means of virtual source method (see Section 4.2.3) implemented for the VSFE model.

To illustrate the methods described for the implementation of the VSFE model, a series of results is presented for each level of approximation, namely transverse isotropic, isotropic and incompressible fluid with the approximation errors denoted as ε^T,ε^I,ε^F, respectively. Table 4.1 lists the piezoelectric coupling and relative permittivity used for calculating the analysis field p^s. Table 4.2 the elastic properties for each simplified material model using the procedure described in Section 4.1.2. The mass density for the material model studied here is fixed to $\rho = 7500\ \mathrm{kg\,m^{-1}}$ despite the fact that the real mass density of PZT-5A is $\rho = 7753\ \mathrm{kg\,m^{-1}}$. The approximating

errors are calculated using the expression

$$\varepsilon = \frac{\mathbf{p}_s - \mathbf{p}_{VSFE^A}}{max\left(\mathbf{p}_s\right)} \tag{D.1}$$

where the superscript A denotes each level of approximation T, I, or F.

Figures D.1 to D.7 show the results for different transducer design and point source positioning. Each figure shows the analysis field p^s and the approximation errors for different acoustic impedance ratio ranging from $Z_r = 11.25$ to $Z_r = 22.5$. Results for circular shape are shown in Figures D.1 to D.3, for smooth hexagonal shape in Figures D.4 to D.6 and for sharp hexagonal shape in Figures D.7 to D.9. A summary of the findings is presented below.

- Circular shape with $r_o = 0$ (see Figure D.1): The fluid-like material model approximates best for lower Z_r and closest agreement is always achieved for higher approximation level.
- Circular shape with $r_o = 1.25\lambda$ (see Figure D.2): Low accuracy is attained throughout approximation levels and Z_r and closest agreement is only achieved for $Z_r = 22.5$ and higher approximation level.
- Circular shape with $r_o = 1.75\lambda$ (see Figure D.3): Low accuracy and indifferent approximation error is attained throughout approximation levels.
- Smooth hexagonal shape with $r_o = 0$ (see Figure D.4): The isotropic material model approximates better than the transverse isotropic for higher Z_r and indifferent for lower Z_r.
- Smooth hexagonal shape with $r_o = 0.625\lambda$ (see Figure D.5): Low accuracy is attained throughout approximation levels and Z_r and worst agreement for fluid-like material model with $Z_r = 15$.
- Smooth hexagonal shape with $r_o = 1.25\lambda$ (see Figure D.6): Same as previous results but approximation errors are overall higher than for $r_o = 0.625\lambda$.
- Sharp hexagonal shape with $r_o = 0$ (see Figure D.7): Low accuracy is attained throughout approximation levels and Z_r and closest agreement is only achieved for higher Z_r and approximation level.
- Sharp hexagonal shape with $r_o = 1.25\lambda$ (see Figure D.8): Low accuracy is attained throughout approximation levels and Z_r and worst agreement for fluid-like material model with $Z_r = 22.5$.
- Sharp hexagonal shape with $r_o = 1.75\lambda$ (see Figure D.9): Low accuracy and indifferent approximation error is attained throughout approximation levels.

The results investigated demonstrate that each material modelling presents a unique boundary behaviour which makes a common trend difficult to identify. Some resonant modes are excited for particular boundary shapes, point source location and material model.

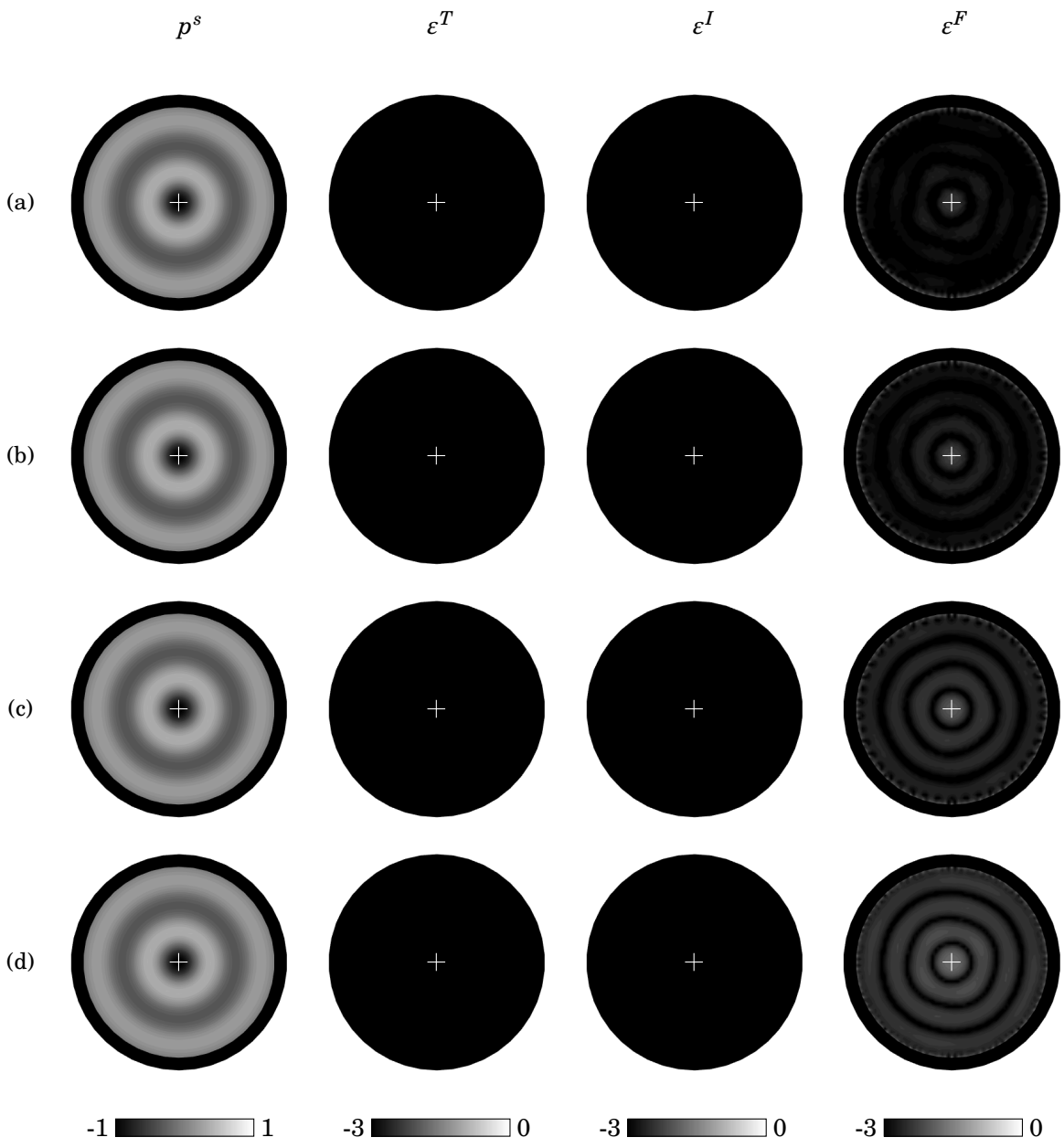

FIGURE D.1. Simulated VSFE-piezo analysis field for the circular shape with centred point source $r_o = 0$. Results are compared with various material modelling approximation levels. Real value analysis field p^s and approximating errors ε^T,ε^I,ε^F are in log scale, for $Z_r = 11.25$ (a), 15 (b), 18.75 (c),22.5 (d). White cross represents the point source position r_o

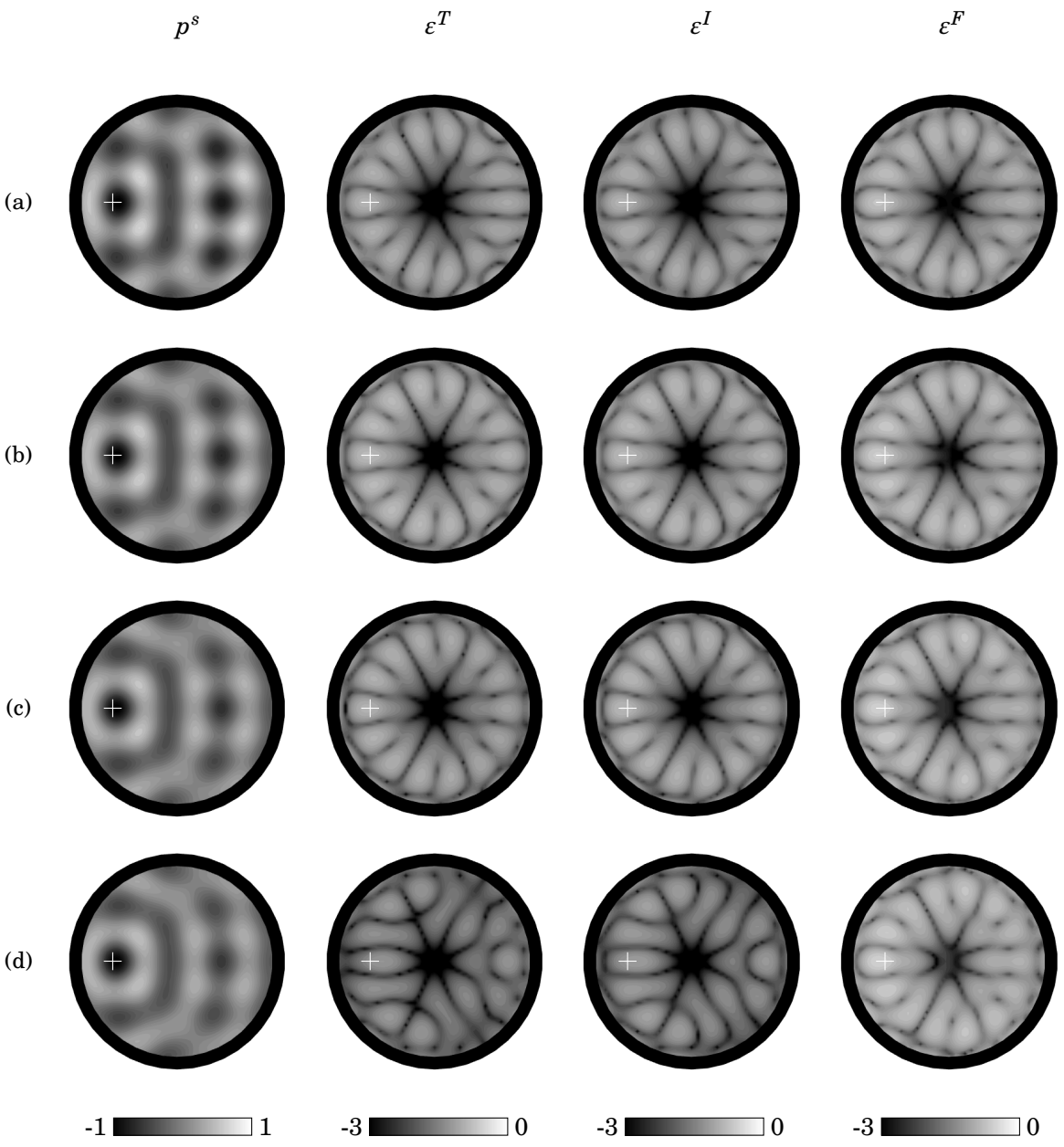

FIGURE D.2. Simulated VSFE-piezo analysis field for the circular shape with off-centred point source $r_o = 1.25\lambda$. Results are compared with various material modelling approximation levels. Real value analysis field p^s and approximating errors ε^T,ε^I,ε^F are in log scale, for $Z_r = 11.25$ (a), 15 (b), 18.75 (c),22.5 (d). White cross represents the point source position r_o

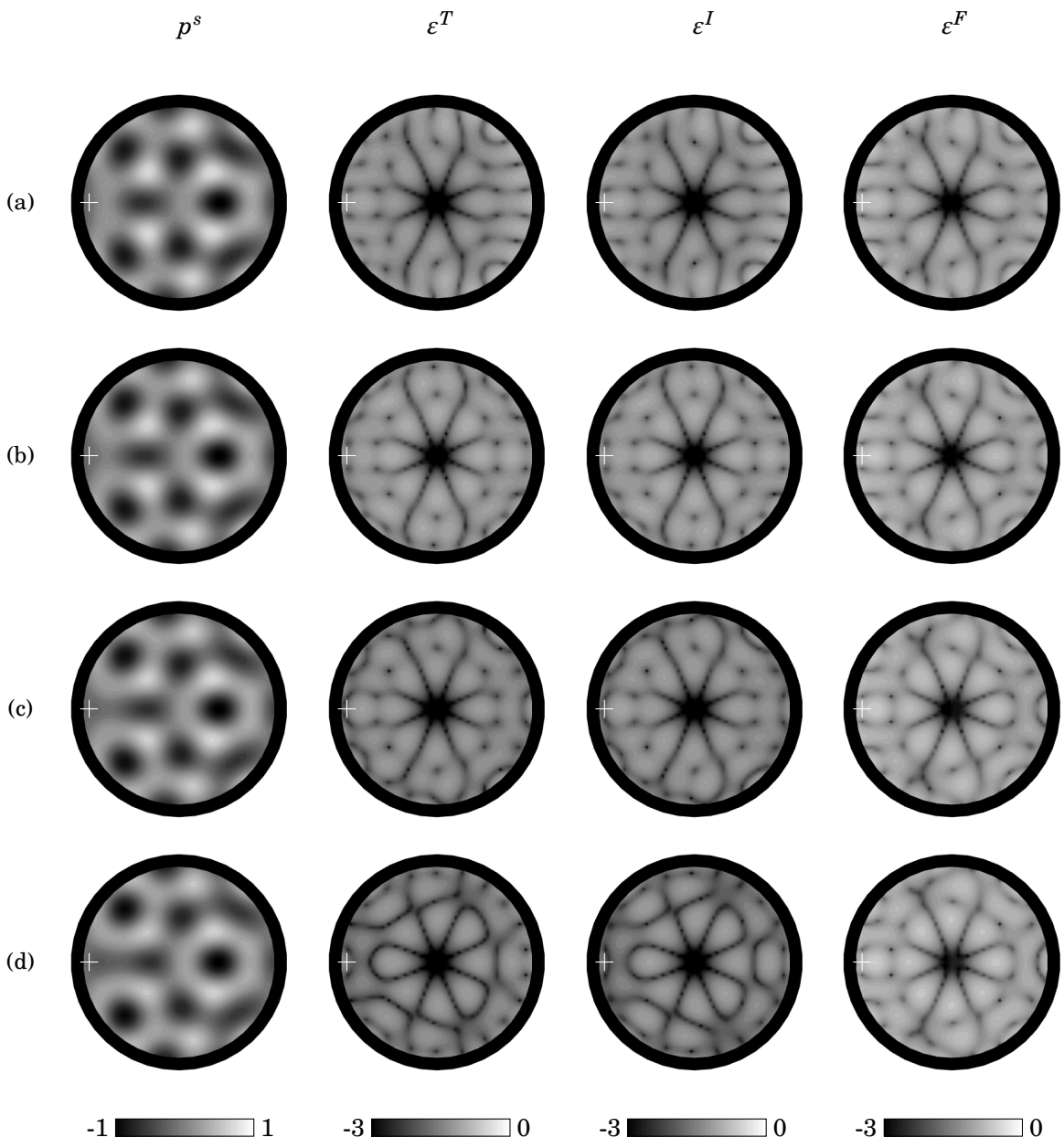

FIGURE D.3. Simulated VSFE-piezo analysis field for the circular shape with off-centred point source $r_o = 1.75\lambda$. Results are compared with various material modelling approximation levels. Real value analysis field p^s and approximating errors ε^T,ε^I,ε^F are in log scale, for Z_r = 11.25 (a), 15 (b), 18.75 (c),22.5 (d). White cross represents the point source position r_o

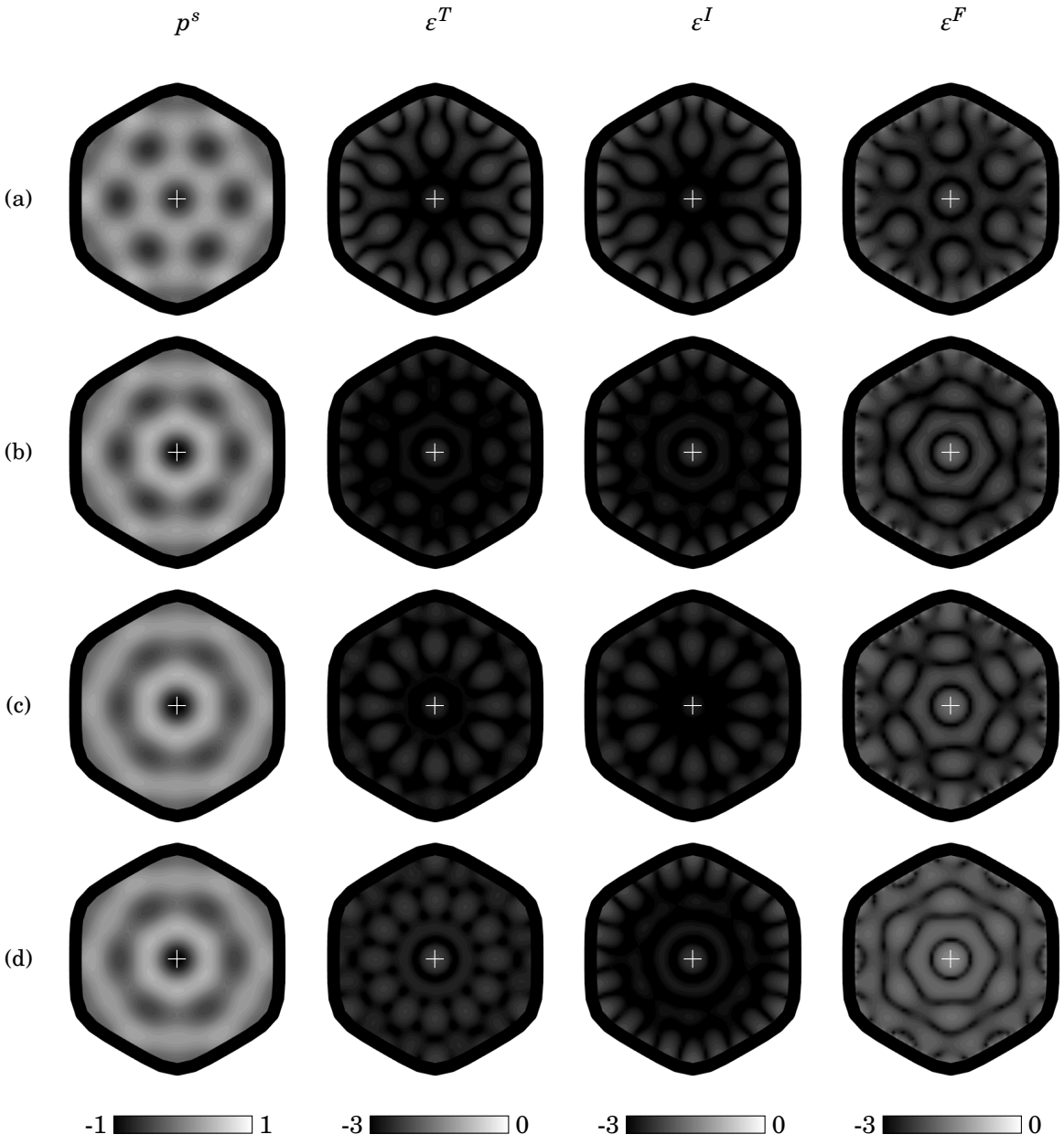

FIGURE D.4. Simulated VSFE-piezo analysis field for the smooth hexagonal shape with centred point source $r_o = 0$. Results are compared with various material modelling approximation levels. Real value analysis field p^s and approximating errors ε^T,ε^I,ε^F are in log scale, for $Z_r = 11.25$ (a), 15 (b), 18.75 (c),22.5 (d). White cross represents the point source position r_o

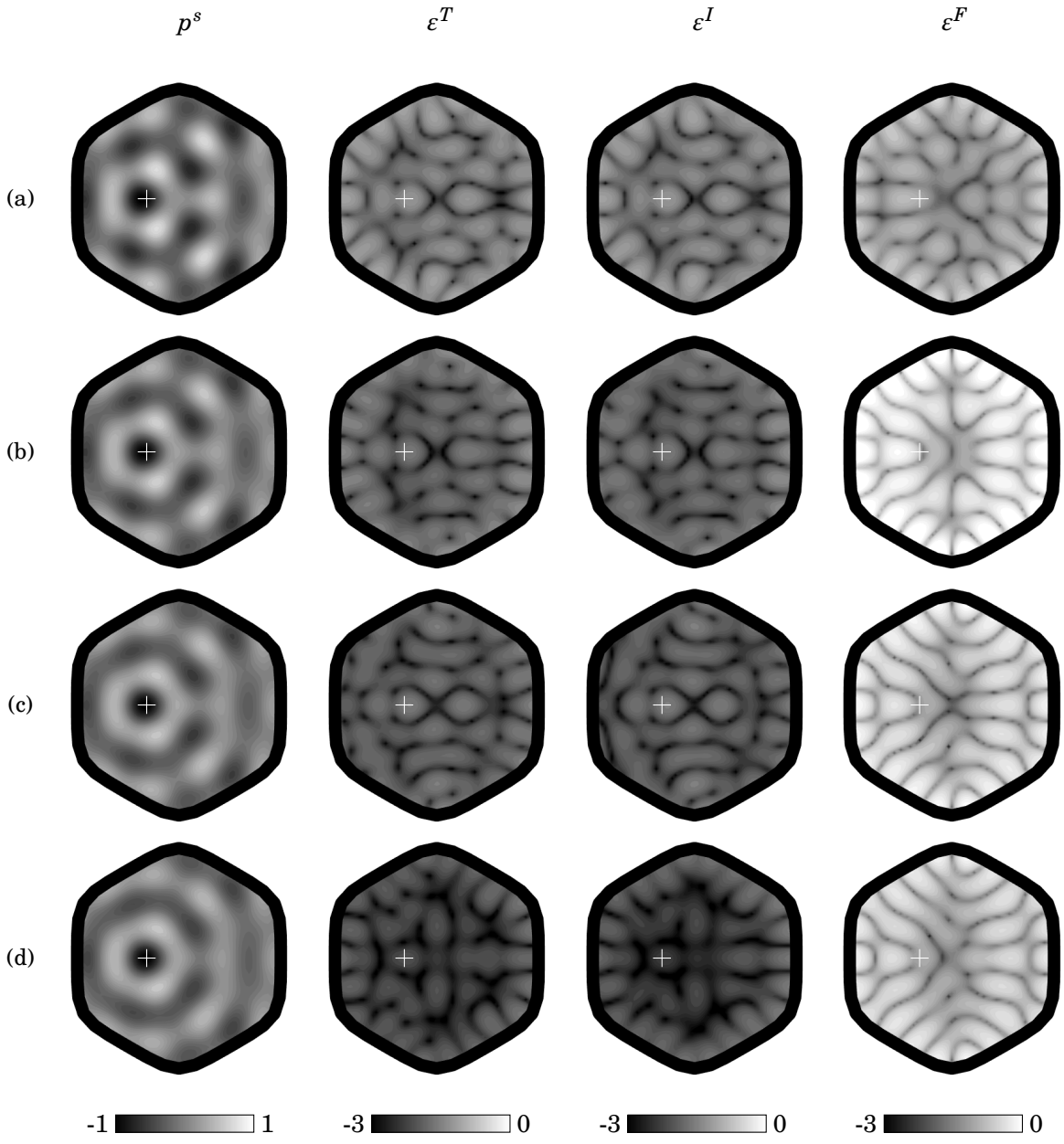

FIGURE D.5. Simulated VSFE-piezo analysis field for the smooth hexagonal shape with off-centred point source $r_o = 0.625\lambda$. Results are compared with various material modelling approximation levels. Real value analysis field p^s and approximating errors ε^T,ε^I,ε^F are in log scale, for Z_r = 11.25 (a), 15 (b), 18.75 (c),22.5 (d). White cross represents the point source position r_o

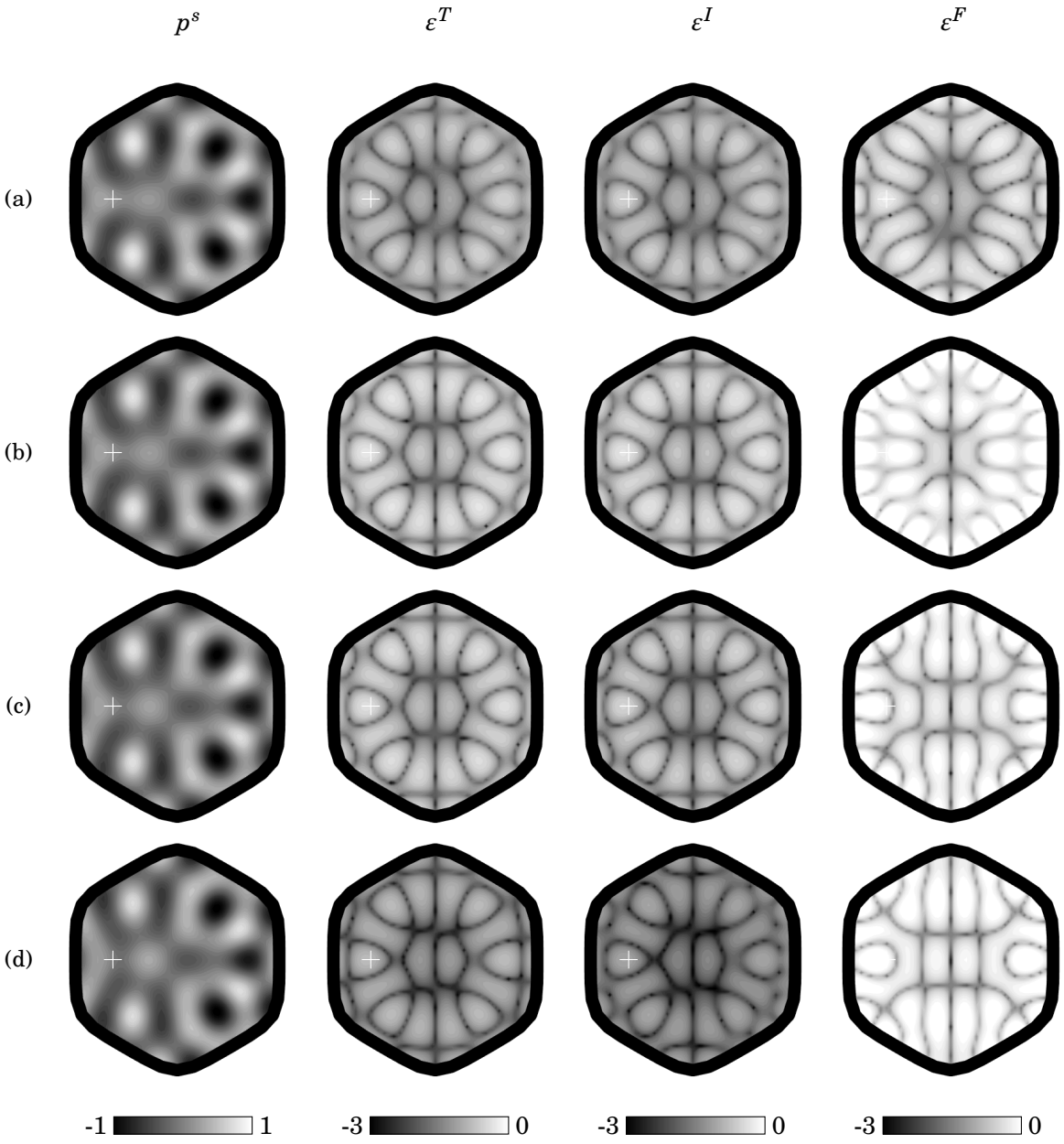

FIGURE D.6. Simulated VSFE-piezo analysis field for the smooth hexagonal shape with off-centred point source $r_o = 1.25\lambda$. Results are compared with various material modelling approximation levels. Real value analysis field p^s and approximating errors ε^T,ε^I,ε^F are in log scale, for $Z_r = 11.25$ (a), 15 (b), 18.75 (c),22.5 (d). White cross represents the point source position r_o

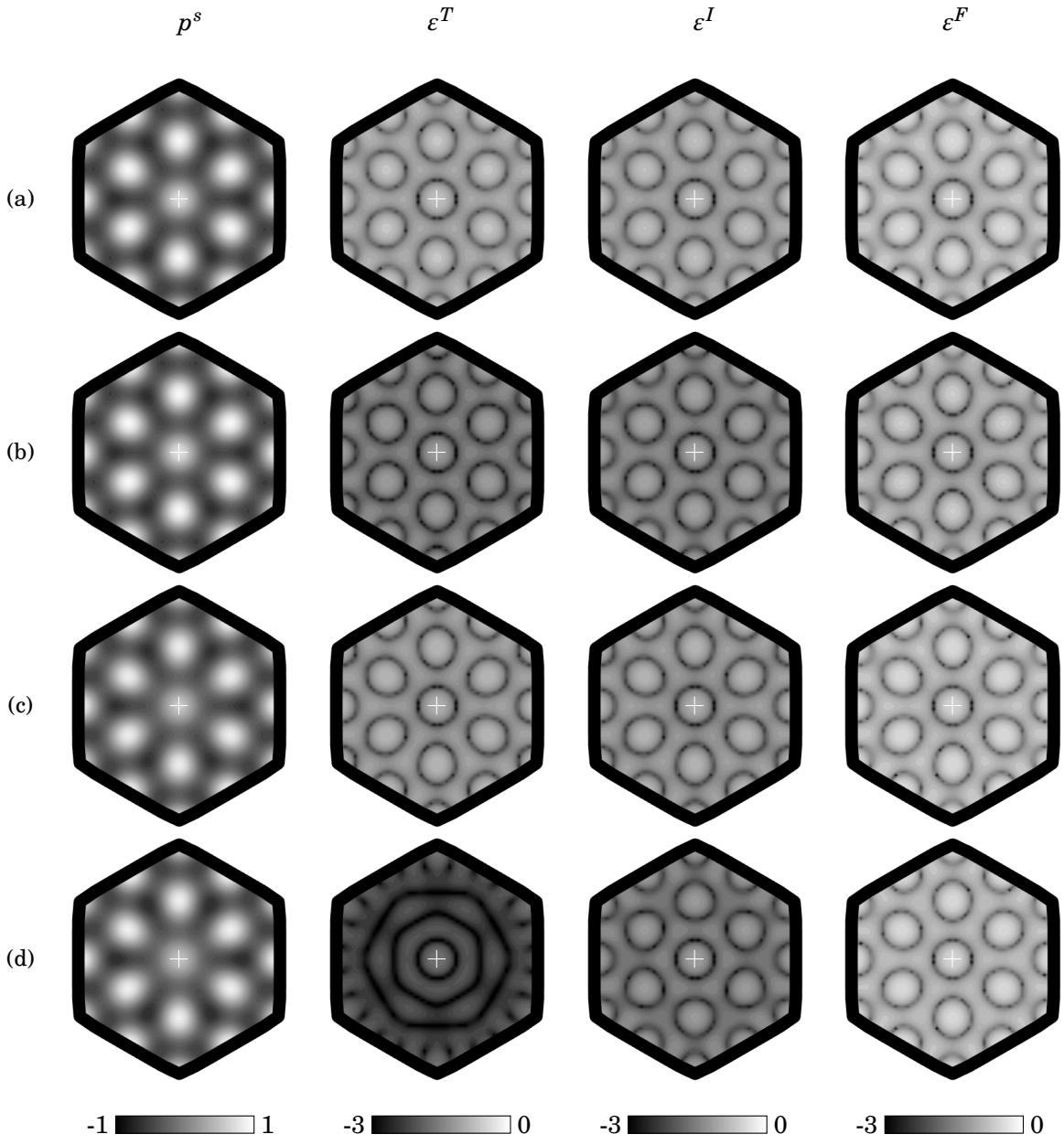

FIGURE D.7. Simulated VSFE-piezo analysis field for the sharp hexagonal shape with centred point source $r_o = 0$. Results are compared with various material modelling approximation levels. Real value analysis field p^s and approximating errors ε^T,ε^I,ε^F are in log scale, for $Z_r = 11.25$ (a), 15 (b), 18.75 (c),22.5 (d). White cross represents the point source position r_o

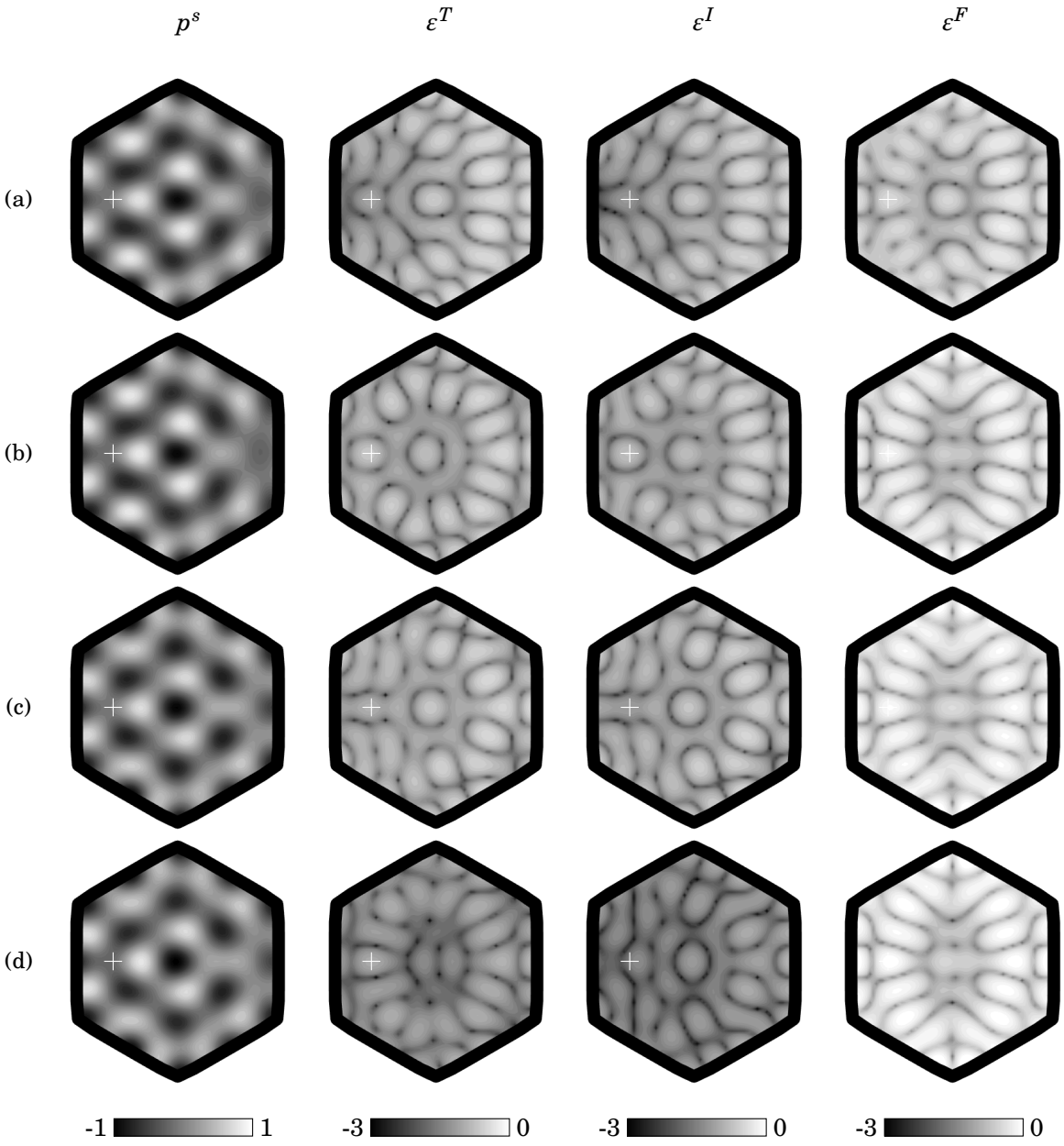

FIGURE D.8. Simulated VSFE-piezo analysis field for the sharp hexagonal shape with off-centred point source $r_o = 1.25$. Results are compared with various material modelling approximation levels. Real value analysis field p^s and approximating errors ε^T,ε^I,ε^F are in log scale, for $Z_r = 11.25$ (a), 15 (b), 18.75 (c),22.5 (d). White cross represents the point source position r_o

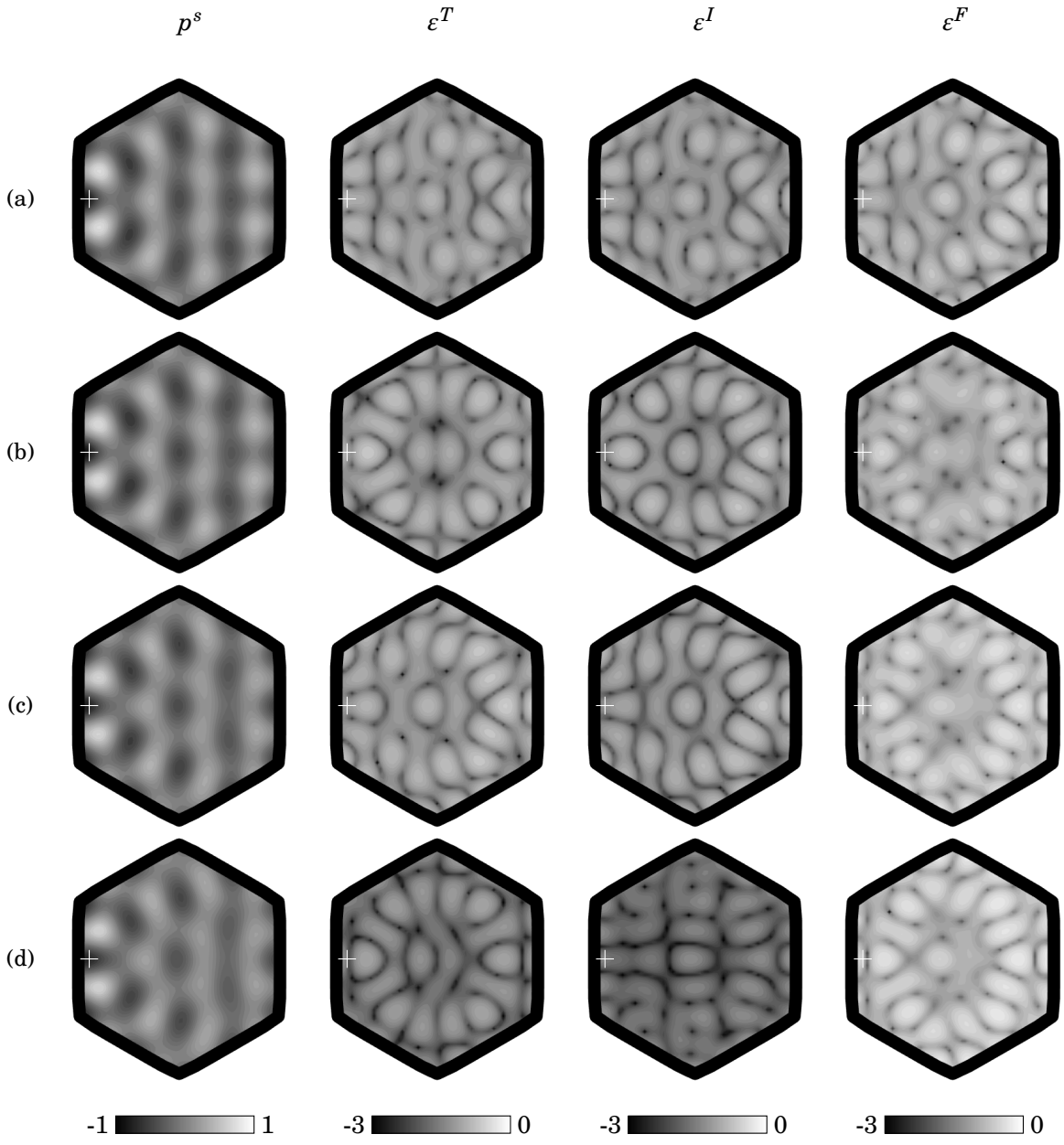

FIGURE D.9. Simulated VSFE-piezo analysis field for the sharp hexagonal shape with off-centred point source r_o = 1.75. Results are compared with various material modelling approximation levels. Real value analysis field p^s and approximating errors ε^T,ε^I,ε^F are in log scale, for Z_r = 11.25 (a), 15 (b), 18.75 (c),22.5 (d). White cross represents the point source position r_o

REFERENCES

M. Abramowitz. *Handbook of Mathematical Functions, With Formulas, Graphs, and Mathematical Tables,*. Dover Publications, Incorporated, 1974.

A. Abrar and S. Cochran. Mathematical Optimization of Multilayer Piezoelectric Devices with Nonuniform Layers by Simulated Annealing. *IEEE Transactions on Ultrasonics, Ferroelectrics, and Frequency Control*, 54(10):1920–1929, 2007.

H.-H. AC. and D. B. Finite Element Analysis of Piezoelectric Transducers. In A. E. Safari A., editor, *Piezoelectric and Acoustic Materials for Transducer Applications*. Springer, Boston, MA, 2008.

H. Allik and T. J. R. Hughes. Finite element method for piezoelectric vibration. *International Journal for Numerical Methods in Engineering*, 2(2):151–157, 1970.

M. A. B. Andrade and N. Pérez. Matrix method for acoustic levitation simulation. *IEEE Transactions On Ultrasonics Ferroelectrics and Frequency Control*, 58(8):1674–1683, 2011.

M. A. B. Andrade, F. Buiochi, and J. C. Adamowski. Finite element analysis and optimization of a single-axis acoustic levitator. *IEEE transactions on ultrasonics, ferroelectrics, and frequency control*, 57(2):469–79, 2010.

M. A. B. Andrade, N. Pérez, and J. C. Adamowski. Review of Progress in Acoustic Levitation. *Brazilian Journal of Physics*, 48(2):190–213, apr 2018.

X. Antoine and H. Barucq. On the Construction of Approximate Boundary Conditions for Solving the Interior Problem of the Acoustic Scattering Transmission Problem. In *Domain Decomposition Methods in Science and Engineering*, volume 40, pages 133–140. Springer-Verlag, Berlin/Heidelberg, 2005.

T. Asaki and P. Marston. Acoustic radiation force on a bubble driven above resonance. *The Journal of the Acoustical Society of America*, 96(November 1994):3096–3099, 1994.

F. Asano and D. C. Swanson. Sound equalization in enclosures using modal reconstruction. *The Journal of the Acoustical Society of America*, 98(4):2062–2069, 1995.

A. Ashkin, J. M. Dziedzic, J. E. Bjorkholm, and S. Chu. Observation of a single-beam gradient force optical trap for dielectric particles. *Optics Letters*, 11(5):288, 1986.

B. A. Auld, M. E. Drake, and C. G. Roberts. Monolithic acoustic imaging transducer structures with high spatial resolution. *Applied Physics Letters*, 25(9):478–479, 1974.

D. Baresch, J.-L. Thomas, and R. Marchiano. Three-dimensional acoustic radiation force on an arbitrarily located elastic sphere. *The Journal of the Acoustical Society of America*, 133(1): 25–36, 2013.

D. Baresch, J.-L. Thomas, and R. Marchiano. Observation of a Single-Beam Gradient Force Acoustical Trap for Elastic Particles: Acoustical Tweezers. *Physical Review Letters*, 116(2): 024301, jan 2016.

E. Benes, M. Groschl, H. Nowotny, F. Trampler, T. Keijzer, H. Bohm, S. Radel, L. Gherardini, J. J. Hawkes, R. Konig, and C. Delouvroy. Ultrasonic separation of suspended particles. In *Ultrasonics Symposium, 2001 IEEE*, volume 1, pages 649–659 vol.1, 2001.

A. J. Berkhout, D. de Vries, and P. Vogel. Acoustic control by wave field synthesis. *The Journal of the Acoustical Society of America*, 93(5):2764–2778, 1993.

A. Bernassau and D. Cumming. Acoustic tweezing at the nodes or antinodes of a heptagonal multi piezoelectric transducer cell. *2011 IEEE International Ultrasonics Symposium*, pages 1537–1540, 2011.

A. L. Bernassau, C. K. Ong, Y. Ma, P. G. A. Macpherson, C. R. P. Courtney, M. Riehle, B. W. Drinkwater, and D. R. S. Cumming. Two-dimensional manipulation of micro particles by acoustic radiation pressure in a heptagon cell. *IEEE Transactions on Ultrasonics, Ferroelectrics, and Frequency Control*, 58(10):2132–2138, 2011.

A. L. Bernassau, C. R. P. Courtney, J. Beeley, B. W. Drinkwater, and D. R. S. Cumming. Interactive manipulation of microparticles in an octagonal sonotweezer. *Applied Physics Letters*, 102 (16), 2013.

A. L. Bernassau, P. Glynne-Jones, F. Gesellchen, M. Riehle, M. Hill, and D. R. S. Cumming. Controlling acoustic streaming in an ultrasonic heptagonal tweezers with application to cell manipulation. *Ultrasonics*, 54(1):268–74, 2014.

E. A. Berndt and I. Sevostianov. Green's function for unbounded piezoelectric material of class 6. *International Journal of Solids and Structures*, 83:81–89, 2015.

T. Betlehem and T. D. Abhayapala. Theory and design of sound field reproduction in reverberant rooms., 2005.

R. T. Beyer. Radiation pressure-the history of a mislabeled tensor. *The Journal of the Acoustical Society of America*, 63(4):1025–1030, apr 1978.

J. J. Bowman, T. B. A. Senior, and P. L. E. Uslenghi. *Electromagnetic and acoustic scattering by simple shapes (Revised edition)*. New York, Hemisphere Publishing Corp., 1987.

D. Brill and H. Überall. Transmitted waves in the diffraction of sound from liquid cylinders. *The Journal of the Acoustical Society of America*, 47(5B):1467–1469, 1970.

H. Cao and J. Wiersig. Dielectric microcavities: Model systems for wave chaos and non-Hermitian physics. *Reviews of Modern Physics*, 87(1):61–111, 2015.

W. T. Coakley. Ultrasonic separations in analytical biotechnology. *Trends in biotechnology*, 15(12): 506–11, 1997.

W. T. Coakley, J. J. Hawkes, M. A. Sobanski, C. M. Cousins, and J. Spengler. Analytical scale ultrasonic standing wave manipulation of cells and microparticles. *Ultrasonics*, 38:638–641, 2000.

D. Colton and R. Kress. *Inverse Acoustic and Electromagnetic Scattering Theory*. Springer Science & Business Media, 2012.

D. Colton and R. Kress. *Integral Equation Methods in Scattering Theory*. Society for Industrial and Applied Mathematics, Philadelphia, PA, 2013.

COMSOL AB. Infinite elements. In *AC/DC Module User's Guide*, pages 310–321. COMSOL Multiphysics® v. 5.2., Stockholm, Sweden, 2015.

M. Costabel and E. Stephan. A direct boundary integral equation method for transmission problems. *Journal of Mathematical Analysis and Applications*, 106(2):367–413, mar 1985.

C. R. P. Courtney, C.-K. Ong, B. W. Drinkwater, P. D. Wilcox, C. Demore, S. Cochran, P. Glynne-Jones, and M. Hill. Manipulation of microparticles using phase-controllable ultrasonic standing waves. *The Journal of the Acoustical Society of America*, 128(4):EL195–9, 2010.

C. R. P. Courtney, C.-K. Ong, B. W. Drinkwater, a. L. Bernassau, P. D. Wilcox, and D. R. S. Cumming. Manipulation of particles in two dimensions using phase controllable ultrasonic standing waves. *Proceedings of the Royal Society A: Mathematical, Physical and Engineering Sciences*, 468(2138):337–360, 2011.

C. R. P. Courtney, B. W. Drinkwater, C. E. M. Demore, S. Cochran, A. Grinenko, and P. D. Wilcox. Dexterous manipulation of microparticles using Bessel-function acoustic pressure fields. *Applied Physics Letters*, 102(12):123508, 2013.

C. R. P. Courtney, C. E. M. Demore, H. Wu, A. Grinenko, P. D. Wilcox, S. Cochran, and B. W. Drinkwater. Independent trapping and manipulation of microparticles using dexterous acoustic tweezers. *Applied Physics Letters*, 104(15):154103, 2014.

J. Curie and P. Curie. Développement, par pression, de l'électricite polaire dans les cristaux hémièdres à faces inclinées. *Bulletin De La Sociétè Mineralogique de France*, 91:294–295, 1880.

A. Doicu, Y. Eremin, and T. Wriedt. Discrete sources method in acoustic theory. In *Acoustic and Electromagnetic Scattering Analysis Using Discrete Sources*, pages 67–92. Elsevier, 2000.

V. Domínguez, M.-L. Rapún, and F.-J. Sayas. Dirac delta methods for Helmholtz transmission problems. *Advances in Computational Mathematics*, 28(2):119–139, 2006.

B. Drinkwater. Dynamic-field devices for the ultrasonic manipulation of microparticles. *Lab Chip*, 16:2360–2375, 2016.

B. W. Drinkwater and P. D. Wilcox. Ultrasonic arrays for non-destructive evaluation: A review. *NDT and E International*, 39(7):525–541, 2006.

M. Drozdz, L. Moreau, M. Castaings, M. J. S. Lowe, and P. Cawley. Efficient numerical modelling of absorbing regions for boundaries of guided waves problems. *AIP Conference Proceedings*, 820 I(2006):126–133, 2006.

J. Dual and D. Möller. Acoustofluidics 4: Piezoelectricity and application in the excitation of acoustic fields for ultrasonic particle manipulation. *Lab on a Chip*, 12(3):506–514, 2012.

A. G. Every. General closed-form expressions for acoustic waves in elastically anisotropic solids. *Phys. Rev. B*, 22(4):1746–1760, 1980.

A. G. Every and A. K. McCurdy. Phonon focusing in piezoelectric crystals. *Physical Review B*, 36 (3):1432–1447, jul 1987.

A. Franklin, A. Marzo, R. Malkin, and B. W. Drinkwater. Three-dimensional ultrasonic trapping of micro-particles in water with a simple and compact two-element transducer. *Applied Physics Letters*, 111(9), 2017.

A. Gérard, H. Überall, and A. Guran. Generalized Debye series for acoustic scattering from objects of separable geometric shape. *Acta mechanica*, 176:147–176, 1999.

P. Glynne-Jones and M. Hill. Acoustofluidics 23: acoustic manipulation combined with other force fields. *Lab Chip*, 13(6):1003–1010, 2013.

P. Glynne-Jones, R. J. Boltryk, and M. Hill. Acoustofluidics 9: Modelling and applications of planar resonant devices for acoustic particle manipulation. *Lab on a chip*, 12(8):1417–26, 2012a.

P. Glynne-Jones, C. E. M. Démoré, C. Ye, Y. Qiu, S. Cochran, and M. Hill. Array-controlled ultrasonic manipulation of particles in planar acoustic resonator. *IEEE transactions on ultrasonics, ferroelectrics, and frequency control*, 59(6):1258–66, 2012b.

Gor'Kov, L P. On the forces acting on a small particle in an acoustical field in an ideal fluid. *Soviet Physics Doklady*, 6(9):773–775, 1962.

G. N. Greaves, A. L. Greer, R. S. Lakes, and T. Rouxel. Poisson's ratio and modern materials. *Nature Materials*, 10(11):823–837, 2011.

J. Greenhall, F. Guevara Vasquez, and B. Raeymaekers. Continuous and unconstrained manipulation of micro-particles using phase-control of bulk acoustic waves. *Applied Physics Letters*, 103(7):074103, 2013.

J. Greenhall, F. Guevara Vasquez, and B. Raeymaekers. Ultrasound directed self-assembly of user-specified patterns of nanoparticles dispersed in a fluid medium. *Applied Physics Letters*, 108(10), 2016.

A. Grinenko, P. D. Wilcox, C. R. P. Courtney, and B. W. Drinkwater. Proof of principle study of ultrasonic particle manipulation by a circular array device. *Proceedings of the Royal Society A-Mathematical Physical and Engineering Sciences*, 468(2147):3571–3586, 2012.

G.S. Settles. *Schlieren and shadowgraph techniques : visualizing phenomena in transparent media*. Springer Berlin Heidelberg, 2001.

P. Hahn, O. Schwab, and J. Dual. Modeling and optimization of acoustofluidic micro-devices. *Lab Chip*, 14(20):3937–3948, 2014.

R. F. Harrington. Time-Harmonic Electromagnetic Fields. In *Time-Harmonic Electromagnetic Fields*. McGraw-Hill, 1961.

T. Hasegawa. Acoustic radiation force on a sphere in a quasistationary wave field-experiment. *The Journal of the Acoustical Society of America*, 65(1):41–44, 1979.

T. Hasegawa and K. Yosioka. Acoustic Radiation Force on a Solid Elastic Sphere. *The Journal of the Acoustical Society of America*, 46(5):1139–1143, 1969.

M. Hill. The selection of layer thicknesses to control acoustic radiation force profiles in layered resonators. *The Journal of the Acoustical Society of America*, 114(5):2654, 2003.

M. Hill, R. J. Townsend, and N. R. Harris. Modelling for the robust design of layered resonators for ultrasonic particle manipulation. *Ultrasonics*, 48(6-7):521–8, 2008.

R. Hill. The Elastic Behaviour of a Crystalline Aggregate. *Proceedings of the Physical Society. Section A*, 65(5):349–354, may 1952.

Y. J. Hill M. andShen, J. J. Hawkes, M. Hill, Y. Shen, and J. J. Hawkes. Modelling of layered resonators for ultrasonic separation. *Ultrasonics*, 40(1-8):385–92, 2002.

R. O. H. Hoernig. *Green's Functions and Integral Equations for the Laplace and Helmholtz Operators in Impedance Half-spaces*. Pontificia Universidad Católica de Chile, 2010.

Z. Hong, J. Zhang, and B. W. Drinkwater. Observation of Orbital Angular Momentum Transfer from Bessel-Shaped Acoustic Vortices to Diphasic Liquid-Microparticle Mixtures. *Physical Review Letters*, 114(21):214301, 2015.

G. Hsiao and L. Xu. A system of boundary integral equations for the transmission problem in acoustics. *Applied Numerical Mathematics*, 61(9):1017–1029, 2011.

A. Ibáñez, C. Fritsch, M. Parrilla, and J. Villazón. Monochromatic transfer matrix method for acoustic field simulation thorough media boundaries. *Physics Procedia*, 3(1):883–890, 2010.

T. Ikeda. *Fundamentals of Piezoelectricity*. Oxford science publications. Oxford University Press, 1996.

S. Ise. A Principle of Sound Field Control Based on the Kirchhoff-Helmholtz Integral Equation and the Theory of Inverse Systems. *Acta Acustica united with Acustica*, 85(1), 1999.

John D. Cutnell and K. W. Johnson. *Physics, Volume Two: Chapters 18-32, Volume 2*. John Wiley & Sons, Carbondale, 2014.

D. A. Johnson and D. L. Feke. Methodology for fractionating suspended particles using ultrasonic standing wave and divided flow fields. *Separations Technology*, 5(4):251–258, 1995.

S.-T. K. S.-T. Kang and C.-K. Y. C.-K. Yeh. Potential-well model in acoustic tweezers. *IEEE Transactions on Ultrasonics, Ferroelectrics and Frequency Control*, 57(June):1451–1459, 2010.

J. T. Karlsen and H. Bruus. Acoustic Tweezing and Patterning of Concentration Fields in Microfluidics. *Physical Review Applied*, 7(3):1–10, 2017.

L. V. L. King. On the acoustic radiation pressure on spheres. *Proceedings of the Royal Society of London. Series A - Mathematical and Physical Sciences*, 147(861):212–240, 1934.

L. E. Kinsler. *Fundamentals of acoustics*. Wiley, New York ; Chichester, 3rd edition, 1982.

C. Y. Kiyono, N. Pérez, and E. C. N. Silva. Determination of full piezoelectric complex parameters using gradient-based optimization algorithm. *Smart Materials and Structures*, 25(2):25019, 2016.

T. Kozuka, T. Tuziuti, H. Mitome, and T. Fukuda. Acoustic micromanipulation using a multi-electrode transducer. In *MHS'96 Proceedings of the Seventh International Symposium on Micro Machine and Human Science*, pages 163–170. IEEE, oct 1996.

T. Kozuka, T. Tuziuti, H. Mitome, T. Fukuda, and F. Arai. Control of position of a particle using a standing wave field generated by crossing sound beams. *1998 IEEE Ultrasonics Symposium. Proceedings*, 1:657–660, 1998.

T. Kundu and D. Placko. Ultrasonic field modeling: a comparison of analytical, semi-analytical, and numerical techniques. *IEEE Transactions On Ultrasonics Ferroelectrics and Frequency Control*, 57(12):2795–2807, 2010.

L. D. Landau and E. M. Lifshits. *Fluid mechanics*. A-W series in advanced physics. Pergamon Press, 1959.

M. Lax and H. Feshbach. Absorption and Scattering for Impedance Boundary Conditions on Spheres and Circular Cylinders. *Journal of the Acoustical Society of America*, 20(2):108–124, 1948.

M. Lebental, N. Djellali, C. Arnaud, J.-S. Lauret, J. Zyss, R. Dubertrand, C. Schmit, and E. Bogomolny. Inferring periodic orbits from spectra of simply shaped microlasers. *Physical Review A*, 76(2):023830, 2007.

S. Lee. Review: The Use of Equivalent Source Method in Computational Acoustics. *Journal of Computational Acoustics*, 25(01):1630001, 2017.

R. Lerch. Simulation of piezoelectric devices by two- and three-dimensional finite elements. *IEEE transactions on ultrasonics, ferroelectrics, and frequency control*, 37(3):233–47, 1990.

S. Li, L. Zheng, W. Jiang, R. Sahul, V. Gopalan, and W. Cao. Characterization of full set material constants of piezoelectric materials based on ultrasonic method and inverse impedance spectroscopy using only one sample. *Journal of Applied Physics*, 114(10):104505, 2013.

T. M. Llewellyn-Jones, B. W. Drinkwater, and R. S. Trask. 3D printed components with ultrasonically arranged microscale structure. *Smart Materials and Structures*, 2016.

A. E. H. Love. A Treatise on the Mathematical Theory of Elasticity. *Dover Publishers, New York*, pages 163–164, 1906.

V. Mallardo and M. Aliabadi. Boundary element method for acoustic scattering in fluid-fluidlike and fluid-solid problems. *Journal of Sound and Vibration*, 216(3):413–434, sep 1998.

P. L. Marston. Radiation force of a helicoidal Bessel beam on a sphere. *The Journal of the Acoustical Society of America*, 125(6):3539–3547, 2009.

P. L. Marston. Phase-shift expansions for approximate radiation forces on solid spheres in inviscid-acoustic standing waves. *The Journal of the Acoustical Society of America*, 142(6): 3358–3361, 2017.

V. Marx. Biophysics : using sound to move cells. *Nature Publishing Group*, 12(1):41–44, 2015.

A. Marzo, S. A. Seah, B. W. Drinkwater, D. R. Sahoo, B. Long, and S. Subramanian. Holographic acoustic elements for manipulation of levitated objects. *Nature Communications*, 6(May): 8661, 2015.

A. B. Matsko and V. S. Ilchenko. Optical resonators with whispering-gallery modes - Part I: Basics, 2006.

J. D. Maynard, E. G. Williams, and Y. Lee. Nearfield acoustic holography: I. Theory of generalized holography and the development of NAH. *The Journal of the Acoustical Society of America*, 78(4):1395–1413, 1985.

K. Melde, A. G. Mark, T. Qiu, and P. Fischer. Holograms for acoustics. *Nature*, 537(7621):518–522, 2016.

F. G. Mitri. Acoustic radiation force on a sphere in standing and quasi-standing zero-order Bessel beam tweezers. *Annals of Physics*, 323(7):1604–1620, 2008.

F. G. Mitri. Acoustic radiation force of high-order Bessel beam standing wave tweezers on a rigid sphere. *Ultrasonics*, 49(8):794–798, 2009.

F. G. Mitri and Z. E. A. Fellah. New expressions for the radiation force function of spherical targets in stationary and quasi-stationary waves. *Archive of Applied Mechanics*, 77(1):1–9, 2006.

F. G. Mitri and G. T. Silva. Off-axial acoustic scattering of a high-order Bessel vortex beam by a rigid sphere. *Wave Motion*, 48(5):392–400, 2011.

P. M. Morse. *Methods of Theoretical Physics part I*. McGraw-Hill, New York, NY, 1954.

P. Nelson. Active Control Of Acoustic Fields And The Reproduction Of Sound. *Journal of Sound and Vibration*, 177(4):447–477, 1994.

K. C. Neuman and S. M. Block. Optical trapping. *Review of Scientific Instruments*, 75(9): 2787–2809, 2004.

A. Nilsson, F. Petersson, H. Jönsson, and T. Laurell. Acoustic control of suspended particles in micro fluidic chips. *Lab Chip*, 4(2):131–135, 2004.

J. U. Nöckel and A. D. Stone. Ray and wave chaos in asymmetric resonant optical cavities. *Nature*, 385(6611):45–47, 1997.

S. Oberti, A. Neild, and J. Dual. Manipulation of micrometer sized particles within a micromachined fluidic device to form two-dimensional patterns using ultrasound. *The Journal of the Acoustical Society of America*, 121(2):778–785, 2007.

D. Placko and T. Kundu. *DPSM for Modeling Engineering Problems*. Wiley, 2007.

M. A. Poletti and T. D. Abhayapala. Interior and exterior sound field control using general two-dimensional first-order sources. *The Journal of the Acoustical Society of America*, 129(1): 234–44, 2011.

W. H. Press, S. A. Teukolsky, W. T. Vetterling, and B. P. Flannery. *Numerical Recipes in C (2Nd Ed.): The Art of Scientific Computing*. Cambridge University Press, New York, NY, USA, 1992.

M. Prisbrey, J. Greenhall, F. Guevara Vasquez, and B. Raeymaekers. Ultrasound directed self-assembly of three-dimensional user-specified patterns of particles in a fluid medium. *Journal of Applied Physics*, 121(1), 2017.

Y. Qiu, H. Wang, S. Gebhardt, A. Bolhovitins, C. E. M. Démoré, A. Schönecker, and S. Cochran. Screen-printed ultrasonic 2-D matrix array transducers for microparticle manipulation. *Ultrasonics*, 62:136–46, 2015.

P. Rajagopal, M. Drozdz, E. A. Skelton, M. J. S. Lowe, and R. V. Craster. On the use of absorbing layers to simulate the propagation of elastic waves in unbounded isotropic media using commercially available Finite Element packages. *NDT and E International*, 51:30–40, 2012.

P. Raju, S. Rao, and S. Sun. Application of the method of moments to acoustic scattering from multiple infinitely long fluid filled cylinders. *Computers & Structures*, 39(1-2):129–134, 1991.

L. Rayleigh. XXXIV. On the pressure of vibrations. *The London, Edinburgh, and Dublin Philosophical Magazine and Journal of Science*, 3(15):338–346, 1902.

L. Rayleigh. CXII. The problem of the whispering gallery. *The London, Edinburgh, and Dublin Philosophical Magazine and Journal of Science*, 20(120):1001–1004, 1910.

A. Riaud, M. BauCdoin, J.-L. Thomas, and O. Bou Matar. Cyclones and attractive streaming generated by acoustical vortices. *Physical Review E*, 90(1):013008, 2014.

A. Riaud, J. L. Thomas, E. Charron, A. Bussonnière, O. Bou Matar, and M. BauCdoin. Anisotropic Swirling Surface Acoustic Waves from Inverse Filtering for On-Chip Generation of Acoustic Vortices. *Physical Review Applied*, 4(3):1–10, 2015.

M. Saito, T. Daian, K. Hayashi, and S.-y. Izumida. Fabrication of a polymer composite with periodic structure by the use of ultrasonic waves. *Journal of Applied Physics*, 83(7):3490, 1998.

M.-S. Scholz, B. Drinkwater, and R. Trask. Ultrasonic assembly of anisotropic short fibre reinforced composites. *Ultrasonics*, 54(4):1015–9, 2014.

A. Seybert, C. Cheng, and T. Wu. The solution of coupled interior/exterior acoustic problems using the boundary element method. *The Journal of the Acoustical Society of America*, 88 (September 1990):1612–1618, 1990.

A. F. Seybert, B. Soenarko, F. J. Rizzo, and D. J. Shippy. A special integral equation formulation for acoustic radiation and scattering for axisymmetric bodies and boundary conditions. *Journal of the Acoustical Society of America*, 80(4):1241–1247, 1986.

F. Shi, W. Choi, E. A. Skelton, M. J. Lowe, and R. V. Craster. A time-domain finite element boundary integration method for ultrasonic nondestructive evaluation. *IEEE Transactions on Ultrasonics, Ferroelectrics, and Frequency Control*, 61(12):2054–2066, 2014.

W. Shockley, D. Curran, and D. Koneval. Energy Trapping and Related Studies of Multiple Electrode Filter Crystals. In *17th Annual Symposium on Frequency Control*, pages 88–126. IEEE, 1963.

E. C. N. Silva. Synthesis with Piezoelectric Actuation. In S. Ananthasuresh, editor, *Optimal Synthesis Methods for MEMS*, volume 13 of *Microsystems*. Springer US, Boston, MA, 2003.

G. T. Silva. An expression for the radiation force exerted by an acoustic beam with arbitrary wavefront (L). *The Journal of the Acoustical Society of America*, 130(6):3541–3544, 2011.

G. T. Silva and H. Bruus. Acoustic interaction forces between small particles in an ideal fluid. *Physical Review E - Statistical, Nonlinear, and Soft Matter Physics*, 90(6):1–11, 2014.

G. W. Stewart. On the Early History of the Singular Value Decomposition. *SIAM Review*, 35(4): 551–566, 1993.

J.-L. Thomas and R. Marchiano. Pseudo angular momentum and topological charge conservation for nonlinear acoustical vortices. *Physical review letters*, 91(24):244302, 2003.

J.-L. Thomas, R. Marchiano, and D. Baresch. Acoustical and optical radiation pressure and the development of single beam acoustical tweezers. *Journal of Quantitative Spectroscopy and Radiative Transfer*, 195:55–65, 2017.

J. F. Thompson, Z. U. A. Warsi, and C. Wayne Mastin. Boundary-fitted coordinate systems for numerical solution of partial differential equations. *Journal of Computational Physics*, 47 (1):1–108, 1982.

H. F. Tiersten. Thickness Vibrations of Piezoelectric Plates. *Journal of the Acoustical Society of America*, 35(1):53–58, 1963a.

H. F. Tiersten. Wave Propagation in an Infinite Piezoelectric Plate. *The Journal of the Acoustical Society of America*, 35(2):234–239, 1963b.

H. F. Tiersten. Hamiltons Principle For Linear Piezoelectric Media. *Proceedings of the Institute of Electrical and Electronics Engineers*, 55(8):1523–1524, 1967.

W. Tobocman. Calculation of acoustic wave scattering by means of the Helmholtz integral equation. II. *Journal of the Acoustical Society of America*, 76(5):1549–1554, 1984.

A. Velichko and P. D. Wilcox. A generalized approach for efficient finite element modeling of elastodynamic scattering in two and three dimensions. *The Journal of the Acoustical Society of America*, 128(3):1004–14, 2010.

P. C. Waterman. New Formulation of Acoustic Scattering. *The Journal of the Acoustical Society of America*, 45(6):1417, 1969.

J. Wiersig. Hexagonal dielectric resonators and microcrystal lasers. *Physical Review A*, 67(2): 023807, 2003a.

J. Wiersig. Boundary element method for resonances in dielectric microcavities. *Journal of Optics A: Pure and Applied Optics*, 5(1):53–60, 2003b.

P. D. Wilcox and A. Velichko. Efficient frequency-domain finite element modeling of two-dimensional elastodynamic scattering. *The Journal of the Acoustical Society of America*, 127 (1):155–65, 2010.

E. G. Williams. *Fourier Acoustics: Sound Radiation and Nearfield Acoustical Holography*. Academic Press, 1999.

J. Wu. Acoustical tweezers. *The Journal of the Acoustical Society of America*, pages 2140–2143, 1991.

Y. Yamamoto and R. E. Slusher. Optical Processes in Microcavities. *Physics Today*, 46(6):66–73, 1993.

K. Yosioka and Y. Kawasima. Acoustic radiation pressure on a compressible sphere. *Acta Acustica united with Acustica*, 5(3):167–173, 1955.

O. C. Zienkiewicz. *The finite element method : its basis and fundamentals.* Elsevier Butterworth-Heinemann, Amsterdam, 6th ed. / edition, 2005.

O. C. Zienkiewicz and Y. K. Cheung. *The finite element method in structural and continuum mechanics*. Number v. 1 in European civil enginering series. McGraw-Hill, 1967.